

NETS - 2017

Nuclear and Emerging Technologies for Space

ANS Aerospace Nuclear Science and Technology Division

CONFERENCE PROCEEDINGS



Table of Contents

Paper 19763 – <i>A New Manned Space Flight Mission for NASA</i>	1
Paper 20048 – <i>Nuclear & Thermal Hydraulic Design for a Low-Enriched Nuclear Thermal Rocket</i>	9
Paper 20099 – <i>The Paucity Problem: Where Have All the Space Reactor Experiments Gone?</i>	19
Paper 20157 – <i>Overview of Rayleigh-Taylor Instability & the Impact on Target Design for a Pulsed Fusion / Fission Propulsion System</i>	29
Paper 20159 – <i>Progress on Fusion Modeling & the Charger-1 Pulsed Power Facility at UAH</i>	37
Paper 20176 – <i>Analysis of Operating Strategies Using Alternative Target Designs for ²³⁸Pu Production</i>	45
Paper 20177 – <i>Optimal Nuclear Thermal Propulsion Thrust Level for Human Mars Exploration</i>	55
Paper 20182 – <i>Idaho National Laboratory Radioisotope Power Systems Nuclear Operations: Readiness Assessments Supporting a Nuclear-enabled NASA Mission</i>	66
Paper 20183 – <i>Cassini Power Subsystem</i>	74
Paper 20194 – <i>10 We Radioisotope Thermophotovoltaic (RTPV) Power Source Demonstration</i>	82
Paper 20224 – <i>Thermal-Control Consideration & Preliminary Analysis of a Heat Pipe Cooled Space Reactor Power System</i>	90
Paper 20458 – <i>Criticality Safety Design and Analysis of the Heat-pipe Nuclear Reactor</i>	100
Paper 20482 – <i>Control System Requirements for a Nuclear Thermal Propulsion System</i>	108
Paper 20484 – <i>Updated Mars Mission Architectures Featuring Nuclear Thermal Propulsion</i>	118
Paper 20512 – <i>Zirconium – Rates of Reaction for a Common Getter Material</i>	125
Paper 20536 – <i>Robust Exploration & Commercial Missions to the Moon Using NTR / LANTR Propulsion & Lunar-Derived Propellants</i>	135
Paper 20537 – <i>Optimization of Radiation Shielding for Space Nuclear Propulsion</i>	143
Paper 20547 – <i>Survey of Fuel System Options for Low Enriched Uranium (LEU) Nuclear Thermal Rockets</i>	153
Paper 20574 – <i>Autonomy for Space Reactor Power Systems</i>	165
Paper 20575 – <i>TERRA Project: A Brazilian View for Nuclear Energy Application to Space Exploration</i>	172
Paper 20591 – <i>ELMOE: Europa Lander, Melter, & Oceanic Explorer</i>	180

A New Manned Space Flight Mission for NASA

Philip C. Fisher

*Ruffner Associates, LTD., 5306 Peace Court, Fairfield, CA 94533
1-707-427-8035, pcfisher@earthlink.net*

Abstract. Definition of a manned space flight mission into deep space was initiated by an unsolicited proprietary proposal to NASA Headquarters in February 1973. That and subsequent similar proposals to NASA of 1998, 2004, and 2013 are contained in the Philip C. Fisher Papers of the Niels Bohr Library and Archives of the American Institute of Physics (scheduled to be publicly available one year after the author's death). Part of the contents of the 1998 proposal was published in 1999. By 2013 the five technical variables of 1998 had increased to over ten. An updated version of the effort was published last year when it was stated the proposed effort seemed to be superior to any effort that NASA had publicly advocated. To help "size" the effort two tables from 2016 and additional data are presented here. The purpose of this presentation is to encourage NASA to use the information provided to decide if it is willing to ask the United States Congress to fund the first flight of the mission involving a few specified leading governing nations plus all other interested qualifying governments.

Keywords: manned space flight, nuclear reactor.

INTRODUCTION

In 1972 and 1973 while on an unpaid leave of absence from the Lockheed Missiles and Space Company the subject of this talk [1] was conceived. Although only an experiment, or mission, objective was identified, the effort was proposed to NASA Headquarters. About a year later Lockheed and I parted company. Many years later work on the subject was fairly quietly resumed. Still later, in 1994 I was surprised to receive encouragement in the form of requests for biographical information. The data provided were published in 1997 [2] (and 2005 [3] respectively) and publication caused me to pursue today's subject further. The description of the effort has been divided into four segments, the first being this introduction.

The second segment of the talk describes some features of my first or 1998 attempt at a comprehensive proposal [4], an unusual venue for meetings was proposed to distinguish the effort from other NASA programs. Part of the proposal was published [5]. Additional data about defining and costing technical variables were added in several subsequent proposals [6, 7]. The final proposal was submitted in 2013. A distinguishing feature of all these proposals (and the 1999 publication) was the need to define a suitable means of propulsion. The 1998 proposal naively ignored astronaut protection from cosmic radiation. The cover page of the 2013 proposal is included here.

The third segment presents a table updating the elementary characteristics of two flights published seventeen years earlier. Three modes of propulsion were included, and one was selected to illustrate tasks to define and cost the first flight. Both the elementary characteristic and task data [8] are reproduced here. Although seven references were used to select the means of propulsion and five reference were used to consider cosmic ray effects on astronauts, none of this information was discussed. Some additional management features were described and it was noted that the mission seemed superior to any publicly advocated by NASA.

A fourth segment brings efforts up to date. There is now at least one (private) corporation, SpaceX, seeking to colonize Mars so NASA supremacy in that area may not be feasible. Presumably NASA's Technology Roadmap

program is developing resources for a deep space mission. Some new comments are given that would permit very crude cost estimates to be made.

In the last segment my conclusions are given in the form of several questions.

EFFORT EVOLUTION TO 2013

The brief first table in the 1999 publication presented potential parameters for two related flights. The main purpose was to hold a meeting to define the best primary propulsion system of the first flight. At the time the gas dynamic fusion reactor of Terry Kammash [9] seemed the best choice. He gave a table for the mass of fuel needed and the time required to fly round-trip missions to several planets. I arbitrarily selected a seven-year flight involving a planet Pluto flyby. So the first problem was to find a means of propulsion or situation where the fuel mass of Kammash could be reduced enough that a manned spacecraft could be included. If the best propulsion device could be agreed upon it was hoped yearly extensions of the effort might take place until four other technical variables could be established.

Two items in the acknowledgement section of the 1999 publication were: first, that the related proposal was written while I was on an unpaid leave of absence from Lockheed; and second, that both NASA and Lockheed "may possess proprietary rights...to the information presented". While there is FedEx waybill data proving the 2004 proposal was received as intended, there is no proof that it or any earlier proposal was read or evaluated.

Now note some management features of the 2013 proposal cover page given in Figure 1. The most obvious feature is that the proposal is addressed first to the Governing Board (now the Board of Trustees) of the American Institute of Physics (or AIP) and then to the Administrator of NASA and the General Counsel of the Lockheed Martin Corporation. The fourteen-year earlier publication also said both NASA and Lockheed "may possess some proprietary rights."

The proposal suggested speakers and observers for a first meeting to discuss propulsion and astronaut shielding from cosmic rays. A Cost Review Team was discussed, and a very detailed cost estimate for a paper study to determine mission costs was made. Costs NASA had already committed to for prototype components for existing programs were not included. The proposal was prepared with minimal research into related NASA progress.

FedEx waybill data show the 2013 proposal was delivered to the desired addressees, but after a day or two the NASA copy was returned to me unopened. Several possibilities for this behavior exist. Based on somewhat obscure historical records I have thought of a small variety of possibilities for this behavior, and they have been documented.*

2016 UPDATE OF EFFORT

To update the 2013 proposal, many documents related to NASA plans for Mars and related activities were read. An abstract for an American Physical Society talk noting some of this knowledge was submitted. It was only after the abstract was accepted that it was learned only 12 minutes was allotted for the talk.

The table of elementary flight characteristics published seventeen years earlier was revised as shown in Table 1. There was no time to discuss any of the entries in the table. But the concern about primary propulsion had now been partially resolved by NASA's heavy lift rocket program which split lifting things off the ground to launching things from somewhere in space. Three means of spacecraft primary propulsion were listed in the table. A magnetoplasma engine was chosen to help illustrate the various tasks (see Table 2 at end of this section) in a mission that needed to be evaluated technically and costed. In retrospect, several errors in commission and omission were made.

Much of the 2016 update was concerned with securing international cooperation in the management of individual tasks, as well as the senior management of the complete effort. I believe the effort could not be successful without China in a leadership role, and for this to happen the United States Congress must waive its law preventing Chinese

PROPOSAL TO INITIATE
MANNED INTERSTELLAR/INTERGALACTIC SPACE FLIGHT, III

Unsolicited proposal submitted to:

Governing Board of the American Institute of Physics

14 February 2013,
and:

Administrator, National Aeronautics and Space Administration;

General Counsel, Lockheed Martin Corp.;

16 April 2013.

first year contract requested start date: 1 October 2013

Philip C. Fisher
Ruffner Associates. LTD.
5306 Peace Court
Fairfield, California 94533

NON-RESPONSIBILITY STATEMENT (from source document of calendar 1973)

This document was prepared while the author was on an unpaid leave of absence from The Lockheed Missiles and Space Company (LMSC) of Palo Alto, California. The comments made herein are partly the results of experiments carried out over a number of years. For a portion of this time, both the National Aeronautics and Space Administration (NASA) and LMSC financed the author's space astronomy investigations. It may be that either or both these institutions may possess some proprietary rights to portions of the ideas and information presented.

NOTICE: The information (data) contained in this proposal is privileged information. It is furnished to the Government in confidence with the understanding that it will not, without permission of the offeror, be used or disclosed other than for evaluation purposes; provided, however that in the event an agreement is reached to conduct the effort described in this proposal, the Government shall have the right to use and disclose this information (data) to the extent provided in the contract (or other agreement). This restriction does not limit the Government's right to use or disclose this information (data) if obtained from another source without restriction.

FIGURE 1. Copyrighted data taken from Fisher [7], and reprinted by permission of the AIP.

TABLE 1. Flight Characteristics, Second Approximation

	First Flight	Second Flight
Launch year	~2035	~2050
Launch time	before solar minimum (or anytime, ?)	anytime, ?
Solar flare shielding	yes, trivial	yes, trivial
Cosmic ray shielding	yes?, how much	yes?, how much
Flight duration (years)	7	20, ?
Crew size	24	44 initially, 88 max
Crew age (years)	>40	few > 30
Primary propulsion	nuclear electric, hypergolic, magnetoplasma	to be determined
Characteristic	free of all planets gravity	one way prototype

Copyrighted data taken from Fisher [8], and reprinted by permission of the AIP.

participation in at least this United States space activity.

The last figure of the 2016 update repeated the goal of the 1973 proposal, which is given in Figure 2. So my proposal is not a deep space mission for the sake of scientific exploration. Just like Horoshima and Nagasaki, the proposal is an experiment in psychology. To distinguish the effort from other NASA programs, as in the 1998 proposal to NASA, this talk suggests that if they were willing the venue for infrequent meetings should be The Hoover Institution for War Revolution and Peace, at Stanford, California. It is suggested that the first group of nations to provide senior scientific individuals to supplement the original very small oversight team should come from nations that do not tolerate Islamic militants, or nuclear proliferators, and act to respect the sovereignty and territorial integrity of other nations, and possess atomic weapons and ballistic missiles to deliver those weapons. I concluded the 2016 talk by saying what I thought was obvious, and that was that for over forty years I had believed that if it chose to do so, NASA could make a unique contribution to world peace.

B. First Flight Objectives and Priorities

The primary goal of the first manned interstellar flight is here defined as sending an international crew as far outside the solar system as possible. By arbitrary definition, the flight must be sufficiently perilous that the crew might not return. Having the lives of its own countrymen at stake should provide a strong incentive for cooperation by the nations that might participate.

FIGURE 2. Copyrighted data taken from Fisher [1], retyped and printed by permission of the AIP. (Figure number and caption are differently arranged on copyright-applied-for version of this paper.)

FedEx waybill data shows the (later published) 2016 peace manuscript was received by NASA Headquarters for the Administrator of NASA and by Lockheed Martin for the General Counsel of the Lockheed Martin Corporation. When awarded the copyright of the copyright applied for manuscript will be assigned to the AIP if time permits.

Table 2 referred to earlier is given on the next page. At the left of each line is a task to be performed and at the right of each line is a preferred provider. In retrospect, there were errors of commission and omission.

CURRENT STATUS

To further understand the situation, some mostly speculative comments are continued.

In 2015 NASA let eight grants to start developing a means to convert solid human waste into edible food. [10]. How to do this and what efficiency can be achieved are not known. Since the grants are moon and Mars oriented, the large volume required to grow and tend plants is not a major constraint as would be the case in a flight mission. It is also assumed that a process without a plant growing phase is more complicated and more subject to breakdown.

TABLE 2. Potential Meetings for Various Activities (second cut, made early 2016)

1. Program Description Philosophy, Contract/Grant Philosophy	
Reports: Magnetoplasma Engine Development	[J. Tate, A. Semekin, ITER-?]
Genomic Change Tolerances	[NASA-?, N. Buckley]
Spacecraft Design (Custom Modules, Bigelow Array, or?)	[V. de Korver, ?]
Food/Recycle	[present U.S. Contractor, China-?, G/K. O’Neil]
Computer Requirements	[G. Lazana, Dell-?, Samsung-?]
NASA Schedule Synchronization	[C. Miller, India-?]
Encourage International Interest, Commitment (contracts/grants)	
Define/Let Contracts. Grants to Secure Better Technical Answers and Cycle	
2. Preliminary Technical Reports for First Meeting Contracts/Grants	
Spacecraft Assembly (Leo, lunar, cislunar, L5)	[V. de Korver, ESA-?]
Crew Assembly (including return to earth)	[V. de Korver, ?]
Primary Engine Propellant Accumulation (and connections)	[C. Miller, Palestine-?]
Primary Propulsion Backup (to salvage crew)	[Pakistan,?, Israel-?]
Micrometeorite, Orbital Debris, Oort Cloud Shielding	[Palestine-?, England-?]
Water for Drinking, H for Shielding	[Mexico-?, LLNL-?]
Tertiary Propulsion (Backup Vernier Trajectory, salvage crew)	[INL-?, Germany-?]
On-Board Power for Crew/Instruments (shadow shielding, ?)	[Jordan-?, France-?]
Power for Crew/Instruments Backup (shadow shielding-?)	[C. Morrison, India-?]
Tertiary Propulsion (Three-fold Redundant Vernier Adjustment for Spacecraft Trajectory (crew salvage)	[China-?, ?-?]
Crew Demographics (need 2 psychologists, ethnicity, gender)	[Oversight Team]
Medical Provisions (magnetic fields, radiation)	[NASA-?, Brazil-?]
Define/Let Contracts/Grants to Secure Better Technical Answers and Costs	
3. Publish/Review Final Reports of First Year Meeting Contracts/Grants	
Preliminary Technical Reports on Second Meeting Contracts/Grants	
Crew Training (by function)	[NASA-?, Egypt-?]
Program Critique to Guide/Correct (2x\$)	[NASA-Goddard-?, JPL-?, Bechtel]
Science Program and Instrumentation	
Plasma Physics	[D. McCammon, J. Cladis, M. Walt, R. L. McNutt, Jr.]
Exoplanet “Telescope”	[NASA-Ames-?, ESO-?]
Other Astronomical Investigations/Apparatus	[J. S. Mulchaey, Byurakan-?]
Cost Review Team Present First Cost Estimate	
Discuss Participation and Cost Sharing with Other Nations	
Define/Let Contracts/Grants to Secure Better Technical Answers and Costs	
4. Publish/Review Final Reports for Second Year Meeting Contracts/Grants	
Preliminary Technical Reports on Third Meeting Contracts/Grants	
Review Program for Safety	[Riken Keiki Fine-?, Malaysian Air Lines-?]
Mission Profile (Free of Pluto Gravity)	[Saudi Arabia-?, A. Semekin]
Seven Year Crew Launch to Recovery (based on ISS)	[NASA-HQ-?]
Cost Review Team Present Second Cost Estimate	
Seek Financial Commitments from Interested Nations	
Second Flight	[R. Zubrin, T. Kammash, F. Chang Diaz, A. Kazykin, +?]
Define/Let Contracts/Grants to Secure Better Technical Answers and Costs	
5. Publish Final Reports for Last Two Meetings, Review All Technical Reports	
Cost Review Team Last Cost Estimate	
Review Financial Commitments from Interested Nations	
Submit Results to NASA for Review and Submission to U.S. Congress	

Copyrighted data taken from Fisher [8], and reprinted by permission of the AIP.

Until further information becomes available on each approach the only conservative approach is the procedure involving growing plants. This would probably require an astronaut accessible volume at least comparable to that for the astronauts. And this must include an allowance for at least the water required for the conversion process.

Eugene Parker [11] was the first to evaluate the increased risk of cancer due to an astronaut's prolonged exposure to cosmic rays, and to describe several means to reduce the exposure. Of the order of five heavy lift rockets might be required to lift enough hydrogen rich material to shield an orbiting astronaut adequately. Several years ago CERN scientists were working on superconducting coils to produce a magnetic field [12] to shield astronauts and several other approaches are now being examined. NASA has now performed an experiment involving a pair of identical twins, one in low earth orbit for a year and one on the ground. I have not read the final NASA report's conclusions. However, one encouraging datum has just been published [13]. That datum is that in ten (or twenty) years almost all cancers can be eliminated with knowledge of a patient's immunological system. Unfortunately, this good news was quickly followed by a notice [14] that some experimental evidence indicated that deep space travel might result in significant "changes within and between brain cells." A permissible dose needs to be established for this effect.

The International Space Station or ISS gets its power from solar cells. At the distance of Mars a several times larger array would be required, but if a spacecraft could get as far as Jupiter a solar cell array would need to be so large that an alternate mode of power should be considered. One obvious choice is a light weight nuclear fission reactor with no moving parts coupled to a thermoelectric converter.

I estimate at least two heavy lift rockets will be required to lift several pieces of a custom built spacecraft off the ground, and two similar capacity rockets are needed to lift a total of ten or preferably twelve astronauts to the assembled spacecraft. The spacecraft must be as light as possible, and as small as feasible to preserve astronaut sanity. Small size presumably facilitates use of significant compactness in at least a magnetic field shielding system.

There is much published information about space stations to provide undefined assistance. While a space station for currently ill-defined activities may well exist in ten years as a logical successor to the International Space Station, any new station is expensive to create and use. But now other propellants and a first flight past Mars would become feasible. So a new set of tasks like those in Table 2 needs to be established. That table might be partly based on hardware for a Mars or Jupiter flyby.

Although not noted previously a gravity assist from one or more planets is assumed to be feasible. I do not possess the ability to make such calculations.

On 30 November 2016, the National Space Society issued the results of an 8 October 2016 Space Science Workshop that made five recommendations for the new political government of the United States. These recommendations seem to be compatible with reference [8] ideas but seem to ignore the most important near term contribution NASA might make, as described in that reference.

For various reasons the Principal Investigator, or PI, of the 1998 proposal was labeled "depends on choice of NASA Headquarters." The PI for the 2013 proposal was defined by saying the proposer requested to be given consideration for filling the function of PI, but his acceptance was not a requirement for acceptance of the proposal. A supplementary proposal considered my inclusion. The PI for the 2016 update was to be selected by the Board of Directors (now Trustees) of the AIP. If the manned space flight mission for peace is to be pursued by NASA, I suggest the AIP recommend a non-NASA scientific leader. These arrangements were proposed because of the adversarial relation between myself and NASA and several other entities mentioned in [8].

As in my 2016 talk, I conclude by saying that for over forty years I have believed that if it chose to do so NASA could make a unique contribution to world peace.

CONCLUSIONS

A. Are our new President and the United States Congress willing to encourage NASA to sponsor a mission into deep space whose scientific leaders come from the governments listed in my 2016 publication?

B. Is NASA willing to subordinate its Mars orbiter/lander missions to a deep space mission whose primary motivation is world peace?

APPENDIX

My background related to this talk included working with bare uranium 235 [15] and other critical assemblies, and sharing responsibility for nuclear criticality safety at the Los Alamos Scientific Laboratory in the 1950's.

This was followed by initiation and flight for NASA of several successful rocket and one (failed because of vehicle failure) satellite experiments [16-32]. This work was done while I was at the Lockheed Missiles and Space Company in the 1970's. Reference [28], received for publication by The Astrophysical Journal on 31 July 1967, gives a summary of the Lockheed discovery experiment. Reference [31] contains a 28 July 1967 cover letter for that manuscript which was sent as a private communication to eleven persons about a month before the late August 1967 international meeting which presented information contained in reference [29]. The reference [28] manuscript was published in January 1968. R. Giacconi was the first to discover a cosmic x-ray source [33]. Using two attitude controlled rockets and an observing program proposed over a year before Giacconi's discovery, I and others were able to verify the most important part of my prediction and so complete a coincident investigation that was superior to Giacconi's because I had made a prediction about the location of the apparently brightest non-solar cosmic x-ray sources before any source had been observed and my prediction proved to be true. Most of the reasons my discovery investigation have been ignored have been carefully documented with copyrights assigned to the AIP. *

ACKNOWLEDGMENTS

The Lockheed cosmic x-ray discovery experiment was supported by NASA contracts NAS 5-1174 and NASw-909 and the Lockheed Independent Research Program. The advice and encouragement of James E. Kupperian, Jr. and Nancy G. Roman of NASA were especially useful. At least, the successful efforts of Leo Goldberg (President of Commission 44 of the International Astronomical Union, or IAU), and probably Herbert Friedman, to have the Executive Committee of the IAU take special action to recognize my efforts at its 1967 General Assembly [34] was as surprising as someone's action decades later to have the Marquis Who's Who editor ask for and publish biographical information. Important contributions were also made by Allan R. Sandage of the Carnegie Observatories, and Consultants Geoffrey R. Burbidge of U. C. San Diego, and William A. Fowler of the California Institute of Technology. My work since 1985 has been financed by successive forms of Ruffner Associates.

REFERENCES

- [1] Fisher, P. "The Large Space Telescope as a Unique Opportunity," no organization listed, 12 (14 February 1973).
- [2] Fisher, P. C., *Who's Who in America*, Marquis Who's Who Publications LLC, New Providence (1997 to 2004).
- [3] Fisher, P. C., *Who's Who in the World*, Marquis Who's Who Publications LLC, New Providence, 22nd edition, 667 (2005).
- [4] Fisher, P. C., "Proposal to Initiate Manned Interstellar/Intergalactic Space Flight," Ruffner Associates, Inc., (30 June 1998). *
- [5] Fisher, P. C., "Reentering the Gravitational Fringe Field of the Solar System," *ASP Conf. Series* (S. Unwin and R. Stachnik eds.) **194**, 373 (1999).
- [6] Fisher, P. C., "Proposal to Initiate Manned Interstellar/Intergalactic Space Flight, II," Ruffner Associates, Inc. (26 December 2004). *
- [7] Fisher, P. C., "Proposal to Initiate Manned Interstellar/Intergalactic Space Flight, III," Ruffner Associates, LTD., (14 February 2013). *
- [8] Fisher, P. C., "Proprietary Manned Space Flight Proposals 1973 to 2013, plus," published on line by permission of the American Institute of Physics (2016).
- [9] Kammash, T., "Mirror-Machine to Mars?" *Ad Astra* **10** No. 2, 34 (1998).

- [10] [http:// www.rt.com/usa/312784-nasa-recycling-poop-food/](http://www.rt.com/usa/312784-nasa-recycling-poop-food/).
- [11] Parker, E. N., "Shielding Space Travelers," *Scientific American* **294** No. 3, 40 (2006).
- [12] [http:// www.ibtimes.com/cern-scientists-test-superconducting -magnet...](http://www.ibtimes.com/cern-scientists-test-superconducting-magnet...)
- [13] Beil, L., "Cancer moonshot priorities outlined," *Science News*, 10 (1 October 2016).
- [14] LiveScience.com, *Sigma Xi SmartBrief*, (12 October 2016).
- [15] Fisher, P. C., and Engle, L. B., "Delayed Gammas from Fast Neutron Fission of Th²³², U²³³, U²³⁵, U²³⁸, and Pu²³⁹," *Phys. Rev.* **134B**, 796 (1964).
- [16] Fisher, "Proposal for Mapping the Night Sky in the 10 to 16 keV Photon Range," Lockheed Missiles and Space Division, LMSD 702172 (12 December 1960) [unpublished]. *
- [17] Fisher, P. C., Typo in above document explained, Five Appendices, A - 43, Ruffner Associates, LTD., (13 August 2011) [unpublished]. *
- [18] Fisher, P. C., "Proposal for Rocket Study of Stellar X-ray Emission," Lockheed Missiles and Space Company, LMSC/895673 (10 May 1963) [unpublished]. *
- [19] Fisher, P. C., and Meyerott, A. J., "Reply to Letter of Stuart Bowyer," *Ap. J.* **140**, 821 (1964).
- [20] Fisher, P. C., Jordan, W. C., and Meyerott, A. J., "Night Sky X-ray Sources," *Quasars and High Energy Astronomy, Including Proceedings of the Second Texas Symposium on Relativistic Astrophysics*, 15 - 19 December 1964, (K. N. Douglas et al. eds.), Gordon and Breach Science Publishers, New York, 253 (1969).
- [21] Fisher, P. C., "Night Sky X-ray Experiment for Orbiting Astronomical Observatory A," Lockheed Missiles and Space Company, LMSC-893577-1 (27 July 1964) [unpublished]. *
- [22] Giacconi, R., et al., "Some Observational Aspects of X-ray Astronomy," *Proc. International School of Physics "Enrico Fermi", at Varenna Italy, 12 - 24 July 1965* (L. Gratton ed.), Academic Press, New York **73**, 74 (1966).
- [23] Oda, M., "X and Gamma-Ray Astronomy," *Proc. Int. Conf. Cosmic Rays*, 68 (1965).
- [24] Fisher, P. C., "Final Report Contract NASw-909," (17 January 1966) [unpublished]. *
- [25] Fisher, P. C., Johnson, H. M., Jordan, W. C., Meyerott, A. J., and Acton, L. W., "Observations of Cosmic X-rays," *Ap. J.* **143** No. 1, 203 (1966).
- [26] Fisher, P. C., Jordan, W. C., Meyerott, A. J., Acton, L. W., and Roethig, D. T., "Resolution of X-ray Sources at Low Galactic Longitude," *Nature* **211** No. 5022, 920 (1966).
- [27] Fisher, P. C., and Meyerott, A. J., "High Sensitivity Detectors for Few-keV X-rays," *IEEE Trans. on Nuclear Science*, NS-13, 580 (1966).
- [28] Fisher, P. C., Jordan, W. C., Meyerott, A. J., Acton, L. W., and Roethig, D. T., "Observations of Galactic X-ray Sources," *Ap. J.* **151**, 1 (1968).
- [29] "three" authors, "Joint Discussion of Commissions 28, 33, 34, and 44 X-ray Astronomy," *Highlights of Astronomy* (L. Perek ed.), D. Reidel, Dordrecht, Holland and Springer-Verlag, New York, 179 - 201 (1968).
- [30] Fisher, P. C., "X-ray Astronomy Discovery Experiments, II", published online by permission of the AIP, (May 2009).
- [31] Fisher, P. C., "X-ray Astronomy Discovery Experiments, III", published online by permission of the AIP, (June 2011).
- [32] Hirsh, R., "Oral History Interview with P. C. Fisher, 1976 July 6," Owing Repository: AIP Niels Bohr Library and Archives, Call No. 33407 [last altered 2016].
- [33] Giacconi, R., et al., "Evidence for X-rays from Sources Outside the Solar System," *Phys. Rev. Lett.* **9**, 439 (1962).
- [34] Goldberg, L., "Members (of Commission 44 at end of 1967 IAU General Assembly, prepared by outgoing Commission President)," *Transactions of the IAU* (L. Perek ed.), D. Reidel, Dordrecht, Holland and Springer Verlag, New York, **IIIB**, 249 (1968).

* Complete documents are in the Philip C. Fisher Papers of the Niels Bohr Library and Archives of the AIP, to be available one year after the author's death.

! With a 5 October 1975 cover letter thesis student Colin R. Dean of the University of Edinburgh was provided as enclosure C the cover plus pages 1 to 3 of the December 1960 Lockheed proposal. Near the bottom of page 2 the goal of my investigation was clearly stated. However, Dean quoted the goal of the first flight given on page 14 of the proposal, information I had not provided to him. With a 13 July 1976 cover letter thesis student Richard F. Hirsh of the U. of Wisconsin was provided all the materials given to Colin Dean plus a complete copy of my December 1960 Lockheed proposal. On page 88 of his thesis Hirsh falsely stated one of the goals of my investigation. If the data provided Dean and Hirsh still exist, they provide redundant proof of my 1960 goal. A copy of my letter to Hirsh was also provided to E. M. Ball of Lockheed.

Ruffner Associates, LTD, sought a copyright for this "Full Paper" (plus meeting identity) in early February 2017.

Nuclear and Thermal Hydraulic Design for a Low-Enriched Nuclear Thermal Rocket

Samuel J. Cope¹, Joseph J. Cambareri¹, Nina C. Sorrell¹, J. Michael Doster¹

¹*Department of Nuclear Engineering, North Carolina State University, Raleigh, NC 27695
336-904-9353; sjcope@ncsu.edu*

Abstract. In efforts to realize the first manned mission to Mars, engineers have been faced with many unique challenges; requiring exceptional thrust from a relatively lightweight engine in order to fulfill time and acquired dose restrictions. This new nuclear thermal rocket (NTR) design seeks to provide a comparable low-enriched uranium (LEU) engine providing vehicle thrust for the orbit-to-orbit transfer.

The core design involves a cylindrical block of nuclear grade graphite from which holes will be drilled to allow fuel elements and moderator components to be added. The core is approximately a square cylinder with an active fuel height of 70 cm and diameter of roughly 80 cm. There are 483 hexagonal fuel elements and 978 moderator elements with designs similar to those from the historic NERVA program. The approximately two moderator elements to one fuel element configuration allows for sufficient moderation reaching a desirable k_{eff} while meeting thermal limits. The radial reflector contains 12 rotating control drums to allow for reactor control, and a top reflector helps to maximize neutron economy. The reflectors are beryllium oxide, selected based on beneficial scattering and absorption cross sections with the control drums containing a crescent moon-shaped section of boron carbide for primary reactivity control.

A thermal hydraulic analysis determined that the integrity of the core was maintained while providing the thrust and specific impulse to meet the DRA 5.0 mission requirements. The LEU fuel elements are $(\text{U}_{0.1}, \text{Zr}_{0.45}, \text{Nb}_{0.45})\text{C}$ and based off the NERVA design, featuring 19 coolant channels surrounded by $\text{ZrH}_{1.8}$ moderator elements. A once through coolant system was employed to ensure the integrity of core components while maximizing the coolant exit temperature. The coolant is hydrogen, with a core averaged exit temperature of 1325 K producing a specific impulse of 615 s and the required thrust of 111.2 kN. Previous NERVA studies and the DRA 5.0 mission describe operation of the core at four times for approximately 45 minutes each. The reactor will burn to assist in breaking LEO towards Mars and slowing to enter Mars' orbit upon arrival; similar uses exist for the return trip.

Criticality safety for an NTR addresses possible accident scenarios including failure of a single control drum and core submersion upon launch. Analysis of the failure of the highest worth control drum at nominal core operating temperatures determined that the value for k_{eff} remains at 0.92709 ± 0.00043 . Consideration of launch failure accidents discovered core submersion in a large body of fresh water to be the most limiting case. Using a design which allows for disassembly of the core, preliminary results demonstrate these smaller pieces remain subcritical for all submersion scenarios. Additional reactivity control measures are incorporated to address the large reactivity changes due to temperature differences between shutdown and operating conditions.

Keywords: LEU, Mars, criticality safety

INITIAL SCOPE

This work describes the design of a nuclear thermal rocket (NTR) to support a manned mission to Mars. The National Aeronautics and Space Administration (NASA) has previously considered using nuclear reactors to support deep space exploration based on drastic reductions in space travel time due to an increased power density and specific impulse. The design scope for the NTR is limited to orbit-to-orbit transfer to and from Mars along with accident scenarios upon launch. The NTR design utilizes LEU fuel with core cooling and propellant thrust provided by hydrogen gas. An LEU core design allows for international collaboration, privatization, and reduced proliferation concerns. Design constraints were such that the core remains subcritical with a k_{eff} below 0.90 in the event of submersion or other accidents during launch, and shielding to limit crew dose to 2 rem for the entire mission.

Historical Reactor Designs

NASA examined highly enriched uranium (HEU) nuclear engines for nuclear rocket applications in the 1960s (NERVA). NASA Glenn Research Center (GRC) modeled four high enriched reactors, considered to be the most successful results of the Rover/NERVA era of rocket development [1]. These models include small and large engine varieties of the uranium carbide and the CERMET (ceramic metallic) fuel types. The (U,Zr)C-graphite fuel is shaped into hexagonal fuel elements with 19 evenly spaced coolant channels. The tie tube (moderator) elements are arranged around the fuel elements within the core. The tie tubes have hydrogen flowing from bottom to top through the inner coolant passage, and then from top to bottom through the outer plenum. With the twice through design, more heat is removed by the hydrogen translating to thrust improvements compared to once through systems. These designs implemented a thick beryllium reflector surrounding the core for power shaping with rotary control drums capable of reactor control [1].

FUEL AND MODERATOR ELEMENT DESCRIPTIONS

The fuel composition in this design is based on previously tested NERVA ($\text{U}_{0.1}, \text{Zr}_{0.45}, \text{Nb}_{0.45}$)C type fuel suspended in a graphite matrix [2]. A NERVA based design with 19 evenly dispersed cooling channels in a hexagonal element allows for greater heat transfer to the coolant, bringing the maximum temperature of the fuel matrix below its melting temperature as seen in Fig. 1.

In order to address the structural and chemical interactions between the fuel composite and the coolant, a multi-layer metallic coating (MMC) consisting of Mo/ZrC/Mo-Nb/Mo.C is applied [3]. The MMC coats the coolant channels extending from the end of the top third to the midpoint of the channel. This is the region where cracking occurred during NERVA testing. Application of the MMC to this region helps address the cracking issues by minimizing thermal expansion differences [4]. In order to prevent erosion, the remainder of the fuel coolant channels along with the annulus regions in the moderator elements are coated with a tapered thickness layer of ZrC from 50 μm at the inlet to 150 μm at the exit [5].

The moderator element is composed of zirconium hydride ($\text{ZrH}_{1.8}$), providing the bulk of moderation, with the remainder of the element composed of graphite. The melting point of $\text{ZrH}_{1.8}$, 1073 K, is the most limiting thermal constraint for the core, and requires considerable design consideration. To satisfy this constraint, a double annular flow channel is implemented in the element as seen in Fig. 2. The center core of the moderator element is composed of $\text{ZrH}_{1.8}$ with graphite surrounding the first annulus. A design challenge is the high coolant mass flow rate required in the center annulus. Higher mass flow rates lead to lower core exit temperatures, resulting in a lower specific impulse. The moderator element design provides an adequate thermal margin to the melt temperatures while maintaining a reasonable average core exit temperature and achieving the primary goal of increasing the neutron economy within the core.

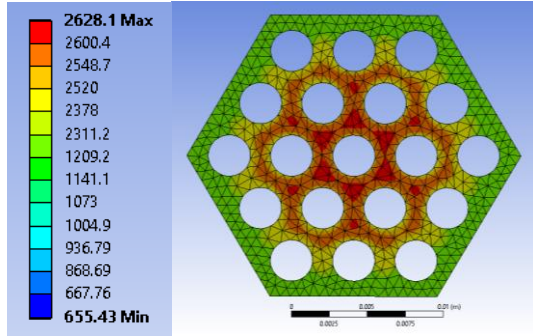


FIGURE 1. 19 coolant channels.

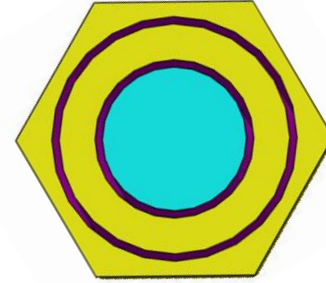


FIGURE 2. Moderator element design.

TABLE 1. Core fuel and moderator element parameters.

Parameter	Value
Core Lattice	Hexagonal
Core Mass (Total/ ²³⁵ U)	1050.3/ 18.8 kg
Fuel Enrichment	19.20%
Core Height	70 cm
Flat-to-Flat	1.905 cm
Core Diameter	80 cm
Control Drum Diameter	9.75 cm
Coolant Tube Diameter	0.2794 cm
Coolant Annulus Thickness	0.06 cm
Coolant Tube Coating Thickness	0.01 cm
Moderator Radius	0.5 cm
Inner Moderator Coolant Annulus Location	0.5 - 0.55 cm
Outer Moderator Coolant Annulus Location	0.8 - 0.85 cm
# Control Drums	12
# Fuel Elements	483
# Moderator Elements	978
# Coolant Tubes Per Fuel Element	19

Core Description

The NTR will have thrust provided from three identical cores located at the back of the rocket, farthest from the crew habitation module. Each of the three cores is expected to be utilized four times for approximately 45 minutes per run accomplishing acceleration and deceleration for orbit-to-orbit transfer.

The fuel elements are placed in a hexagonal lattice with a single fuel element surrounded by six moderator elements as seen in Fig. 3. The moderator elements serve as cooling and structural components for the core. The approximate 2:1 ratio of moderator elements to fuel elements provides sufficient moderation of the core in order to reach a critical configuration and maintain thermal limits.

Core dimensions reflect an approximately square cylinder chosen to optimize neutron economy. It is assumed that a cylindrical block of graphite will be drilled to allow insertion of fuel elements and moderator components. On the outer edge of the core, the solid graphite provides additional structural integrity as seen in Fig. 4. Inconel is employed for structural support and tie plates while Zircaloy is utilized in other areas, minimizing the effects of local parasitic absorption [6].

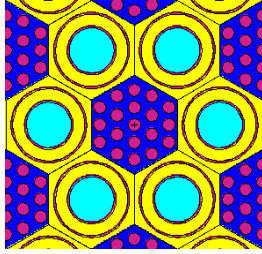


FIGURE 3. Fuel/Moderator arrangement.

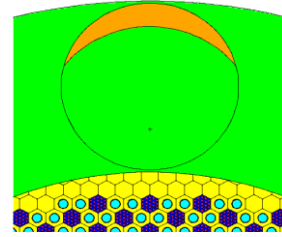


FIGURE 4. Detailed view of core edge.

A beryllium oxide radial reflector is added to flatten the radial power distribution and minimize core size. The radial reflector thickness is set at 20 cm and contains twelve 9.75 cm radius control drums which are the primary form of reactivity control for the core. The control drums are composed of beryllium oxide with a 42.4 cm³ crescent moon-shaped section of neutron absorbing boron carbide as seen in Fig. 4. These control drums have 180° rotational capability with the absorber region facing fully into the core for shutdown conditions. Symmetric distribution of the 12 control drums around the core provides roughly quarter symmetry in drum reactivity worth.

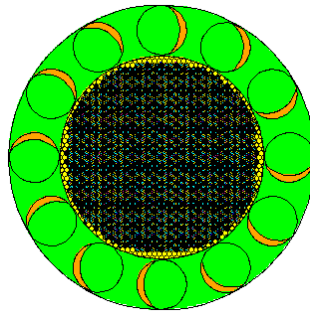


FIGURE 5. Critical Drum Position at operational hot full power (2500 K).

In order to increase total reactivity and shift the peak heat generation to the top of the core, a top reflector is added. This allows for the coolest hydrogen to flow in the hottest section of the core, improving the heating of the hydrogen and reducing the maximum temperatures of the fuel elements. The top reflector is 28 cm thick based on positive reactivity requirements as well as the diminishing benefits seen with increased thickness. Drilling coolant holes in the top reflector negligibly impacts overall reactivity, and allows for improved coolant flow distribution. A 2 cm upper plenum exists between the top reflector and the core to allow for flow redistribution and obviates the need for perfect alignment of the coolant holes.

Balance of Plant

The scope of the design extended to the auxiliary components that support the core, including the coolant system and nozzle. Coolant is stored as liquid hydrogen before it is pumped up to system pressure through the use of turbopumps. From there, coolant flows around the nozzle and up through the radial reflector, cooling both of these components while gaining the necessary preheat to generate system power within the turbopump. The coolant exits the reflector and enters the turbopump with temperatures up to 260 K. A bypass valve was added to divert excess coolant not required for system power. The coolant flow is recombined after the turbopump and enters the inlet plenum of the core at 239 K. The inlet plenum, 20 cm in length, allows the flow to be partitioned between the fuel and moderator elements. Unlike previous designs, the core features a once-through design, allowing for simplification in machining of core components and reducing the required amount of piping. Upon exiting the core and entering the nozzle, the coolant reaches an average temperature of 1326 K. With an area ratio of 290 from the nozzle throat and exit, a specific impulse of 615 seconds and 111.2 kN thrust are produced [5].

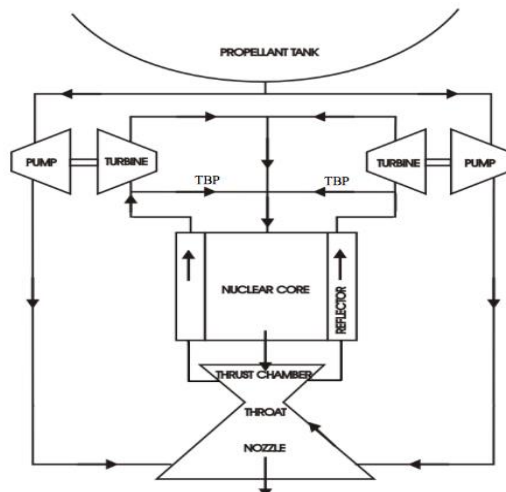


FIGURE 6. Coolant flow path [7].

NEUTRONICS RESULTS

MCNP6 utilizing ENDF/B-VII.1 libraries was used to determine the core power distribution and investigate criticality safety and reactivity control [8]. Much of the reactivity study focused on softening the neutron spectrum as well as improving overall neutron economy. To accomplish this goal and provide preheating for the hydrogen coolant, a top reflector was added to shift the axial flux profile toward the upper half of the core. The energy distribution can be seen in Fig. 7 noting a high epithermal flux. Fig. 8 and Fig. 9 display the heat generation rates calculated with MCNP6 in the average fuel and moderator elements respectively. Direct heating of the reflector was not calculated. The drop in the fuel element heat generation rate seen around the 30 cm point is not attributed to any aspect of the core configuration, but is suspected to be the result of statistical error and an outlier from the remainder of the data.

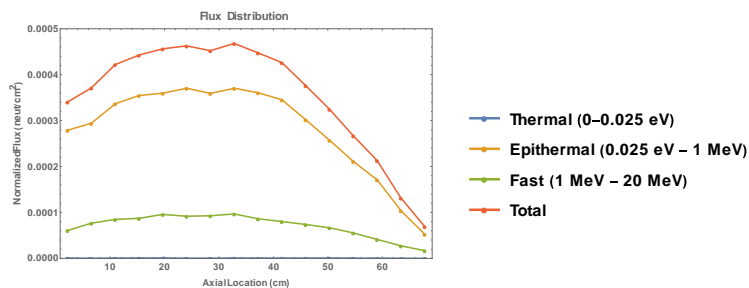


FIGURE 7. Flux energy distribution.

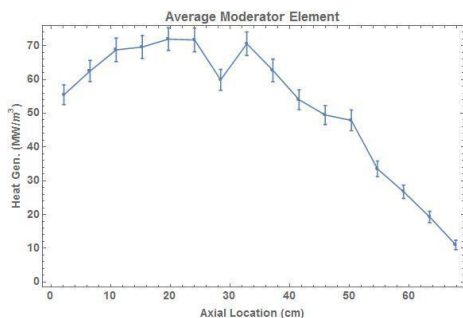


FIGURE 8. Heat generation rate in an average fuel element.

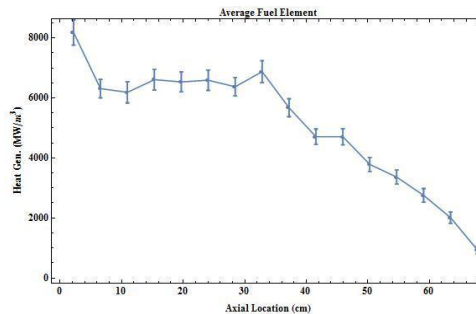


FIGURE 9. Heat generation rate in an average moderator element.

Fig. 10 illustrates the radial power distribution 6.56 cm from the top of the core and correlates to a radial peaking factor of approximately 1.2. For an operating temperature range spanning 293.6 to 2500 K, the Doppler and moderator temperature coefficients were calculated as -2.23 ± 0.054 pcm/K and -0.0814 ± 0.048 pcm/K respectively. Reactivity feedback as a function of temperature is approximately linear in this range.

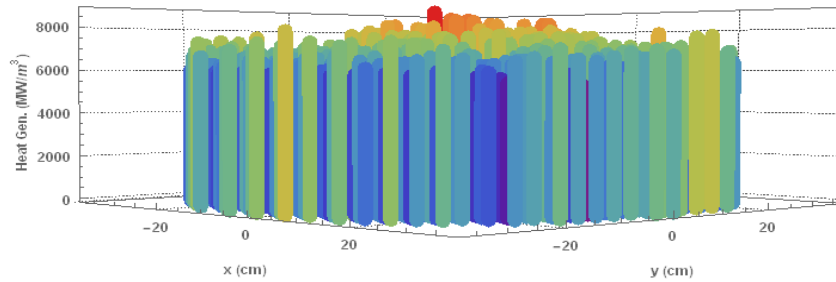


FIGURE 10. Radial heat generation profile.

In order to ensure reactivity control, twelve rotating control drums are placed within the radial reflector. The individual worth's of each control drum are approximately symmetric across the core. The total worth of all the drums totals 13994 +/- 245 pcm with the highest worth drum (1240 +/- 69 pcm) located at the 10 o'clock position. Critical drum positions are predicted to be 39% rotated out for hot zero power (HZP) corresponding to a temperature of 293.6K and 52% rotated out for hot full power (HFP) corresponding to a temperature of 2500K. Not requiring full rotation out allows for additional reactivity and possible longer runtimes. However, shutdown margin with the highest worth control drum rotated fully out decreases as the reactor cools. Table 2 gives the k_{eff} values as a function of the core temperature. Based on the available temperatures for the cross section libraries, at 293.6 K, a shutdown margin of about 3000 pcm is ensured. In the absence of an external heat source, or increased control drum worth during shutdown, recriticality is a concern if the core cools to very low temperatures. Due to the short burn times, any effects due to Xenon are anticipated to be negligible. This was confirmed by computing burnup for a full power (350 MW) run for one hour followed by shut down for 24 hours. The resulting Xenon worth at the end of this maneuver was computed to be 327 pcm.

TABLE 2. Reactivity as a consequence of reactor cooling.

Drums	Temp (K)	k_{eff}	error	pcm
	2500	0.92709	0.00043	7864
All in with 10 o'clock out	293.6	0.97098	0.00043	2989
	250	0.97380	0.00046	2690
	0.1	0.99681	0.00041	320

An alternative to maintaining the core temperature to avoid recriticality concerns would be to increase the effective area of the absorber material in each drum. Studies were not performed regarding increasing the absorber region however adding a 13th drum provided negligible impact on shutdown margin. After the 500 day mission the reactor will be generating 4.7 W of decay heat which is insufficient to maintain an average core temperature above 293.6 K, such that thermal stresses on the system are reduced and adequate shutdown margin exists. Therefore, it is proposed to use radioisotope thermoelectric generators in addition to decay heat to maintain core heating and provide auxiliary power for the crew compartment and other electrical systems.

THERMAL HYDRAULIC RESULTS

A thermal analysis of the core was completed using ANSYS FLUENT and power distribution data computed from MCNP6. The temperature distribution throughout the core was modeled to determine the propellant outlet temperature and guarantee-core components maintain a sufficient margin to their respective melt temperatures while meeting all performance requirements. From MCNP6, the heat generation is found to peak radially approximately at the center of the core. A model of the highest-powered fuel element was developed utilizing the ANSYS FLUENT

Steady-State Thermal module. Fig. 11 displays the temperature distribution within the highest-powered element and the surrounding moderator elements.

As the flow enters the core it is partitioned between the fuel and moderator coolant channels such that the pressure drops across the flow channels are equal. Table 3 gives the flow partitioning among the flow channels. The axial temperature profile of the hydrogen coolant, fuel and moderator elements are illustrated in Fig. 12 for the highest powered element. The UC fuel, graphite and ZrH_{1.8} moderator remain below their respective melting temperatures over the entire axial span. Table 4 gives the maximum temperatures of the core components along with their respective melt temperatures.

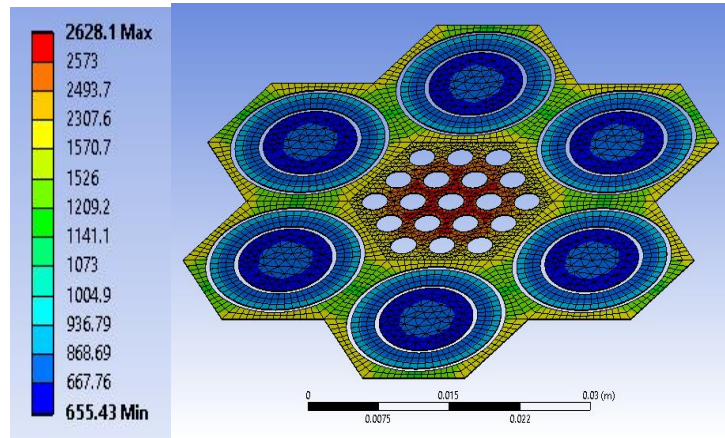


FIGURE 11. 2-D thermal plot of the core hotspot.

TABLE 3. Coolant flow description.

Parameter	Mass Flow (kg/s)	Percent of Core Flow (%)
Fuel Coolant Channel	0.00096	-----
Fuel Element	0.018	46.4
Inner Moderator Coolant Annulus	0.0038	19.6
Outer Moderator Coolant Annulus	0.0066	34
Core Total	19	100

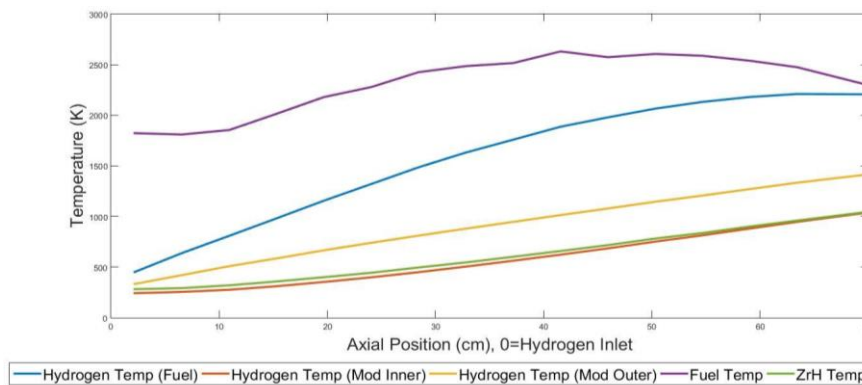


FIGURE 12. Axial temperature distributions in the core hotspot.

The coolant temperature profile for the hottest coolant channel in the highest powered fuel element is shown in Fig. 13. The hydrogen exit temperature from this channel is noted to be 2344 K, resulting in an average element exit temperature of 1895 K. The hottest channel has a corresponding Reynold’s number of 13743 using the k-epsilon turbulence model. However, despite this high Reynold’s number the flow appears to be laminar. This can be

attributed to laminarization experienced in high temperature, high pressure gases which has been described before in high temperature gas reactors cooled with helium [9].

During normal operation the core average coolant exit temperature is 1326 K with an exit temperature of 1895 K from the highest powered fuel element. Additionally, the exit temperatures of the hydrogen from the moderator elements surrounding the highest-powered fuel element are 1055 K and 1420 K for the inner and outer annuli respectively. This results in maximum temperatures of 1046 K for the ZrH_{1.8} and 2628 K for the fuel.

TABLE 4. Tabulated thermal results.

Parameter	Value
Max Fuel Temperature (Melt Temp)	2628 K (2803 K)
Max ZrH Temperature (Melt Temp)	1046 K (1073 K)
Max Graphite Melt Temperature (Melt Temp)	1729 K (4300 K)
Average Core Exit Hydrogen Temperature	1326 K
Thrust/Core	111.2 kN
Specific Impulse	615 s

Due to the narrow margin to the melt temperature of ZrH_{1.8}, a limited sensitivity analysis was performed to investigate the impact of uncertainty in thermal conductivity on peak temperatures. Table 5 displays these results and confirms that worst case thermal conductivity values still provide some margin to melt.

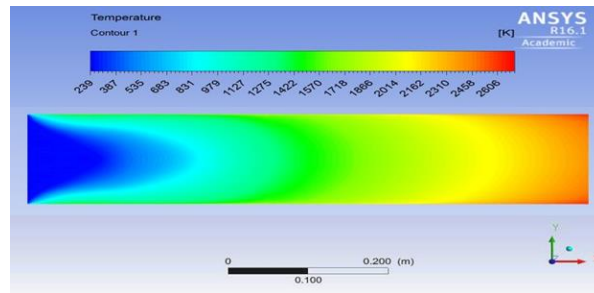


FIGURE 13. Temperature contour of fuel coolant channel.

TABLE 5. Thermal sensitivity analysis results.

	Thermal Conductivity (W/m-K)			Maximum Temperature (K)		Margin to Melt (K)	
	Graphite	UC	ZrH	UC	ZrH	UC	ZrH
Expected Values	90	21	17	2628	1046	170	24
Moderator Worst Case	140	21.3	16	--	1059	--	14
Fuel Worst Case	78	20.9	18	2632	--	168	--
Melt Temperatures	3600 K	2800 K	1073 K	--	--	--	--

Shielding

The total dose limit was set to 2 rem for the entire mission. This criterion is set such that the total dose to the crew from all sources including cosmic radiation is less than established yearly limits. To reduce the radiation from the core, an external disc shield is placed outside the cores as seen in Fig. 14. A shadow shield made of boron carbide followed by a tungsten alloy, MT-18C, was implemented to protect against both gamma and neutron radiation. An additional internal neutron shield of lithium hydride was placed between the reactor and the turbopump assemblies, feed lines, valves, and external instrumentation within the pressure vessel. Neutron and gamma dose rates were also computed with MCNP6.

The shield design was biased towards the neutron shield, attempting to minimize the amount of MT-18C due to expense and weight considerations. With a neutron shield thickness of 45 cm, gamma shield thickness of 15 cm and core run time of 3 hours, the total dose at the crew compartment from the core was $0.528 \text{ rem} \pm 0.0938 \text{ rem}$. Of this dose, gammas contribute 22% and neutrons 78%. To produce conservative results, void was assumed between the shield and crew compartment. These conservative scoping studies show the crew dose during reactor operation is within the self-imposed limit and potential exist for reductions in the amount of shielding material.

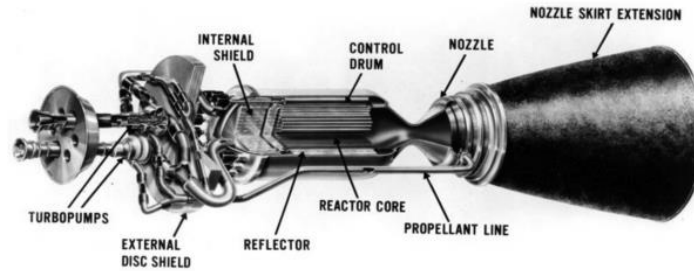


FIGURE 14. Overview of NTR with shielding [2].

It is assumed that any dose from neutrons becomes immediately negligible at shutdown requiring only photon dose to be examined. The gamma flux tally at shutdown in the crew compartment was determined and then multiplied by a dose conversion function from ICRP 21 to determine the dose. This dose was then allowed to decay over time after shutdown. To account for the shutdown dose over the remainder of the transit, the response function was integrated over the 211 days shutdown time to compute the dose for a single shutdown. The total shutdown dose for the entire mission is expected to be approximately 0.00016 rem . This results in a total mission dose of $0.53 \pm 0.094 \text{ rem}$, meeting the design limit of 2 rem.

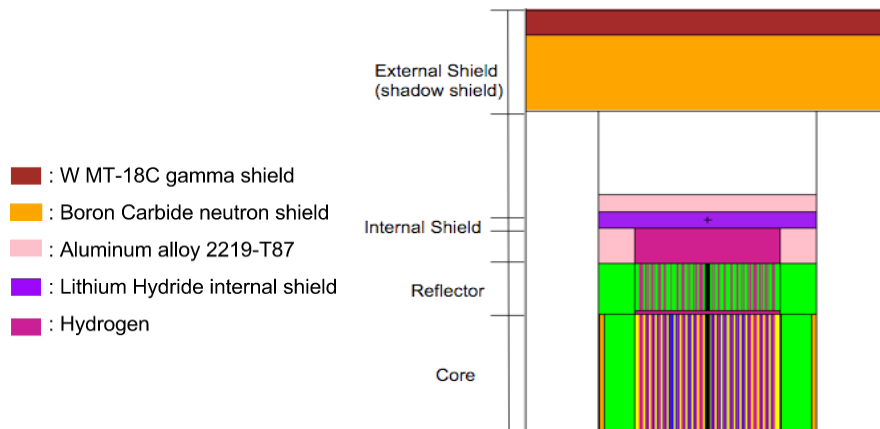


FIGURE 15. Full core model with neutron and gamma shields.

Accident Analysis

Criticality safety for an NTR addresses both partial nuclear system failure as well as additional, broader mission aspects. Possible accident scenarios include failure of a single control drum where the absorber region is rotated fully out of the core. In this case, the value for k_{eff} remains at 0.92709 ± 0.00043 with the highest worth control drum full-out at nominal core operating temperatures. Additionally, the value of k_{eff} will only increase to 0.97098 ± 0.00043 as the temperature falls to 293.6 K. Below this temperature, criticality is possible, such that additional reactivity control measures are necessary to either maintain the core at or above this temperature at all times, or provide additional control elements.

As a consequence of an under-moderated thermal reactor, the most limiting accident stems from a LEO launch failure where the core is submerged in a large body of freshwater introducing significant amounts of positive reactivity. Initial criticality results demonstrate freshwater submersion to be the most limiting case as compared with submersion in salt water, sand, or a water and sand mixture. Submersion for the models is defined to include all core void spaces filled with the surrounding environment. The k_{eff} values for full core submersion in fresh water are significantly above safe shutdown criteria.

To address this concern, features causing the reflector and core to split into sections upon impact have been previously explored in space reactor designs [10]. It is proposed here that a system be designed such that upon launch failure, the core is deconstructed into one-sixth sections which will remain subcritical even with full reflection and additional moderation. Ideally in this process, the reflector will also dismantle. Given 1/6th of the core at 293.6 K with the reflector region still intact, submersion in freshwater yielded a resulting k_{eff} value of 0.89919 ± 0.00078 . The dismantled sections of the core will remain sufficiently subcritical in the most limiting submersion scenario.

CONCLUSION

This LEU core design is able to maintain thermal limits and meet thrust requirements for current Mars mission plans. The unique once-through design with double annuli moderator cooling provides comparable specific impulse. Reactivity control is maintained with control drums, and subcriticality should be ensured for submersion accidents. Additional analysis of the thermal sensitivity of the system and methods to maintain a core temperature of at least 300 K, such as radioisotope thermoelectric generators, must be completed to meet subcriticality margins. Compliant with the DRA 5.0 mission, dose limits are met in these validation tests, but crucial optimization of the shielding is required. Further shielding analysis regarding material selection, thickness and associated dose along with in-depth thermal sensitivity studies of material degradation near state transition points are necessary.

ACKNOWLEDGMENTS

The authors express their thanks to Mohamed Bourham (NCSU), Vishal Patel (INL) and Stanley Borowski (NASA GRC) for their input and support of this work. Thanks is also given to team members Cole Manring, Casey Stocking, Jacquelyn Holshouser, Mason Mullmann, Kevin Horlback and Jessica Rhodes.

REFERENCES

- [1] Webb, J., Gross, B., and Taitno, W., "Conceptual Design of a CERMET NTR Fission Core Using Multiphysics Modeling Techniques," in proceedings of AIAA Joint Propulsion Conference, INL/CON--11-21551, San Diego, n.a., (2011).
- [2] Venneri, P. ad Kim, Y., "A Feasibility Study on Low Enriched Uranium Fuel for Nuclear Thermal Rockets - II: Rocket and Reactor Performance," *Progress in Nuclear Energy*, **87**, 156-167, (2015).
- [3] Borowski, S., et al., "Affordable Development and Demonstration of a Small NTR Engine and Stage: A Preliminary NASA, DOE and Industry Assessment," in proceedings of 51st AIAA Joint Propulsion Conference and Exhibit, Joint Propulsion Conferences (AIAA-2015-3774), Orlando, n.a., (2015).
- [4] Nam, S., Venneri, P., Choi, J., Jeong, Y., and Chang, S., "Preliminary Design Study of an Innovative High-Performance Nuclear Thermal Rocket Utilizing LEU Fuel," in proceedings of *Nuclear and Emerging Technologies for Space (2015)*, NETS Conference Proceedings, Albuquerque, pp. 58-67, (2015).
- [5] Borowski, S.K, McCurdy, D.R, and Packard, T.W., "Modular Growth NTR Space Transportation System for Future NASA Human Lunar, NEA and Mars Exploration Missions," in proceedings of *AIAA SPACE 2012 Conference and Exposition*, AIAA SPACE Forum (AIAA 2012-5144), Pasadena, n.a., (2012).
- [6] Venneri, P. ad Kim, Y., "A Feasibility Study on Low Enriched Uranium Fuel for Nuclear Thermal Rockets - I: Reactivity Potential," *Progress in Nuclear Energy*, **83**, 406-418, (2015).
- [7] Plancher, J., "Thermal and Fluid Design Analysis of a Square Lattice Honeycomb Nuclear Rocket Engine," *University of Florida*, pp. 14, (2002).
- [8] T. Goorley, et al., "Initial MCNP6 Release Overview", *Nuclear Technology*, **180**, pp 298-315 (Dec 2012).
- [9] Valentin, F., Pulido, J., Anderson, R., and Kawaji, M., "Investigation of Abnormal Heat Transfer and Flow in a VHTR Reactor Core," in proceedings of *American Nuclear Society*, ANS Transactions **110**, Reno, pp. 653-656, (2014).
- [10] Belair, M., Sarmiento, C., and Lavelle, T., "Nuclear Thermal Rocket Simulation in NPSS," in proceedings of 49th AIAA/ASME/SAE/ASEE Joint Propulsion Conference, Joint Propulsion Conferences (AIAA 2013-4001), San Jose, n.a., (2013).

The Paucity Problem: Where Have All the Space Reactor Experiments Gone?

John D. Bess and Margaret A. Marshall

*Idaho National Laboratory, Idaho Falls, ID 83415
208-526-4375; john.bess@inl.gov*

Abstract. The Handbooks of the International Criticality Safety Benchmark Evaluation Project (ICSBEP) and the International Reactor Physics Experiment Evaluation Project (IRPhEP) together contain a plethora of documented and evaluated experiments essential in the validation of nuclear data, neutronics codes, and modeling of various nuclear systems. Unfortunately, only a minute selection of handbook data (twelve evaluations) is of actual experimental facilities and mockups designed specifically for space nuclear research. There is a paucity problem, such that the multitude of space nuclear experimental activities performed in the past several decades have yet to be recovered and made available in such detail that the international community could benefit from these valuable historical research efforts. Those experiments represent extensive investments in infrastructure, expertise, and cost, as well as constitute significantly valuable resources of data supporting past, present, and future research activities. The ICSBEP and IRPhEP were established to identify and verify comprehensive sets of benchmark data; evaluate the data, including quantification of biases and uncertainties; compile the data and calculations in a standardized format; and formally document the effort into a single source of verified benchmark data.

The recovery of space nuclear experiments before they become permanently lost plays a synergistic role with current-day needs and could be of great service to unknown future efforts. Numerous experiments were performed investigating the capability to construct and operate autonomous compact nuclear reactors in harsh, remote locations. Such capabilities are of interest supporting development of small modular reactors for terrestrial applications. Unique materials such as tungsten, tantalum, lithium, and potassium, to name a few, were investigated in some of the space programs. Some of these experiments may represent our best, if not only, experiments available for refinement and integral validation of some nuclear data libraries. Interest in advanced modeling and simulation of multi-physics experiments can benefit from modern space nuclear experimentation, which includes the measurement of thermal, hydraulics, or material effects coupled with the neutronic conditions. Fission product buildup, minor actinide cross sections and decay properties, and radiation shielding aspects for building advanced fast reactors have needs that must be addressed to support both terrestrial and space nuclear applications.

So where have all the space reactor experiments gone? More importantly, what must be done to preserve these components of our nuclear heritage before the usefulness of what remains to be recovered becomes insignificant? Recorded knowledge beyond summary reports and journal articles such as logbooks, memos, and drawings need located and digitized. While the time and cost necessary to completely evaluate all space nuclear experiments is limited, the first key step is to recover and preserve what can be found, making that information publicly available such that we enable our next generation of nuclear scientists and engineers to someday evaluate and apply the information before designing and implementing next generation test facilities and reactors. Otherwise, if we continue to ignore, and effectively support, this paucity problem, our next generation may well take its first steps reinventing heritage space nuclear research.

Keywords: Benchmarks, Data, Experiments, Preservation, Validation.

INTRODUCTION

Numerous benchmark experiments have been evaluated and documented for use in the validation of nuclear data, neutronics codes, and models of various nuclear systems. These approved benchmarks are available internationally through the Organisation for Co-operation and Development (OECD) Nuclear Energy Agency (NEA) in the *International Handbook of Evaluated Criticality Safety Benchmark Experiments* (ICSBEP Handbook) [1] and the *International Handbook of Evaluated Reactor Physics Benchmark Experiments* (IRPhEP Handbook) [2]. Unfortunately, to date only a minute selection of data within these handbooks pertains directly to actual experimental facilities and mockups designed specifically for space nuclear research. A summary of these twelve evaluations, available in entirety within the IRPhEP Handbook, is provided in Table 1. Both the International Criticality Safety Benchmark Evaluation Project (ICSBEP) and the International Reactor Physics Experiment Evaluation Project (IRPhEP) were established to identify and verify comprehensive sets of benchmark experiment data; evaluate the data, including quantification of biases and uncertainties; compile the data and calculations into a standardized format; and formally document the effort within a single source of verified benchmark data. A summary of the benchmark evaluation process is provided in Figure 1.

TABLE 1. Available Neutronics Benchmark Data for Space Nuclear Systems in the IRPhEP Handbook [2].

Reactor/Facility	IRPhEP Identifier	Evaluation Title
Oak Ridge Critical Experiment Facility (ORCEF)	ORCEF-SPACE-EXP-001	Fast Neutron Spectrum Potassium Worth for Space Power Reactor Design Validation
Small Compact Critical Assembly (Performed at ORCEF)	SCCA-SPACE-EXP-001	Critical Configuration and Physics Measurements for Assemblies of U(93.15)O ₂ Fuel Rods
	SCCA-SPACE-EXP-002	Critical Configuration and Physics Measurements for Assemblies of U(93.15)O ₂ Fuel Rods (1.506-cm Pitch)
	SCCA-SPACE-EXP-003	Critical Configuration and Physics Measurements for Beryllium Reflected Assemblies of U(93.15)O ₂ Fuel Rods (1.506-cm Pitch and 7-Tube Clusters)
TOPAZ Critical Assemblies at the Narciss-M Facility	TOPAZ-SPACE-RESR-001	Intermediate Heterogeneous Assembly with Highly Enriched Uranium Dioxide (96% ²³⁵ U) and Zirconium Hydride Moderator
	TOPAZ-SPACE-RESR-002	Intermediate Heterogeneous Assembly with Highly Enriched Uranium Dioxide and Sand/Water Radial Reflector
UKS-1M Critical Facility	UKS1M-SPACE-EXP-001	Beryllium- and Molybdenum-Reflected Cylinders of Highly Enriched Uranium
Zero Power Physics Reactor (ZPPR)	ZPPR-SPACE-EXP-001	ZPPR-20 Phase C: A Cylindrical Assembly of U Metal Reflected by Beryllium Oxide
	ZPPR-SPACE-EXP-002	ZPPR-20 Phase D: A Cylindrical Assembly of Polyethylene-Moderated U Metal Reflected by Beryllium Oxide and Polyethylene
	ZPPR-SPACE-EXP-003	ZPPR-20 Phase E: A Cylindrical Assembly of U Metal Reflected by Beryllium Oxide and Sand
	ZPPR-SPACE-EXP-004	ZPPR-20 Phase D: A Cylindrical Assembly of Polyethylene-Moderated U Metal Reflected by Beryllium Oxide and Polyethylene
Zero Power Reactor (ZPR)	ZPR-SPACE-EXP-001	ZPR-9 Assemblies 7, 8 and 9: Cylindrical Cores with HEU (93% ²³⁵ U), Tungsten, and Aluminum or Aluminum Oxide with a Dense Aluminum, Aluminum Oxide, or Beryllium Oxide Reflector

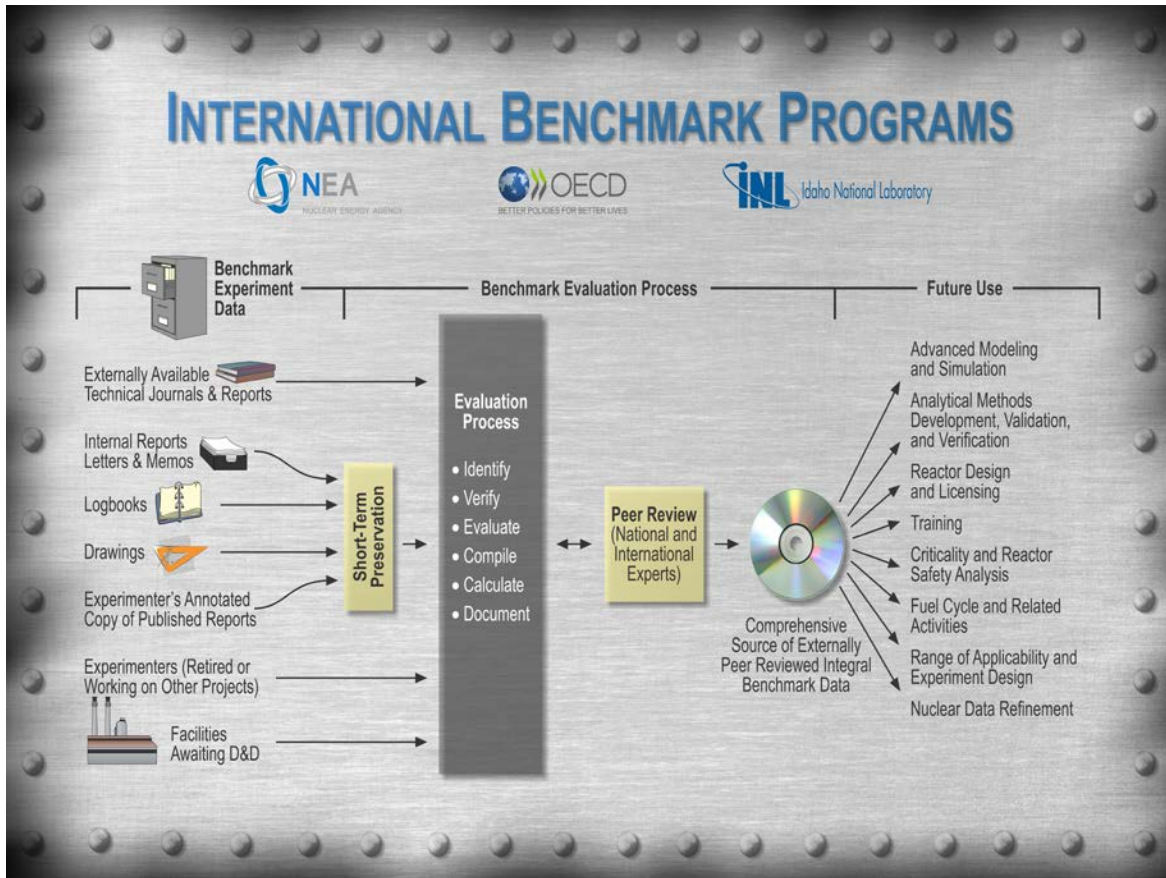


FIGURE 1. Benchmark Evaluation Process for the ICSBEP and IRPhEP.

There is paucity problem, such that of the multitude of space nuclear experimental activities performed over the past several decades, not just in the United States but also internationally, have yet to be recovered, evaluated, and made available in such detail that the international community could benefit from these valuable historical research efforts. Those experiments represent extensive investments in infrastructure, expertise, and cost. The comprehensive recovery and subsequent evaluation of those significantly valuable data serve as resources supporting past, present, and future research activities for both terrestrial and space reactor applications.

EXISTING BENCHMARKS AND POTENTIAL FOR MORE

Existing Neutronic Benchmark Data

Of the twelve benchmark evaluations listed in Table 1, most only represent the critical, or subcritical, configurations, (i.e. a single snapshot) of the experiment relative to the various supporting reactor physics measurements performed on a given assembly or at a given facility, within a given campaign. The Oak Ridge Critical Experiment Facility (ORCEF) experiment provides a simple geometry for the testing of potassium coolant worth (see Figure 2) [3]. A similar potassium worth measurement (see Figure 3) was performed for the mockup configuration of the Small Compact Critical Assembly (SCCA) [4]. Unfortunately, modern calculations with contemporary nuclear simulation codes and nuclear data libraries cannot reproduce the benchmark experiment values, indicating either a flaw in the experimental measurements, errors in potassium cross section data, errors in the models, or some combination of all three. Potassium coolant has been a recurring option for use in space nuclear reactor design and proper simulation of its worth in reactor design is important not just for operational considerations but simulated accident and criticality safety conditions. The evaluation of additional experimental data for systems with potassium would be of benefit in resolving this issue. Increased availability of benchmark experiment data facilitates the means to address discrepancies between simulations and data. Higher quality

benchmark data supplants older data and allows for integral validation and improvement of modern nuclear codes and data.

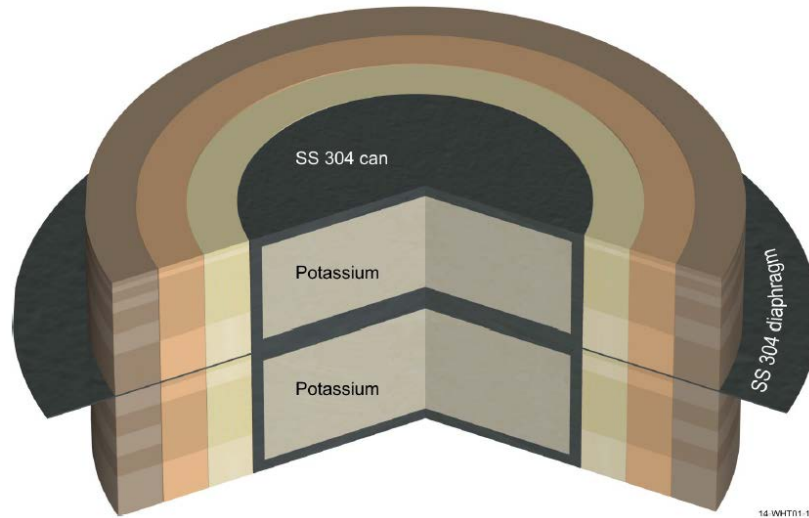


FIGURE 2. ORCEF Experiment for Measurement of Fast Neutron Spectra Potassium Worth.

The first two SCCA evaluations provide different configurations of graphite-reflected mockup cores and the third evaluation provides mockup configurations with beryllium reflectors. In addition to criticality, benchmark measurements and specifications for the graphite-reflected configuration are provided that include cadmium ratio radial distributions, simple fuel and graphite worth measurements, axial fission-rate distributions, and radial fission-rate distributions. The beryllium-reflected evaluation of SCCA includes cadmium ratio distributions, various fuel and material reactivity worth measurements, axial and radial fission-rate distributions, as well as the potassium worth measurement. This series of experiments were performed to support study of power plants for electrical power production in space vehicles.

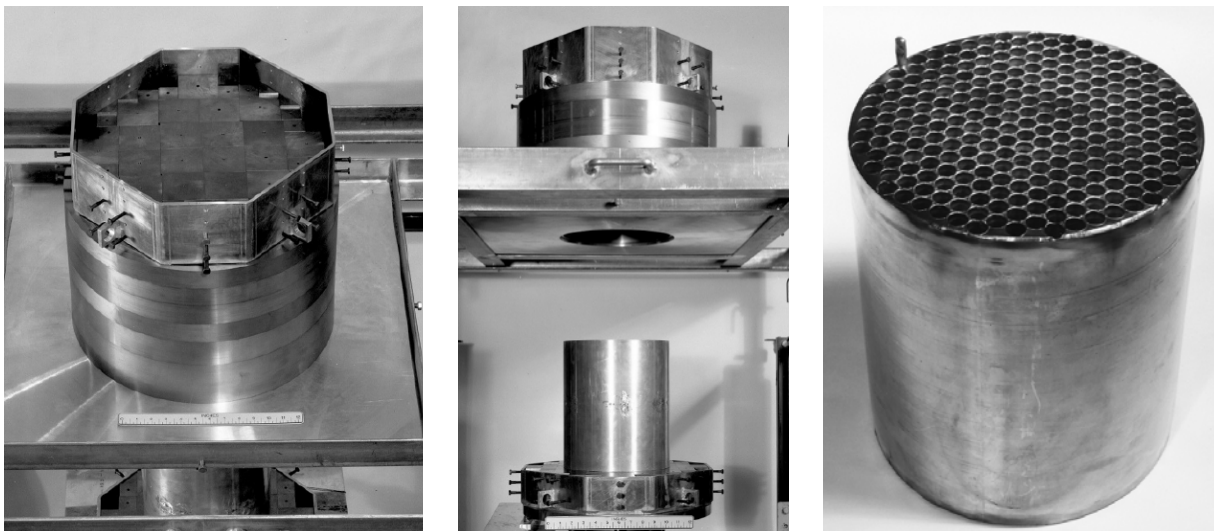


FIGURE 3. Photos of the SCCA Mockup for Potassium Worth Measurements.

The TOPAZ critical experiments (see Figure 4) were performed to investigate the accidental water immersion of a thermionic intermediate reactor-converter with highly-enriched fuel. The first evaluation includes six configurations representing water ingress into various reactor cavities and complete water immersion. The second evaluation includes five configurations representing water ingress into various reactor cavities and immersion in sand and water. While a large number of additional reactivity-worth and neutron activation cross section were performed on these configurations, currently none have been evaluated as additional benchmark data. A subcritical configuration

with dry sand reflection was not evaluated as a benchmark, but details and sample calculations are provided in an appendix of the second TOPAZ evaluation.

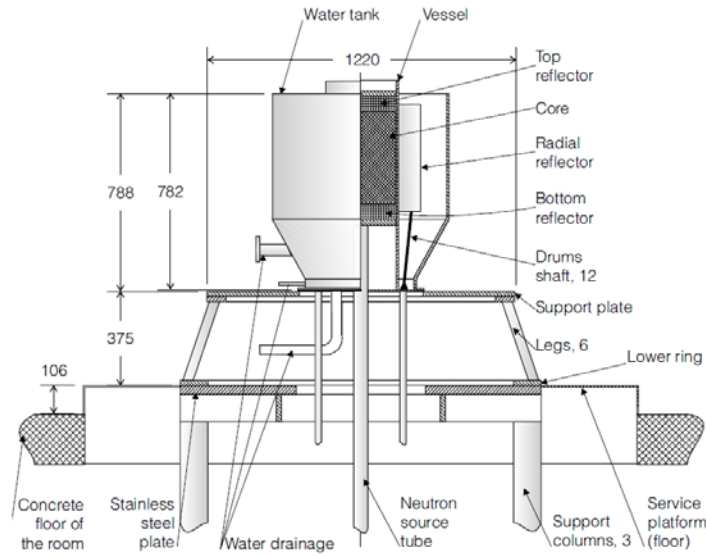


FIGURE 4. Schematic of TOPAZ Critical Assembly.

The UKS-1M experiment evaluation contains benchmark specifications for six critical assemblies of highly-enriched U-3.32Mo fuel surrounded by varying arrangements of beryllium and/or molybdenum reflectors (see Figure 5). The purpose of these loadings was to support reactor design of a power supply for outer-space apparatus with a reactor operating with a fast-neutron core moderated by varying reflector materials. Asymptotic neutron-flux decay constants were measured for each configuration but not evaluated as benchmark data.

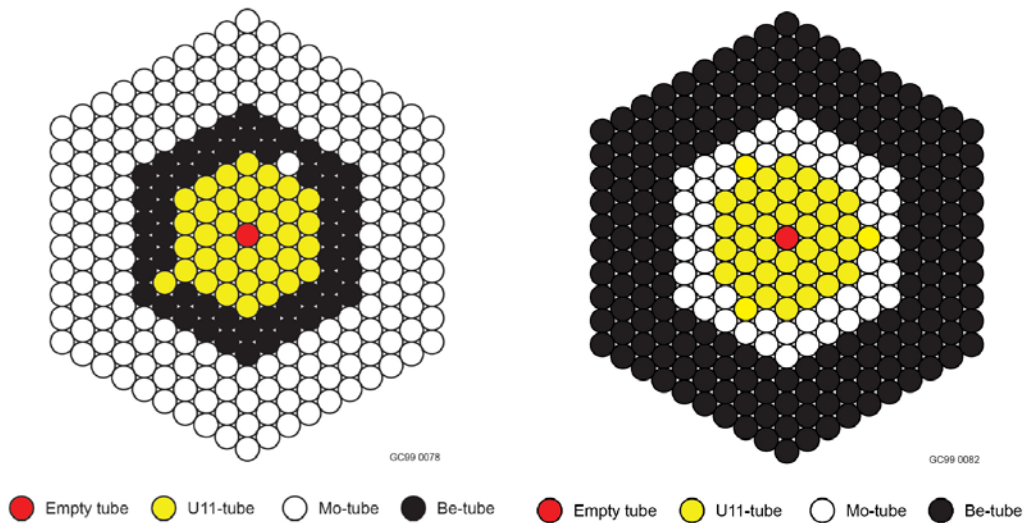


FIGURE 5. Example Core Loadings for UKS-1M Critical Assembly.

The four Zero Power Physics Reactor (ZPPR) benchmark evaluations correspond to various loadings of ZPPR-20 that were constructed to support design of the SP-100 core with some material substitutions due to availability of materials at the time. ZPPR-20C (see Figure 6) serves as the reference flight configuration for the reactor design. Phases D and E simulated accident scenarios: water immersion scenario during a launch accident, and earth burial scenario during a launch accident, respectively. The first two ZPPR-20 evaluations are critical loadings while the second two are subcritical. Numerous additional measurements were performed during the ZPPR-20 experiments, the bulk of which pertained to Phase B; measurements were performed for all configurations from Phases A through

G. Only the reference critical and subcritical loadings of these four evaluations have been evaluated currently as benchmark experiments.

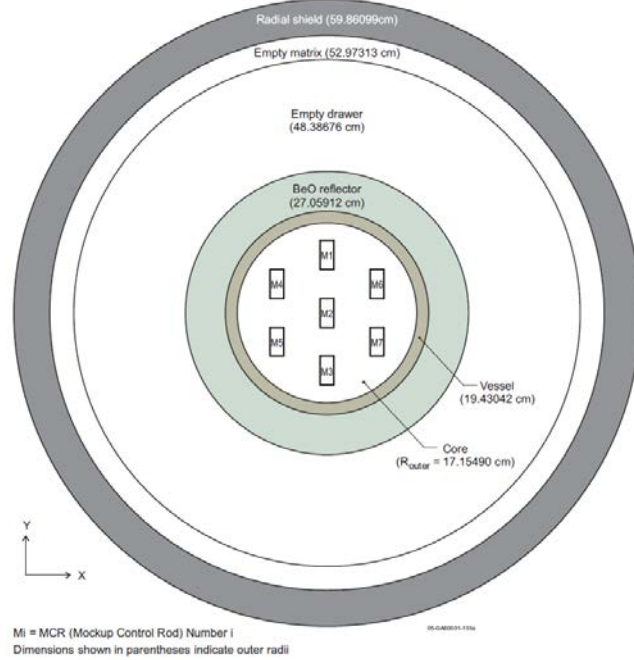


FIGURE 6. Benchmark Model Midplane Geometry for ZPPR-20C.

The Zero Power Reactor (ZPR) evaluation of ZPR-9 (see Figure 7) Assemblies 7, 8 and 9 represent three members of a series of cores built to study the neutronics of high temperature fast reactors proposed for the nuclear rocket program. The reactor contains tungsten refractory metal with varying lightweight reflector materials. Development of the final core design is documented as benchmark configurations of Assemblies 1 through 6 and is available on the ICSBEP Handbook [1] in IEU-MET-FAST-013, IEU-MET-FAST-01, HEU-MET-FAST-060, and HEU-MET-FAST-067. Currently only the three critical configurations are evaluated as benchmark experiment data. Additional measurements performed for these loadings, but not currently evaluated, include kinetics parameters, control rod calibrations, reaction-rate distributions, and reactivity worths for various materials, poisons, reflectors, fuel, and gaps.



FIGURE 7. ZPR-9 Critical Facility.

Potential Benchmark Progression

There were, and still are, numerous experiments performed worldwide that appear throughout the annals of literature as potential candidates for benchmark evaluation. Unfortunately time, funding, and effort are now necessary to potentially recover sufficient data for modern benchmark evaluation assessment. The recovery of space nuclear experiments before they become permanently lost plays a synergistic role with current-day needs and could be of great service to unknown future efforts. Experiments were performed to test and investigate the capability to construct and autonomously operate robust, compact nuclear reactors in harsh, remote locations. Such capabilities are of interest when supporting development of small modular reactors for terrestrial applications as well. Unique materials such as tungsten, tantalum, lithium, and potassium, to name but a few, once investigated as part of space programs also represent some of our best, if not only, experiments available for refinement and integral validation of nuclear data libraries needed to evaluate future reactor designs.

Synergy exists with nuclear criticality safety programs throughout the world. Benchmark validation data for fluorine and chlorine does not exist currently in the ICSBEP Handbook. Fluorine is of interest regarding the safe storage of uranium hexafluoride. The series of experiments culminating in the spherical gas core critical experiment [5] provides excellent benchmark data to support gas core reactor design but also supports fluorine cross section validation (see Figure 8). Spent nuclear fuel management in geological repositories requires investigation into the neutron absorption in water from impurities such as chlorine [6]. Improvement of cross section data for chlorine would support more realistic analysis of seawater immersion studies for space reactor accident considerations.

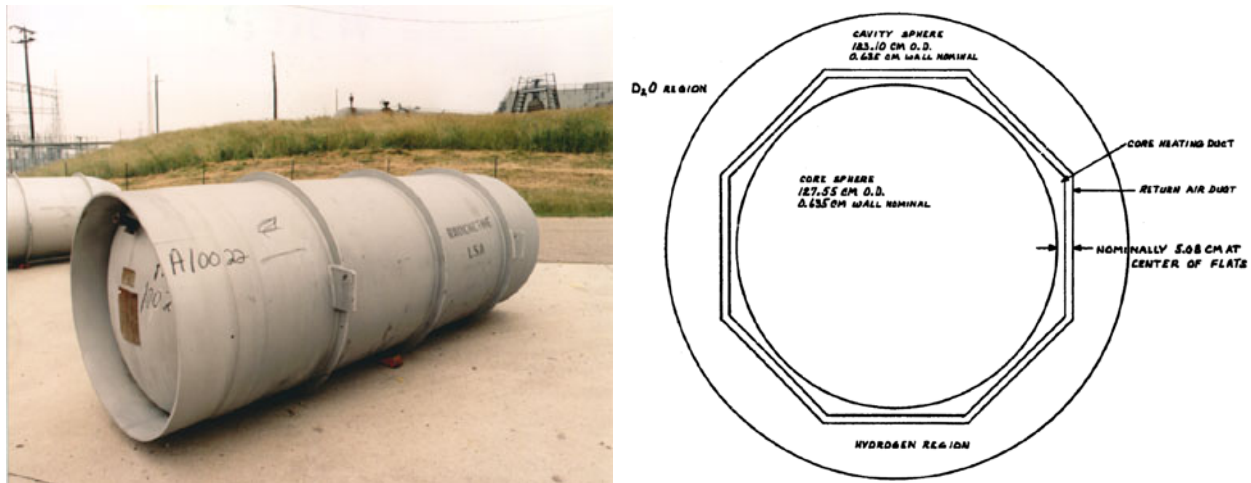


FIGURE 8. UF₆ Transportation Cylinder (Left) and Spherical Gas Core Reactor Schematic (Right).

There is an ever growing interest in the advanced modeling and simulation of multi-physics experiments that can benefit from historic and modern space nuclear experimentation, including measurement of thermal, hydraulics, and/or material effects coupled amongst themselves or also with neutronics conditions. Significant effort went into the development of Systems for Nuclear Auxiliary Power (SNAP) reactors [7] culminating in the launch of a SNAP-10 reactor into space. Various tests relevant to space nuclear reactor design historically still apply today and the ability to satisfactorily simulate extreme reactor accident conditions, such as the SNAPTRAP destructive tests [8], using modern capabilities are vital in overcoming prohibitive experimental costs. A simpler modern example of a coupled multi-physics experiment capable of serving as a benchmark is the Demonstration Using Flattop Fission (DUFF) test that coupled the Flattop critical assembly to a heat-pipe-powered Stirling converter [9]. The OECD NEA has established an Expert Group on Multi-physics Experimental Data, Benchmarks and Validation (EGMPEBV) to address the many activities associated with certification of experimental data and benchmark models, along with establishing the processes and procedures for using them for validation of modelling and simulation tools and data. The efforts to develop a handbook for multi-physics benchmark data follow along the heritage of the ICSBEP and IRPhEP Handbooks.

Fission product buildup, minor actinide cross sections and decay properties, and radiation shielding aspects for advanced fast reactors have needs that must be addressed to support both terrestrial and space nuclear applications. Benchmark evaluation of space reactor tests and experiments provide insight into the development and testing of

ground reactors. Similarly, evaluation of terrestrial fast reactor irradiation experiments can serve to improve the nuclear data available for modeling and simulation of space reactor concepts. For example, various high-purity actinide samples were irradiated in the Dounreay Prototype Fast Reactor to support evaluation of neutron cross-section data and burnup calculations [10].

ADDRESSING THE PAUCITY PROBLEM

So where has all the space reactor experiments gone? More importantly, what must be done to preserve these components of our nuclear heritage before the usefulness of what information remains recoverable becomes insignificant? Recorded knowledge beyond summary reports and journal articles such as logbooks, memos, and drawings need located and digitized. Often the typical end-point for an extensive experimental series culminates with publication of final reports dutifully summarizing what was actually performed without providing the information necessary to simulate the experiments in detail. Benchmark specifications require known geometries, material properties, quantities, environmental conditions, and measured parameters for quality development and implementation. Uncertainties in the reported parameters, and known biases, while not typically reported for experimental conditions are equally important and often developed during the benchmark evaluation process to ascertain the quality of the derived benchmark specifications.

While the time and cost necessary to completely evaluate all space nuclear experiments is limited, the first key step is to recover and preserve what can be located, making that information publicly available such that we enable our next generation of nuclear scientists and engineers to someday evaluate and apply the information prior to designing and implementing next generation test facilities and reactors. Otherwise, if we continue to ignore, and effectively support, this paucity problem, our next generation may well take its first steps reinventing heritage space nuclear research.

The first step requires donning your Fedora hat, coiling your bullwhip, and holstering your pistol, with the intention to get down and dirty with your nuclear archaeology. It isn't enough to rely solely upon the conventional institutional data preservation techniques of digitizing remaining interim and final reports. Heritage data needs identified and preserved beyond these basic summaries. Where the proverbial "tribal knowledge" yet remains, that information needs transcribed and retained for future use. The IRPhEP Handbook allows for the contribution of experimental data prepared into the proper format for handbook data preservation. While such means allows for the preservation of a comprehensive set of space nuclear reactor data, it will be marked as a Draft evaluation and not considered a formally evaluated benchmark. However, sufficient information might be retained that should time, funding, and interest prevail, future engineers could complete the benchmark evaluation(s) to support their future intended use. The challenge is set before us to actively engage ourselves in the preservation of historic and contemporary space nuclear experimental data.

Two key obstacles to address in moving forward include funding and classification concerns. Historically the United States has had hiccup-like progression in its space nuclear reactor endeavors. The early days of Rover, NERVA, and SNAP ended in the early 1970s. Later years of the 1970s resulted in efforts to develop SP-100, only to see its termination in the early 1990s. Space nuclear power and propulsion programs continue to appear and disappear, with the end of each program dumping the availability of information into the public realm without ever really making it accessible. The termination of a project does not provision the funds to do more than place everything in storage boxes, if that, until the space is needed for some future undetermined project. Where civilian space nuclear power can be publicly shared, the militarization of space nuclear activities remains classified and the gray area between the two is not always readily defined on a per-space-reactor-program basis [11].

Where contribution to the IRPhEP Handbook is a multinational collaborative effort, contributions from the U.S. would ideally be countered with contributions from other countries, such as the Russian space reactor efforts. Should concerns regarding classification issues and distribution of space reactor work remain, then development of a U.S. space reactor handbook patterned after the IRPhEP Handbook guidelines would be ideal for temporary evaluation and preservation until a time when the classification problems have been resolved. The opportunity to retain and evaluate what data remains of these legacy experiments should not be passed up due to the concerns regarding their classification and disposition.

Ultimately it comes down to the desires of the existing space nuclear generation. If there is no interest in preserving, evaluating, and using historic space reactor data, then the paucity of data is no longer a problem and we can move on to our next big terrestrial adventure on paper. However, it will take the current generation to push their managers and government to fund data recovery efforts to support the modern validation efforts. It will take the current generation to actively engage themselves in the recovery and preservation of data and lessons learned. We should include funding and address classification concerns in our modern programs to preserve lessons learned and the data as benchmarks while that information is readily available. Otherwise modern experiments such as DUFF will also slip into the annals of history to join the ranks of forgotten space reactor data.

CONCLUSION

There is currently a very limited data set of benchmark data to support validation of nuclear data, neutronics codes, and modeling of space nuclear reactor systems. Those neutronics benchmarks currently available are found in the ICSBEP and IRPhEP Handbooks available through the OECD NEA. There is a paucity problem, such that the multitude of space nuclear experimental activities performed over the past several decades have yet to be recovered in sufficient detail to provide comprehensive data to support development of high-quality benchmark specifications in support of current and future research activities. Data recovery becomes paramount as access to historic drawings, logbooks, personnel, and facilities becomes more difficult. Synergy exists between space nuclear and terrestrial activities such as criticality safety, cross section data validation, and small modular reactor design, not just for neutronics but complete multi-physics studies using modern simulation tools. Efforts should be undertaken to collect and make available existing space nuclear data not just as an act of preservation, but a preliminary step in sifting through remaining information to optimize future benchmark evaluation work. An existing available option includes submission of space nuclear reactor experimental data to the IRPhEP Handbook.

ACKNOWLEDGMENTS

The ICSBEP and IRPhEP are collaborative efforts that involve numerous scientists, engineers, and administrative support personnel from over 20 different countries. The author would like to acknowledge the efforts of all of these dedicated individuals without whom these projects would not be possible. This paper was prepared at the Idaho National Laboratory for the U.S. Department of Energy under Contract Number (DE-AC07-05ID14517).

REFERENCES

- [1] *International Handbook of Evaluated Criticality Safety Benchmark Experiments*, OECD-NEA, Paris, France (2016).
- [2] *International Handbook of Evaluated Reactor Physics Benchmark Experiments*, OECD-NEA, Paris, France (2016).
- [3] Bess, J. D., "Benchmark Experiment for Fast Neutron Spectrum Potassium Worth Validation in Space Power Reactor Design," in proceedings of *Nuclear and Emerging Technologies for Space (NETS-2015)*, Albuquerque, NM, (February 23-26, 2015).
- [4] Marshall, M. A. and Bess, J. D., "Evaluation of Potassium Worth Measurements in a Beryllium-Reflected Space Reactor," in proceedings of *International Conference on Nuclear Criticality Safety (ICNC-2015)*, Charlotte, NC, (September 13-17, 2015).
- [5] Lofthouse, J. H. and Kunze, J. F., "Spherical Gas Core Reactor Critical Experiment," IN-1443, Idaho Nuclear Corporation, Idaho Falls, ID, (February 1971).
- [6] Sobes, V., Scaglione, J. M., Wagner, J. C., and Dunn, M. E., "Validation Study for Crediting Chlorine in Criticality Analyses for Spent Nuclear Fuel Disposition," in proceedings of *International Conference on Nuclear Criticality Safety (ICNC-2015)*, Charlotte, NC, (September 13-17, 2015).
- [7] "An Evaluation of Systems for Nuclear Auxiliary Power," TID-20079, U.S. Atomic Energy Commission, Washington, DC, (January 1964).
- [8] Johnson, R. P., "SNAPTRAN 10A/2 Kinetics Testing and Destruct Reactor Experiments," NAA-SR-11906, Atomics International, Springfield, VA, (July 1966).

- [9] Gibson, M. A., Briggs, M. H., Sanzi, J. L., and Brace, M. H., "Heat Pipe Powered Stirling Conversion for the Demonstration Using Flattop Fission (DUFF) Test," in proceedings of *Nuclear and Emerging Technologies for Space (NETS-2013)*, Albuquerque, NM, (February 25-28, 2013).
- [10] Tsujimoto, K., Kohno, N., Shinohara, N., Sakurai, T., Nakahara, Y., Mukaiyama, T., and Raman, S., "Validation of Minor Actinide Cross Sections by Studying Samples Irradiated for 492 Days at the Dounreay Prototype Fast Reactor – II: Burnup Calculations," *Nucl. Sci. Eng.*, **144**, 129-141, (2003).
- [11] Aftergood, S., "Background on Space Nuclear Power," *Sci. Global Sec.*, **1**, 93-107 (1989).

Overview of Rayleigh-Taylor Instability and the Impact on Target Design for a Pulsed Fusion / Fission Propulsion System

Brian D. Taylor¹, Jason T. Cassibry², Robert B. Adams³

¹*Propulsion Systems Department, Marshall Space Flight Center, Huntsville, AL 35812*

²*Propulsion Research Center, University of Alabama in Huntsville, Huntsville, AL 35899*

³*Propulsion Research & Development Laboratory, Marshall Space Flight Center, Huntsville, AL 35812*

Abstract. This document presents an overview of the Rayleigh-Taylor instability for a pulsed z-pinch target. The overview presents information gathered in an ongoing literature review on the subject. Theory and past work is discussed. This instability is of particular interest to the authors due to its importance in the magnetic inertial confinement of fusion and fission fuels in a z-pinch. A related z-pinch based fusion/fission propulsion system is reviewed. The influence of the Rayleigh-Taylor instability upon the design of a z-pinch target is discussed, specifically in how it relates to a pulsed fusion/fission propulsion system. The paper concludes with a discussion of future work in regards to how to address and manage the instability to achieve the density and confinement time required to burn an adequate percentage of the fuel.

Keywords: plasma, stability, fission, fusion

FOREWARD

Advanced forms of propulsion are required to drastically improve upon the limits of existing technology and enable deep space exploration. Nuclear reactors, both fission and fusion, have great potential as systems with high energy density for spacecraft propulsion. There are a variety of nuclear propulsion concepts that have been proposed over the last several decades. Some of these rely on the confinement of plasmas by both magnetic and inertial means. When discussing the plasma confinement one must consider the stability of the system. The conditions of the plasma dictate the burn rate of the nuclear fuel; therefore, the plasma must maintain a minimum set of conditions in order to achieve an adequate burn. Instabilities limit plasma confinement through growing fluctuations in density and pressure. This results in turbulent mixing and loss of confinement. Thus it is desirable to find ways of reducing the impact of instabilities that arise in order for a sufficient burn of the fuel such that surplus energy can be converted into a propulsive force. Note that the same instabilities plaque the confinement of plasmas for terrestrial power generation.

The MAGNETO-RAYLEIGH-TAYLOR INSTABILITY

Plane Interface

Although plasma instabilities take many forms, the Rayleigh-Taylor Instability (RTI) is the primary interest of the authors due to its importance in inertial confinement systems. This has been a heavily researched topic and remains a major obstacle to achieving breakeven fusion conditions.

The Rayleigh-Taylor Instability arises due to an acceleration and a density gradient with opposite unit vectors in a fluid system. In this situation a heavier fluid is supported or accelerated by a lighter fluid. Small perturbations (often

assumed to be sinusoidal) at the interface seed the growth of the unstable surface. The early stage of the process can be approximated as linear. In this approximation an exponential function is often used to describe the displacement of the interface. See Eq. 1 [1].

$$\varepsilon(z, t) = \varepsilon(z)e^{i(k_y y + k_x x - \omega t)} \quad (1)$$

The wave numbers in the x and y direction are represented by k and ω is the square root of the eigenvalue that represents the growth rate. The following stages consist of highly nonlinear turbulent mixing. The classical result for the growth rate in a planar system is given by equation 2 and 3 [2]. The growth rate is given by γ , the acceleration by g, the density by ρ , and the Atwood number by A.

$$\gamma = \sqrt{kgA} \quad (2)$$

$$A = \frac{\rho_h - \rho_l}{\rho_h + \rho_l} \quad (3)$$

A diagram of the unstable interface of a plane layer is presented in Figure 1 [3].

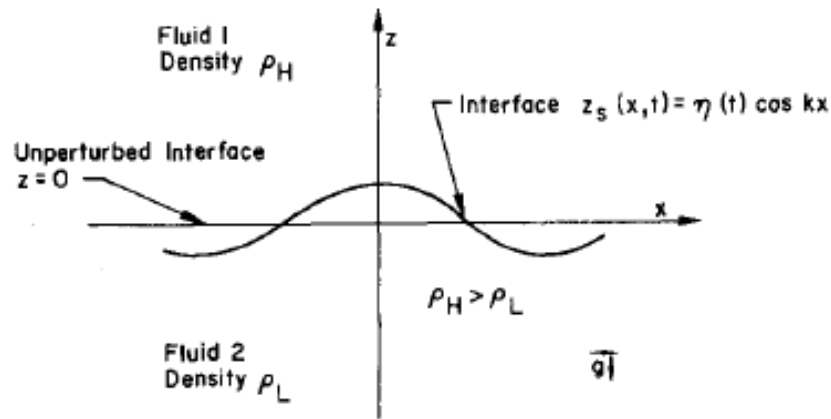


FIGURE 1. Diagram of RTI unstable interface [3]

RTI in Magnetohydrodynamics

When studying RTI in the context of plasmas it is often useful to use linear magnetohydrodynamic theory (MHD). This theory combines the fluid equations of continuity, momentum and energy with Maxwell's equations describing electromagnetism. The equations are linearized and an eigenvalue problem is developed for the spectral analysis of the growth rate [4]. This is of particular interest to the authors when placed in cylindrical coordinates due to its applicability to the pulsed fusion/fission propulsion concept and the z-pinch discussed later in this document.

When placed into cylindrical coordinates the radial displacement is of interest with the wave number in the axial direction and a mode number, m, in the azimuthal direction. When a magnetic field compressing a cylindrical plasma the magnetic field acts as the lighter fluid with a density of zero. The equations 1 and 2 are thus modified [2].

$$\varepsilon(r, t) = \varepsilon(z, r) e^{i(m\theta + kz - \omega t)} \quad (4)$$

$$\gamma = \sqrt{kg} \quad (5)$$

Note that this process is closely related to the MHD instability that occurs when the confining magnetic pressure is in equilibrium with the plasma pressure (no acceleration).

Equation 5 shows that the growth rate increases with decreasing wavelength. Dissipative processes reduce the growth rate, especially for short wavelengths. This leads to a finite wavelength at which the growth rate is at a maximum. Many dissipative processes exist (e.g. viscosity, resistivity, axial magnetic field). These are the subject of much research. Application may lead researchers close to achieving break even fusion conditions as well as more stable longer lived plasmas.

INSTABILITY MITIGATION IN PAST EXPERIMENTS

Some interesting experiments have been conducted by various research teams that display a decrease in the development of the Rayleigh-Taylor Instability. These experiments are particularly exciting due to the potential to apply lessons learned to reach the higher compression ratios and life spans needed for energy generation.

Frozen Deuterium Exploding Wires

In the second half of the 1980's a series of experiments were conducted in which frozen deuterium wires were compressed in a z-pinch. These experiments exhibited an unexpected level of stability. Loss of stability was shown to coincide with the maximum current at $dI/dt=0$ and the production of neutrons scaling proportional to I [5,6]. Numerical modeling of a pinch under equilibrium conditions has been found to be stable if sufficiently resistive. Other modeling efforts also suggest the presence of an ablating cold dense core may play a role in the stability seen in these experiments. The processes of resistivity and ablation may be important processes to consider in the design of a z-pinch target for fusion/fission propulsion [4].

Suppression of Instability with a Dielectric

Recently another series of experiments have shown promising stabilization. In these experiments a dielectric coating is applied to the outer radius of an aluminum liner. The dielectric suppresses the formation of perturbations at the interface with the liner that are a result of electrothermal instabilities. Electrothermal instabilities seed the formation of RTI. It is shown that by suppressing the electrothermal instabilities that develop during plasma formation and the early stage of collapse a higher compression ratio can be achieved [7,8]. An example of these results can be seen in Fig. 2 in which the coated rod is clearly more stable [7].

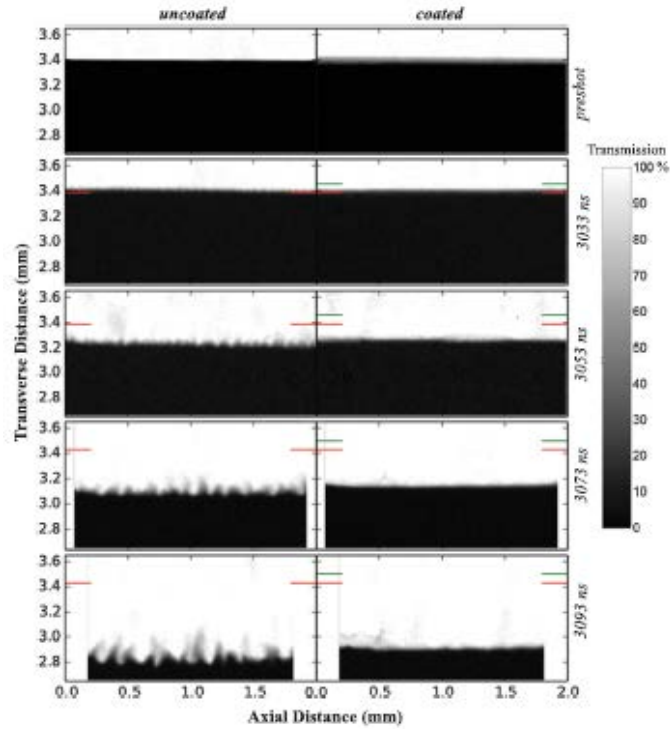


FIGURE 2. X-ray images of a coated and an uncoated rod at several points in time. The red line indicates initial position of the Al and the green line the initial position of the dielectric [7].

Axial Magnetic Field

The most dangerous instability modes occur at $k \cdot B = 0$. The wave number represented by k and the magnetic field represented by B . Calculations have shown that an axial magnetic field inside of a liner can promote stability during the collapse [6]. Recently, experiments have shown notable stability improvement in z-pinch experiments with a metallic liner, deuterium gas filled (pre-ionized with a laser), and an axial magnetic field. It is expected that the collapse of the liner compresses the axial magnetic field to large values. The high magnetic shear in this system has been shown to improve the stability and reduce RTI development. A helical structure develops in these experiments rather than the expected sausage instability [9].

Radiograph images in Fig. 3 show three different implosions with varying axial magnetic field. One can see the change in RTI development and the development of the helical structure with the addition of an axial magnetic field [10].

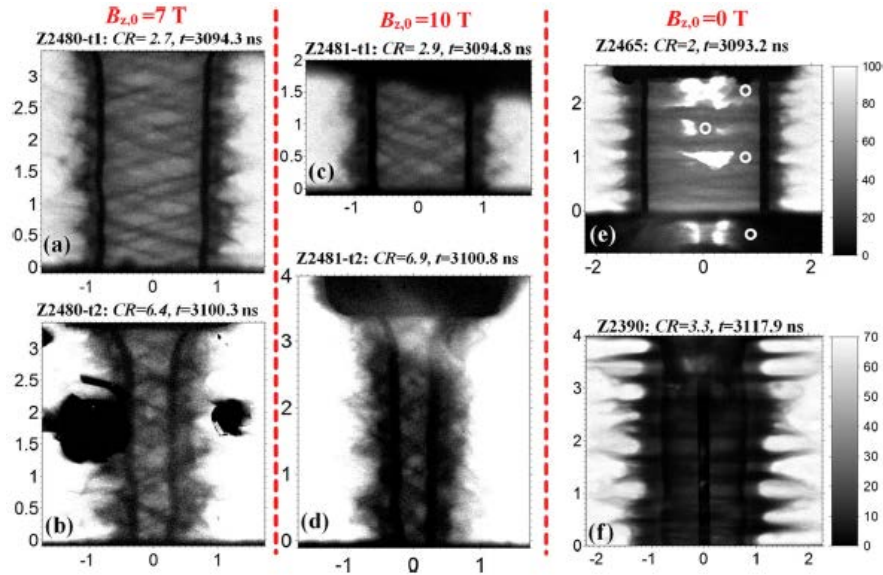


FIGURE 3. Radiographs of pinches with varying B_z [10]

Other Mechanisms of Stabilization

Other methods of stabilization may be useful for target design as well. Collapsing shock waves have been shown to have a stabilizing effect [11]. Tailored density profiles have been shown to help stabilize a gas puff collapse. In this case the density of the gas fill increase toward the axis in such a way that the collapsing shock wave experiences zero acceleration [12]. Staged annular gas puffs have been used to successfully increase yield [13]. Also, high axial velocity shear and rotation have been shown to reduce RTI development [14,15].

PULSED FUSION/FISSION PROPULSION AND THE Z-PINCH

Over the last several years there has been research relating to the development of a Pulsed Fission-Fusion Engine (PuFF) conducted by the authors and others at their respective institutions. The propulsion system concept centers on the use of a z-pinch to compress a plasma in order to induce nuclear reactions. The plasma along with the additional energy released by the fission and fusion processes is expanded with a magnetic nozzle to produce thrust. The concept, if developed, is expected to have an improvement in specific impulse of several orders of magnitude in comparison with chemical propulsion systems [16].

The z-pinch has been explored in the past as a method to confine a plasma for fusion power generation. It suffers; however, from instabilities that so far have prevented break even conditions. This propulsion concept introduces fission as a means of relaxing the confinement conditions of a pure fusion system.

The z-pinch can be described as a cylindrical or annular plasma through which a current is applied along the axis over a short (ns) period of time at high power. The current induces an azimuthal magnetic field. This process produces the Lorentz force the compresses the plasma. A diagram of this can be seen in Fig. 3 [16].

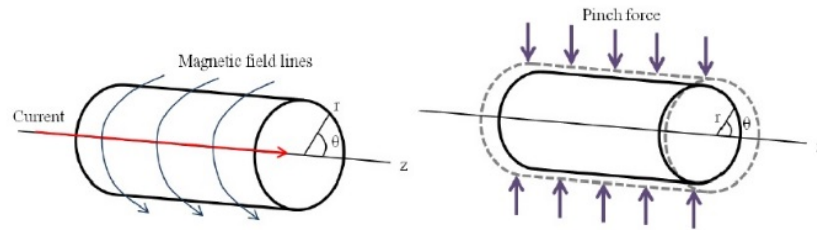


FIGURE 4. Diagram of a Z-Pinch¹⁶

In order for this concept to be successful the target must be designed to mitigate or manage the instabilities in the process, of which the Magneto-Rayleigh-Taylor Instability is the most destructive, in order to reach required plasma conditions. The target must also meet system and nuclear requirements. As one would imagine, the design of a target is a complex problem. This paper focuses on the instabilities aspect. In an effort to mitigate and manage the instabilities, processes that have been shown or theorized to reduce or modify the growth rate of the instability will be explored. The goal being to integrate techniques into the design of the target to obtain a relative stability adequate for a proper burn.

STABILITY AND TARGET DESIGN

One of the goals of target design is to control or limit the development of instabilities. For this reason one should consider processes that have a mitigating effect on the instability. One must also consider that target design must meet nuclear and system requirements in addition to stability. This all must be accounted for in order to optimize the design. There are several dissipative processes such as; shear flow, shocks, tailored density profiles, viscosity, resistivity, ablation, and magnetic shear that have varying implications and applicability for the target design. Below is a discussion of some of the most interesting in terms of potential application many of which can be found in the discussion in reference [17].

Frozen Deuterium/Uranium Wire

Some interesting experiments mentioned above have inspired a frozen deuterium/uranium wire concept. The authors propose a concept target designed to take advantage of these stabilizing phenomena. The concept target consists of a frozen deuterium core surrounded by a layer of enriched uranium which is in turn surrounded by another layer of frozen deuterium. This forms a wire consisting of frozen deuterium and uranium in 3 layers.

The outer layer of deuterium is intended to serve as a dielectric to suppress electrothermal instabilities and RTI development. The electrical properties of frozen deuterium will need to be investigated further. It may be prudent to use another dielectric in the outer layer. Uranium will carry the bulk of the current. As the uranium changes to plasma the cold dense core will ablate. The core ablation is expected to have stabilizing effect as well.

It is hoped the compression of this system will result in a hot dense layer of deuterium and uranium in which fusion and fission reactions can take place. Ideally the resistivity of the outer layer as well as the ablating core will stabilize the system long enough for significant fuel burn between the two.

Uranium/Deuterium Liner with Magnetic Shear

In light of the stabilizing effect of magnetic shear, the authors propose a concept target composed of a uranium liner with a frozen deuterium coating to suppress electrothermal instabilities, or possibly another dielectric. The interior of the liner is to be filled with a pre-ionized, pre-magnetized deuterium plasma. The goal is to promote stability with the processes of magnetic shear and dielectric coating much as was done in Ref 8. Contrary to Ref 8, this target would consist of enriched uranium and deuterium in order to achieve both fusion and fission reactions.

Uranium Wire and Deuterium/Lithium Staged Collapse

A target for the PuFF propulsion system may be designed with a uranium wire/pellet at the core to provide the fissile fuel with annular stages of deuterium/lithium plasma that collapse upon the uranium wire. The deuterium/lithium would collapse upon the ablating uranium wire to hopefully achieve high compression and fuel burn up. The lithium would add momentum to the annular plasma collapse and could also be used to breed tritium and improve the fusion yield. The deuterium/lithium plasma fill may be designed in various ways to take advantage of the processes listed above to achieve maximum stability.

FORWARD WORK

At this point these are initial concepts based upon an ongoing literature review. Further study of past work will continue. Going forward these concepts will be matured based upon previous work and merged with other nuclear and systems requirements. It is the intent of the authors to model target concepts using a smooth particle fluid magneto hydrodynamic code. Results will be compared with experimental data available in literature and used to design an experiment to be conducted with the Charger One facility at UAH. Charger One is a 1 TW pulsed power facility in development as a joint effort between the University of Alabama in Huntsville and NASA Marshall Space Flight Center.

ACKNOWLEDGMENTS

The authors would like to thank Marshall Space Flight Center, the University of Alabama in Huntsville and the Aerophysics Laboratory for their ongoing support of this work.

REFERENCES

- [1] H. Goedbloed and S. Poedts, *Principles of Magnetohydrodynamics*, Cambridge University Press, NY (2004).
- [2] M G Haines, "A review of the dense Z-pinch," *Plasma Physics and Controlled Fusion*, **53**, (2011)
- [3] D H Sharp, "An Overview of Rayleigh-Taylor Instability," *Physics*, Elsevier Science Publishers B.V., (1984)
- [4] M Liberman, J De Groot, A Toor, R Spielman; *Physics of High-Density Z-Pinch Plasmas*, Springer, NY (1999)
- [5] J. D. Sethian, A. E. Robson, K. A. Gerber, and A. W. DeSilva; "Enhanced Stability and Neutron Production in a Dense Z-Pinch Plasma Formed from a Frozen Deuterium Fiber," *Physical Review Letters*, **59**, 8 (1987)
- [6] Peng Zhang, et al; "Effects of magnetic shear on magneto-Rayleigh-Taylor instability," *Physics of Plasmas*, **19**, 022703 (2012)
- [7] K. J. Peterson, et al.; "Electrothermal Instability Mitigation by Using Thick Dielectric Coatings on Magnetically Imploded Conductors," *Physical Review Letters*, **112**, 135002 (2014)

- [8] T. J. Awe, et al.; “Experimental Demonstration of the Stabilizing Effect of Dielectric Coatings on Magnetically Accelerated Imploding Metallic Liners,” *Physical Review Letters*, **116**, 065001 (2016)
- [9] M. R. Gomez, et al.; “Experimental Demonstration of Fusion-Relevant Conditions in Magnetized Liner Inertial Fusion,” *Physical Review Letters*, **113**, 155003 (2014)
- [10] T. J. Awe, et al; “Observations of Modified Three-Dimensional instability Structure for Imploding z-Pinch Liners that are Premagnetized with an Axial Field,” *Physical Review Letters*, **111**, 235005 (2013)
- [11] S.M. Gol’berg and A. L. Velikovich, “Suppression of Rayleigh-Taylor instability by the snowplow mechanism,” *Physics of Plasmas*, **5**, 1164 (1993)
- [12] A. L. Velikovich, F.L. Cochran, and J. Davis; “Suppression of Rayleigh-Taylor Instability in Z-Pinch Loads with Tailored Density Profile,” *Physical Review Letters*, **77**, 5 (1996)
- [13] H. Sze, et al; “Magnetic Rayleigh-Taylor instability mitigation and efficient radiation production in gas puff Z-pinch implosions,” *Physics of Plasmas*, **14**, 056307 (2007)
- [14] M. R. Douglas, C. Deeney, and N. F. Roderick; ”Effect of Sheath Curvature on Rayleigh-Taylor Mitigation in High-Velocity Uniform-Fill, Z-Pinch Implosions,” *Physical Review Letters*, **78**, 24 (1997)
- [15] U. Shumlak and N. F. Roderick, “Mitigation of the Rayleigh-Taylor instability by sheared axial flows,” *Physics of Plasmas*, **5**, 6 (1998)
- [16] D. D. Rutov, M. S. Derzon and M. K. Matzen; “The physics of fast Z pinches,” *Review of Modern Physics*, **72**, 1 (2000)
- [17] R Adams, J Cassibry, D Bradley, L Fabisinski, G Statham; “Developing the Pulsed Fission-Fusion (PuFF) Engine,” *AIAA Propulsion and Energy Forum*, Cleveland, OH (2014)

Progress on Fusion Modeling and the Charger-1 Pulsed Power Facility at UAH

Ross J. Cortez¹, Jason T. Cassibry², Robert B. Adams³, Glen E. Doughty³, Brian D. Taylor³, Anthony J. DeCicco⁴

¹*Aerophysics Research Center, Research Institute, University of Alabama in Huntsville, Huntsville, AL 35899*

²*Propulsion Research Center, University of Alabama in Huntsville, Huntsville, AL 35899*

³*Propulsion Research & Development Laboratory, National Aeronautics and Space Administration, Marshall Space Flight Center, MSFC, AL 35812*

⁴*University of Maryland, College Park, MD 20742
(256) 464-8000 x32; cortezr@uah.edu*

Abstract. This paper summarizes the current progress in fusion modeling activities and the operational status of the Charger-1 pulsed power facility at the University of Alabama in Huntsville. We review the current efforts in modeling fusion burn processes through incorporation of stopping power routines in a 3-D smooth particle hydrodynamics code followed by discussion of some burn scenarios of interest. This discussion is followed by a summary of the progress to date on the initial operational capability of the Charger-1 pulsed power facility. We will describe what has been accomplished, what is left to be completed, and the initial tests being performed on the system. Finally, the future direction of research activities at UAH is discussed with a focus on the long-term goal of an operational fusion propulsion system to enable routine trips to and from Mars.

Keywords: fusion, z-pinch, advanced propulsion

INTRODUCTION

Our objective in this paper is to describe and illustrate the on-going efforts at the University of Alabama in Huntsville in fusion modeling and the status of the Charger-1 pulsed power facility. Previously, the authors put forward the case and development path for fusion propulsion and described future directions and goals that will help direct our research and development efforts [1]. Specifically, the discussion in reference [1] illustrates the reasoning for using deuterium (D) and lithium-6 (⁶Li) as the primary fuel for in-space propulsion. The motivation for using this fuel is based on four considerations: (1) D⁶Li exists as a salt with a mass density $\sim 800 \text{ kg/m}^3$; (2) the reactivity is quadratic with number density, n ; (3) D⁶Li is a solid at room temperature, eliminating the need for cryogenic storage; and (4) D and ⁶Li are both abundant and therefore more cost effective than other commonly considered fuels such as tritium (T), helium-3 (³He), and boron-11 (¹¹B). These considerations thus lead to a more pragmatic approach to our first generation fusion propulsion systems.

Currently, the major effort at the University of Alabama in Huntsville (UAH) focuses on development of experimental and modeling/simulation capabilities that will enable us to pursue the use of pulsed z-pinch plasmas as the foundation for the first generation of fusion propulsion systems for interplanetary transit. In pursuit of these efforts, the UAH Fusion Research Group, along with our partners at NASA, and colleagues in industry and academia, have met objectives and surpassed some major milestones in our plan. This paper will first describe developments in our modeling capabilities that include significant upgrades to our smooth particle hydrodynamics (SPH) code, SPFMax, enabling three dimensional simulations of implosion, ignition, and burn wave propagation in fusion targets. Specifically, we describe the stopping power model recently implemented in the code and show results from some example simulations. Following this, we then give an overview of the accomplishments to date in our effort to bring the Charger-1 pulsed power facility to initial operational capability (IOC). We describe the current status of the major auxiliary support systems, the overall system readiness level, and list the objectives remaining before reaching IOC.

Finally, we close with a discussion of the future research activities at UAH, focusing on the long-term goal of an operational fusion propulsion system for routine transit to and from Mars.

MODELING EFFORTS

In this section we describe and illustrate the SPH code under development at the University of Alabama in Huntsville. We discuss current efforts to integrate a charged particle stopping power model into the code and then illustrate an example calculation used in verifying the results.

The SPH Code

The Fusion Research Group at UAH is actively developing the Smoothed Particle Fluid with Maxwell equation solver (SPFMax) code. SPFMax is a GPU parallelized 3D code, and is a hybrid between a smooth particle hydrodynamic plasma fluid solver and a 3D time dependent Maxwell equation solver that uses the finite difference time domain method. It is ideally suited for modeling compressible fluid and plasma flows, and has recently been used to model plasma liner formation and implosion of several hundred jets for a plasma driven magnetoinertial fusion (MIF) concept [2, 3]. SPFMax includes analytical and tabular equations of state, shock capturing, viscosity, thermal conduction, and several radiation transport models; the code is currently being upgraded to include models of electromagnetic field propagation, current flow from externally driven sources, fusion reaction rates, and fast ion transport models.

Stopping Power Modeling

The theory of stopping power in hot, dense plasmas is a prominent area of interest in fusion physics [4, 5, 6, 7, 8]. Past studies have involved the stopping power in plasmas composed of fuels such as DT [8] and even DT mixed with uranium (U) [9]. It is imperative to continue to improve the accuracy of stopping power models because it provides insight into many particle flow models such as electron and thermal conductivity, temperature relaxation, and diffusion [5]. It also directly effects efforts in inertial confinement fusion [8, 7, 10, 4] and alpha particle deposition in thermonuclear fuels [8, 10].

Recently, Grabowski et al. compared theoretical models of charged particle stopping power with nonrelativistic molecular dynamics (MD) simulations [5]. They examine the models over a wide range of plasma intratarget coupling and projectile-target coupling parameters. Further, they extend the models in their study to better describe nonlinear effects and collective phenomena, and introduce a new formulation for stopping power based on their MD simulations. The new method is accurate over a larger parameter space than the commonly used models. Based on the accuracy and parameter range considerations of Grabowski et al.'s model, we chose to implement it in the SPFMax code. Implementing a stopping power model in the code will enable the user to simulate thermonuclear burn wave propagation in a variety of three dimensional geometries.

Our interest is to extend the body of work that has already been performed examining thermonuclear burn and ignition in fusion plasmas composed of D, T, ^3He , etc. to scenarios using the D^6Li fuel cycle in magnetized target fusion scenarios. In light of these objectives we have verified that the stopping power model we have implemented is working properly by comparing results from its calculations with those of other studies. FIGURE 1 and FIGURE 2 illustrate an example of this verification. The reference data in FIGURE 1 were taken from reference [9] where the authors evaluated the effects of uranium contamination on stopping power in a DT plasma. The conditions referenced are for a 3.5 MeV alpha particle slowing down in a DT plasma background at a temperature of 5 keV and mass density of 500 g/cm^3 . Since we are only concerned with stopping power in pure fusion fuel plasmas (i.e. without further contamination by other elements), we consider the black line in the plot in FIGURE 1 which represents a 0% relative uranium contamination. Our calculations match up with the data with slight differences. The calculated value of the stopping power at the end of the alpha's range matches identically with the value in Wang et al's study. The variation in our model and theirs shows up in the distance traveled: we calculate a range of $R \sim 2.088 \mu\text{m}$ while their final value is $\sim 2.845 \mu\text{m}$. We believe this difference is due to the fact that the model of Grabowski et al. [5] does not include quantum corrections and thus considers only purely classical repulsive Coulomb systems. According to FIGURE 1 (Figure 1a in [9]) the quantum correction can approach up to a $\sim 39.7\%$ difference in the calculated value. The

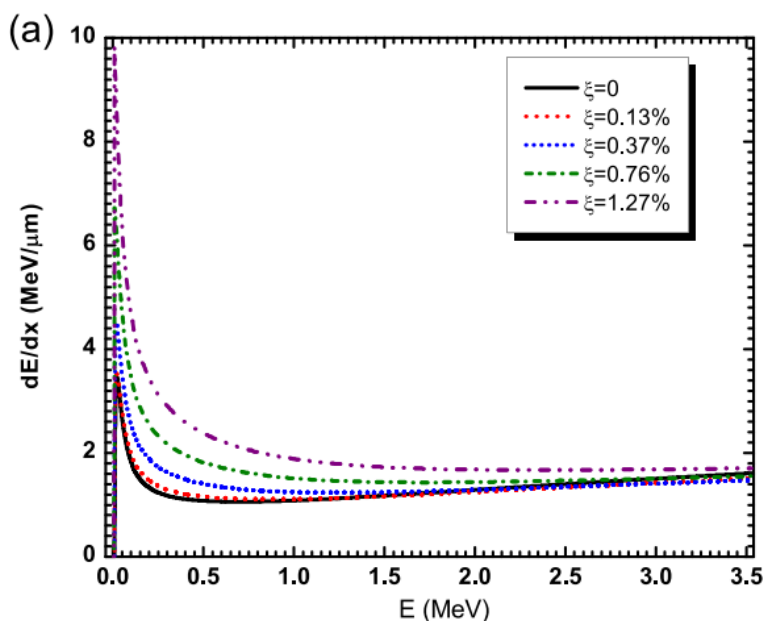


FIGURE 1. Example data from reference [9] used for validating stopping power results.

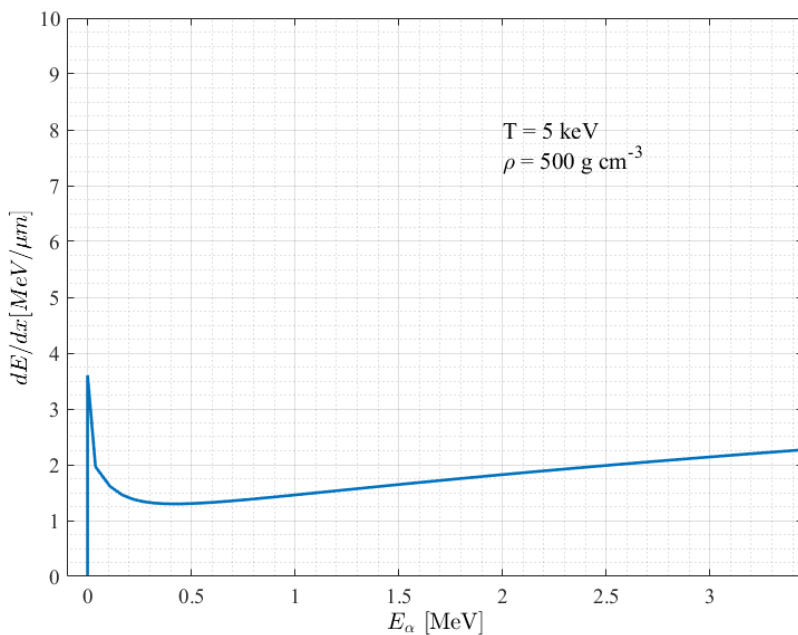


FIGURE 2. Results of stopping power calculations generated by our model for conditions matching those of reference [9].

difference between our calculated range and theirs is $\sim 27\%$, which would point to the quantum corrections causing this variance. Since the burning plasmas we are studying will be sufficiently hot so that degeneracy effects are minimal (the Coulomb logarithm is generally >10), we are confident in our decision for the Grabowski et al. model.

PROGRESS ON CHARGER-1

The University of Alabama in Huntsville, with support from Boeing Company, has obtained a 3 TW pulse power machine, originally named Decade Module 2 (DM2), from the Defense Threat Reduction Agency (DTRA). DM2, now renamed as Charger-1, is a 580 kJ pulsed power machine capable discharges up to 2 MA at voltages up 1.5 MV. DM2 was the last prototype serving as a test model for the development of the Decade Machine, built at the Arnold Engineering Development Center (AEDC) in Tennessee for nuclear weapons effects testing. Built by Physics International in 1995, DM2 has played an active role in developing plasma radiation sources for the DTRA's cold x-ray source development program. Now designated Charger-1 (FIGURE 3), the module resides at the UAH Aerophysics Research Center and is being assembled by employees from UAH, NASA Marshall Space Flight Center (MSFC), and The Boeing Company.



FIGURE 3. The Charger-1 pulsed power facility.

In this section, we describe the accomplishments to date and current status of the Charger-1 pulsed power facility at UAH. The progress and current status of each of the major auxiliary support systems is reviewed, and we outline the future developments required for each of these systems to bring the Charger-1 research endeavor to fruition.

Accomplishments to Date

Oil Purification

A large amount of transformer oil is needed for Charger-1 in order to insulate the capacitors and other components in the Marx tank, as well as the A-K (anode/cathode) gap of the high voltage tube at the front of the output line. The oil purification subsystem consists of installed storage and transfer components, a recirculation and filtration skid, and the associated plumbing and controls (FIGURE 4). The oil was delivered at the end of November 2015, and the plumbing was installed and tested in the last 5 months.

Water Deionization System

The water system (FIGURE 5) was delivered and assembled during the spring and early summer of 2016. The system required that all components and materials contacting the water must be corrosion-free and meet the following criteria:

- A minimum resistivity of 17 M Ω ·cm at the output of the system
- A 100 gallon per minute output delivery from the deionizer with a pressure of 20 psi
- Deionized water must be particulate-free to 1.0 μ m
- An ultra violet sterilizer system must prevent biological contamination

- The system consists of powder-coated steel frames that support the system’s major components while also allowing access for maintenance and operation. The DIRS systems have been supplied as single skids. Schedule 80 PVC and pigmented polypropylene socket fusion is used for the plumbing of the system.

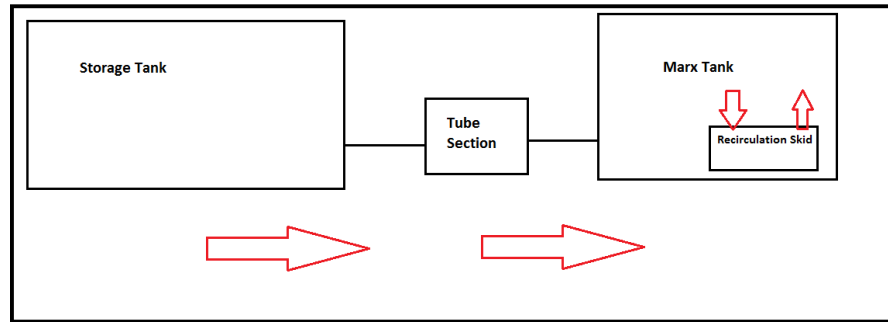


FIGURE 4. Charger-1 oil system architecture.



FIGURE 5. Deionization tanks for the water system.

Systems to be Completed

Pulsed Power and Control Systems

At this point, we are in the final phase of the assembly where we are addressing issues that are fundamental to the operation of the machine. The key systems involved here are the pulsed power systems and the Remote Instrumentation Command and Control (RICC) system. The RICC system was completed and communicating with the machine in December of 2016.

We are now focusing on the pulsed power system. This consists of the power supplies and trigger units for charging and discharging the Marx bank. FIGURE 6 shows the main trigger system used to fire the main Marx bank; it is named the “Mini-Marx” since it is also in a Marx configuration. We have redesigned some of the trigger units for the machine based on the previous designs, and we are in the process of integrating these new circuits into the machine.

Magnetically Insulated Transmission Line (MITL)

The magnetically insulated transmission line (MITL) carries the output power from Charger-1 to the load and must do so as quickly as possible. The design for the MITL incorporates slits machined into the surface to prevent azimuthal current flow in the wave front. We calculated design curves to achieve constant impedance along the length of the MITL from the output line to the load.

FIGURE 7 and FIGURE 8 below illustrate the MITL and its position in a vacuum chamber assembly. Construction will take approximately 3 months in total, including completion of all the parts and assembly on Charger-1.



FIGURE 6. Mini-Marx system used to trigger the main Marx bank.

FUTURE DIRECTIONS OF RESEARCH ACTIVITIES AT UAH

Although we intend for Charger-1 to be a pulsed power facility to be used for multiple purposes, the experiments relevant to fusion propulsion will involve z-pinch diodes and pulsed fuel injection. We will begin with standard wire array diodes for benchmarking against prior work. The next phase will begin the examination of lithium wires imploding into a D^6Li core. Critical to the research program will be the measurement of parameters such as fusion yield to build up a database that will provide guidance for how to scale a conceptual design beyond breakeven. More on this point is discussed in reference [1]. In support of the experiments we plan to perform, modeling and simulation will be performed using SPFMax with its new integrated capabilities for calculating the physics of ignition and burn wave propagation in fusion targets. The results from our modeling effort will form the basis for our target designs. Indubitably, the models will be further optimized by the data from these experiments.

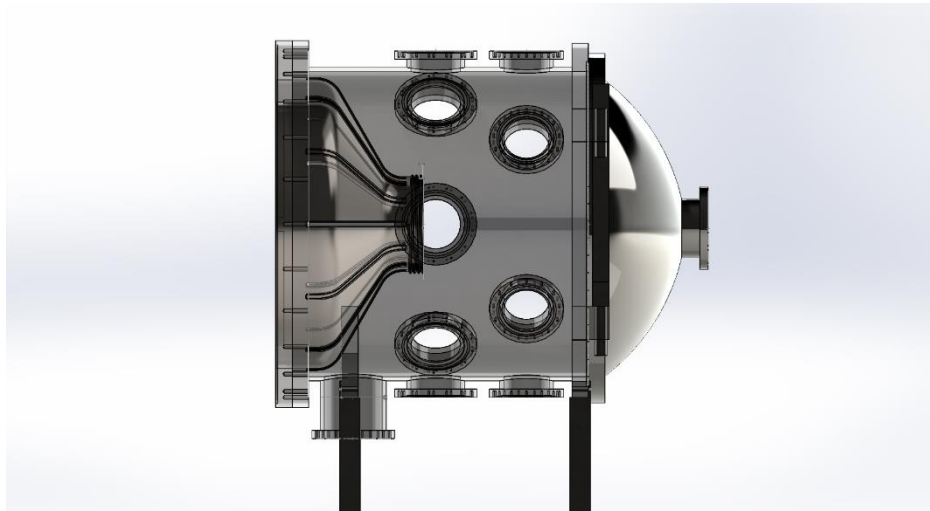


FIGURE 7. UAH MITL assembly, 10 ohm. The MITL is in the left side of the chamber.



FIGURE 8. UAH MITL assembly, 10 ohm. Exploded view showing anode and cathode clearly.

REFERENCES

- [1] J. Cassibry, R. Cortez, M. Stanic, A. Watts, W. Seidler II, R. Adams, G. Statham and L. Fabisinski, "Case and Development Path for Fusion Propulsion," *AIAA Journal of Spacecraft and Rockets*, vol. 52, pp. 595-612, 2015.
- [2] J. Cassibry, R. Samulyak, K. Schillo, W. Shih and S. Hsu, "Numerical Modeling of Plasma-Liner Formation and Implosion for the PLX-alpha Project," *Bulletin of the American Physical Society*, vol. 61, no. 18, 2016.
- [3] K. Schillo, J. Cassibry, R. Samulyak, W. Shih and S. Hsu, "Ion-Viscosity Effects on Plasma-Liner Formation and Implosion via Merging Supersonic Plasma Jets," *Bulletin of the American Physical Society*, vol. 61, no. 18, 2016.
- [4] L. Brown, D. Preston and R. Singleton, Jr., "Charged particle motion in a highly ionized plasma," *Physics Reports*, vol. 410, no. 4, pp. 237-333, 2005.
- [5] P. Grabowski, M. Surh, D. Richards, F. Graziani and M. Murillo, "Molecular Dynamics Simulations of Classical Stopping Power," *Physical Review Letters*, vol. 111, no. 215002, 22 November 2013.
- [6] J. Jacoby, H. Hoffmann, W. Laux, R. Muller, H. Wahl, K. Weyrich, E. Boggasch, B. Heimrich, C. Stockl, H. Wetzler and S. Miyamoto, "Stopping of Heavy Ions in a Hydrogen Plasma," *Physical Review Letters*, vol. 74, no. 9, 27 February 1995.
- [7] C. K. Li and R. Petrasso, "Charged-particle stopping powers in inertial confinement fusion plasmas," *Physical Review Letters*, vol. 70, no. 20, p. 3059, 17 May 1993.
- [8] K. Long and N. Tahir, "Theory and Calculation of the Energy Loss of Charged Particles in Inertial Confinement Fusion Burning Plasmas," *Nuclear Fusion*, vol. 26, no. 5, pp. 555-592, 1986.
- [9] Z. Wang, Z. G. Fu and P. Zhang, "Theoretical studies on the stopping power of deuterium-tritium mixed with uranium plasmas for alpha particles," *Physics of Plasmas*, vol. 21, no. 102307, 2014.
- [10] B. Badger, F. Arendt, K. Becker, K. Beckert, R. Bock, D. Bohne, I. Bozsik, J. Brezina, M. Dalle Donne, L. El-Guebaly, R. Engelstad, W. Eylich, R. Frohlich, N. Ghoniem, B. Goel, A. Hassanein, D. Henderson, W. Hobel, I. Hofmann, E. Hoyer, R. Keller, G. Kessler, A. Klein, R. Kreutz, G. Kulcinski, E. Larsen, K. Lee, K. Long, E. Lovell, N. Metzler, J. Meyer-ter-Vehn, U. von Mollendorff, N. Moritz, G. Moses, R. Muller, K. O'Brien, R. Peterson, K. Plute, L. Pong, R. Sanders, J. Sapp, M. Sawan, K. Schretzmann, T. Spindler, I. Sviatoslavsky, K. Symon, D. Sze, N. Tahir, W. Vogelsang, A. White, S. Witkowski and H. Wollnik, "HIBALL - A Conceptual Heavy Ion Beam Driven Fusion Reactor Study," Madison, WI, 1981.
- [11] R. Cortez, J. Cassibry, W. Seidler and W. Rogerson, "Teaching an Old Dog New Tricks: Use of Decade Module 2 in Fusion Propulsion Research," 2013.
- [12] S. Atzeni and J. Meyer-ter-Vehn, *The Physics of Inertial Fusion*, Oxford: Oxford University Press, 2004.

Analysis of Operating Strategies Using Alternative Target Designs for ^{238}Pu Production

Tomcy Thomas¹, Rapinder S. Sawhney¹, and Steven R. Sherman^{2,3}

¹*Department of Industrial and Systems Engineering, University of Tennessee, 525 John D. Tickle Engineering Building, 851 Neyland Drive, Knoxville, TN 37996-2315. tomcy@vols.utk.edu*

²*Nuclear Materials Processing Group, Nuclear Security and Isotope Technology Division, Oak Ridge National Laboratory, PO Box 2008, MS6423, Oak Ridge, TN 37831-6423.*

³*Corresponding author: (865) 576-8267, shermansr@ornl.gov*

Abstract. A research and development effort is under way to reestablish capability to produce ^{238}Pu oxide at the kilogram scale in the United States. A multi-step batch process is being developed to produce this important material. Recently, a portion of this process was studied using discrete-event simulation tools to determine whether the conceptual process may achieve its yearly production goal. The study showed the conceptual process can meet the yearly production goal under some circumstances, but process improvements would be needed to ensure greater likelihood of success. This study extends the previous work by examining the effect of changing the reactor target design on the yearly process output and production rate. Two new reactor target configurations are considered – an aluminum-clad reactor target containing 50% greater ^{237}Np oxide content than the original target and a zirconium-alloy-clad target using no aluminum. The results indicate use of the new aluminum-clad target may allow the process to achieve its yearly production goal in less time using fewer targets. If the zirconium-alloy-clad target is used, then even fewer targets would be needed to reach the production goal, but some process changes might be required to handle the zirconium cladding. The number of days needed to complete a production plan, the expected yearly outputs, and average daily production rates are determined by simulation and compared to results obtained from the initial study.

Keywords: Discrete event simulation, lean production, bottleneck determination

INTRODUCTION

A multi-laboratory team, including Oak Ridge National Laboratory (ORNL), Idaho National Laboratory (INL), and Los Alamos National Laboratory (LANL), is reestablishing domestic production of ^{238}Pu oxide for use in power supplies for deep-space missions [1]. The process being developed includes retrieval of neptunium feedstock material from storage at INL; transport of the material to ORNL; pressing of the material to make pellets; incorporation of the pellets into aluminum-clad targets; irradiation of targets to produce ^{238}Pu ; chemical processing of irradiated targets to separate and purify the plutonium produced in the targets; conversion of plutonium to an oxide; recycle of unreacted neptunium; and transport of plutonium oxide to LANL for further processing into pellets suitable for use in radioisotope thermoelectric generators (RTGs) [2] and radioisotope heating units (RHUs).

An optimization study was recently completed of the chemical processing section [3]. The study used discrete event simulation to evaluate potential operating strategies and production rates and the effects of operational detractors on production rates. The study concluded that the full-scale process may achieve its yearly production rate goal – 1,500 g heat source PuO_2 (HS- PuO_2) per year – if operational detractors are minimized, but more development work is needed to increase the likelihood of success.

In this work, the effect of changing the target design on production rate or total productivity is considered. The purpose of changing the target design would be to increase the amount of ^{237}Np in the target, thus reducing the total number of targets needed per year to achieve the same ^{238}Pu process output. Two target designs are considered – an aluminum-clad reactor target containing 50% more ^{237}Np than the original target design and a zirconium-alloy-clad target containing no aluminum. These designs are hypothetical and are only a subset of alternative target designs under consideration. Although there are unanswered questions on the fabrication method and safety of the proposed target design, it is assumed the proposed target can be fabricated and it is safe to use. Multiple operating strategies were simulated using each target type, and the results from those simulations were compared to the results from Ref. [3] to learn how changing the target design might affect process productivity.

SIMULATION APPROACH

In this study, the target design with 50% greater ^{237}Np is called the Mod 1 target design, and the zirconium-alloy-clad target with no aluminum is called the Mod 2 target design. Using the original target design, at least 432 targets must be processed per year to produce the required amount of HS-PuO₂, 1,500 g per year. If the Mod 1 target design is used, then at least 288 targets per year must be processed to meet the same production goal, and if the Mod 2 target design is used, then at least 96 targets per year must be processed. It is hypothesized that increasing the amount of neptunium in the target design will allow for higher production rates.

At present, process developers believe the rate-limiting step of the ^{238}Pu supply process lies within the chemical processing section [3] (the section downstream from the “Irradiate Al/NpO₂ Targets” box in Figure 1). To simplify the modeling process, the simulation model only includes the chemical processing section, and irradiated targets are assumed to be available whenever the chemical processing section is ready to receive them.

PROCESS DIAGRAM

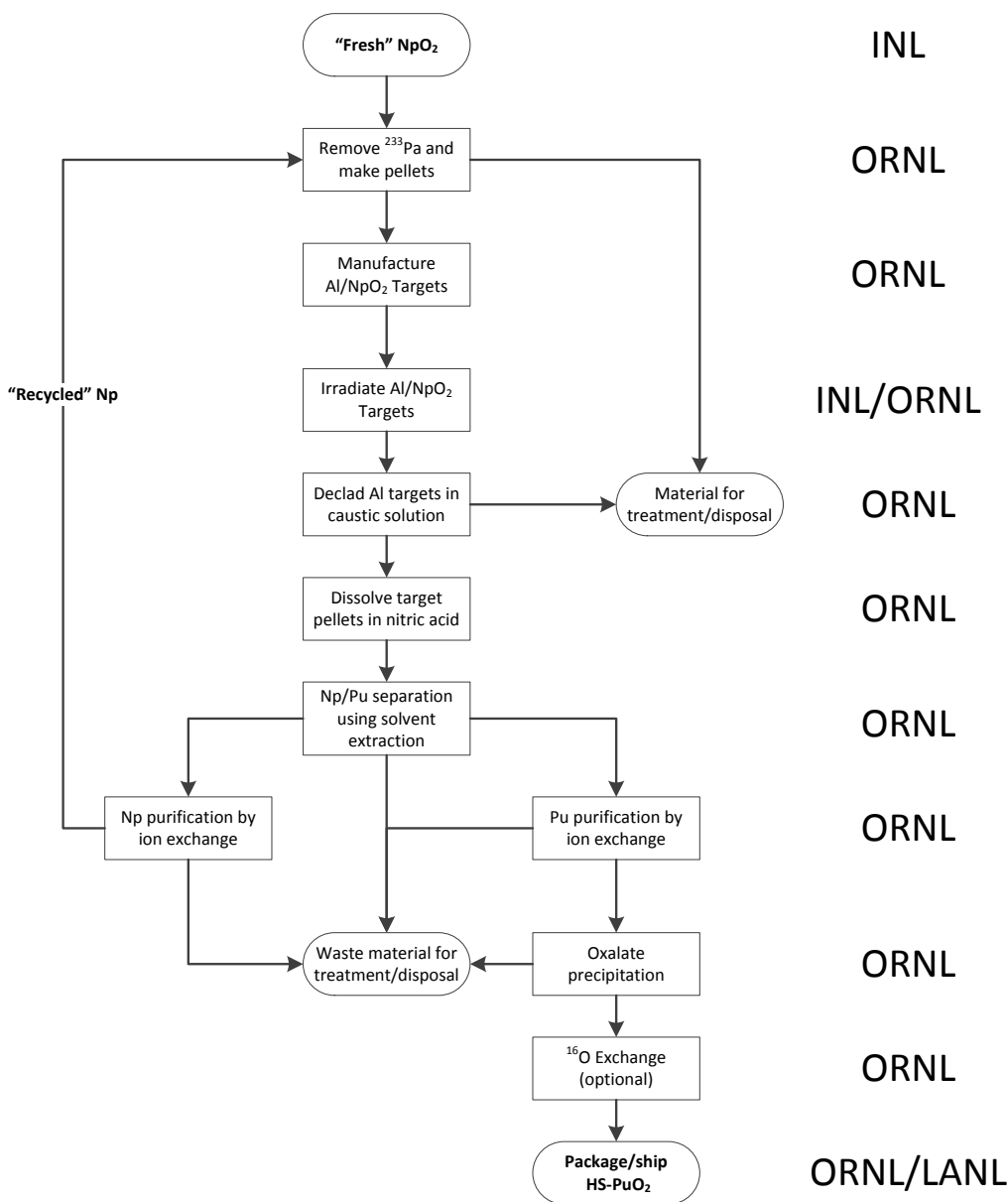


FIGURE 1: Block Diagram of ^{238}Pu supply process [3].

For each target type, production options were examined to search for operating strategies that may allow for shorter production times while still preserving the ability to meet the required production goal, 1,500 g HS-PuO₂ per year. Available equipment sizes prevent processing of a full year of irradiated targets all at once, and the inventory of irradiated targets must be sub-divided and processed in batches over one or more processing campaigns. Figure 2 shows a simplified representation of the process sequence of a chemical processing campaign. In a campaign, one or more batches of targets are dissolved. The solution from the target batches is consolidated and subject to solvent extraction and potentially ion exchange to purify the plutonium. The purified plutonium is precipitated and heat-treated to form a plutonium-oxide product, and the product is packaged and shipped to LANL

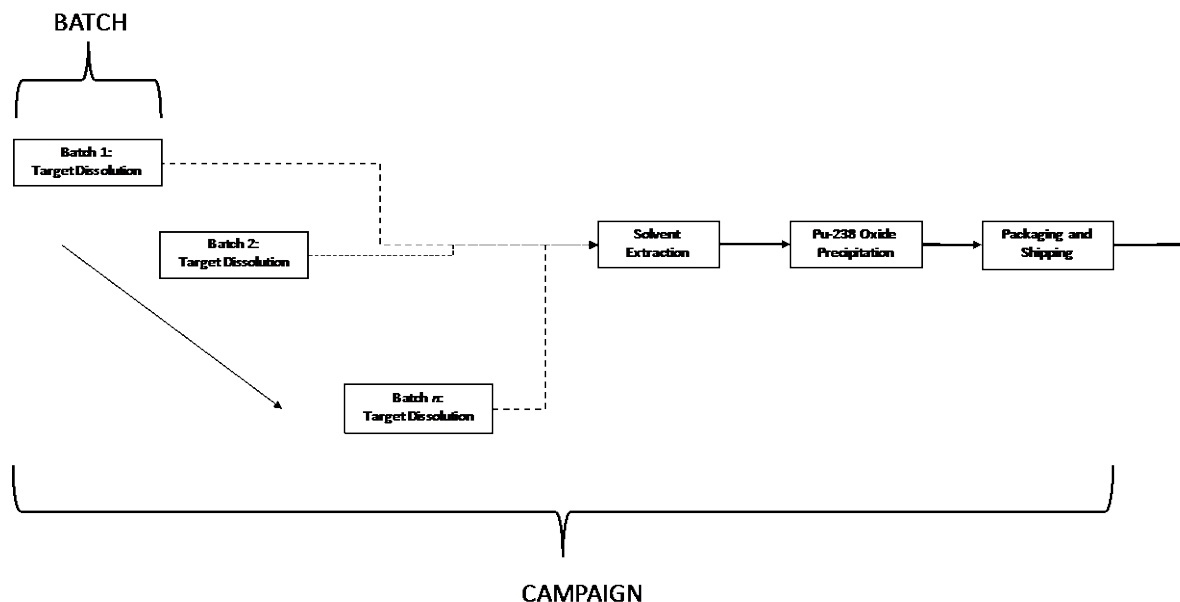


FIGURE 2: Process sequence of a campaign.

Material moves forward from one step to the next only when the downstream step is ready to receive it. Otherwise, material remains in place after the processing step is performed, blocking the forward movement of material from upstream processes. Campaigns may overlap in staggered fashion, as governed by the availability of the target dissolution equipment.

A processing step includes the activity itself (e.g., dissolve targets) and batch setup, batch loading, administrative hold points, batch unloading, and equipment cleanout (if needed). In the simulation model, processing equipment is declared available when it is ready to receive a batch. Once batch preparation begins, the processing equipment becomes unavailable and it does not become available again until either the batch is unloading or equipment cleanout is completed.

Table 1 shows the process options considered in this study. Each option varies the number of target batches per campaign, and the number of campaigns per year, while processing at least the minimum number of targets needed to achieve the yearly production goal (i.e., 1,500 g HS-PuO₂). Varying the number of batches per campaign, and the number of campaigns per year while holding the total number of targets at a fixed number affects total processing time because the processing steps must occur in a defined sequence and the time needed to perform each processing step (the step duration) is different. Option 1 is the best-performing operational strategy from Ref. [3], while Options 2 through 6 are new to this analysis. For Options 2 through 6, a new constraint was applied to the number of targets processed per batch. The number of targets processed in a year was constrained to be an integer multiple of seven targets because in practice the targets are irradiated in modules containing seven targets per module. Processing targets in multiples of seven avoids the step of splitting target modules.

TABLE 1. Simulation Scenarios

Process Options	No. Targets/Batch	No. Batches/Campaign	No. Campaigns/Year
<i>Original Target Design</i>			
Option 1 – 432 Targets	54	4	2
Option 2 – 441 Targets	49	3	3
<i>Mod 1 Target Design</i>			
Option 3 – 315 Targets	35	3	3
Option 4 – 294 Targets	49	2	3
<i>Mod 2 Target Design</i>			
Option 5 – 126 Targets	21	2	3
Option 6 – 105 Targets	35	1	3

In the simulation model, it is assumed target dissolution takes 17 days, pre-conditioning of the target dissolution solution for extraction takes 14 days, solvent extraction takes 45 days, and production and packaging of a 300-g shipment of HS-PuO₂ takes 25 days. These estimates were obtained from operator experience and expert opinion.

Production scenarios were examined assuming these step durations and scenarios where the step durations were increased by 5%, 10%, 15%, 20%, 25%, and 30%. The percentage increase in step durations model conditions where processing steps take longer than expected are due to delays, unplanned holds, equipment breakdowns, or overly optimistic estimates of process step durations. All simulation scenarios shown in Table 1 use the same baseline step durations at the 0%, 5%, 10%, 15%, 20%, 25% and 30% increased duration levels.

The baseline process step duration estimates are conservative, and it is very unlikely the step duration estimates, which are based on long-term operating experience, would all be underestimated by up to 30%. Instead, occasional process disruptions to individual steps are more likely. However, adjusting the step durations by a percentage factor is a convenient way to study the generalized effect of process disruptions without having to assign specific probability-based time estimates for each processing step.

When all parts of the system are empty and available, the time needed to perform one campaign is equal to the sum of the process durations, but when the system is processing material, processing delays can occur when the processing steps are not synchronized. For example, for Option 1 at 0% increased step durations, the process simulation determined the first campaign spanned 152 d to 181 d, which is equivalent to the sum of the step durations ($4 \times 17 \text{ d} + 14 \text{ d} + 45 \text{ d} + 25 \text{ d} = 152 \text{ d}$) when using baseline step durations and the extra time needed to process the product in excess of 300 g. The second campaign began on Day 68 and wasn't completed until Day 251, meaning the second campaign required 183 d to reach completion. Determining the impact of waiting delays on processing time would have been difficult without running the discrete event simulation model.

The simulation software used for this work was Process Simulator (2014 Professional Version 9.2.4) by ProModel Corporation [4].

Three performance measurements were recorded for each simulation scenario; yearly yield of plutonium oxide given a maximum processing time of 300 days (i.e., Yearly HS-PuO₂ Production), the time needed to complete the processing of all targets (i.e., Time to Complete), and the average daily production rate of HS-PuO₂. If the yearly yield was greater than or equal to 1,500 g HS-PuO₂, and the completion time was 300 days or less, then the scenario was considered a success. Among the successful scenarios, the better performing operation strategies had the highest yearly yields with the shortest completion times or highest average daily production rates.

SIMULATION RESULTS

Simulations with Baseline Target Designs

The results for Options 1 and 2 are shown in Figure 3. In Option 1, the process provided 1,500 g HS-PuO₂/year in less than 300 days under most conditions except when the process durations were increased by 30%. The precipitous drop in output at the 30% level occurred because process yield is incremented only when a product package is shipped, and the process was unable to complete shipment of the last product package in less than 300 days.

The results for Option 2 are similar. In Option 2, the number of targets processed per batch was adjusted to be an integer multiple of seven targets. Also, the number of batches processed per campaign was decreased from four to three, and the number of campaigns per year was increased from two to three. At these conditions, Option 1 requires dissolution of eight target batches and two solvent extraction runs, while Option 2 requires dissolution of nine target batches and three solvent extraction runs. Overlap was allowed for successive campaigns, but forward movement of materials through the simulation only occurred when downstream processing units were ready to receive new material (i.e., no accumulation queue between processing steps).

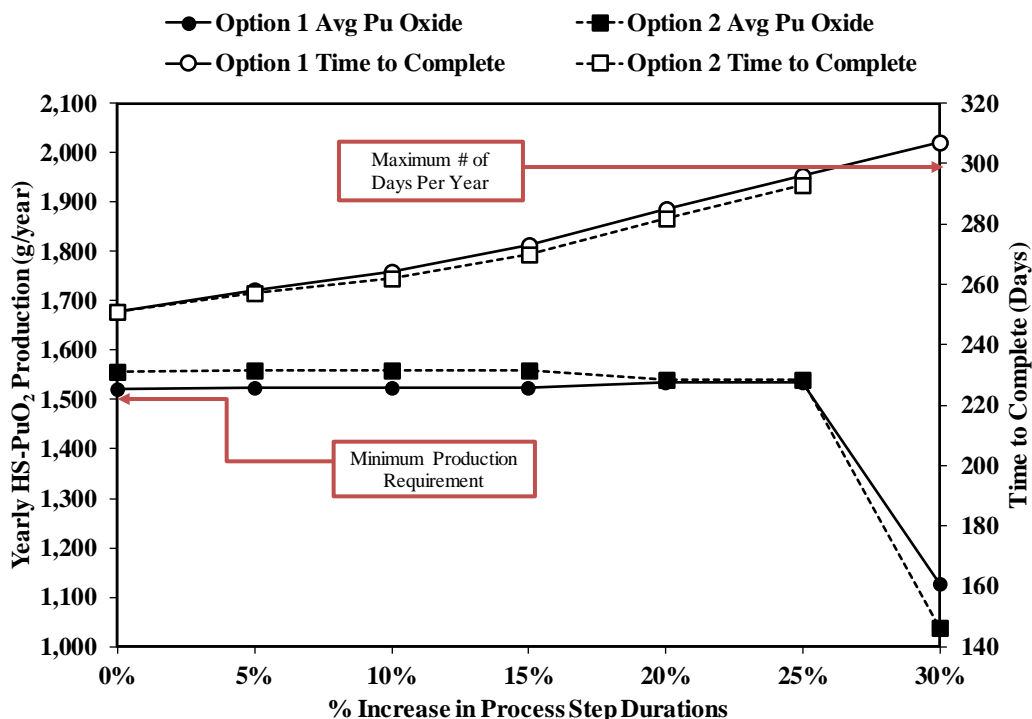


FIGURE 3. Simulation Outputs for Options 1 and 2 with original target design.

Simulations with Mod 1 Target Design

The simulation results for Options 3 and 4 are shown in Figure 4. Option 3 requires dissolution of nine target batches and the performance of three solvent extraction runs per year, while Option 4 requires dissolution of six target batches and three solvent extraction runs per year. Overlap was allowed for successive campaigns, but forward movement of materials through the simulation only occurred when downstream processing units were ready to receive new material (i.e., no accumulation queue between processing steps). Minimally, the production goal is met in less than 300 days for both options in all simulation scenarios.

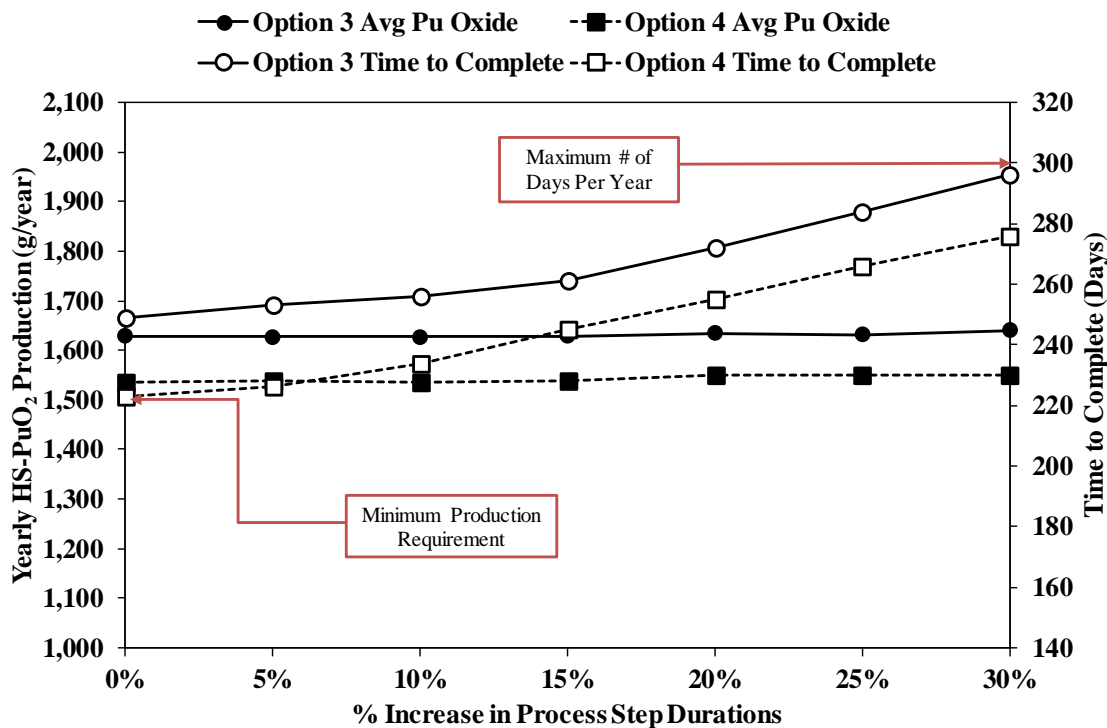


FIGURE 4. Simulation outputs for Options 3 and 4 with Mod 1 target design.

Comparing Option 3 to Option 4, Option 3 results in a greater HS-PuO₂ output, about 1 650 g HS-PuO₂/year versus 1,550 g HS-PuO₂/year. With the Option 4 operating strategy, the production runs were completed in less time, in about 20 to 25 fewer days.

Simulations with Mod 2 Target Design

When the Mod 2 target design is used, the irradiated target dissolution process changes. The Mod 2 design does not contain aluminum, and the target cannot be dissolved in the same way as an aluminum-clad target [5,6]. Instead, the targets must be cut into small pieces to expose irradiated target material to facilitate dissolution. The dissolution process will not dissolve zirconium alloy, and the leftover cladding pieces would be disposed of after the dissolution is complete. It has not yet been determined how long it would take to perform this modified dissolution process, but it is expected to take less time than dissolving an aluminum-clad target. Conservatively, it was assumed the modified dissolution process has a duration of 17 days, the same duration as used for dissolution of aluminum-clad targets.

The simulation results for Options 5 and 6 are shown in Figure 5. Option 5 requires six target dissolutions and three solvent extraction runs per year, while Option 6 requires three target dissolutions and three solvent extraction runs per year. Overlap was allowed for successive campaigns, but forward movement of materials through the simulation

occurred only when downstream processing units were ready to receive new material (i.e., no accumulation queue between processing steps).

The production goal is met in less than 300 days for both options in all scenarios.

Comparing Option 5 to Option 6, Option 5 results in a greater HS-PuO₂ output, about 2,000 g HS-PuO₂/year versus 1,650 g HS-PuO₂/year for Option 6. With the Option 6 operating strategy, the production runs were completed in less time, in about 40 fewer days.

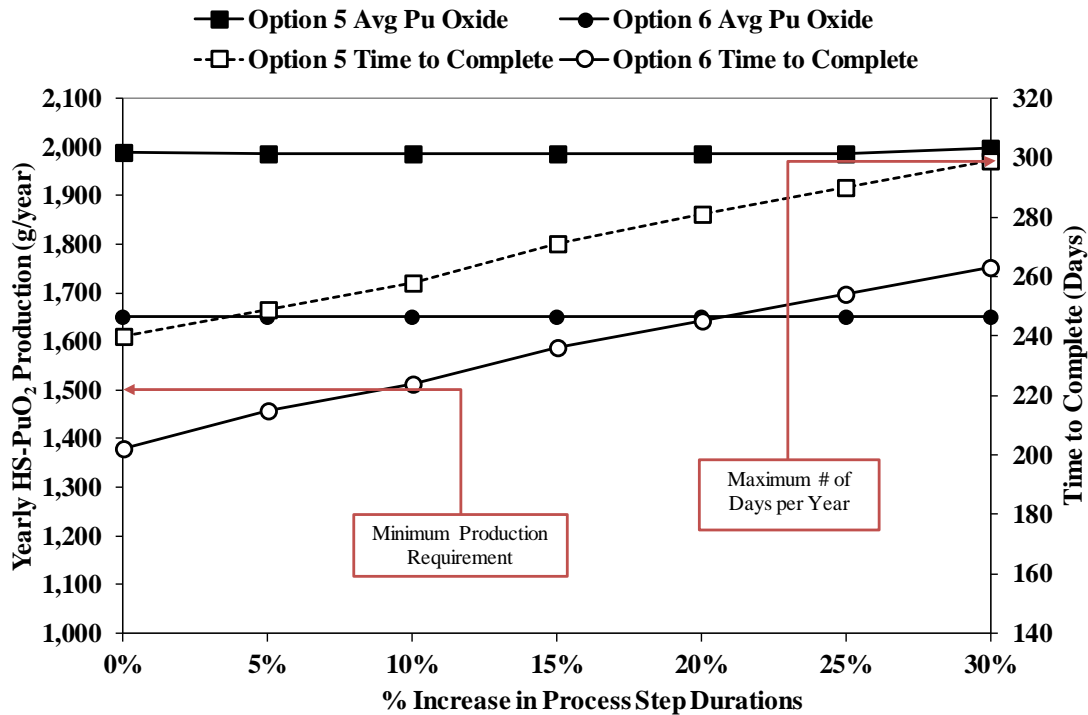


FIGURE 5. Simulation outputs for Options 5 and 6 with Mod 2 target design.

Production Rate Comparison

Figure 6 shows a comparison of the average daily production rates of HS-PuO₂ for Options 1 through 6. The average daily production rate was determined by dividing the total HS-PuO₂ produced in one year by the number of days needed to produce that amount of material. HS-PuO₂ is not produced daily, but this metric is useful when comparing the productivity or production efficiency of similar processes.

The figure shows a correlation between target design and average daily production rate. The minimum required average daily rate is 5 g/day, which is equivalent to producing 1,500 g HS-PuO₂ in 300 days. When the original target design was used, average daily production rate varied between 6.1-6.3 g/day at the 0% level to 3.7 g/day at the 30% level. When the Mod 1 target design was used, average daily production rate varied between 6.5-6.9 g/day at the 0% level to 5.5-5.6 g/day at the 30% level. When the Mod 2 target design was used, average daily production rate varied between 8.2-8.3 g/day at the 0% level to 6.2-6.8 g/day at the 30% level. The average daily production rate of HS-PuO₂ increased at all percentage levels when the neptunium content of the target was increased. The Option 2 target design has the most neptunium in it, and use of that target design resulted in the highest average daily production rate.

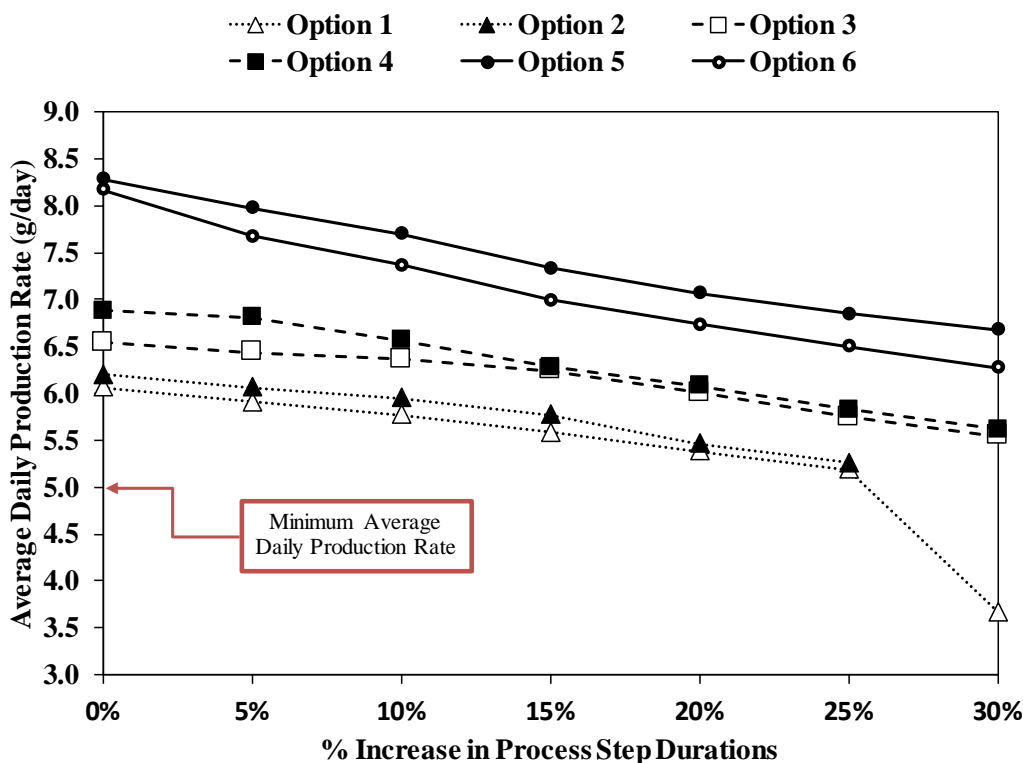


FIGURE 6. Comparison of average daily production rates for Options 1 through 6.

CONCLUSION

Discrete-event simulations of the proposed ^{238}Pu supply process showed the process can achieve its production goals using either the original target design, a Mod 1 target design, or a Mod 2 target design using expert-identified step duration estimates and when the step durations are increased. Higher production rates are achieved when step durations are less, and when the neptunium content of the target is increased. The highest average daily production rates were achieved using the Mod 2 target design. If the Mod 2 target design is not available for use, then at least the Mod 1 target design would be preferable over the original target design because it produces a higher average daily production rate.

If a Mod 2 target design is utilized, then Option 5 is favored because it results in a marginally higher average daily production rate than Option 6. If a Mod 1 target design is used, then Option 4 is favored because it produces a marginally higher production rate than Option 3. If the original target design is used, then either Option 1 or Option 2 could be used because they produce similar results.

These results are encouraging, but the current simulation model is somewhat simplistic in its approach. Limitations include:

- Nuclear material inventory limits were not recognized as constraints. Recognition of nuclear material inventory limits may limit batch sizes and affect batch sequencing.
- Tank volume limits or storage restrictions were not recognized as constraints. Recognition of these constraints may limit batch sizes or the capacity of batch accumulation areas.
- Step durations were treated as constants in the simulation rather than as probabilistic estimates. Assigning probabilistic distributions to the step durations would better model the actual process in which the time needed to accomplish a processing step will vary about an expected value.

- The simulation model is a simplified representation of a more detailed process which decreases accuracy. For example, the target dissolution step includes two distinct chemical operations, aluminum dissolution, and oxide dissolution.
- The rate-limiting step for the entire production process was assumed to lie within the chemical processing section. This may be true, but simulation model cannot identify a process bottleneck in a part of the process that is not modeled.

The model must be improved to recognize nuclear material inventory limits, recognize resource limitations, to define step durations as probabilistic distributions instead of fixed values, and to account for greater process complexity. In future work, nuclear inventory limits will be introduced to the model, and new production options will be identified that do not require the use of larger storage tanks than are available in the current facility. Probabilistic step durations will be identified and substituted in the model. Once these changes are made, the model will then be improved by subdividing it into smaller processing steps, and to expand the model to include other parts of the process such as the pellet- and target-making operations. As the model is improved, production options will be re-examined to determine workable operating strategies.

ACKNOWLEDGMENTS

This manuscript has been authored by The University of Tennessee and UT-Battelle, LLC under Contract No. DE-AC05-00OR22725 with the U.S. Department of Energy. The United States Government retains and the publisher, by accepting the article for publication, acknowledges that the United States Government retains a nonexclusive, paid-up, irrevocable, worldwide license to publish or reproduce the published form of this manuscript, or allow others to do so, for United States Government purposes. The Department of Energy will provide public access to these results of federally sponsored research in accordance with the DOE Public Access Plan (<http://energy.gov/downloads/doe-public-access-plan>).

This material is based upon work supported by the U.S. Department of Energy, Office of Nuclear Energy.

REFERENCES

- [1] Witz, A., “Nuclear power: Desperately seeking plutonium,” *Nature*, 515(11), 2014, pp. 484–486. doi: 10.1038/515484a.
- [2] Rosenberg, K.E., and Johnson, S.G., “Assembly and Testing of a Radioisotope Power System for the New Horizons Spacecraft,” Proceedings of 4th *International Energy Conversion Engineering Conference and Exhibit (IECEC)*, San Diego, California, June 26–29, 2006, #4192. Available at: <http://dx.doi.org/10/2514/6.2006-4192>. Accessed: April 15, 2016.
- [3] Thomas, T., Sherman, S.R., and Sawhney, R.S., “Seeking an Improved Pu-238 Supply Process Using Industrial Engineering Methods,” submitted to *AIChE Journal*, December 2016, for consideration of publication.
- [4] <https://www.promodel.com/products/processsimulator>, accessed October 20, 2016.
- [5] McFarlane, J., Benker, D., DePaoli, D.W., Felker, L.K., and Mattus, C.H., “Dissolution and Separation of Aluminum and Aluminosilicates,” *Separation Science and Technology*, 50:18, 2015, pp. 2803–2818, DOE: 10.1080/01496395.2014.975362.
- [6] DePaoli, D.W., Benker, D., Delmau, L.H., Burns, J.D., Wham, R.M., “Development of Chemical Processes for Production of Pu-238 from Irradiated Neptunium Targets,” Proceedings of the 2016 Nuclear and Emerging Technologies for Space (NETS-2016), Huntsville, Alabama, February 22–25, 2016.

Optimal Nuclear Thermal Propulsion Thrust Level for Human Mars Exploration

C. Russell Joyner II¹, Timothy Kokan², Daniel J. H. Levack³, John Crowley², and Frederick Widman²

¹*Aerojet Rocketdyne, West Palm Beach, Florida 33410, USA,*

²*Aerojet Rocketdyne, Huntsville, Alabama 35806, USA,*

³*Aerojet Rocketdyne, Canoga Park, California 91309, USA,
561-882-5349; claude.joyner-ii@rocket.com*

Abstract. Future human exploration missions to Mars are being studied by NASA and industry. One of the key architecture decisions involves selecting the propulsion used to transport the crew from Earth orbit to Mars. Nuclear Thermal Propulsion (NTP) is a proven technology that provides the performance to enable significant benefits for crewed missions to Mars due to its high specific impulse. The potential benefits to human Mars exploration include: reduction in interplanetary transit time for astronaut safety and health; reduced launch mass for improved affordability; increased payload mass; improved abort options; and widened launch and departure windows for mission flexibility.

Aerojet Rocketdyne (AR) performed an extensive study to assess the optimum NTP engine thrust for a Mars campaign involving crewed missions in 2033, 2039, and 2043. The study assumed a set of ground rules and assumptions consistent with a NASA Evolvable Mars Campaign (EMC) architecture that uses low-thrust Solar Electric Propulsion for efficient delivery of cargo to Mars and high-thrust propulsion to more rapidly transport the crew to Mars. Building on NASA work, AR assessed NTP as the high-thrust propulsion option to transport the crew.

The impacts of NTP vehicle configuration, number of engines, engine out capability, Earth aggregation/departure orbit, payload mass, and transfer time on optimal engine thrust were assessed. Prior NTP mission architecture studies were also assessed to determine the impact of different architecture scenarios on NTP thrust level. In addition, NTP engine development constraints on thrust size were included in the assessment. This paper provides results of the study and provides a recommendation and associated rationale for an optimal NTP engine thrust level.

Keywords: Nuclear, Mars, EMC, Thrust, Propulsion.

METHODOLOGY

To determine the number of engines to use and the nominal thrust per engine appropriate for an NTP engine design, AR conducted an NTP-based Mars architecture assessment based on the human Mars architecture defined by the NASA EMC [1, 2]. The payloads to be delivered and the mission dates were taken from the EMC studies. The NTP engine and stage was defined by AR.

The NTP engine was modeled from 10 klbf (44.48 kN) to 50 klbf (222.41 kN) to ensure a smooth curve of results. However, below 15 klbf (66.72 kN) was considered higher risk for development as an engine, and recommendations were limited to 15 klbf (66.72 kN) and higher. The NTP engine thrust-to-weight curve was anchored to Low-enriched uranium (LEU) and Highly-enriched uranium (HEU) design data and is shown in Figure 1.

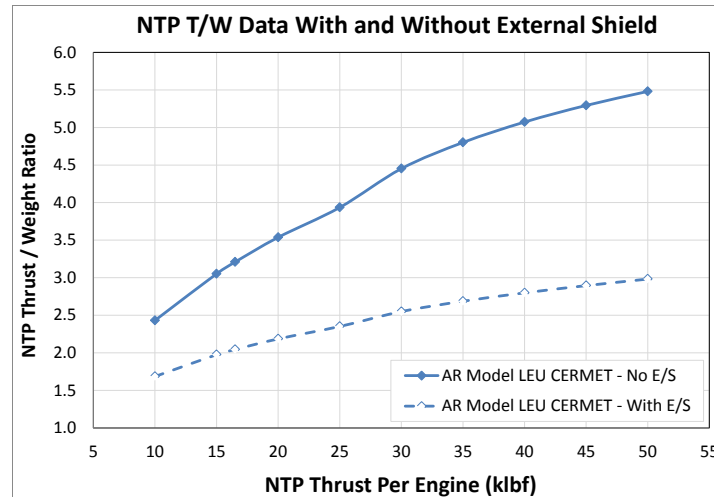


FIGURE 1. LEU Engine Thrust-to-Weight Used.

Sensitivities to the following parameters were examined:

- NTP vehicle configuration: core+inline, core+drop tank, and core+prepositioned Earth return propellant;
- Earth departure years: 2033, 2039, 2043;
- Number of engines: 2, 3, 4;
- Payload mass: 43 – 80 Mt;
- Transfer time: 120 – 200 days each way;

The following ground rules and assumption were used:

Propellant Tanks and Structures – Al-Li 2195 tanks (Spray on Foam Insulation (SOFI) + Multi-layer Insulation (MLI) insulation); Composite primary structures;

Power – Photovoltaic array – sized to provide power for avionics, cryo-coolers, and propulsion;

Propulsion

NTP Main Engine: LEU/CERMET, Isp=900 seconds (steady-state), Pc=1,000 psia (6,894.76 kPa), Exhaust Temp: ~2,740K, Area Ratio: 300;

LOX/CH₄ Attitude Control System/Reaction Control System (ACS/RCS): Isp=340 seconds, Thrust: 1,000 lbf (4.448 kN) axial engine, 100 lbf (444.82 N) ACS engines (consistent with EMC – Storable ACS/RCS option is also viable – the choice is unlikely to impact NTP thrust trades);

Cryo-Fluid Management: Passive SOFI+MLI with cryo-coolers for LH₂, LOX, and CH₄ tanks;

Unusable Propellant: Based on EMC assumptions

- 4% flight propellant reserve on delta-V for all primary burns; 0% for secondary burns,
- 3% additional reserves and residuals (trapped propellant, loading/mass gauging uncertainty),
- Start-up and shutdown = 3% (accounts for lower Isp during start-up and shutdown transients);

ACS/RCS Delta-V Requirements

ACS/RCS delta-V's aligned with EMC requirements

Earth Sphere of Influence: 40 m/s for each rendezvous and docking maneuver; 50-475 m/s for perigee raise/lower maneuvers; 240 m/s for orbital maintenance; 220-400 m/s for maneuvers into and out of Lunar Distant Retrograde Orbit (LDRO) (when required),

Heliocentric: 40 m/s for trajectory correction and attitude control maneuvers to and from Mars,
 Mars Sphere of Influence: 250 m/s for plane change maneuvers.

Non-NTP related assumptions were anchored to EMC. NTP related assumptions were consistent with past NTP architecture studies [3-7].

Five Earth aggregation orbits were examined: LDRO, Lunar Distant Highly Elliptical Orbit (LDHEO), Low Earth Orbit (LEO), and two highly elliptical orbits between LDHEO and LEO termed Highly Elliptical Orbits 1 and 2 (HEO1, HEO2). The elliptical aggregation orbit perigees are set to 2,000 km to avoid orbital debris fields. These orbits are shown in Figure 2. The five orbits cover the range of delta-V that would be used for Trans Mars Injection (TMI) burns. When LDRO is used as the aggregation orbit, the vehicle stack is transferred to LDHEO for the TMI

burn. The crew rendezvouses with the vehicle stack in the aggregation orbit, performs vehicle checkout, moves from the aggregation orbit to an orbit with the same apogee but a perigee set to 407 km (using RCS propulsion) to minimize overall delta-V requirements, and departs for Mars within one orbit to minimize time spent in the Van Allen Belts.

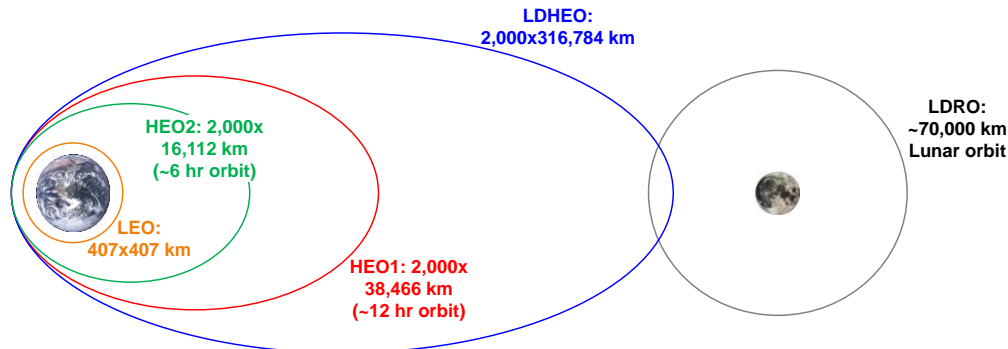


FIGURE 2. Aggregation Orbits Included Cover Range of All Likely Choices.

Figure 3 shows the impact of TMI thrust-to-weight for the various departure orbits. The lower the departure orbit apogee, the higher the required TMI delta-V and the more sensitive the delta-V is to TMI thrust-to-weight.

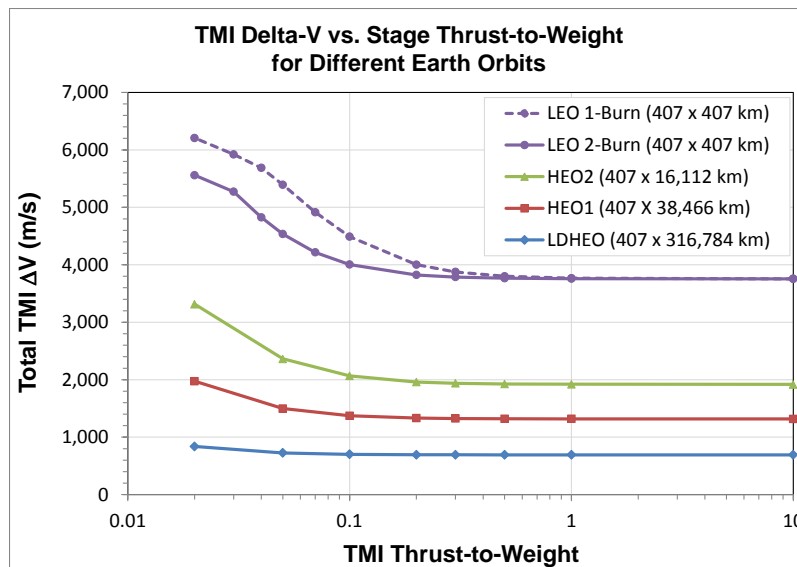


FIGURE 3. Impact of Thrust-to-Weight and Aggregation Orbit on TMI Delta-V.

EMC BASED ARCHITECTURE SENSITIVITY TRADES

The first architecture sensitivity examined was to the NTP configuration. Three NTP configuration options were examined: core+inline, core+drop tank, and core+prepositioned Earth return propellant. Figure 4 shows the three configurations.

The core+inline configuration option results in the heaviest overall vehicle because the entire vehicle stack is carried to Mars and back, but it requires the least demanding mission Concept of Operations (CONOPS) because there is no staging or prepositioning. The core+prepositioned Earth return propellant configuration option results in the lightest overall vehicle but it calls for the most demanding mission CONOPS. Figures 5 and 6 show the results for the highest apogee orbit and one of the lowest apogee orbits.

NTP Config	Crew Propulsive Stack at Earth Departure	Prepositioned Element at Mars	Jettisoned Element at Mars	Crew Propulsive Stack at Mars Departure
Core + Inline	TEI + EOI TMI + MOI			TEI + EOI Empty TMI + MOI
Core + Drop Tank	TEI + EOI TMI + MOI		Empty TMI + MOI	TEI + EOI
Core + Pre-pos Return Prop	TMI + MOI	TEI + EOI		Empty TMI + MOI TEI + EOI

FIGURE 4. NTP Configuration Examined.

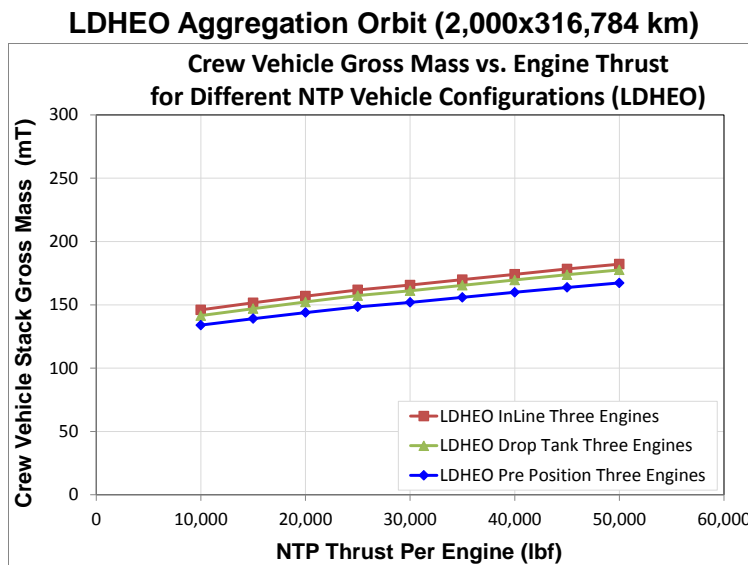


FIGURE 5. Impact of Thrust and Aggregation Orbit – LDHEO.

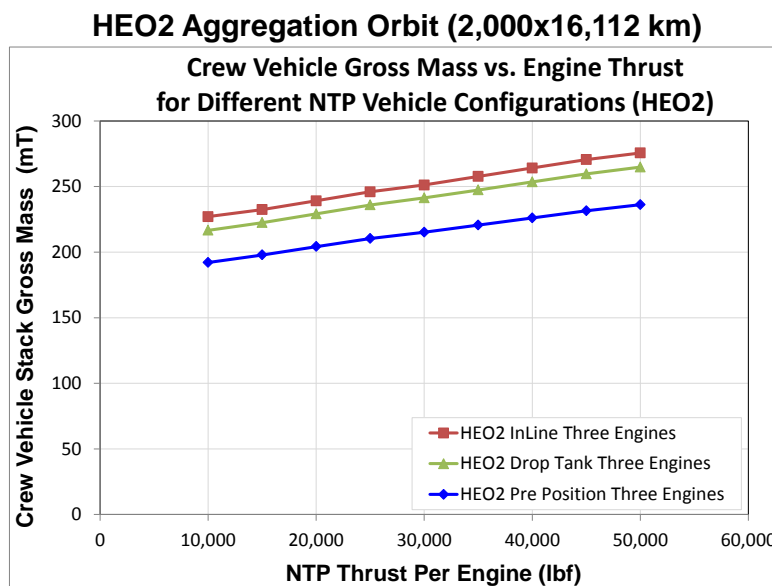


FIGURE 6. Impact of Thrust and Aggregation Orbit – HEO2.

The examined vehicle configuration options show similar thrust trends for all aggregation orbits: the drop tank and pre-positioning configurations provide modest benefit over the inline configuration at the cost of more complex CONOPS. The magnitude of the benefit increases as the Earth aggregation orbit is lowered.

The vehicle stack gross mass decreases with engine thrust because lower thrust level equates to lower engine mass and there is no delta-V penalty due to thrust-to-weight for the range of thrusts examined. The thrust trends are seen to be insensitive to the NTP vehicle configuration so subsequent trades perform using the conservative inline configuration.

The next architecture sensitivity examined departure year sensitivity. The impacts of 2033, 2039, and 2043 missions were examined. Figure 7 shows the results.

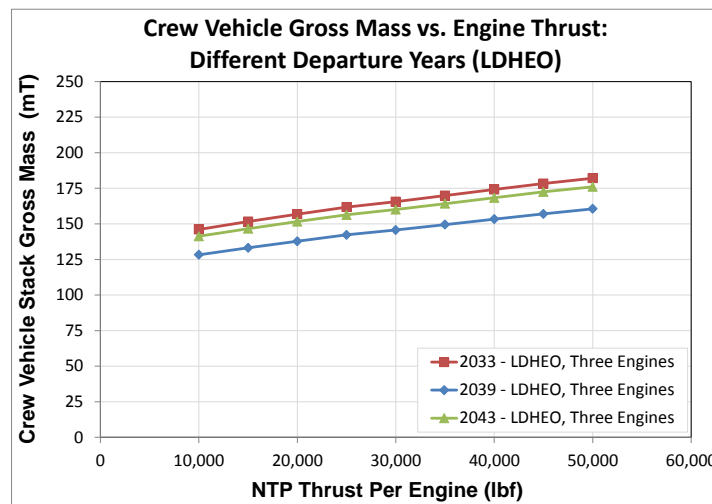


FIGURE 7. Impact of Thrust and Departure Year.

Again, the vehicle stack gross mass decreases with engine thrust because lower thrust drives to lower engine mass and there is no delta-V penalty due to thrust-to-weight for the range of thrusts examined. The thrust trends are seen to be insensitive to the departure year. Subsequent trades concentrated on the 2033 mission/opportunity due to its having the highest delta-V requirements to be conservative.

The number of engines to allow reasonable engine out capability was examined. Two, three, and four engines were considered. Engine out was assumed for all primary burns. The inline configuration and the 2033 departure date were used. LEO is the most stressing departure orbit and was considered using a two-burn TMI maneuver. Figure 8 shows the results. The two engine configuration is typically lighter than three and four engine configurations when engine out is not assumed (solid lines). When engine out is assumed (dotted lines), the three engine configuration is typically lighter than the two and four engine configurations over the 15-25 klb (66.72-111.21 kN) thrust range.

The two engine configuration requires a significant gross mass increase to allow for engine out (up to 50%), while the three engine and four engine configurations require more modest increases to allow for engine out:

- less than 16% increase for all engine thrust levels examined;
- less than 7% increase for 15 klb (66.72 kN) thrust per engine and above.

The two engine configuration was removed from further study due to the significant gross mass increase needed to allow for engine out. Three engine and four engine configurations have more modest increases.

Figure 9 shows the impact of the number of engines on the crew vehicle stack gross mass for three and four engines and for the most favorable orbit.

Noting the results in Figures 8 and 9, the three engine configuration typically provides a lower gross mass solution than the four engine configuration for a wide range of aggregation orbits and thrust levels, with or without engine out. Consequently, the three engine configuration was selected for subsequent trades.

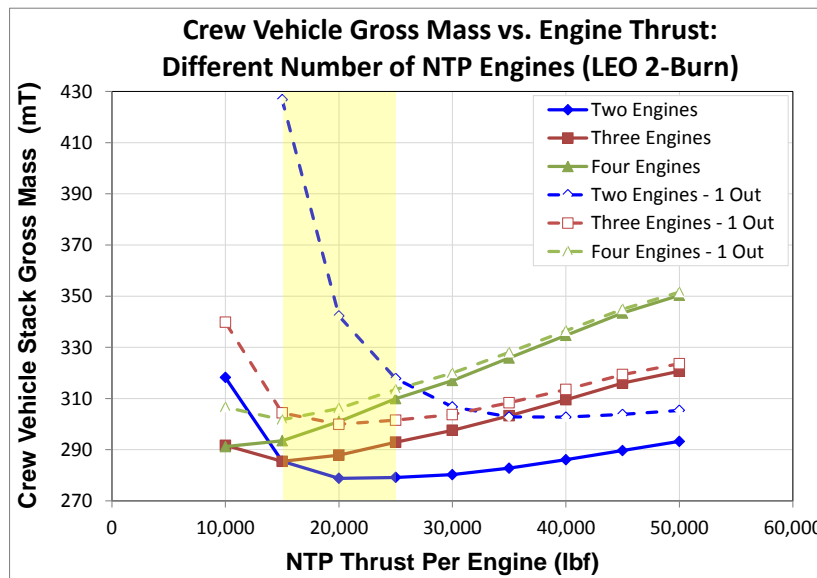


FIGURE 8. Impact of Thrust, Number of Engines, and Engine-Out – LEO (2-Burn).

LDHEO Aggregation Orbit (2,000x316,784 km)

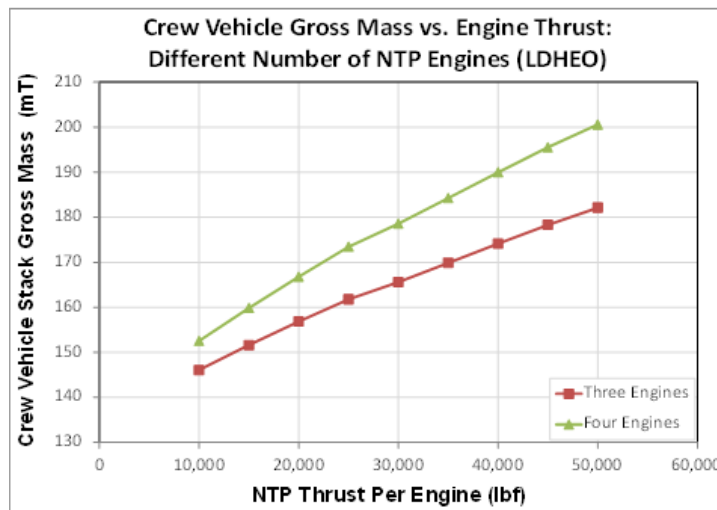


FIGURE 9. Impact of Thrust and Number of Engines – LDHEO.

Based on the preceding trades, the sensitivity to Earth aggregation orbit was examined using the inline configuration, three engines, the 2033 departure date, and with all cases returning to LDHEO at the end of the mission. Figure 10 shows the results.

Lower aggregation orbits desire higher NTP engine thrust. Crew vehicle gross masses for the 15-25 klbf (66.72-111.21 kN) thrust per engine cases are all within ~10% of the optimal thrust level for each aggregation orbit. The 15-25 klbf (66.72-111.21 kN) NTP engine thrust range provides robust solutions for a wide range of aggregation orbits.

Because the payload going to Mars could grow, the sensitivity of the engine thrust to the payload mass was examined using the inline configuration, three engines, the 2033 departure date, and with all cases returning to LDHEO at the end of the mission. Figure 11 shows the results for a LDHEO orbit and Figure 12 shows the results for a LEO orbit.

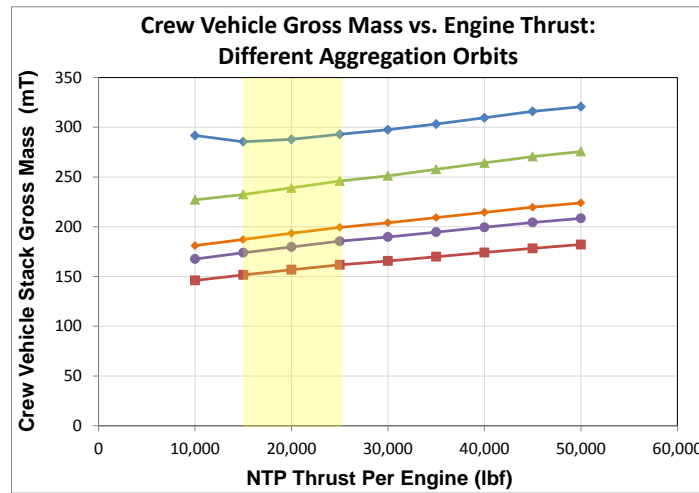


FIGURE 10. Impact of Thrust/Engine and Aggregation Orbit.

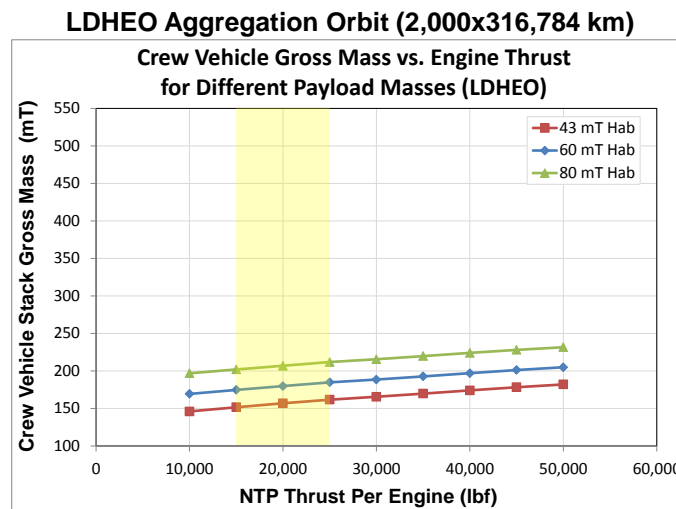


FIGURE 11. Impact of Thrust/Engine and Payload Mass – LDHEO.

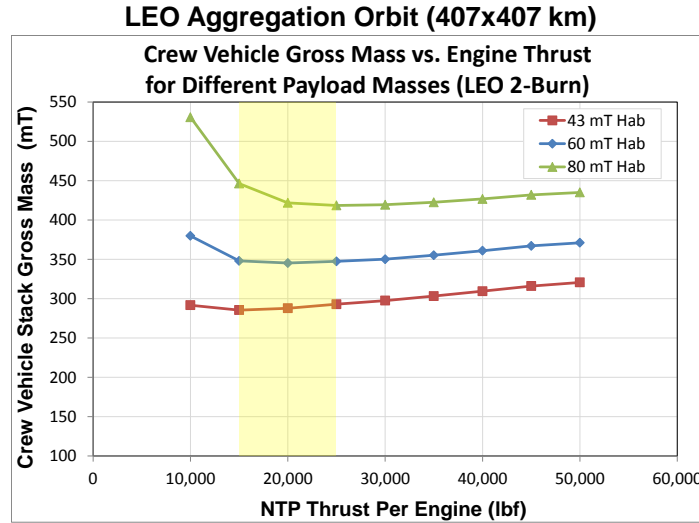


FIGURE 12. Impact of Thrust/Engine and Payload Mass – LEO (2-Burn).

Higher payload mass cases optimize at higher engine thrust levels for the lowest aggregation orbit and have no effect at the highest aggregation orbit. The crew vehicle gross masses for the 15-25 klbf (66.72-111.21 kN) thrust per engine cases are all within 10% of the optimal thrust level for each payload mass/aggregation orbit combination. The 15-25 klbf (66.72-111.21 kN) NTP engine thrust range provides a robust solution for a wide range of payload masses and Earth aggregation orbits.

One of the significant potential benefits of using NTP propulsion is to shorten the Earth-Mars and the Mars-Earth trip times. The previous trades have been for minimum energy trajectories that produce trip times of about 198 days each way. Decreasing the trip times increases the required delta-V and thus the Earth departure vehicle gross mass. Figure 13 shows the delta-V's needed.

Total Transfer Time (days) (Outbound + Return)	Mars Stay Time (days)	ΔV (km/s) from LDHEO (407 x 316,784 km)		ΔV (km/s) from LEO (407 x 407 km)	
		Earth to Mars (TMI & MOI)	Mars to Earth (TEI & EOI)	Earth to Mars (TMI & MOI)	Mars to Earth (TEI & EOI)
395 (198+197)	565	0.518	1.0573	3.5810	1.0573
		1.3010	0.5226	1.3010	3.5852
360 (180+180)	600	0.53094	1.13163	3.59352	1.13163
		1.37533	0.52396	1.37533	3.58654
320 (160+160)	636	0.61040	1.35939	3.67299	1.35939
		1.68319	0.57615	1.68319	3.63874
280 (140+140)	668	0.77110	1.72788	3.83369	1.72788
		2.21826	0.71565	2.21826	3.77823
240 (120+120)	701	1.10946	2.36217	4.17205	2.36217
		2.93033	0.94727	2.93033	4.00985
200 (100+100)	734	1.69837	3.35227	4.76096	3.35227
		3.97442	1.37651	3.97442	4.43909

FIGURE 13. Impact of Trip Time on Required Delta-V.

Figures 14 and 15 show the results for various trip times for the LDHEO orbit and the LEO orbit for a 2033 conjunction class mission with optimized departure dates and stay times. The transfer times shown are each way (example: 160 days Earth-to-Mars and 160 days Mars-to-Earth).

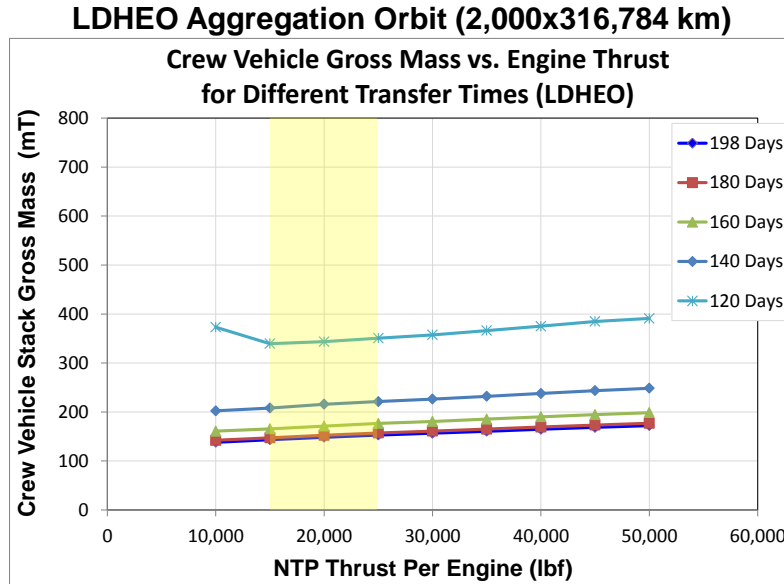


FIGURE 14. Impact of Thrust/Engine and Trip Time – LDHEO.

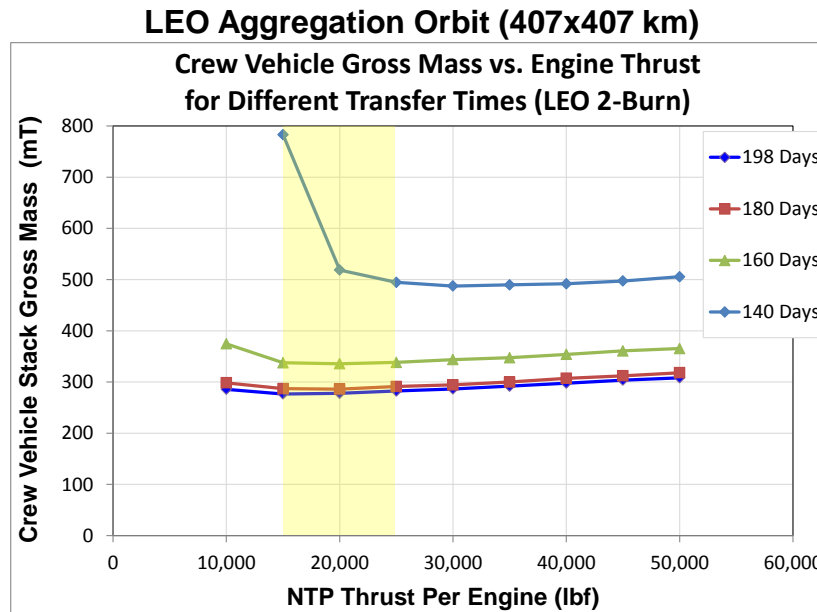


FIGURE 15. Impact of Thrust/Engine and Trip Time – LEO (2-Burn).

Shorter crew transfer times optimize at higher engine thrust levels. The crew vehicle gross masses for the 15-25 klbf (66.72-111.21 kN) thrust per engine range cases are all within 11% of the optimal thrust level for each transfer time/aggregation orbit combination (the 15 klbf (66.72 kN) 140 days/LEO case would require an additional engine). The 15-25 klbf (66.72-111.21 kN) NTP engine thrust range provides a robust solution for a wide range of transfer times and Earth departure orbits.

PAST NTP MISSION ARCHITECTURE STUDIES

A number of previous studies [3-7] have been conducted and have determined a thrust level. Figure 16 summarizes some of them. These past NTP mission architecture studies indicate that thrusts in the range of 15-25 klbf (66.72-111.21 kN) per engine meets most requirements.

Architecture Name	Destination	Number of Engines	Thrust / Engine (klbf)	Notes
NASA Mars DRA 5 / Addendum 2 (2014)	Mars Surface	3	25	LEO departure Payload: 6 Crew, ~52 mT habitat*, ~15 mT Orion
NASA Waypoint Architecture DRMv0.9 2012	Earth-Lunar L2	1	25	LEO departure Payload: ~27 mT Cargo
NASA TM-2014-218104 "Fast Transit Human Missions to Mars"	Mars Fast 100-130 Day Transit	4	25	LEO departure Payload: 4-6 Crew, ~50 mT habitat*, ~15 mT Orion
NASA TM-1998-208830	Lunar Vicinity / Surface	2-3	15	LEO departure Payload: 4 Crew/Lander or 10 Person Cab
AR NETS 2015/2016	Mars Vicinity	3-4	15-22	LEO departure Payload: 4 Crew, 40 mT habitat*, ~15mT Orion

*Habitat/crew/logistics/samples

FIGURE 16. Previous Studies Show Similar Thrust/Engine Results.

CONCLUSIONS

AR utilized a combination of inputs as a basis for determining the optimum NTP thrust per engine and number of engines that is appropriate for a wide range of potential Mars architectures (Figure 17).

Input	Result
An NTP-based Mars architecture assessment based on the human Mars architecture defined by the NASA Evolvable Mars Campaign (EMC)	Three 15-25 klbf engines
Past NTP mission architecture studies	15-25 klbf / engine
NTP engine DDT&E constraints (test facilities, liquid rocket engine, etc)	≤ 25 klbf / engine

FIGURE 17. Various Approaches Lead to Similar Thrust/Engine Results.

Based on architecture trade results, AR recommends three engines and an NTP thrust per engine of 15-25 klbf (66.72-111.21 kN). This recommendation is not affected by LEU/HEU or Composite/CERMET choices. Three engines were selected as a compromise for minimizing stage mass while allowing for engine out. The 15-25 klbf (66.72-111.21 kN) thrust per engine selection provides a robust capability across a range of Lunar and Mars architecture options (NTP vehicle configurations, departure orbits, payload sizes, and transfer times) while also accounting for NTP engine design considerations (test facility limitations, engine controllability/stability, start and shutdown transients, fuel burn-up per power and enrichment level, and use of liquid hydrogen rocket engine hardware for early non-nuclear testing to reduce mission risk). Test facility cost constraints drive the engine thrust size to be less than 50klbf or major facility changes are required. The 25klbf thrust size thus provides a more affordable development testing path. A conservative choice for designing a nominal engine is three 25 klbf (111.21 kN) engines.

REFERENCES

- [1] Percy, Thomas K., McGuire, Melissa, Polsgrove, Tara, "In-Space Transportation for NASA's Evolvable Mars Campaign", AIAA Space 2015 Conference and Exposition, August 31-September 2, 2015, Pasadena, California, AIAA 2015-4519.

- [2] Polsgrove, Tara, Chapman, Jack, Sutherlin, Steve, Taylot, Brian, Fabisinski, Leo, Vollins, Tim, Dwyer-Cianciolo, Alicia, Samareh, Jamshid, Robertson, Ed, Studak, Bill, Vitalpur, Sharada, Lee, Allen Y., Rakow, Glenn, “Human Mars Lander Design for NASA’s Evolvable Mars Campaign”, 2016 IEEE Aerospace Conference, Big Sky, Montana, March 5-12, 2016, IEEE 2016-8.0111.
- [3] Drake, Bret G., Watts, Kevin D., (editors), *Human Exploration of Mars Design Reference Architectures 5.0 Addendum #2*, NASA/SP-2009-566-ADD2, NASA Johnson Space Center, Houston, Texas, March 2014.
- [4] Personal Communication: Larry Koss/NASA MSFC-NASA Waypoint Architecture Analysis - DRMv0.9 2012.
- [5] Borowski, Stanley K., McCurdy, David R., Packard, Thomas W., *Nuclear Thermal Propulsion (NTP): A Proven Growth Technology for ‘Fast Transit’ Human Missions to Mars*, NASA TM-2014-218104, NASA Glen Research Center, Cleveland, Ohio, 2014.
- [6] Borowski, Stanley K., Duzinski, Leonard A., “2001: A Space Odyssey” Revisited – *The Feasibility of 24 Hour Commuter Flights to the Moon Using NTR Propulsion with LUNOX Afterburners*, NASA TM-1998-208830, NASA Glen Research Center, Cleveland, Ohio, 1998.
- [7] Joyner II, C. R., Levack, Daniel J. H., Crowley, J., “Determining Mars Mission NTP Thrust Size and Architecture Impact for Mission Options”, AIAA Propulsion and Energy Forum and Exposition 2015, Orlando, Florida, July 27-29, 2015, AIAA 2015-3956.

Idaho National Laboratory Radioisotope Power Systems Nuclear Operations: Readiness Assessments Supporting a Nuclear-enabled NASA Mission

Kelly L. Lively^{1a} and Drake C. Kirkham^{1b}

^{1a}Radioisotope Power Systems Department Manager and ^{1b}Quality Assurance Department Manager, Idaho National Laboratory, Idaho Falls, ID 83415-6122
(208)533-7388; Kelly.Lively@inl.gov

Abstract. The Radioisotope Power Systems (RPS) Program, located at Idaho National Laboratory (INL), is responsible for assembling, testing, and delivering plutonium oxide-fueled RPSs for use in powering missions in remote, harsh environments such as deep space. An informative presentation will be given discussing the readiness assessments involved in performing nuclear operations to support providing these systems to end users for the Department of Energy (DOE). Readiness for start-up is determined through independent assessment against established acceptance criteria to ensure activities can be performed safely and within a well-defined nuclear safety envelope. There is also an RPS Program approval element for product quality requiring additional readiness review before nuclear operations can begin. Typically, the assessments/review criteria requires, at a minimum, review of operating instructions to ensure technical safety requirements are adequately identified, review of training records to ensure personnel are adequately trained to perform the specified work scope, personnel are interviewed to determine adequacy of level of knowledge for work scope, and a high-fidelity performance of the operation to ensure the operating instructions and conduct of operations are adequate to perform the work scope. As each assessment/review is conducted, a formal report delineating any issues in the form of findings, observations, and noteworthy practices will be issued. Before start-up approval is obtained, all issues must be resolved to the satisfaction of the individual teams. Approval for start-up is formally communicated by memorandum from DOE. Programmatic approval is also formally communicated where vested Program representatives in the RPS community (to include DOE Nuclear Energy (DOE NE) and DOE Idaho Operations Office (DOE ID) representatives) ensure personnel, documentation, and materials are in place to perform the activity. RPS assembly and testing operations to support the Mars 2020 Mission, the next planned space mission using a nuclear power system, will require about of year of assessments/reviews before the nuclear operations are performed. From a regulatory perspective, Title 10 of the Code of Federal Regulations (CFR), Part 830[1] governs DOE and its contractors conducting activities that affect, or may affect, the safety of DOE Nuclear Facilities. Further, DOE Order 425.1[2] and 414.1[3] establish requirements to verify readiness for startup or re-start of Hazard Category 1, 2, and 3 nuclear-facility activities and to ensure products and services meet or exceed customer's requirements and expectations, respectively.

Keywords: INL, Operations, Assessments, DOE, Quality Assurance, QA.

RADIOISOTOPE POWER SYSTEMS

A Radioisotope Power System (RPS) such as the Multi-Mission Radioisotope Thermoelectric Generator (MMRTG) (ref. Figure 1) is an electrical generator that converts the heat generated by decay of iridium clad, $^{238}\text{PuO}_2$ fuel pellets into electricity. RPSs are used as power sources for use in remote, harsh environments such as space. The Department of Energy's (DOE) Idaho National Laboratory (INL) is the only national facility capable of performing nuclear activities to safely fuel, test, store, transport, and perform end-user handling for mission testing and integration. The INL serves as part of the DOE, RPS community providing RPSs to customers for use in remote, harsh environments such as deep space.



FIGURE 1. MMRTG RPS

Facilities

The INL is an 860-square mile, federal reservation located in a remote, desert site of southeast Idaho. The Materials and Fuels Complex, located on the INL site, is home to the to the Space Nuclear Power and Isotope Technologies Division. Nuclear and non-nuclear facilities house equipment needed to perform required activities. Two primary facilities, located within the security-protected confines of MFC, are utilized to perform nuclear and non-nuclear activities, the Space and Security Power Systems Facility (SSPSF) (ref. Figure 2) and the Engineering Development Laboratory (EDL) (ref. Figure 3), respectively.



FIGURE 2. SSPSF



FIGURE 3. EDL

SSPSF is categorized as a DOE Hazard Category 2 (HC-2) Non-Reactor Nuclear Facility based on the estimated inventory of radioactive materials. It is a two-story, 10,000 square foot building. The first floor houses RPS assembly and testing equipment, including gloveboxes, fume hoods, testing equipment and a high-bay (7.5-ton crane) for receipt and handling of Department of Transportation (DOT) shipping packages. EDL is a two-story, 4,000 square foot building. The first floor houses a high temperature vacuum furnace, electron beam welder, forming presses (30 ton) and laser etcher. The partial, second floor is a mezzanine and houses a graphite vacuum furnace with access to a glovebox, and two welding gloveboxes. An overhead crane (5-ton) is located on the second

floor that reaches to the first floor. Facility systems include heating and ventilation, process chilled water, glovebox-related vacuum pumps, and normal power.

Human Resources

The RPS Program is comprised of a multi-disciplined work force of degreed Engineers (mechanical, electrical, materials, instrumentation and control); certified Quality Engineers, Quality Assurance Inspectors, Nuclear Operators, and technicians (electrical, mechanical, and welding). The RPS Program is governed by a Quality Assurance Program Plan (QAPP)[4] which is dedicated to the RPS Program and described in more detail hereafter. The Engineering Staff provides System and Applied Engineering, Tool Design and Testing, Training Development and execution to support the RPS Processes and associated equipment. Nuclear Operators and technicians supply the trained, qualified work force to complete the hands-on nuclear and non-nuclear work scope. An RPS Program Manager, Nuclear Facility Manager, SSPSF Operations Manager, Laboratory Space Manager, RPS Department Manager and Technical Leads round out the Program providing Programmatic Project Management.

Operations

Operations at the INL include non-nuclear operations of module pre-assembly and bake-out and nuclear operations of General Purpose Heat Source (GPHS) Module Assembly (ref. Fig. 4) that generates heat through decay of Plutonium Oxide fuel pellets; assembly of GPHSs into an RPS (power system that converts the heat generated by the GPHS fuel pellet into electrical power), and RPS Acceptance Testing performed after RPS Assembly—Vibration Testing simulating the launch pad environment, Mass Properties Testing measuring the center of gravity and moment of inertia, Magnetics Testing mapping the magnetic-field strength generated by the electric-current generating RPS, thermal vacuum testing to collect power performance data when the RPS is placed in a near-earth space vacuum. The assembled and tested RPS is then maintained in storage until it is transported to a remote location for vehicle integration. Transportation and RPS integration activities take nuclear activities on the road to remote locations. Space missions dictate delivery of the RPS, a radioactive payload, to locations such as Kennedy Space Center for installation of flight hardware on the RPS, integrated system testing (powering a space vehicle for testing) and storage until the final integration before launch. Department of Transportation (DOT) certified, Type-B shipping casks are used to transport radioactive, payloads across the nation in the form of 1) radioactive, iridium clad, fuel pellets for INL assembly into GPHSs and 2) RPS units after they are fueled with GPHS and tested for end use. The INL is the custodian of these shipping casks and the transportation trailers used for transporting the shipping casks used for RPS transportation to the remote locations.

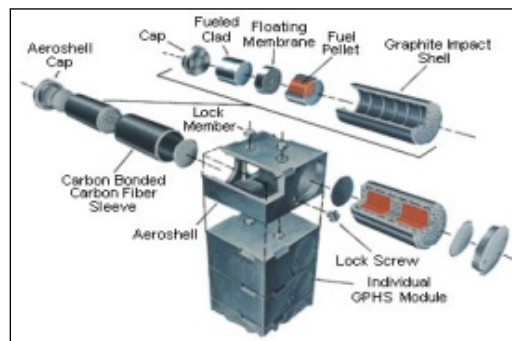


FIGURE 4. GPHS Assembly

READINESS ASSESSMENTS

Title 10 of the Code of Federal Regulations (CFR), Part 830[1] governs DOE and its contractors conducting activities that affect, or may affect, the safety of DOE Nuclear Facilities. Further, DOE Order 425.1[2] and 414.1[3] establish requirements to verify readiness for startup or re-start of Hazard Category 1, 2, and 3 nuclear-facility

activities and to ensure products and services meet or exceed customer's requirements and expectations, respectively. Readiness for start-up is determined through independent assessments and programmatic reviews[5] against established acceptance criteria to ensure activities can be performed safely and within a well-defined nuclear safety envelope[6] and to the quality of the product that will be provided meets the DOE quality requirements[4]. A number of DOE approved, INL procedures implement the requirements of these DOE Orders and regulatory requirements. INL performs a screening[7] to determine the level of independent readiness verification needed to perform an identified scope of work. INL presents a plan of action to determine readiness to the DOE Operational Safety Board for approval. DOE examines the operation or activity and determines the level of independent verification of readiness needed to start or restart operations in a Hazard Category 1, 2 or 3 nuclear facility. A graded, assessment approach for readiness verification is used and can be as simple as no assessment requirement to a DOE Readiness Assessment (DOE RA) or an Operational Readiness Review (ORR). DOE grants approval to perform the nuclear operations based upon successful completion of any assessment requirements including satisfactory resolution of assessment issues. In preparation for the DOE assessments, the INL would determine a plan of action ensuring readiness to perform the same nuclear activity. If the screening identifies a DOE-level assessment, then the INL performs a Management Self Assessment (MSA) and a Contractor Readiness Assessment in preparation for performance of the DOE-level assessment.

Historically, RPS Program, nuclear activities screen to perform DOE-level assessments and Programmatic Reviews. The INL typically conducts the following assessments/reviews in the following order of progression before authority to perform the activities is granted: Management Self Assessment (MSA), Contractor Readiness Assessment (CRA), DOE Readiness Assessment (DOE RA), Production Readiness Review (PRR) and lastly, the Segmented Readiness Review (SRR). Twelve assessment criteria are reviewed and a selection of the criteria is identified for assessment on a graded approach. Review criteria typically requires, at a minimum, review of operating instructions to ensure technical safety requirements are adequately identified, review of training records to ensure personnel are adequately trained to perform the specified work scope, personnel are interviewed to determine adequacy of level of knowledge for work scope, and a high-fidelity performance of the operation to ensure the operating instructions and conduct of operations are adequate to perform the work scope. As each assessment/review is conducted, a formal report delineating any issues in the form of findings, observations, and noteworthy practices will be issued. Before start-up approval is obtained, all issues must be resolved to the satisfaction of the individual teams. Approval for start-up is formally communicated by memorandum from DOE. Programmatic approval is documented in the SRR where vested Program representatives in the RPS community (to include DOE Nuclear Energy (DOE NE) and DOE Idaho Operations Office (DOE ID) representatives) ensure personnel, documentation, and materials are in place to perform the activity.

GENERAL REGULATORY REQUIREMENTS

The requirements governing assessment activities relating to the RPS Program at the INL are described in multiple documents at several tiers ranging from Federal Law to program specific instructions. Each tier encapsulates the tier above and adds specific implementing requirements within their scope as shown in Figure 5. These tiers and their associated assessment related requirements are described here in more detail.

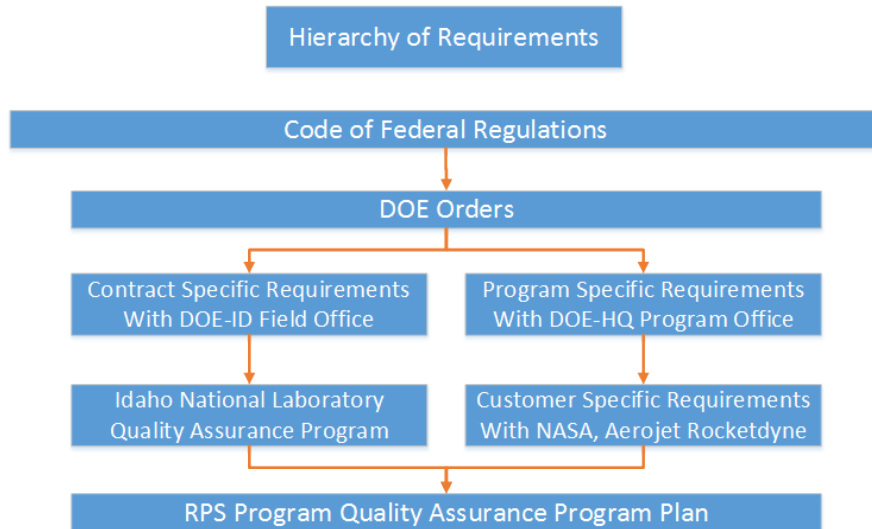


FIGURE 5. Hierarchy of Requirements Pertaining to the RPS Program at the INL

Code of Federal Regulations

The Code of Federal Regulations (CFR) is an annual codification of the general and permanent rules published in the Federal Register by the executive departments and agencies of the Federal Government[8]. The purpose of the CFR is to present the official and complete text of agency regulations in one organized publication[8]. The coding system is based on Titles, Parts and Subparts. For example, Title 10: Energy PART 830 – NUCLEAR SAFETY MANAGEMENT Subpart A – Quality Assurance Requirements[1], would be shortened to read 10 CFR 830 Subpart A when referenced in program documents. Many CFRs apply to specific activities performed at the INL. Most CFRs apply only to a sub-population of the INL, for example, 10 CFR 71 *Packaging and Transportation of Radioactive Material*. Only one CFR applies to the entire INL, 10 CFR 830 Subpart A.

DOE Orders

DOE Orders encapsulate CFR requirements and mandate any additional requirements for the DOE and its contractors. DOE Orders are numbered with the current revision in the title. The associated DOE Order to 10 CFR 830 Subpart A is DOE O 414.1D, QUALITY ASSURANCE, Admin Chg 1[3]. The criteria that apply to the INL are identical to the criteria found in 10 CFR 830 Subpart A. There are ten criteria with specific requirements for each topic area. The DOE Order adds two additional requirements, one regarding the prevention of suspect/counterfeit items and another regarding safety software utilized in nuclear facilities.

Criterion 9 and Criterion 10 apply specifically to assessment:

Criterion 9—Assessment/Management Assessment. Ensure that managers assess their management processes and identify and correct problems that hinder the organization from achieving its objectives.

Criterion 10—Assessment/Independent Assessment.

- a. Plan and conduct independent assessments to measure item and service quality, to measure the adequacy of work performance, and to promote improvement.
- b. Establish sufficient authority and freedom from line management for independent assessment teams.
- c. Ensure persons who perform independent assessments are technically qualified and knowledgeable in the areas to be assessed.[1,9]

INL Contract with the DOE-ID Field Office

The American Society of Mechanical Engineers (ASME) NQA-1-2008 with the 2009 addenda[9] is an American national consensus standard called out in the contract between INL and DOE-ID and is structured with eighteen requirements. The requirements in NQA-1 completely encompass the requirements found in 10 CFR 830 as well as DOE O 414.1D and add additional rigor or specificity in several areas. Requirement 18 - Audits has eight sections that apply directly to the INL audit function. These sections are:

100	Basic
200	Scheduling
300	Preparation
400	Performance
500	Reporting
600	Response
700	Follow-Up Action
800	Records[2]

Each of these sections directly impact the format, content and mechanisms used for assessment at the INL and subsequently within the RPS Program.

INL Quality Assurance Program Description (QAPD)

The INL QAPD, found in PDD-13000, *Quality Assurance Program Description* encapsulates all of the contractual requirements for the INL as a whole[11]. The purpose statement summarizes the intent of the document.

This Idaho National Laboratory (INL) quality assurance program (QAP) program description document (PDD) is the top-level document that describes the quality assurance policy, applicable contractual quality assurance requirements, assigns major functional responsibilities for INL work activities conducted by or for INL, describes the application of the graded approach for those QA requirements and implementing procedures documented in the requirements management system database, and describes the management systems that incorporate QA requirements[11].

All work activities at the INL are covered within the scope of PDD-13000. As part of the Program Description, “Performance and improvements require thorough, rigorous assessments and effective corrective actions ...[11]” Section 6.18 specifically addresses the implementation of assessments and audits at the INL. The goals of the INL assessment program are to:

- Identify and correct problems that hinder INL from achieving its mission and objectives
- Measure items and service quality
- Measure adequacy of work performance
- Promote improvement
- Verify compliance to QAP requirements
- Verify that performance criteria are met
- Determine the effectiveness of the program[11]

Section 6.18.1, Quality Assurance Program Audits, states “QAP audits of activities are performed in such a manner as to assure that an audit of all applicable QAP elements is completed within a period of 3 years. QAP audits are

scheduled based on an approved triennial topics schedule in a manner to provide coverage and coordination with ongoing activities, based on the status and importance of the activity[11].”

The RPS Program Quality Assurance team performs these audits within the Program, the results of which are verified by the 3rd party auditors on a periodic basis. Corrective actions identified are also managed within the program unless entities outside of the Program are impacted.

Section 6.18 also defines the difference between Management Assessments and Independent Assessments. Their goals are different as well as the training and experience requirements needed to perform or participate in each. The goals of Management Assessments are to:

- Ensure that their organizations and functions are periodically assessed
- Determine how well they meet customer and performance expectations as well as mission objectives
- Identify strengths or improvement opportunities and correct problems
- Address the effective use of resources to achieve the organization’s goals and objectives

Independent Assessments have a different focus. They are used to evaluate the performance of work processes with regard to:

- Requirements
- Compliance
- Expectations for safely performing work
- Achieving the goals of the organization[11]

Program Specific Requirements with the DOE-HQ Program Office

The requirements specific to the RPS Program from the DOE Headquarters Program office are contained in SDPS/PQAR-1, SPACE AND DEFENSE POWER SYSTEMS PROGRAMMATIC QUALITY ASSURANCE REQUIREMENTS FOR SPACE AND TERRESTRIAL NUCLEAR POWER SYSTEMS[12]. Section 8 ASSESSMENTS, indicates that the DOE-HQ Program Office “... shall plan, schedule, and perform quality assessments of contractor operations and quality program implementation to measure adequacy of work performance, and to assess compliance with technical and quality criteria.[11]” Assessments of contractor operations has been described earlier. Assessments, of quality program implementation, are performed annually by a third-party audit team; consisting of personnel from TechSource Inc. and DOE-ID Field Office Quality Assurance Department. This oversight team audits compliance of the RPS Program to its own QAPP that encapsulates INL requirements and any additional customer-specific or mission-specific requirements. INL QAPP requirements are only considered when they impact the RPS Program directly. This level of oversight ensures that personnel are accustomed to a questioning attitude and are dedicated to the continuous improvement that oversight encourages.

Audits performed in FY13 and FY15 did not indicate any assessment or auditing related findings or observations. Third party auditing has found the RPS Program at the INL *effective* or *highly effective* since its start up at the INL.

Quality Assurance Program Plans (QAPP)

LWP-13012, Addressing Program/Project Specific Quality Assurance Requirements, authorizes individual programs to create quality plans in order to meet customer requirements that may conflict with or exceed specific requirements of the INL in general[13]. These plans are called QAPPs.

The RPS Program QAPP is structured to address the criteria from 10 CFR 830 and DOE O 414.1D directly. Therefore, section 9 addresses Management Assessments and section 10 addresses Independent Assessments. The Management Assessment section includes the mandate for periodic reporting and the content requirements for weekly, monthly, quarterly and annual reports.

The annual Management Assessment is mandated to contain the following in addition to any other items:

- List of assessment activities (inspections, surveillances, management assessments, independent assessments, etc.) pertinent to the RPS Program that were conducted during the reporting period
- List of INL RPS-related deficiencies for which no internal action was generated

- List of INL documents (e.g., Timely Orders, Standing Directives) and processes implemented in SSPSF which did not include RPS Program specific approval
- Results of review of deviations to INL procedures
- Summary of assessment activities required by RPS packaging SARPs

Independent Assessment within the RPS Program is conducted per the associated INL procedures using audit checklists that incorporate all INL top-tier requirements. RPS Program internal audit checklists also include the necessary evaluation to conform to 10 CFR 71[14] (SARPs) which applies to the RPS Program specifically due to the 9904 and 9516 casks as well as the transportation system to carry them that are managed by the Program. Due to the fact that 10 CFR 71 is structured like NQA-1, using the INL checklists with some minor modifications complies with both requirements.

CONCLUSION

DOE Regulations govern conducting nuclear activities that may affect the safety of DOE nuclear facilities. DOE orders require independent verification of operational readiness to a customer-expected level of quality before nuclear operations are performed in a nuclear facility. A graded approach to assessments and programmatic reviews are required to be performed to ensure deliverables are produced safely and at an expected quality standard. INL RPS assembly and testing operations to support the Mars 2020 Mission, the next planned space mission using a nuclear power system, will require about of year of assessments and reviews before the nuclear operations are performed in addition to the general assessments required regardless of any program scope.

REFERENCES

- [1] 10 CFR 830, *Nuclear Safety Management*, Latest Revision
- [2] DOE O 425.1, *Verification of Readiness to Start Up or Restart Nuclear Facilities*, Latest Revision
- [3] DOE O 414.1, *Quality Assurance*, Latest Revision
- [4] R1037-0008-QP, *Radioisotope Power Systems Program Quality Assurance Program Plan*, Latest Revision
- [5] R1037-0034-AP, *Radioisotope Power Systems (RPS) Program Readiness Review Plan (PRRP)*, Latest Revision
- [6] SAR-408-0, *Executive Summary – Safety Analysis Report for the Space and Security Power Systems Facility (MFC 792A/792)*, 01/16/13
- [7] MCP-9902, *Management Control Procedure, Verification of Readiness to Start Up or Restart Nuclear Facilities*
- [8] Federal Register, “About the Code of Federal Regulations”, www.archives.gov/federal-register/cfr/about.html, (August 2016).
- [9] Hughes, Earl, “DOE O 414.1D, QUALITY ASSURANCE, Admin Chg 1,” Department of Energy Directives Program, Office of Management, (May 2013).
- [10] The American Society of Mechanical Engineers, “ASME NQA-1-2008 / NQA-1a-2009 Quality Assurance Requirements for Nuclear Facility Applications”, (2009).
- [11] Jensen, D. K., “Quality Assurance Program Description,” *PDD-13000*, revision 6, (September 2016).
- [12] Bohne, W. A., “SDPS/PQAR-1, SPACE AND DEFENSE POWER SYSTEMS PROGRAMMATIC QUALITY ASSURANCE REQUIREMENTS FOR SPACE AND TERRESTRIAL NUCLEAR POWER SYSTEMS”, *SDPS/PQAR-1*, revision 6, (June 2010)
- [13] Jensen, D. K., “Addressing Program/Project Specific Quality Assurance Requirements,” *LWP-13012*, revision 1, (May 2015).
- [14] 10 CFR 71, “Packaging and Transportation of Radioactive Material,” Subpart H, “Quality Assurance.”

Cassini Power Subsystem

Jonathan Grandidier, John B. Gilbert and Gregory A. Carr

*Jet Propulsion Laboratory, California Institute of Technology, Pasadena, California, 91109, U.S.A.
(818) 354-1566; jonathan.grandidier@jpl.nasa.gov*

Abstract. The electrical output of Cassini's power system has been decaying consistently as predicted during its 20-year mission between October 1997 and September 2017. The power telemetry data is presented for the entire Cassini mission, including launch, cruise, and Saturn tour, up to the most recent available data. The spacecraft has been powered by three independent Radioisotope Thermoelectric Generators (RTGs) connected in parallel, which were able to generate 882 W at the beginning of the mission shortly after launch. The decrease in power energy output has mainly been driven by the heat reduction of the hot side of the RTGs due to the natural radioactive decay of its heat source plutonium (mostly plutonium-238 [^{238}Pu]), degradation of thermoelectric material performance, and interface degradation.

Keywords: Cassini, Power Subsystem, RTG.

INTRODUCTION

The Cassini Power and Pyrotechnic Subsystem (PPS) includes three radioisotope thermoelectric generators (RTGs).[1] The RTG is a thermoelectric conversion power generating system composed of a heat source, which includes ^{238}Pu , and a cool side, that converts thermal energy to electrical energy with a thermoelectric generator (TEG) system using the Seebeck effect. [2] During the entire Cassini mission, power output data has been communicated to Earth and recorded through telemetry data. The exponential decay of its heat source plutonium and material/interface degradation caused a total 30.5% power degradation over 19 years, which was expected per current lifetime performance prediction models (LPPMs). The comparison of LPPM predictions to actual-power-data was redefined in April 2013 and show good agreement, within about 0.3%. This paper will discuss the comparisons and reasons for the small prediction/data deviations. Other external environmental effects due to spacecraft control events can have an impact on the power output of the spacecraft. Environmental temperature variations and different solar exposures can increase the temperature of the cool side of the thermoelectric device and therefore decrease the power output. These spacecraft control events will be discussed and correlated to various power variations seen in the Cassini power telemetry data. This paper will then discuss the Cassini Plasma Spectrometer (CAPS) instrument and finally look at the mission power requirements and compare them with other deep space missions.

CASSINI RTGS

Cassini's three RTGs contain a total of 32.7 kg of plutonium dioxide, which is comprised of 82.2% of ^{238}Pu by weight. The half-life of ^{238}Pu is 87.75 years. It produces uranium-234 (^{234}U) by α decay, which provides the main source of heat energy for the RTGs. Table 1 shows the detailed composition and characteristics of each of Cassini's RTGs.[3] The total heat output of all three RTGs corresponds to 13.2 kWt at beginning of life (BOL). In comparison to the RTG electrical output of 882.1 W, the calculated BOL efficiency is 6.69%.

CASSINI PPS ARCHITECTURE

Cassini PPS relies on the three RTGs and very limited energy storage. It is based on the continuous power production capability of the RTGs and does not include any battery for energy storage. The power bus is regulated at

30 V with a linear-sequential shunt regulator and contains about 1200 μ F for bus stability. The Cassini functional block diagram is depicted in Fig. 1.

TABLE 1. RTGs fuel composition at beginning of life [3]

	RTG 1	RTG 2	RTG 3	Total
²³⁸Pu Weight (g)	7693.70	7774.06	7756.40	23224.15
²³⁹Pu Weight (g)	1426.55	1447.79	1441.78	4316.11
²⁴⁰Pu Weight (g)	199.87	212.38	202.62	614.88
²⁴¹Pu Weight (g)	20.24	20.75	20.54	61.53
²⁴²Pu Weight (g)	11.84	14.13	12.53	38.50
²³⁶Pu Weight (g)	1.07E-04	1.14E-04	1.13E-04	3.34E-04
Total Pu Weight (g)	9352.19	9469.12	9433.87	28255.17
Other Actinides (g)	235.07	166.96	184.74	586.77
Impurities (g)	14.46	15.54	14.26	44.26
Oxygen (g)	1275.94	1243.13	1263.33	3782.40
Total Fuel (g)	10877.65	10894.75	10896.20	32668.60
Pu-238/Total Pu (%)	82.27	82.10	82.22	82.19
Avg. Pellet Weight (g)	151.08	151.32	151.34	151.25
Heat Output (Wt)	4368.06	4413.78	4403.68	13185.52
Avg. Pellet Heat (Wt)	60.67	61.30	61.16	61.04
Avg. Pellet Density (g/cc)	9.83	9.94	9.90	9.89
Activity (Curies)	133934	135368	135040	404342

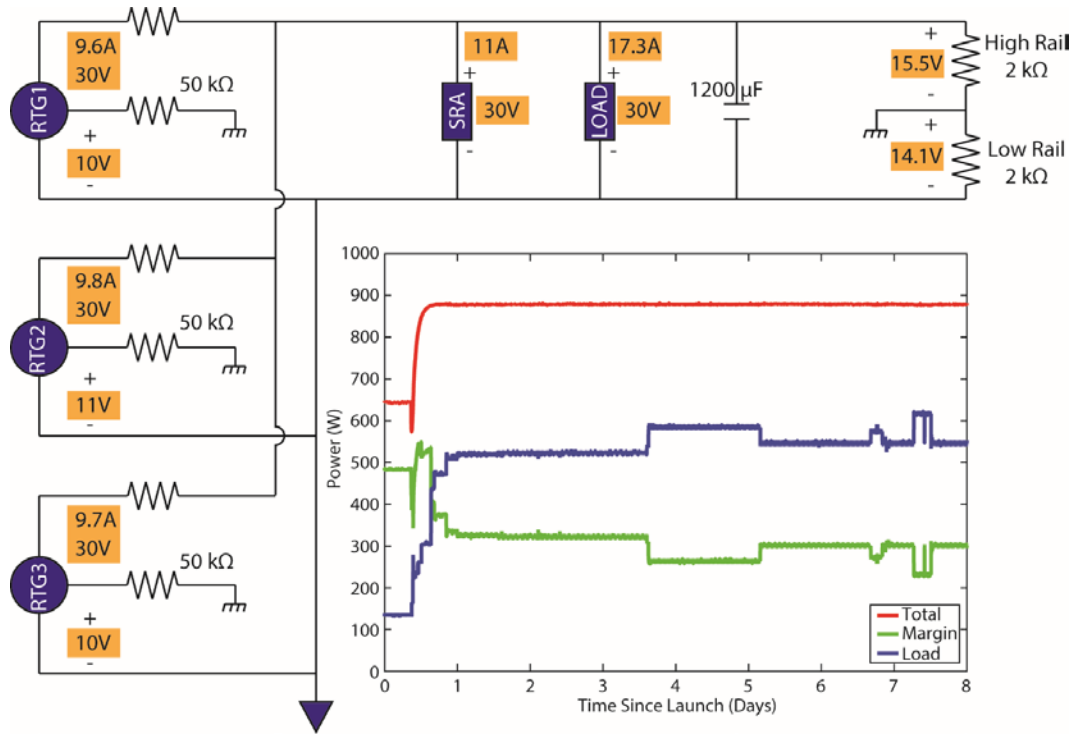


FIGURE 1. Cassini functional block diagram. The plot shows the total, margin and load power during the first eight days of the mission, including launch.

The three RTGs are connected in parallel. Therefore, the current generated by each RTG adds up to the total power output. At the beginning of the mission, the total power output of Cassini peaked at 882.1 W two days after launch. This was the highest recorded data point for the entire mission. Since very limited energy storage is available, Cassini power output needs to supply the overall spacecraft consumption at all times, in addition to a margin of 20 W to cover transient loads. The total spacecraft power consumption, or “LOAD,” averages to 469.18 W over the mission, well below the total power output capability. The excess in power, or “MARGIN,” is discarded from the spacecraft through heat radiation via the Shunt Regulator Assembly (SRA). For energy balance, at all times, the sum of the LOAD and MARGIN adds up to the total power output from the three RTGs. The graph shown in Fig. 1 gives the total power output, and the LOAD and MARGIN values during the first eight days of the mission. The measured current output, voltage, and case voltage arbitrarily chosen two days after launch is reported for each RTG. At the same time, SRA and load current and voltage are shown, as well as High-rail and Low-rail voltages.

CASSINI POWER OVER TIME

Cassini was launched on 15 October 1997 by a Titan 4B launch vehicle. [4] The mission is scheduled to end on September 17th 2017 and therefore, the entire mission is scheduled to last almost 20 years.

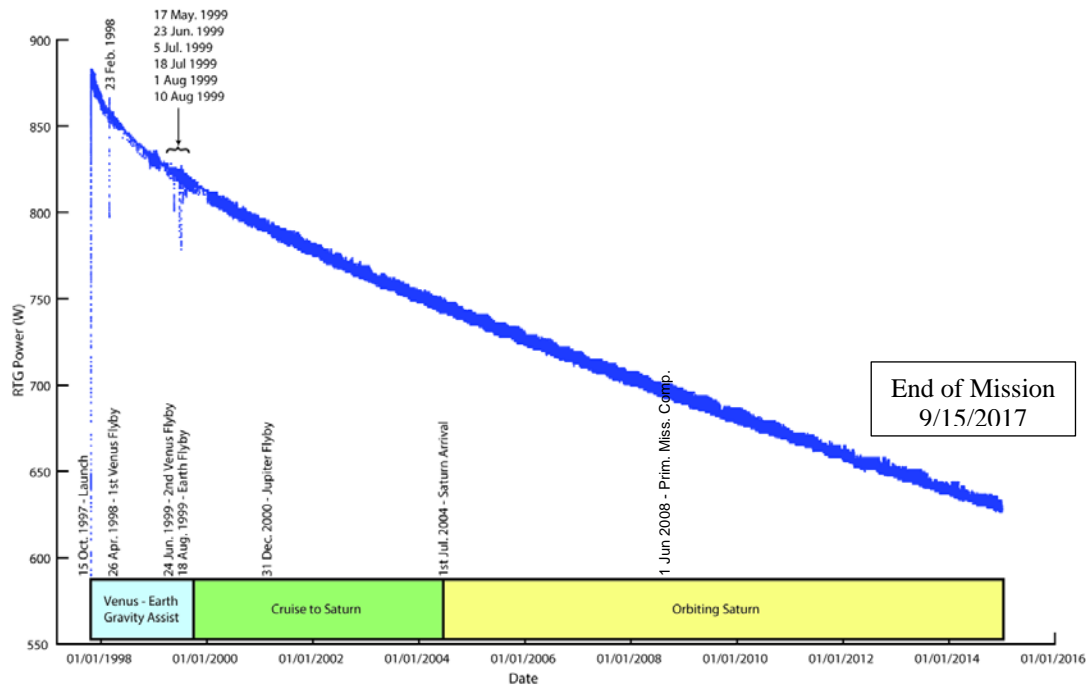


FIGURE 2. Cassini recorded power output telemetry data over the entire mission separated into three phases: The Venus-Earth gravity assist, the cruise to Saturn and Orbiting Saturn.

Fig. 2 shows the entire power history recorded on the spacecraft until 2015, communicated back to Earth through the Deep Space Network (DSN) and archived by Cassini telemetry. The overall decay shows an exponential behavior ranging from 882.1 W in the first days of the mission and predicted to degrade to about 600 W at the end of the mission, corresponding to a power decay of 32% over the 20-year mission. Figure 2 shows the three phases of the mission: (a) the Venus-Earth gravity assist, (b) the cruise to Saturn, and (c) the Saturn tour. The first phase lasted about two years, between October 1997 and October 1999. During this period, the power output decreased to ~820 W, corresponding to a decay of 7% compared to its BOL value. On 23 February 1998, a sharp power drop (i.e. within tens of minutes) was observed, which occurred around the time Cassini performed its first Venus flyby. This drop was 7.1% compared to the nominal power output and it recovered to its nominal value after a few minutes. The power drop was similar for all three RTGs with a power drop of 6.32% for RTG1, 7.66% for RTG2 and 7.31% for RTG3. This is attributed to the fact that during this time, solar exposure on the cool side of the RTGs (due to sun angle changes) created a reduction of the TEG temperature difference, resulting in a power output decrease in the TEG. The slight difference in power decrease between the RTGs is attributed to different solar exposure angles by the different RTGs. The same phenomenon occurred six times between 17 May 1999 and 10 August 1999, around the time of the second Venus flyby. During that second flyby period, the highest power drop observed was 5.32% with a power drop of 6.92% for RTG3. The power drops for RTG1 (3.53%) and RTG2 (5.95%) were less pronounced. For each of these six power drops, the nominal power value recovered after a few minutes. The second phase of the mission was the cruise to Saturn, which lasted about five years, between October 1999 and June 2004. During the cruise phase, the constant power decrease was about 70 W. The major event during this time, was the Jupiter flyby on 31st December 2000. The cruise trajectory is represented in Fig. 3. Major events such as Earth, Venus, and Jupiter flybys are shown.

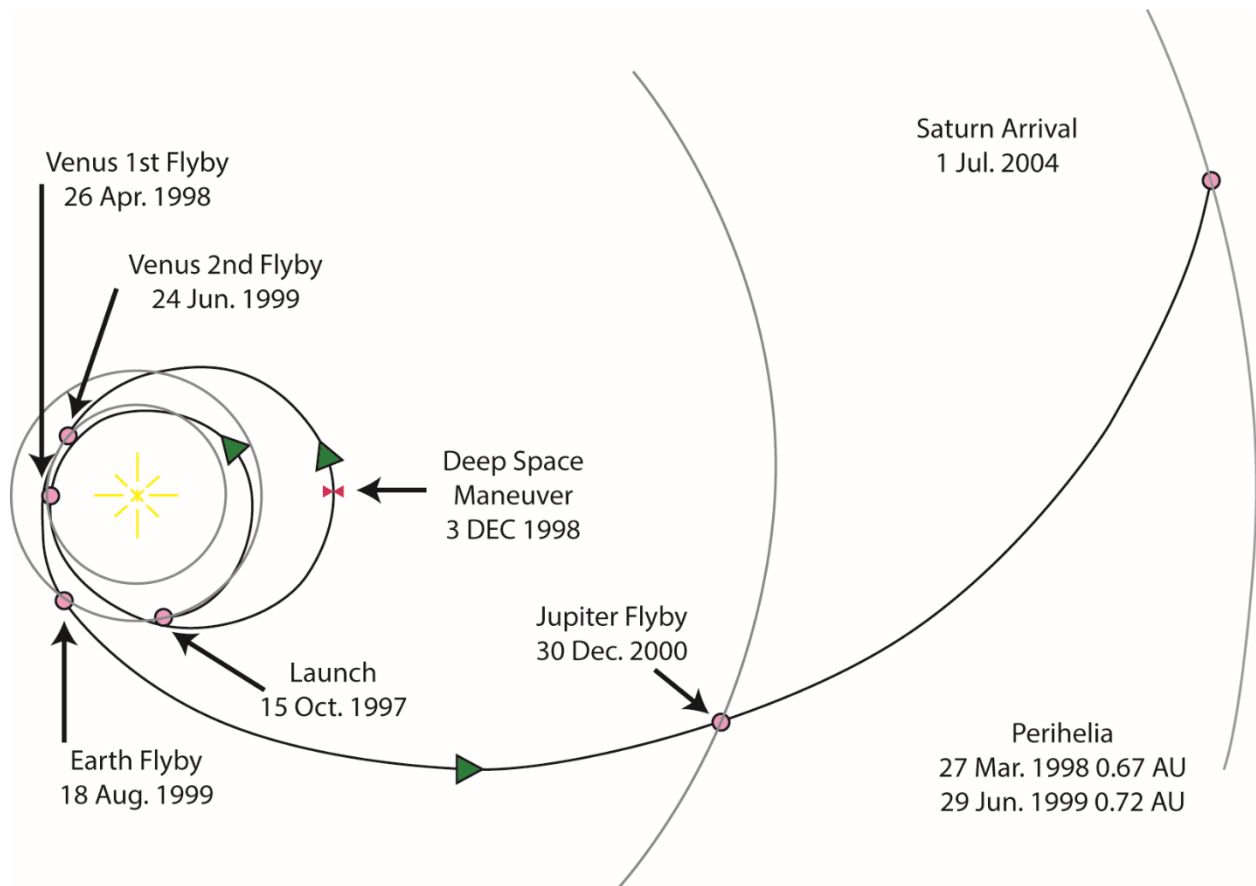


FIGURE 3. Cassini’s seven-year Venus-Earth gravity assists and cruise to Saturn between launch on 15 October 1997 and Saturn arrival on 1 July 2004.

Finally, the third phase started on 1 July 2004 when Cassini achieved orbit insertion into the gravity field of Saturn. The Cassini power output was then 750 W, corresponding to a 15% decrease compared to the beginning of the mission.

The next section will focus on the Cassini Plasma Spectrometer (CAPS), which is one of 12 Cassini instruments, and its major impact on the power subsystem electrical network during the mission.

CASSINI PLASMA SPECTROMETER (CAPS): A SHORT HISTORY

CAPS is designed to measure the energy, charge, mass, and direction of particles in the Saturn magnetosphere, and in the solar wind at Saturn. Scientific goals included understanding the nature and sources of plasma, their transportation, and their “sinks.” In addition, CAPS contributes to multi-instrument observations of the Saturn system. The instrument is comprised of three sensors: an Ion Mass Spectrometer (IMS); an Ion Beam Spectrometer (IBS); and an Electron Spectrometer (ELS).[5, 6]

CAPS became operational just after launch and continued to operate until the instrument was turned off as the result of an onboard solid-state power switch (SSPS) trip on 2 June 2012.

During Saturn tour operations, CAPS experienced a series of short anomalies that affected the power subsystem, and those are summarized in this section. The first anomaly occurred on 28 June 2006, when Cassini experienced a Low Rail short (Low Rail to chassis), which cleared within 48 hours. The short was accompanied by shifts in the RTG case voltages, which were consistent with the shift seen on the Low Rail. At the time, the cause of the short was not

determined, but the robust rail design allowed the spacecraft team to continue to operate Cassini safely. There was no significant change in the state of the power subsystem for the next five years.

On 30 April 2011 a series of RTG case voltage shifts occurred, and the Low and High Rail voltages shifted to 0 volts and 30 volts, respectively. This condition continued for six weeks.

On 11 June 2011 a third shift in the power bus occurred. Analysis indicated that the High Rail shorted to the chassis, which led to a short-lived (< 1 ms) connection between Low and High Rails. As a result of this short the Low and High Rails swapped voltage levels, to 30 and 0 volts respectively. RTG case voltage shifts were also observed. By this time, it was suspected that the CAPS instrument was involved, and four days later it was intentionally commanded off by the spacecraft team. Immediately, the Low and High Rail voltages changed to new magnitudes (7 V and 23 V), where they remained for the next nine months.

In response to the events of April and June 2011, reviews were conducted at JPL, and by the NASA Engineering and Safety Center (NESC). In early 2012, the NESC concluded that tin whiskers were the likely cause of the shorts, and that continued operation of CAPS was safe under that assumption.

The instrument was turned back on 18 March 2012. Two days later the bus levels changed for a fourth time. RTG output dropped by 2 W, and the Low and High Rails again swapped voltage levels (30 V and 0 V). The spacecraft remained in this condition for another 10 weeks.

On 1 June 2012, a series of four shorts occurred in quick succession, finally resulting in an onboard SSPS trip on June 2, which left CAPS powered off.

A second review over the next several months by the NESC found that the new trips differed significantly from previous events. Thermal data pointed to the IMS wax thermal actuator (WTA) as the likely cause of the most recent event, possibly due to anomalous activation of the WTA via an internal short. Ground testing and modeling produced results consistent with this scenario, and in its findings the review board recommended that the CAPS instrument remain powered off.

In the three years since CAPS tripped off, the Low and High Rail voltages have remained steady at 6 V and 24 V. RTG case voltages have also been steady over this duration. There is no plan to operate the instrument for the remainder of the mission.

POWER MISSION REQUIREMENT DISCUSSION AND COMPARISON WITH OTHER MISSIONS

The Cassini power performance over the lifetime of the mission mimics the historical performance of RTGs for many deep space missions. RTGs have an excellent record of providing unparalleled success for extreme solar range and high radiation environments. The Pluto New Horizons mission recently joined the two Voyager missions as spacecraft traveling beyond the planets toward the Kuiper Belt, and ultimately into interstellar space. Galileo was an orbiter with an RTG power system, similar to Cassini, that lasted for many years in the severe radiation environment of the Jovian system. System architects and mission planners have employed the predictable and reliable performance of the RTGs independent of concerns about solar range and the radiation environment.

NASA chose to use RTG power for the Cassini mission based on a number of technical factors, including lower mass and improved attitude control compared to necessarily large solar arrays.

Solar cell efficiency has shown steady improvement over the years since Cassini was developed. NASA's on-going Juno mission is the first solar-powered mission to Jupiter, which was achieved by a combination of solar array design and mission planning. For Juno, solar cell characterization for limiting radiation degradation and optimizing Low Intensity and Low Temperature (LILT) performance resulted in the design of a solar array that can produce 416 W end of mission at 5.5 Astronomical Units (AU).[7] Mission planners designed a Juno tour that remains in

constant solar illumination and avoids the radiation belts around Jupiter to protect the three large solar arrays, in contrast to the RTG-powered Galileo mission, which targeted the icy moons directly in the Jovian radiation belt.

The Juno mission achieved two major milestones in 2016: in January, on its way to Jupiter, Juno surpassed Rosetta to become the most distant solar-powered spacecraft in history, and in July, it successfully completed Jupiter orbit insertion.

In another example, the planned Europa Mission is leveraging the lessons learned from Juno; its baseline design is a solar-powered spacecraft that specifically targets one of the icy moons, Europa.[8] Europa Mission planners are designing a Jovian orbital tour with numerous close flybys of the valuable science target while maintaining solar array power output degradation to less than 30% at the end of mission. The estimated end of mission power is on the order of 600 W, through the use of an approximately 90 m² array. Although the estimated mass of the solar array is a factor of three greater than an equivalent RTG-powered system, the cost could be an order of magnitude lower. Cost and timely availability of hardware are always key factors when designing a mission power system.

A solar-powered Saturn mission at about 10 AU would be more of a challenge, notionally requiring a 300 m² array for a Cassini-like mission with the current solar cell technology and a mass impact factor of nine over an equivalent RTG system. At the time of the Cassini development, a solar-powered Saturn mission would have required about 600 square meters (see Fig. 4).[9] Solar cell technology has improved by a factor of two since the development of Cassini, however even this amount of area (i.e., 300 m²) is challenging. Therefore, even given these advances in solar cell / array technology, a Cassini-type mission with a similar science instrument payload would most likely still require a RTG power system solution.

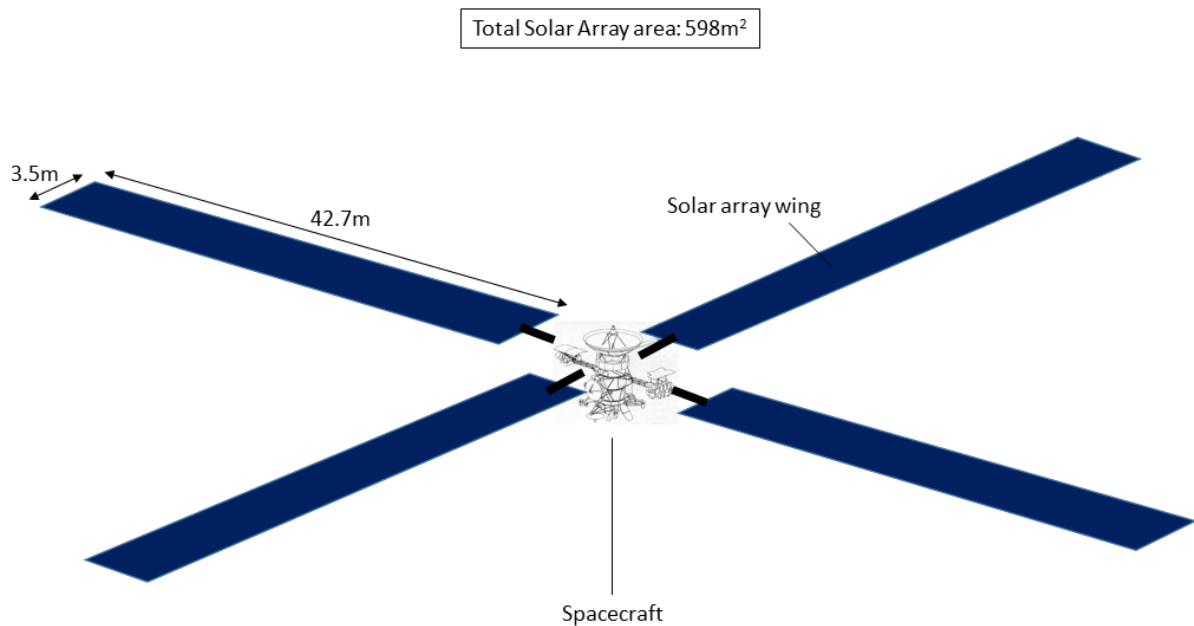


FIGURE 4. A conceptual all-solar dual junction GaAs/Ge configuration for the Cassini spacecraft. Reproduced from [9].

CONCLUSION

A review of Cassini Power Subsystem performance was presented and anomalies associated with the CAPS instrument were discussed. A comparison with other deep space missions and power alternatives was then discussed.

ACKNOWLEDGMENTS

This work was performed at the Jet Propulsion Laboratory, California Institute of Technology, under a contract with the National Aeronautics and Space Administration. The authors would like to acknowledge the valuable contributions from Terry J. Hendricks, Bill J. Nesmith, Laura Burke and Julie L. Webster.

REFERENCES

- [1] Carr, G. and A. Ging, *The Cassini Power System Performance over the Last Decade*, in *5th International Energy Conversion Engineering Conference and Exhibit (IECEC)*. 2007, American Institute of Aeronautics and Astronautics.
- [2] Chasmar, R.P. and R. Stratton, *The Thermoelectric Figure of Merit and its Relation to Thermoelectric Generators*. *Journal of Electronics and Control*, 1959. **7**(1): p. 52-72.
- [3] Astronautics, L.M., *Cassini RTG Program*. 1998.
- [4] Allan, L. and H. Gene, *Cassini Spacecraft Attitude Control System Flight Performance*, in *AIAA Guidance, Navigation, and Control Conference and Exhibit*. 2005, American Institute of Aeronautics and Astronautics.
- [5] Young, D.T., et al., *Cassini Plasma Spectrometer Investigation*. *Space Science Reviews*, 2004. **114**(1): p. 1-112.
- [6] *CAPS Short Circuit Anomaly Assessment*, in *NASA Engineering and Safety Center Technical Assessment Report*. 2013, NASA.
- [7] Dawson, S., et al., *JUNO Photovoltaic Power at Jupiter*, in *10th International Energy Conversion Engineering Conference*. 2012, American Institute of Aeronautics and Astronautics.
- [8] Ulloa-Severino, A., et al. *Power subsystem approach for the Europa mission*. in *European Space and Power Conference*. 2016. Halkidiki, Greece.
- [9] *Cassini Program Environmental Impact Statement Supporting Study*. 1994, JPL.

10 W_e Radioisotope Thermophotovoltaic (RTPV) Power Source Demonstration

Jivan Khatry^{1,5}, Juha Nieminen^{2*,5}, Josh Smith^{3,5}, Kari Slotten^{4,5}

¹, University of Idaho, Idaho Falls, ID 83402

²University of Southern California, Los Angeles, CA 90089

³University of Tennessee, Knoxville, TN 37996

⁴Embry-Riddle Aeronautical University, Daytona Beach, FL 32114

⁵Center for Space Nuclear Research, Idaho Falls, ID 83401

*Contact Author: nieminen@usc.edu, 323-386-1932

Abstract. Long lasting, non-plutonium energy sources would well serve small underwater vehicles and deep space satellites with modest power requirements. Unlike their thermoelectric counterparts, thermophotovoltaic (TPV) energy conversion systems can achieve double-digit conversion efficiency without major advances in materials. The efficiency of a TPV system is largely dictated by the spectral control of the emitted (and absorbed) infrared radiation. Recent advances in selective emitter coatings -both photonic crystals and metamaterials- enable the tailoring of the emitted spectrum to be more suitable for conversion to electrical power at the photovoltaic cell than was possible before. Design for a 1U CubeSat sized AmO₂/tungsten core radioisotope thermophotovoltaic power source producing 10 W_e is presented, along with an electrically heated mockup for performance verification purposes. Radiation shielding analysis didn't reveal any major threat for the personnel or the photovoltaic (PV) cells. However, experimental data for low energy gamma radiation effects on PV cells is scarce. The work was conducted during the Summer Fellow program at the Center for Space Nuclear Research in Idaho.

Keywords: Thermophotovoltaic, Radioisotope, Americium

INTRODUCTION

Radioisotope power sources in use today cater for large deep space spacecraft and rovers. Regardless of the conversion technique, making a small radioisotope power source is more challenging due to increased surface-to-volume ratio, which is detrimental for keeping the core hot. Unlike their thermoelectric counterparts, thermophotovoltaic (TPV) conversion systems don't rely on conductive heat flow through the structure. By suppressing all other forms of heat transfer other than radiation at selected wavelengths, the core can be kept hot enough for efficient conversion.

The hot surface of an ideal TPV system would only emit at wavelengths that the receiving photovoltaic (PV) cells can convert to electricity most efficiently. Recent advances in photonic crystals[1] are a significant step in that direction, and together with suitable wavelength filtering at the PV cells, the amount of thermal leaks can be reduced significantly, even in 1U CubeSat sized systems. The simulated core temperature of our proposed design is 1320 K with 8.4% overall conversion efficiency and 12.6 W_e output power.

The only spaceflight qualified radioisotope is PuO₂. Despite its scarcity it will likely be the fuel of choice in foreseeable future due to its high specific power and flight heritage. AmO₂, on the other hand, would be much easier to procure and as such would be more attractive for underwater applications. We present designs for both AmO₂/W based radioisotope power source and an electrically heated mockup for validation purposes.

The system components responsible for spectral control are explained first, followed by the description of the modeling methods. Our approach was to use the first principles of physics without resorting to photovoltaic efficiencies that are usually specific to certain geometry or operating conditions. Mechanical designs and performance numbers are given next, and finally a radiation shielding analysis is presented which was performed to tally neutron and gamma radiation originating from the system.

SPECTRAL CONTROL AND MODELING

A generic TPV system is shown in Figure 1. Any kind of heat source can be used to heat up the emitter, which then emits its characteristic spectrum (mostly infrared in TPV applications). Part of that spectrum can be converted into electricity using photovoltaic cells. The blue arrows are the convertible photons, whereas the yellow arrows depict wavelengths that would only produce heat in the PV cells if absorbed. It is therefore desirable to reflect them back to the emitter by a filter. PV cells need to be maintained at room temperature for them to work efficiently.

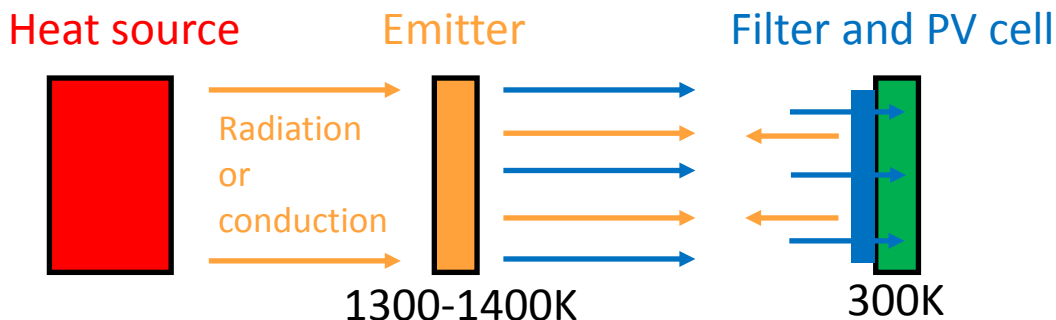


FIGURE 1. Generic TPV System Components.

Efficiency of a TPV system is dictated by how well the incident spectrum matches the external quantum efficiency (EQE) of the PV cell. EQE is zero above the cut-off wavelength corresponding to the bandgap of the PV cell, and typically ~ 0.9 below, meaning that 90% of these photons produce electron-hole pairs. Ideal emitter-filter combination would only allow these wavelengths to be absorbed in the PV cell.

Optical components

The art of selective emitters (SE) is a fairly new one. Only photonic crystals developed at MIT[1,2] have exhibited long term thermal stability at temperatures expected in TPV applications. They are fabricated on Ta/Inconel substrate and diced, and therefore can be brazed as tiles onto a heat source. The cut-off wavelength can be tuned by varying the geometry of the holes. MIT have successfully produced and tested them in a demonstration system[3].

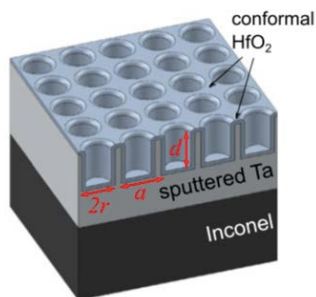


FIGURE 2. HfO₂ Coating Retains the Shape of the Cavities at Elevated Temperatures.

No selective emitter is perfect, so there's still fair amount of long wavelengths in the emitted spectrum. They can be reflected back to the source by coating the front surface of the PV cells with a stack of different materials. The interference filter, in green, and an indiumphosphate layer, in red, together produce the reflective profile shown in blue in Figure 3. This so called tandem filter reflects most of the wavelengths above the 2.1 μm cut-off wavelength, while having high absorption at useful wavelengths below that.

General Atomics have developed 0.6 eV bandgap PV cells with reasonably good fill factor (70-72%)[4], which is a measure of the PV cell quality. They come in 1cm x 1cm size. Lower bandgap cells would be preferable because they would allow operating at lower core temperatures, but so far no good quality PV cells with 0.5 eV bandgap or less have been reported.

Spectral measurements of filter and stack

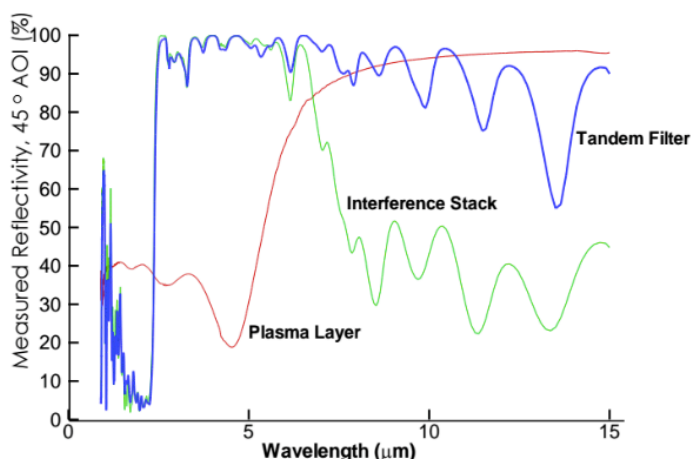


FIGURE 3. Measured Reflectivity of the Tandem Filter (Manufactured by Omega Filters)[4].

Modeling

Heat transfer, structural mechanics, and wavelength dependent radiation calculations were performed using COMSOL Multiphysics. The analytical method[5] of predicting produced electric power from given incident power is too involved to be implemented in COMSOL and was programmed in MATLAB instead.

Radiation calculations are quite intensive which is why COMSOL limits the amount of spectral bands to five. Those bands were allocated based on the emissive properties of the selective emitter and the tandem filter. In Figure 4, the green curve approximates spectrum of a blackbody radiator at 1036 K. The approximation looks rough, but it needs to be refined only below the cut-off wavelength where energies of individual photons matter. All longer wavelengths produce heat, so the distribution there is of no interest, only total power.

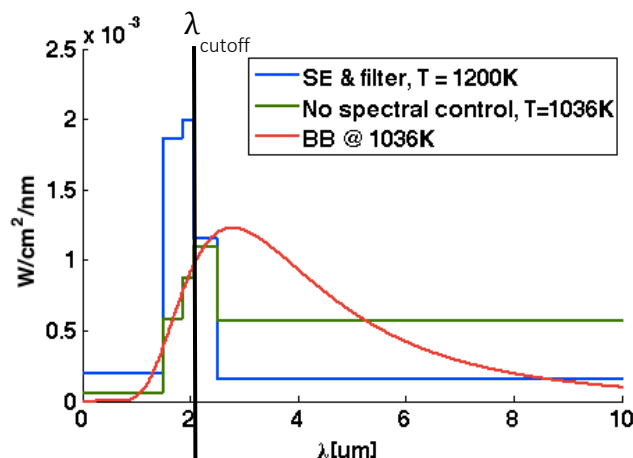


FIGURE 4. Emission Spectrum of a Hypothetical Source with and Without Spectral Control.

Once selective emitter and tandem filter are introduced, some long wavelength photons are contained and reflected back to the source, driving up the source temperature to 1200 K. This also changes the shape of the spectrum to a non-black body one (blue curve). The peak is nicely just below the cut-off wavelength, but there's still a significant amount of power radiated in longer wavelengths that only produce waste heat.

Output power of the PV cells for given illumination can be calculated from an equivalent circuit using circuit theory, when a set of parameters (series and shunt resistances, dark saturation current density, ideality factor, and internal

quantum efficiency) are known[5]. Values used in this work were obtained from data published by General Atomics[4] for their PV cells.

DESIGNS

The most natural shape to contain a radiating radioisotope source is a cylinder, but this poses a problem when flat selective emitters tiles need to be brazed on the surface. A decagon is a good trade-off between radiative efficiency and practicality. Figure 5 shows designs for both the radioisotope powered core and the electrically heated mockup.

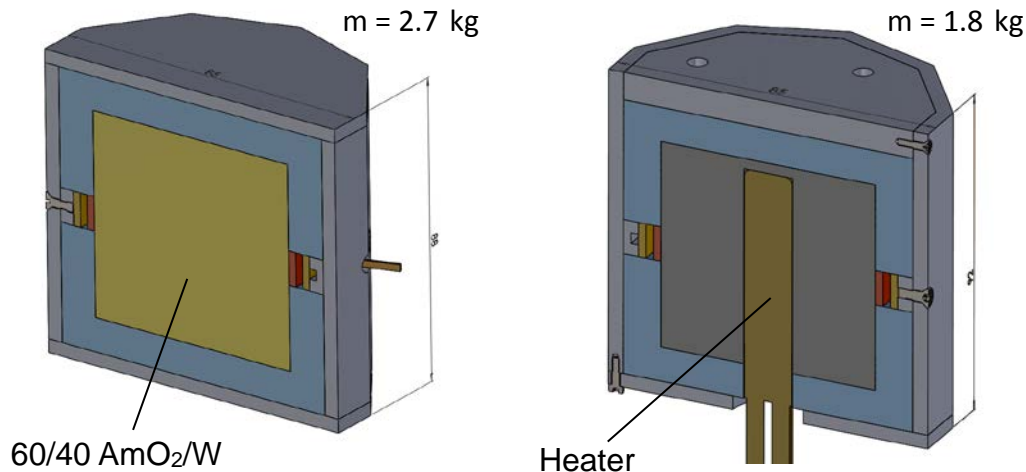


FIGURE 5. Both Designs Fit within the 90x90x90mm CubeSat Envelope.

To keep the core hot enough, both (parasitic) radiative and conductive heat transfer need to be minimized. This is achieved by enclosing the core in opaque insulator material[6], leaving only a narrow window near the equator where the core is allowed to radiate on the PV cells. Produced power depends on the core temperature and total PV cell area, and a 1 cm window height is close to the optimum value and matches with the physical size of the PV cells. Core temperatures can be ramped up by increasing the insulator thickness (1cm) if larger overall volume is permitted.

In the mockup the radioisotope core is replaced by a nickel block which is electrically heated. In both cases the outer shell is made of aluminum. Figure 6 illustrates the structure of the electrically heated version.

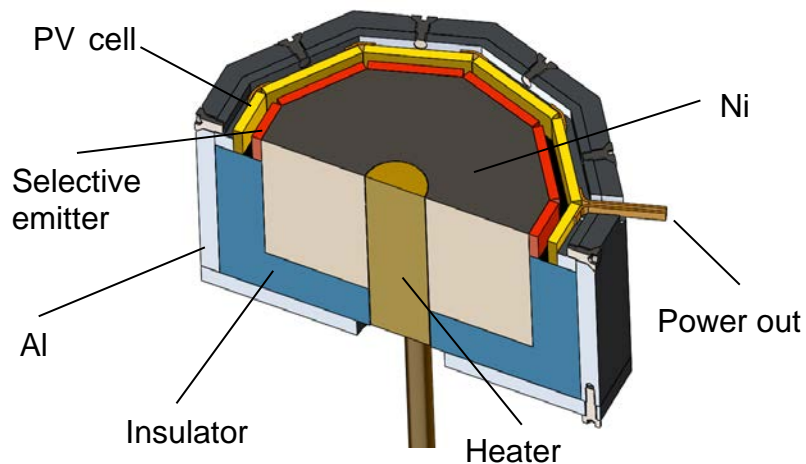


FIGURE 6. Cutout of the Electrically Heated Mockup.

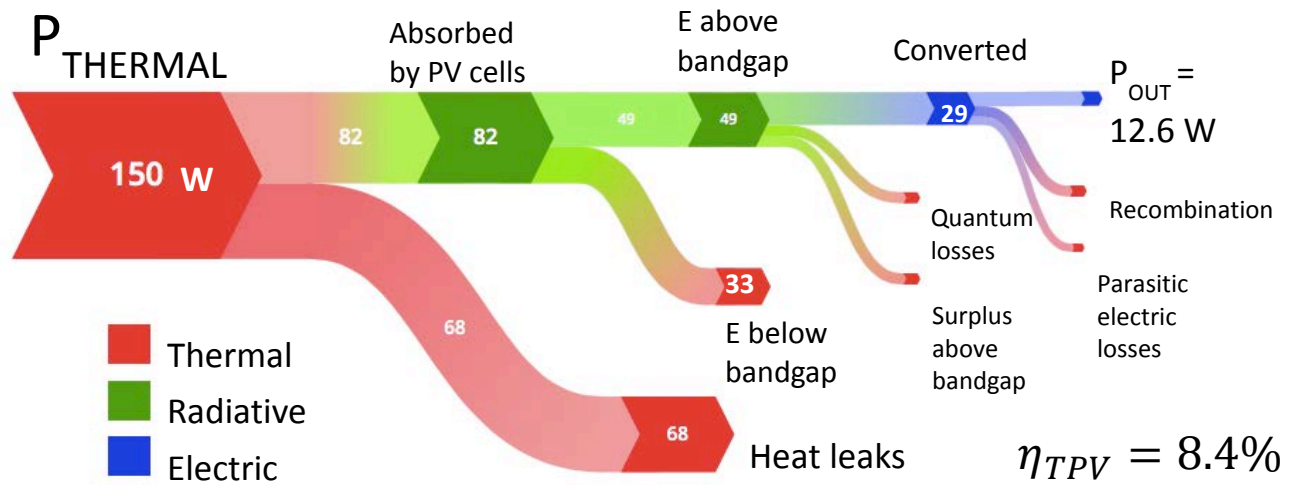
Performance

Table 1 lists performance parameters of both models. Core surface temperature of the mockup is limited by the maximum operational temperature of the cartridge heater (1270 K), which leads to lower power numbers and efficiency.

TABLE 1. Performance Comparison.

Core	T _{CORE} (K)	P _{IN} (W)	P _{OUT} (W)	Efficiency (%)
Radioisotope	1323	150	12.6	8.4
Electric heater	1250	135	9.0	6.7

The Sankey diagram in Figure 7 illustrates the power budget of the radioisotope model. Conductive heat leaks through the insulator material and emissions at long wavelengths constitute the major inefficiencies of the system. These can be addressed by thicker insulation and better spectral control.



Selective emitters and PV cell filters are the most expensive components of the system. A comparison within Table 2 shows the system performance (radioisotope model) if either one -or both- are left out. Even if the selective emitters are left out, the 10 W threshold can still be met. However, omitting the PV cell front side filters is not acceptable.

TABLE 2. Performance of the Radioisotope Model in Different Configurations.

Selective Emitter	PV Cell Filter	P _{OUT} (W)	Efficiency (%)
✓	✓	12.6	8.4
X	✓	10.3	6.9
✓	x	6.6	4.4
X	x	2.5	1.7

Mechanical Issues

Thermal insulation plays a key role in the system as it also serves as a structural component that holds the core in its place. Low thermal conductivity inevitably means low density and low compressive strength. All space flight hardware must survive stringent vibration tests, where the specimen is subjected to accelerations of tens of g's. Monolithic structure of the system is beneficial for shifting the resonance frequencies higher, above the typical launch load frequencies in the range 0-150 Hz. Although hand calculations and COMSOL analysis indicate that the system might survive such high accelerations, an actual test is needed to verify this.

RADIATION SHIELDING ANALYSIS

A crucial aspect of the design of the RTPV system is the shielding of the radiation emitted by the radioisotope core in order to limit the hazards presented to individuals working with the power source, as well as the degradation of the electronic components of the system (i.e. the PV cells) and its surroundings. The radioisotope chosen for our fuel, ^{241}Am , is primarily an α emitter with a few low energy characteristic γ 's with a small probability of spontaneous fission as shown in Figure 8. While the range of the α particles emitted by ^{241}Am is short and thus easier to shield, secondary particles produced by the α particles as they slow down must be considered. Since the fuel used in our design uses americium dioxide encapsulated in a tungsten matrix, the primary reaction of concern for the production of secondary particles is the (α,n) reaction with the oxygen in the fuel, as the neutrons produced by this reaction would be far more difficult to shield than the primary α 's.

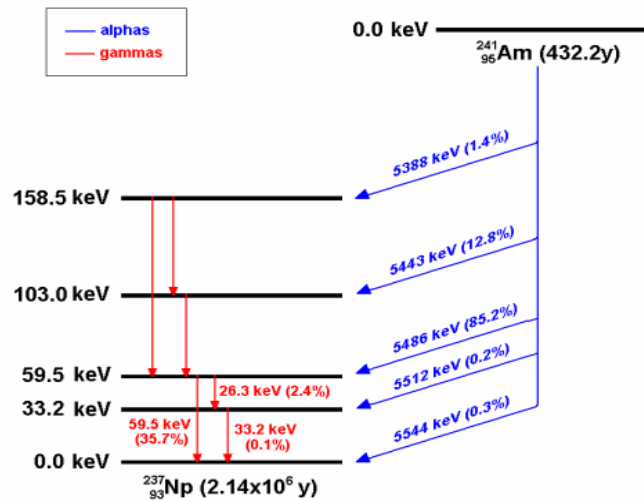


FIGURE 8. The Decay Scheme of Am-241.

For the shielding calculations the particle radiation transport code Monte Carlo N-Particle (MCNP 6.11) was used in conjunction with Evaluated Nuclear Data File (ENDF/B-VII) neutron cross-sections and TALYS-based Evaluated Nuclear Data Library (TENDL-2015) alpha cross-sections. The polygonal prism core was simplified to a cylindrical core of equivalent size, and the cermet core was homogenized as represented in Figure 9.

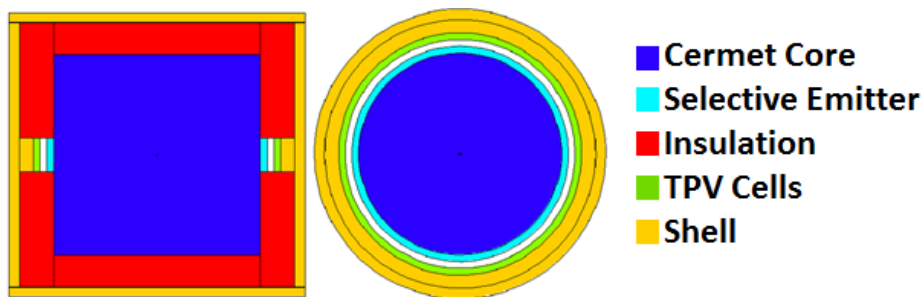


FIGURE 9. The Base MCNP Geometry Used for Shielding Calculations.

Using the MCNP model, the total neutron and photon fluxes at the surfaces of the PV cells were determined as well as the dose rates. The plots in Figure 10 and Figure 11 show the differential photon and neutron fluxes, respectively. As expected, there is a large peak in the photon flux at the low energy γ 's associated with the decay of ^{241}Am . The majority component of the neutron flux are neutrons from the spontaneous fission of ^{241}Am , and not from the (α,n) reaction as initially thought.

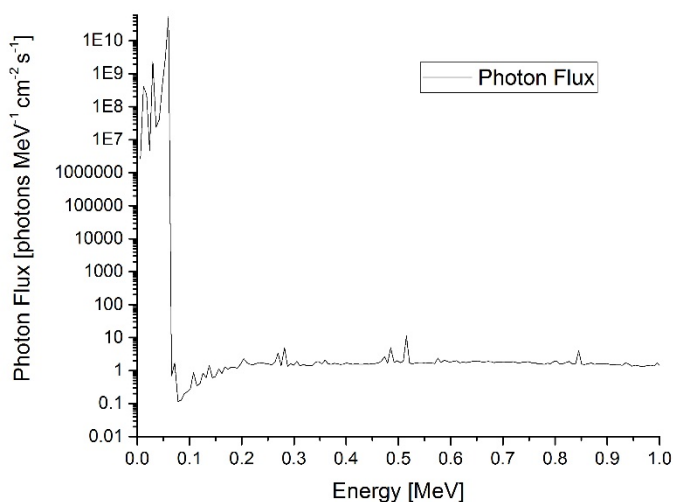


FIGURE 10. The Differential Photon Flux at the Surface of the PV Cells.

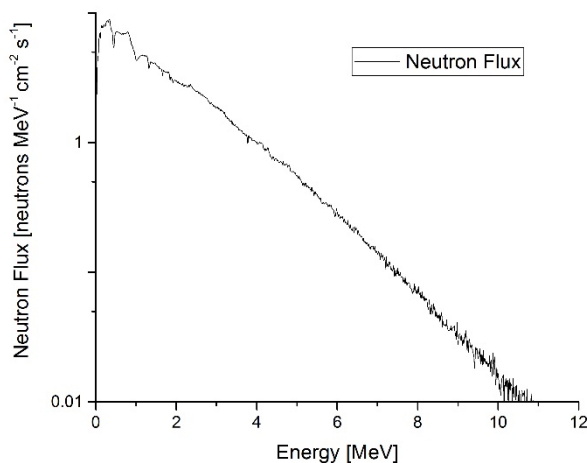


FIGURE 11. The Differential Neutron Flux at the Surface of the PV Cells.

The dose rates for a worker 30 cm away and 1 m away from the unshielded RTPV was calculated by approximating the worker as a 30 cm diameter water sphere and are shown in Table 3. When compared to the annual total effective dose equivalent limit of 0.05 Sv, which can be found in the Nuclear Regulatory Commission (NRC) 10 Code of Federal Regulations 20.1201, the dose rate of the unshielded RTPV could be manageable utilizing proper radiation work procedures.

TABLE 3. Full Body Dose Rate of a Radiation Worker Near an Unshielded RTPV.

	Neutrons (Sv/hr)	Photons (Sv/hr)	Total (Sv/hr)
30 cm away	1.12e-07	1.13e-02	1.13e-02
1 m away	9.36e-09	8.55e-04	8.55e-04

The dose rate at the PV cells was also calculated with different thicknesses of a tungsten shield surrounding the cermet core. Tungsten was selected as the shielding material as it has a high density, good thermal and mechanical properties, as well as being compatible with being attached directly to the cermet core. The low energy gammas are easily shielded

by the thin tungsten shield which drastically reduces the dose rate at the PV cells. This can be seen in the reduction of the dose rate shown in Table 4. Previous studies by Nikolic et. al.[8] showed minimal damage to PV cells from gamma rays even at a dose rate of 100 Sv/hr. However, this study was done using a ^{60}Co source which emits 1.25 MeV gammas that are much more energetic than the gammas emitted by ^{241}Am , which leads us to suggest further investigation of the degradation of the InGaAs PV cells in a neutron and gamma mixed radiation field.

TABLE 4. The Dose Rate at the PV Cells for Different Tungsten Thicknesses at the Core.

	Neutrons (Sv/hr)	Photons (Sv/hr)	Total (Sv/hr)
No Shield	1.76e-05	5.29e-01	5.29e-01
1 mm Tungsten	1.64e-05	6.28e-05	7.93e-05
2 mm Tungsten	1.54e-05	4.90e-05	1.54e-05

CONCLUSION

The study indicates that it is possible to extract 10 W_e from a CubeSat sized radioisotope thermophotovoltaic power source. It requires filtering long wavelengths at the PV cells, and possibly also using selective emitters at the source. However, AmO_2/W cermet fuel hasn't ever been produced, its future looks uncertain, and needs to be flight qualified first (which NASA has no intention of doing). For these reasons it would be feasible to study the use of General Purpose Heat Sources instead, despite the need for plutonium which is scarce for the time being. Dimensions of such system would exceed those of a CubeSat, but it would be lighter, more powerful, and most likely have higher conversion efficiency. Regardless of the core material, the structural integrity of the insulator must be tested to verify that it can survive the vibration environment of a space launch. For underwater applications AmO_2/W is still an attractive choice due to less stringent qualification requirements.

ACKNOWLEDGMENTS

The authors would like to acknowledge the contribution of all the personnel at the Center for Space Nuclear Research at Idaho National Lab for their support and guidance during the course of this work. The authors would also like to thank Mr. Adarsh Rajguru at Jet Propulsion Laboratory for suggesting to study this interesting concept. We are also grateful for the co-operation of personnel at Massachusetts Institute of Technology's Laboratory of Soldier Nanotechnology, Mr. Andre Klein at General Atomics, and Mr. Tom Rahmlow at Omega Filters. Without them the most important technical details of various components would have remained unanswered.

REFERENCES

- [1] Rinnerbauer, V., Yeng, Y. Xiang, Chan, W., Senkevich, J., Joannopoulos, J., Soljačić, M., and Celanovic, I., *High-temperature stability and selective thermal emission of polycrystalline tantalum photonic crystals*, Opt. Express **21**, 11482-11491 (2013)
- [2] Stelmakh, V., Chan, W., Ghebrehbrhan, M., Senkevich, J., Joannopoulos, J., Soljačić, M., and Celanovic, I., *Sputtered Tantalum Photonic Crystal Coatings for High-Temperature Energy Conversion Applications*, IEEE Transaction on Nanotechnology, **15**, No. 2 (2016)
- [3] Wang, X., Chan, W., Stelmakh, V., Celanovic, I., Fisher, P., *Toward high performance radioisotope thermophotovoltaic systems using spectral control*, Nuclear Instruments and Methods in Physics Research A, **833**, 28-32 (2016)
- [4] Strauch, J., Klein, A., Charles, P., Murray, C., Du, M., *General Atomics Thermo-Photovoltaic (TPV) Power Sources*, Presentation at Nuclear and Emerging Technologies for Space, 2015
- [5] Chubb, D., *Fundamentals of Thermophotovoltaic Energy Conversion, 1st Edition*, Elsevier Science, Amsterdam, 2007, 339-388
- [6] *Promalight*, Technical Data Sheet, Promat Inc.
- [7] Nikolić, D., Stanković, K., Timotijević, L., Rajović, Z., & Vujisić, M., *Comparative Study of Gamma Radiation Effects on Solar Cells, Photodiodes, and Phototransistors*, International Journal of Photoenergy (2013)

Thermal-control Consideration and Preliminary Analysis of a Heat Pipe Cooled Space Reactor Power System

Mingyang Ma, Qilin Xie, Wenfeng Liang, Sanbing Wang, Xiaoqiang Fan

*Institute of Nuclear Physics and Chemistry, China Academy of Engineering Physics, Mianyang 621900, China
+86 0816-2496741; mamingyang@caep.cn*

Abstract. Thermal-control design is the core of space reactor power systems. This paper presents the authors' comprehension and suggested research routes of thermal control in space reactor power systems. Based on a general analysis of energy transfer and conversion processes in the power systems, independent system parameters for design and optimization are extracted. Similar to the design of the Safe Affordable Fission Engine (SAFE), a design of a heat pipe cooled space reactor power system is proposed. Steady-state thermal-control analyses are performed, and the results verify that the design is physically feasible. For building a transient physical model of the whole power system, an integration of a point-kinetics model for the reactor, a temperature front model for the heat pipes, an isothermal model for the Stirling engines and a one-dimensional thermal-hydraulic model for the radiator is suggested.

Keywords: Thermal control; System parameter; Heat pipe; Transient model.

INTRODUCTION

For different space missions, various types of energy systems can be applied including nuclear power (radioisotope thermoelectric generators (RTGs) or space reactor power systems (SRPSs)), solar cells, chemical batteries, etc. Chemical batteries are appropriate for demands of short duration and high power. Despite the long duration, solar cells can hardly supply power higher than tens of kilowatts and depends heavily on the solar irradiation condition. RTGs are appropriate for missions of low power and short duration. With high specific characteristics, SRPSs can almost be used in all missions of different durations under various circumstances[1].

Since 1950s, USA and the former Soviet Union/Russia began to systematically study SRPSs followed by some other countries[2-4]. Heretofore, USA has sent 1 SRPS (SNAP-10A) to space while the former Soviet Union/Russia has sent 34 SRPSs (32 BUK systems and 2 TOPAZ-I systems). In addition to these systems in practical use, numerous designs have been suggested along with alternative technologies of reactor, reactor cooling, thermo-electric conversion and heat rejection[1]. Technologies should be carefully evaluated and selected when designing a SRPS, based on thermal-control analyses of both the subsystems and the whole system. In most reported literatures such as Ref. [5, 6], emphasis were usually put on simulation of a specific design, while the connotations and research routes of thermal control were seldom discussed from a general point of view.

Section 1 of this paper presents the authors' comprehension and suggested research routes of thermal control in SRPSs. Based on a general analysis of the energy transfer and conversion processes, independent system parameters are extracted according to basic principles of system optimization. In Section 2, the physical feasibility of a heat pipe cooled space reactor power system design is verified. Considerations of how to build a transient physical model of the whole power system are discussed in Section 3. Main conclusions are listed in Section 4.

THERMAL CONTROL ANALYSES IN A SRPS

Technological Connotations of Thermal Control

SRPSs are complicated engineering projects relating to numerous aspects such as reactor engineering, heat transfer/exchange/rejection and thermo-electric conversion, etc. So system design is of great importance, and thermal control is the key. Thermal control design may consist of two parts: a) A physical model of the whole system should be built to verify the feasibility of the design in different working conditions and to elucidate the relationship between system performance and key parameters, based on the models or experimental data of subsystems; b) On the basis of the work aforesaid, the key parameters of subsystems should be optimized with the system mass and volume being the objective functions. Thermal control design may be performed as follows: 1) The independent system parameters should be extracted without specifying the technological details; 2) Via building the system-level physical model to analyze the system performance under mission profiles, the usable ranges of the independent parameters are to be clarified; 3) Objective functions of the system mass and volume should be built and optimized with the independent system parameters being the variables, and finally the requirements on subsystem parameters are to be acquired.

Analyses of the System Parameters

Without specifying the technological details of the subsystems, the energy generation/transfer/conversion processes of any SRPS can be generally indicated as shown in Figure 1. The performance of each subsystem are defined by numerous parameters, and the parameters can be divided into external and internal ones[7]. External parameters uniquely characterize the role of a subsystem in the whole system. While the internal parameters only define the structure and distribution of the physical fields within a subsystem. For any system comprising a series of subsystems, there must be a group of independent parameters which uniquely define the general performance of the whole system. And these independent system parameters is to be selected from the external parameters of subsystems. The energy transfer and conversion processes of SRPSs will be analyzed in a general way as follows, and the independent system parameters are to be extracted.

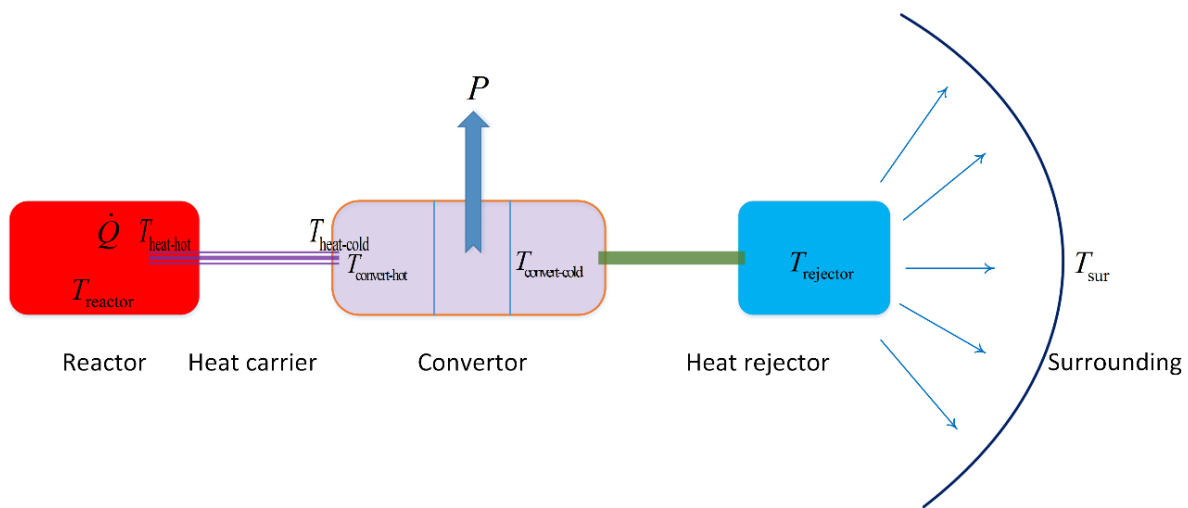


FIGURE 1. The general layout of a SRPS.

The reactor is the energy source of a SRPS, and its function in the whole system can be represented by the outlet temperature T_{reactor} and the thermal power \dot{Q} . The heat exchange rate between the reactor and the heat carrier can be expressed as:

$$\dot{Q} = U_{\text{reactor-heat}} (T_{\text{reactor}} - T_{\text{heat-hot}}) \quad (1)$$

where $U_{\text{reactor-heat}}$ is the heat transfer coefficient.

The generated heat in the reactor is removed by the heat carrier, which could be heat pipes, liquid metal loops, gas loops, etc. The performance of the heat carrier in the whole system can be represented by the heat transfer rate \dot{Q} , the hot-end temperature $T_{\text{heat-hot}}$ and the cold-end temperature $T_{\text{heat-cold}}$.

The thermal carrier exchanges heat with the hot end of the thermo-electric convertor, and this process can be described by following equation:

$$\dot{Q} = U_{\text{heat-convert}} (T_{\text{heat-cold}} - T_{\text{convert-hot}}) \quad (2)$$

Whatever technology the convertor uses, generally speaking, the convertor receives the heat via the hot end, then generates the electricity, and finally rejects the waste heat via the cold end. The performance of the convertor can be represented by the hot-end temperature $T_{\text{convert-hot}}$, the cold-end temperature $T_{\text{convert-cold}}$ and the conversion efficiency η .

In order to keep the universality of the analysis here, no technological detail is specified for the heat rejector in Figure 1. But no matter what the rejector is (panel or liquid), the heat rejection can generally be divided into two processes. The waste heat is firstly transferred to the heat rejector, and this process can be described as:

$$(1 - \eta)\dot{Q} = U_{\text{convert-rejector}} (T_{\text{convert-cold}} - T_{\text{rejector}}) \quad (3)$$

Then the waste heat is radiated to the surrounding at temperature T_{sur} , and the following equation can be used to describe this process:

$$(1 - \eta)\dot{Q} = U_{\text{rejector-sur}} (T_{\text{rejector}} - T_{\text{sur}}) \quad (4)$$

In summary, the system performance of any SRPS can be characterized by 13 system parameters consisting of the heat power \dot{Q} , the temperatures T_{reactor} , $T_{\text{heat-hot}}$, $T_{\text{heat-cold}}$, $T_{\text{convert-hot}}$, $T_{\text{convert-cold}}$, T_{rejector} and T_{sur} , the heat transfer coefficients $U_{\text{reactor-heat}}$, $U_{\text{heat-convert}}$, $U_{\text{convert-rejector}}$ and $U_{\text{rejector-sur}}$, and the conversion efficiency η . Considering the energy relationships described by Equations (1)~(4), 9 out of the 13 parameters are independent. The electric power $\eta\dot{Q}$ and the surrounding temperature T_{sur} are usually specified for a specific mission. So there remains only 7 adjustable independent system parameters. Theoretically, any 7 of the 13 system parameters can be selected to represent the performance of the whole system. To make the design goal of each subsystem straightforward, it is suggested to select \dot{Q} , T_{reactor} , $T_{\text{convert-hot}}$, $U_{\text{reactor-heat}}$, $U_{\text{heat-convert}}$, $U_{\text{convert-rejector}}$ and $U_{\text{rejector-sur}}$ to form the independent parameter group. It is worth noting that the heat power \dot{Q} and the conversion efficiency η should not be simultaneously selected, as the electric power $\eta\dot{Q}$ is preset.

Thus, any SRPS design can be characterized by a group of specific values of the independent system parameters. The independent system parameters are extracted to be the variables for optimizing the system mass, volume, etc. Before the optimization, it needs to be verified that whether the values (or value ranges) of the independent parameters selected can guarantee the physical feasibility of the design.

In addition to meeting the functional demands, high levels of safety, reliability, engineering feasibility and affordability is the design principal. Under this principal, a design of a heat pipe cooled space reactor power system is proposed similar to the design of the Safe Affordable Fission Engine (SAFE)[8] as shown in Figure 2. Stirling generator is selected as the thermo-electric convertor due to its relatively high efficiency and technology readiness level. Sodium heat pipes are used as the heat carrier due to their passive and non-single-point-failure characteristics. The waste heat is rejected by water-cooled radiator. The electric power is 40kWe, and the conversion efficiency is set to be 20%[9]. Taking this design for example, the physical feasibility of the whole system will be verified as follow.

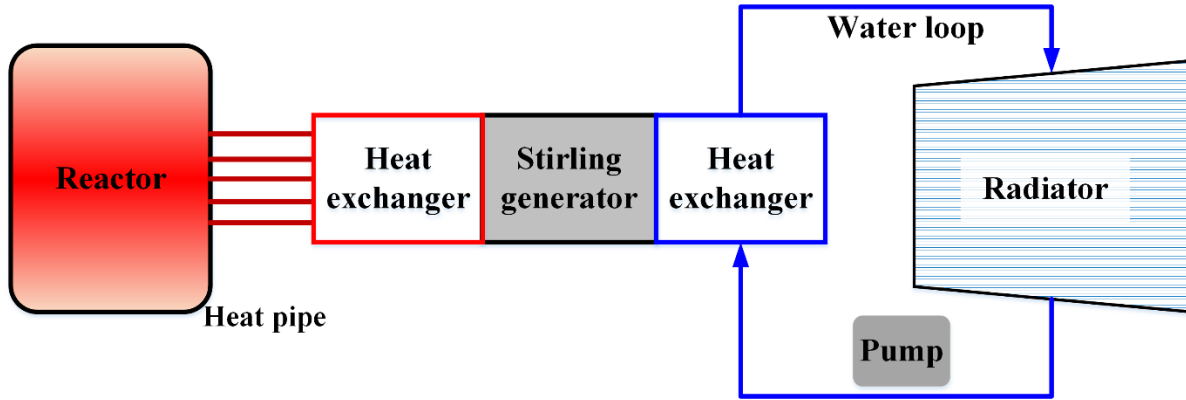


FIGURE 2. The design of a heat pipe cooled SRPS

PRELIMINARY ANALYSIS OF THE HEAT PIPE COOLED SRPS

The Heat Generation and Remove in the Reactor

Neglecting the energy loss (heat loss and electricity consumption by the SRPS itself), the reactor needs to generate 200kWt of heat to guarantee 40kWe of electricity output. To achieve a relatively high thermo-electric conversion efficiency while avoiding failures of the fuel and the structural material, the cladding temperature of the fuel T_{reactor} is set to be 1200K. Considering that the cladding and the heat pipe evaporator are usually joint by welding[10] and that the heat transfer area is large enough due to numerous heat pipes used, the temperature drop between the cladding and heat pipe can be ignored, in other words, the evaporator temperature is equal to T_{reactor} .

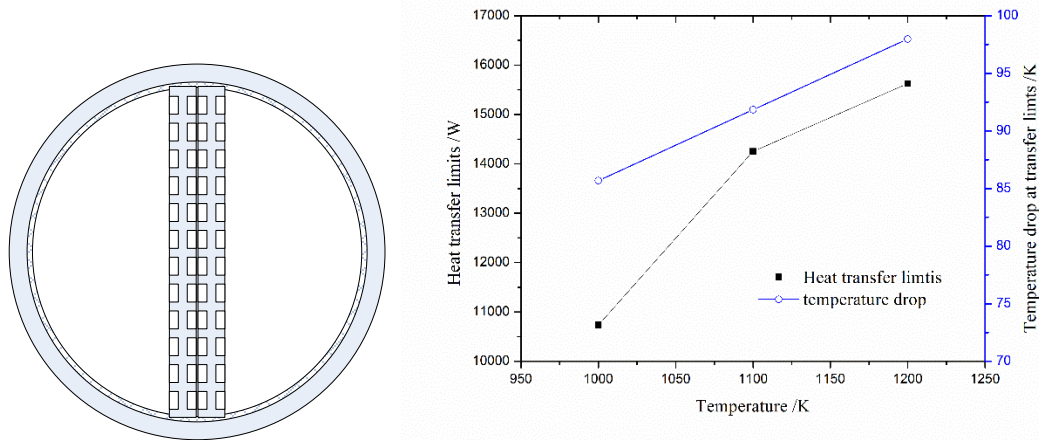


FIGURE 3. The cross-section and the heat transfer limits as well as the temperature drop of the heat pipe

Considering a redundancy of 50%, 60 sodium heat pipes with arteries (Figure 3) are applied to carry the heat out of the reactor. Assuming that 40 heat pipes work normally in the worst conditions, each one needs to transfer 5kWt of heat. The width and depth of the grooves on the artery panel is adjustable, and the typical size is 1mm. Based on Cotter's theory, the heat transfer limits and temperature drops are calculated. The results in Figure 3 show that it is easy to achieve a heat transfer rate of 5kWt. Even if the heat pipe is operated at the limits, the temperature drop ΔT_{pipe} is less than 100K. The temperature drop is much smaller when the heat pipe is operated under standard conditions. As the evaporator temperature is 1200K, the condenser temperature can conservatively be estimated to be 1100K.

Heat Exchange between the Heat Pipe and the Stirling Engine

The imaginary heat exchanger in Figure 4 may be used at the hot end of the Stirling engine: the helium in the engine flows around a bunch of grooves, while the heat pipes are inserted in the grooves.

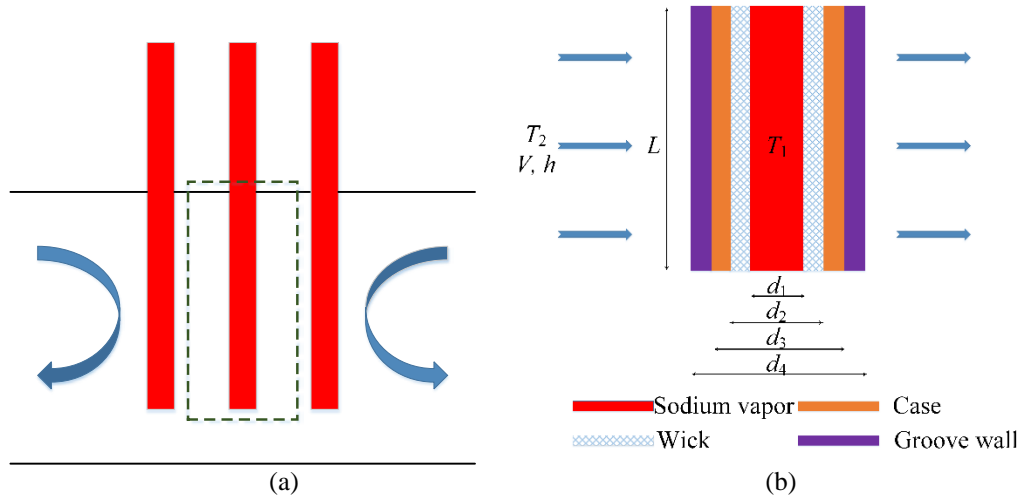


FIGURE 4. The heat exchange between the heat pipe and the Stirling engine: (a) Layout;(b) Single pipe model

As shown in Figure 4, a control volume containing a single heat pipe is analyzed. The heat transfer between the sodium vapor and the helium can be regarded as one-dimensional in the radial direction, as the heat pipe length is much larger than the diameter. The following assumptions are made to perform the analysis: a)The sodium vapor temperature is uniform and denoted as T_1 ; b)There is no temperature difference between the sodium vapor and the internal wall of the wick, as the heat transfer coefficient of condensation is very large; c) The helium temperature T_2 , the velocity v and the convective coefficient h between the groove surface are uniform. In reality, the velocity and temperature fields of the helium are much more complex and it requires delicate simulations or experiments to precisely solve the problem. The temperature T_2 , velocity v and coefficient h can be regarded as average parameters. The thermal resistance method is applied as follows.

The heat transfer processes within the wick, the heat pipe case and the groove wall are conduction, so the relevant resistances can be expressed as:

$$R_{\text{abs}} = \frac{\ln(d_2/d_1)}{2\pi\lambda_{\text{abs}}L} \quad (5)$$

$$R_{\text{shell}} = \frac{\ln(d_3/d_2)}{2\pi\lambda_{\text{shell}}L} \quad (6)$$

$$R_{\text{wall}} = \frac{\ln(d_4/d_3)}{2\pi\lambda_{\text{wall}}L} \quad (7)$$

where R represent the resistances; λ represents the thermal conductivities; the subscribes 'abs', 'shell' and 'wall' denote the wick, the heat pipe case and the groove wall, respectively. The heat transfer between the helium and the groove is convection, and the resistance can be expressed as:

$$R_{\text{conv}} = \frac{1}{\pi h d_4 L} \quad (8)$$

It should be noted that there may exist contact resistances at the wick/case interface as well as the case/groove interface. The contact resistances can be expressed as:

$$R_{\text{abs-shell}} = \frac{R''_{\text{abs-shell}}}{\pi d_2 L} \quad (9)$$

$$R_{\text{wall-shell}} = \frac{R''_{\text{wall-shell}}}{\pi d_3 L} \quad (10)$$

where R'' represents the contact resistance per unit area which is related to the material properties, the roughness, the contact pressure and the filling material. According to Ref. [11], the typical values of R'' for metal interfaces ranges from 10^{-5} to $10^{-4} \text{m}^2 \cdot \text{K}/\text{W}$.

The total resistance between the sodium vapor in the heat pipe and the helium in the Stirling engine is the summary of all the resistances:

$$R_{\text{total}} = R_{\text{abs}} + R_{\text{shell}} + R_{\text{wall}} + R_{\text{conv}} + R_{\text{abs-shell}} + R_{\text{wall-shell}} \quad (11)$$

Then the heat transfer rate can be expressed as:

$$\dot{q} = \frac{T_1 - T_2}{R_{\text{total}}} \quad (12)$$

According to the design, the wick, the heat pipe case and the groove wall are made of porous molybdenum, oxide dispersion strengthened (ODS) steel and nickel alloy, respectively. The key sizes are listed in Table 1.

TABLE 1. The key sizes of heat exchange structure between the heat pipe and the Stirling engine (in mm).

d1	d2	d3	d4	L
11	15	17	21	500

When the heat pipe works, the wick is filled with sodium. The effective thermal conductivity can be calculated via the Wrapped-Screen model[12]:

$$\lambda_{\text{abs}} = \frac{\lambda_{\text{Na}} [\lambda_{\text{Na}} + \lambda_{\text{Mo}} - (1 - \phi)(\lambda_{\text{Na}} - \lambda_{\text{Mo}})]}{\lambda_{\text{Na}} + \lambda_{\text{Mo}} + (1 - \phi)(\lambda_{\text{Na}} - \lambda_{\text{Mo}})} \quad (13)$$

where λ_{Na} and λ_{Mo} equal to 56.6 and 138W/(m·K) at 1000K, while the typical value of the molybdenum porosity ϕ is about 50%. Then the effective thermal conductivity is estimated to be 86.5W/(m·K). The conductivities of the heat pipe case and the groove wall is set to be 27 and 16.8W/(m·K), respectively.

Neglecting the complexity of the helium flow in real working conditions, the helium velocity and temperature are assumed to be uniform, and the flow direction is assumed to be perpendicular to the heat pipe axis. The typical helium velocity v in a Stirling engine is around 10m/s[13], and the Reynolds number can be calculated as:

$$Re = \frac{\rho v d_4}{\mu} = 13661 \quad (14)$$

By substituting the Reynolds number into the Churchill-Bernstein equation for cylinders in perpendicular flow[11], the Nusselt number can be calculated as:

$$Nu = 0.3 + \frac{0.62 Re^{1/2} Pr^{1/3}}{[1 + (0.4 / Pr)^{2/3}]^{1/4}} \left[1 + \left(\frac{Re}{282000} \right)^{5/8} \right]^{4/5} = 61.8 \quad (15)$$

According to the definition of the Nusselt number $Nu = h d_4 / \lambda_{\text{He}}$, the convective coefficient is calculated to be 1042W/(m²·K). Then the convective resistance can be calculated according to Equation (8). By substituting the sizes and the conductivities into the resistance equations, the resistances are calculated as shown in Table 2. The results show that the convective resistance is the major resistance, as 66~80 percent of the total resistance.

By substituting the heat transfer rate of a single heat pipe (5kWt) and the total resistance (in Table 2) into Equation (12), the temperature drop between the sodium vapor and the helium is calculated to be 182~218K. Noting that the

temperature of the heat pipe condenser is 1100K, the hot-end temperature of the Stirling engine is estimated to be 900K.

TABLE 2. The calculated thermal resistances (in K/W).

R_{abs}	R_{shell}	R_{wall}	R_{conv}	$R_{abs-shell}$	$R_{wall-shell}$	R_{total}
0.00114	0.00148	0.00400	0.02909	0.00042~ 0.0042	0.00037~ 0.0037	0.03650~ 0.04361

The Heat Exchange between the Stirling Engine and the Radiator

As the mechanic-electric conversion efficiency of the linear generator is very high (93% in Ref. [14]), the thermo-electric conversion efficiency of the Stirling generator is mainly determined by the thermal efficiency. According to the literature, Curzon-Ahlborn equation[15] is of high accuracy for calculating the thermal efficiency:

$$\eta = 1 - \left(\frac{T_{engine-cold}}{T_{engine-hot}} \right)^{0.5} \quad (16)$$

To ensure a conversion efficiency no less than 20%, the cold-end temperature $T_{engine-cold}$ should not be higher than 576K. Here $T_{engine-cold}$ is conservatively set as 550K.

In the design of the Fission Surface Power System[16], the cold end is cooled with water which flows in annular passages. For such cooling design, a logarithmic mean temperature difference can be defined as:

$$\Delta T_{lm} = \frac{\Delta T_o - \Delta T_i}{\ln(\Delta T_o / \Delta T_i)} \quad (17)$$

where $\Delta T_o = T_{engine-cold} - T_o$ and $\Delta T_i = T_{engine-cold} - T_i$, while T_i, T_o represent the water inlet and outlet temperature, respectively. Denoting the total thermal resistance between the water and the helium as R' , the heat transfer rate can be expressed as $\Delta T_{lm} / R'$. In the FSP design, cooling water with a mass flow rate of 0.28kg/s is used to remove 35kWt of heat from a dual-opposed Stirling engine. The water inlet temperature, the water outlet temperature and the cold-end temperature are 390, 420 and 425K, respectively. Substituting these data into Equation (17), ΔT_{lm} is calculated to be 15.4K, and finally the resistance R is calculated to be 4.4×10^{-4} K/W. Given that 4 dual-opposed Stirling engines are applied in our design, there are 40kWt of heat to be removed from each engine. Assuming that the same design of FSP is used in our design, the temperature rise of the cooling water is 34K according to law of energy conservation. And the logarithmic mean temperature difference is calculated to be 17.6K assuming a same resistance. As mentioned before, the cold-end temperature in our design is 550K. Then the water inlet and outlet temperatures are calculated to be 510K and 544K according to Equation (17), and the average temperature of the radiator is estimated to be 527K.

Heat Rejection

According to the literature, the effective temperature of space is 10K[5]. Considering the extreme conditions, the lowest temperature of moon surface is around 93K and the highest temperature is 423K. Neglecting the solar irradiation, the radiator can be regarded as a small surface in an infinitely large surrounding. Then the heat rejection rate can be expressed as:

$$\dot{Q}_{waste} = A\varepsilon\sigma(T_{rejector}^4 - T_{sur}^4) \quad (18)$$

where A is the radiation area; ε is the emissivity of the radiator surface (around 0.9[5]); σ is Stefan-Boltzmann constant ($5.67 \times 10^{-8} \text{W}/(\text{m}^2 \cdot \text{K}^4)$); \dot{Q}_{waste} equals to 160kWt. The radiator areas in require are calculated for different surroundings as shown in Table 3. As the radiator temperature is relatively high, the radiator areas in this design is much smaller than that in FSP design.

TABLE 3. The calculated radiator areas in different surroundings (in m²).

Surrounding	Space	Moon day	Moon night
Area	40.6	40.7	69.5

Summary

The results of the steady-state thermal control analyses show that the heat pipe cooled SRPS is physically feasible with regard to the energy transfer and conversion processes. The values of the independent system parameters for this design are listed in Table 4, among them some are reversely calculated according to Equations (1)~(4).

TABLE 4. The values of the independent system parameters of the heat pipe cooled SRPS.

\dot{Q} /kW	T_{reactor} /K	$T_{\text{convert-hot}}$ /K	$U_{\text{reactor-heat}}$ /W·K-1	$U_{\text{heat-convert}}$ /W·K-1	$U_{\text{convert-rejector}}$ /W·K-1	$U_{\text{rejector-sur}}$ /W·K-1
200	1200	900	∞	1000	6956	Space: 309 Moon night: 369 Moon day: 1538

SYSTEM –LEVEL TRANSIENT PHYSICAL MODEL

The steady-state characteristics of SRPSs are discussed in Section 2 of this paper. Transient processes may be involved during the actual operation of a SRPS, such as start-up, shut-down, manual or accidental changes of operating parameters, changes of surrounding parameters and breakdowns of subsystems. Therefore, the transient characteristics of a SRPS are also of great importance. In order to analyze the transient characteristics, a system-level transient physical model is in need[5, 6]. As for the heat pipe cooled SRPS design, a model is suggested as shown in Figure 5. As the fast reactor is compact, the point-kinetics model is usually used[17]. The start-up of the heat pipe is complex, relating to multi-physical processes of heat transfer, flow and phase change[18]. The reported experimental[19, 20] and numerical[21, 23] results indicate that two processes are involved in the start-up from frozen-state: 1) the melting of the working medium in the wick represented by the axial propagation of the solid/liquid interface; 2) the development of the vapor flow represented by propagation of the free-molecular/continuous flow interface. The temperature-front model built by Cao[24] is introduced as it well describes the propagations. In order to simulate the transients of the Stirling generator, a coupled model of the piston movement, the working gas flow, the heat transfer processes and the linear generator is needed. According to the comparative study of Ulusoy[25], the isothermal model is accurate while greatly reducing the complexity. In the isothermal model, it is assumed that uniform and steady temperature fields exist in the cold chamber and the hot chamber, while the temperature in the regenerator is linear and steady. In order to simulate the radiator with water loop, the water fluid, the solid conduction, the heat pipe heat transfer need to be considered, as well as the radiative heat transfer between the panel and the surrounding. Based on the work of El-Genk[5], a one-dimensional thermal-hydraulic model for the radiator is suggested. As interfaces exist between the reactor and the heat pipes, the heat pipes and the Stirling engines, as well as the Stirling engines and the radiator, interfacial models need to be built according to the final design. After the system-level model is completely built, numerical methods are to be used to analyze the transient characteristics.

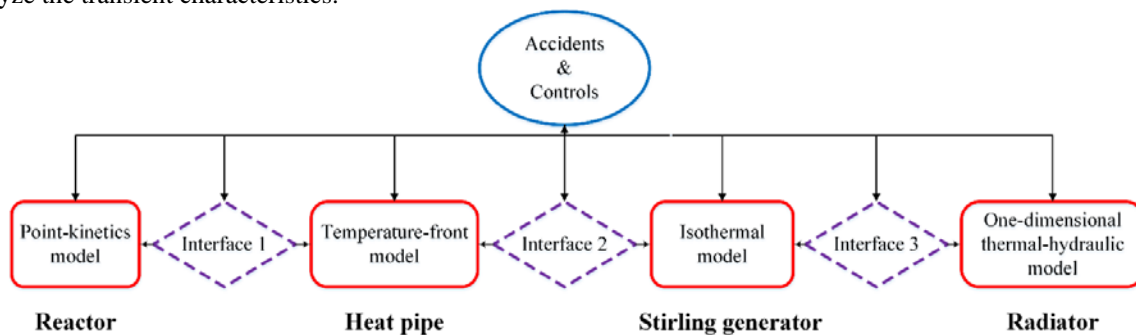


FIGURE 5. The layout of the system-level transient physical model.

CONCLUSION

Technologies should be carefully evaluated and selected when designing a SRPS, based on thermal-control analyses of both the subsystems and the whole system. According to the authors' comprehension, thermal control design may consist of two parts: 1) A physical model of the whole system should be built to verify the feasibility of the design under in different working conditions and to elucidate the relationship between the system performance and key parameters, based on the models or experimental data of the subsystems; 2) On the basis of work aforesaid, the key parameters of subsystems should be optimized with the mass and the volume being the objective functions. Based on a general analysis of the energy transfer and conversion processes in the power systems, 7 independent system parameters for design and optimization are extracted. A design of a heat pipe cooled space reactor power system is proposed. Steady-state thermal-control analyses are performed, and the results verify that the design is physically feasible. For building a transient physical model of the whole power system, an integration of a point-kinetics model for the reactor, a temperature front model for the heat pipes, an isothermal model for the Stirling engines and a one-dimensional thermal-hydraulic model for the radiator is suggested.

NOMENCLATURE

T	=	Temperature	\dot{Q}	=	Heat power
U	=	Heat transfer coefficient	η	=	Conversion Efficiency
h	=	Convective transfer coefficient	v	=	Velocity
R	=	Thermal resistance	d	=	Diameter
λ	=	Thermal conductivity	L	=	Thickness
\dot{q}	=	Heat transfer rate	ϕ	=	Porosity
Re	=	Reynolds number	Nu	=	Nusselt number
ΔT	=	Temperature difference	A	=	Area
ε	=	Emissivity			

ACKNOWLEDGMENTS

We are very grateful for Xiaolin Zhao's valuable advice.

REFERENCES

- [1] Zhang, M., Cai, X.D., Du, Q, Lei, Y.J., Hu, G., and Chen, S., "Research on Nuclear Reactor in Space Application (in Chinese)," *Spacecraft. Eng.*, **22**, 119-126, (2013).
- [2] Bragg-Sitton, S.M., Werner, J.E., Johnson, S.G., Houts, M.G., Palac, D.T., Mason, L.S., Poston, D.I., and Qualls, A.L., "Ongoing Space Nuclear Systems Development in the United States," in *2011 International Nuclear Atlantic Conference*, Belo Horizonte, Brazil, (2011).
- [3] Akimov, V.N., Koroteev, A.A., and Koroteev, A.S., "Space Nuclear Power Systems: Yesterday, Today, and Tomorrow," *Therm. Eng.*, **59**, 953-959, (2012).
- [4] Su, Z.T., Yang, J.C., and Ke, G.T., *Space Nuclear Power* (in Chinese), Shanghai Jiaotong University Press, Shanghai, (2016).
- [5] El-Genk, M.S., and Tournier, J.M., "DynMo-TE: Dynamic Simulation Model of Space Reactor Power System with Thermoelectric Converters," *Nucl. Eng. Des.*, **236**, 2501-2529, (2006).
- [6] Yuan, Y., Shan, J., Zhang, B., Gou, J., Zhang, B., Lu, T., Ge, L., and Yang, Z., "Study on Startup Characteristics

- of Heat Pipe Cooled and AMTEC Conversion Space Reactor System,” *Prog. Nucl. Energ.*, **86**, 18-30, (2016).
- [7] Jia, B.S., Yu, J.Y., and Peng, M.J., *Design and Optimization of Nuclear Power Systems* (in Chinese), Harbin Engineering University Press, Harbin, (2010).
- [8] Van Dyke, M.K., Martin, J.J., and Houts, M.G., “Overview of Nonnuclear Testing of the Safe, Affordable 30-kW Fission Engine Including End-to-End Demonstrator Testing,” NASA/TM-2003-212930, (2003).
- [9] Briggs, M.H., Geng, S.M., and Robbie, M.G., “Status of Kilowatt-Class Stirling Power Conversion Using a Pumped NaK Loop for Thermal Input,” NASA/TM-2010-216265, (2010).
- [10] El-Genk, M.S., “Space Nuclear Reactor Power System Concepts with Static and Dynamic Energy Conversion,” *Energ. Convers. Manage.*, **49**, 402-411, (2008).
- [11] Incropera, F.P., Dewitt, D.P., Bergman, T.L., and Lavine, A.S., *Fundamentals of Heat and Mass Transfer*, Chemical Industry Press, Beijing, (2007).
- [12] Zuo, Z.J., and Faghri, A., “A Network Thermodynamic Analysis of the Heat Pipe,” *Int. J. Heat Mass Tran.*, **41**, 1473-1484, (1998).
- [13] Huang, J.W., Peng, Y.D., Liu, F.M., Chang, T.F., Peng, C.Q., Yin, X., Li, B.Y., “Numerical Simulation Study on the Characteristics of Flow Field in Cylinder of Stirling Engine (in Chinese),” *J. of Hunan Univ. Sci. Tech.*, **27**, 27-31, (2012).
- [14] Langlois, J.L.R., “Dynamic Computer Model of a Stirling Space Nuclear Power System,” US Naval Academy, Trident Scholar project report no. 345, (2006).
- [15] Wood, J.G., Buffalino, A., and Holliday, E., “Free-Piston Stirling Power Conversion Unit for Fission Surface Power, Phase I Final Report,” NASA/CR-2010-216750, (2010).
- [16] Team, F.S.P., “Fission Surface Power System Initial Concept Definition,” NASA/TM-2010-216772, (2010).
- [17] Bragg-Sitton, S.M., “Analysis of Space Reactor System Components: Investigation through Simulation and Non-nuclear Testing,” University of Michigan, Ann Arbor, MI, (2004).
- [18] Cao, Y., and Faghri, A., “Simulation of the Early Startup Period of High-Temperature Heat Pipes From the Frozen State by a Rarefied Vapor Self-Diffusion Model,” *J. Heat Tran.*, **115**, 239-246, (1993).
- [19] Faghri, A., Buchko, M., and Cao, Y., “A Study of High-Temperature Heat Pipes with Multiple Heat Sources and Sinks. Part I. Experimental Methodology and Frozen Startup Profiles,” *J. Heat Tran.*, **113**, 1003-1009, (1991).
- [20] Yu, P., Zhang, H., Xu, H., and Shen, Y., “Restart Characteristics of High-temperature Sodium Heat Pipe (in Chinese),” *Proceedings of the CSEE*, **35**, 404-410, (2015).
- [21] Cao, Y., and Faghri, A., “A Numerical Analysis of High-Temperature Heat Pipe Startup From the Frozen State,” *J. Heat Tran.*, **115**, 247-254, (1993).
- [22] Tournier, J., and El-genk, M.S., “A vapor flow model for analysis of liquid-metal heat pipe startup from a frozen state,” *Int. J. Heat Mass Tran.*, **39**, 3767-3780, (1996).
- [23] Jang, J.H., Faghri, A., Chang, W.S., Mahefkey E.T., “Mathematical Modeling and Analysis of Heat Pipe Start-Up From the Frozen State,” *J. Heat Tran.*, **112**, 586-594, (1990).
- [24] Cao, Y., and Faghri, A., “Closed-Form Analytical Solutions of High-Temperature Heat Pipe Startup and Frozen Startup Limitation,” *J. Heat Tran.*, **114**, 1028-1035, (1992).
- [25] Ulusoy, N., “Dynamic Analysis of Free Piston Stirling Engines,” Department of Mechanical and Aerospace Engineering, Case Western Reserve University, Cleveland, OH, (1994).

Criticality Safety Design and Analysis of the Heat-pipe Nuclear Reactor

Wang SanBing¹, Xie Qilin¹, Guo simao¹, He ChaoHui²

¹*Institute of Nuclear Physics and Chemistry, Chinese Academy of Engineering Physics, Mianyang 621900*

²*School of Nuclear Science and Technology, Xi'an Jiaotong University, Xi'an, 710049*
kiner85@163.com

Abstract. Heat-pipe nuclear reactor was one of the most important reactor-types to enable human future deep space exploration missions, due to its passive safety character from the heat-pipe. Firstly, the designs of heat-pipe nuclear reactor in past researches had been compared in order to re-estimate the criticality design of heat-pipe reactor, and then SAFE-400 reactor invented by Los Alamos National Lab (LANL) was chosen as benchmark reactor because of its excellent performance. Secondly, the criticality safety parameters of SAFE-400 reactor were re-analyzed by MCNP, including the control drum's function, spectrum shift absorber's (SSA's) function and its capability for the launch abortion accident when it lost most of reactivity control sub-system. The calculation results had shown that it was not enough to deal with the immersion accident only relying on the work of the control drums and SSA when it lost most of the control drums. Meanwhile, the calculation results had also given out a fact that SAFE-400 reactor's criticality safety depended on the number of the broken heat-pipe due to great impact during the launch abortion and immersion accident. It meant that making the heat-pipe nuclear reactor completely broken was better to prevent super-criticality accident and ensure the criticality safety than the method keeping reactor integrity and sub-critical after the launch abortion accident happened. This paper was helpful for the designs of heat-pipe reactor in the future.

Keywords: Criticality safety; Heat-pipe Nuclear Reactor; SAFE-400; MCNP.

INSTRUCTION

The space exploration mission had very important research value, which was not only helpful to answer many scientific problems, but it also inspired human to research the other unknown universe. However, in order to push the future research of the deep space science, the deep space detection systems needed more strength power that was over the capability of solar energy battery and other power systems based on the present technology, as reported by NASA [1].

Space nuclear power was considered as the key technology to the future deep space mission [2], such as RTG (Radioisotope Thermoelectric Generator) and SNR (Space Nuclear Reactor) had been applied in the past space missions. Among of them, SNR could provide much more power and also meet the requirement of the future deep space exploration mission with the need of more than several kilowatt electrical powers and 10 years' service life and offer higher safety [3].

In the past 50 years, many SNRs had been designed for various space missions, such as BUK, Topaz [1], SNAP10A [4], Yennisei [5], SP100 [6], SAFE400 [7], MSR [8], SCoRe [9], HOMER25 [10], SUSEE [11], S ~~14~~ and ASFPSS [13]. These reactors had different advantages. But only three types of SNR including BUK, TOPAZ and SNAP10 were launched and applied in space missions and all of their real service lives were not over 1 year. How to improve the reliability and service life of SNR with enough guaranteed nuclear criticality safety always embarrassed scientist.

Due to the passive safety character from the heat-pipe and decreased the special part (such as electromagnetic pump and stabilizer or other types of coolant device), heat-pipe nuclear reactor was considered as one of the most important reactor-types with the compact structure design and had the most potentiality to enable human future deep space exploration missions. Since 1980s, heat-pipe nuclear reactor had got great development. Especially, the concept of SAFE400 was created by Los Alamos national Lab in 2002, and the following designs of heat-pipe nuclear reactor had similar structure with it.

Unfortunately, heat-pipe nuclear reactor did not get the chance of being applied in the mission until today although the experiment results strongly verified its distinguished performance. The most important reason was always that the design of criticality safety of heat-pipe nuclear reactor did not get enough guarantees to release the public concern. Therefore, it was necessary to re-estimate the design of heat-pipe reactor to help its future design and did not repeat the past work blindfold.

Aimed at analyzing the criticality safety of heat-pipe nuclear reactor and the strategy to deal with the submersion accident following the launch abortion accident, this paper took SAFE400 as benchmark reactor and firstly introduced the design of SAFE400 and analyzed its performance, and then it discussed the criticality safety design of SAFE400, such as control drum, shift spectrum absorber (SSA) and reflector outside of activity core. This paper was helpful for the designs of heat-pipe reactor in the future.

DESIGN AND ANALYSIS OF SAFE400

Structure of SAFE400

SAFE400 was invented by Los Alamos national Lab in 2002. Its activity core was composed by 127 molybdenum modules and 39 BeO reflector rods. Every molybdenum module contained 3 UN fuel rods (with 93% ^{235}U enrichment) and 1 Mo-Na heat-pipe rod. The fuel rod was 0.5525cm radius \times 50cm high with 4cm thickness BeO reflector layer in the top and bottom of rod cap, which was used to decrease the neutron leakage in the axial direction. Outside of activity core distributed 6 B_4C control drums in the 10.5cm thickness Be reflector layer to executive the startup, shutdown and the other operation command of reactor. Every control drum was 6cm radius and 54cm high with 1.5cm thick B_4C as shown in Fig.1.

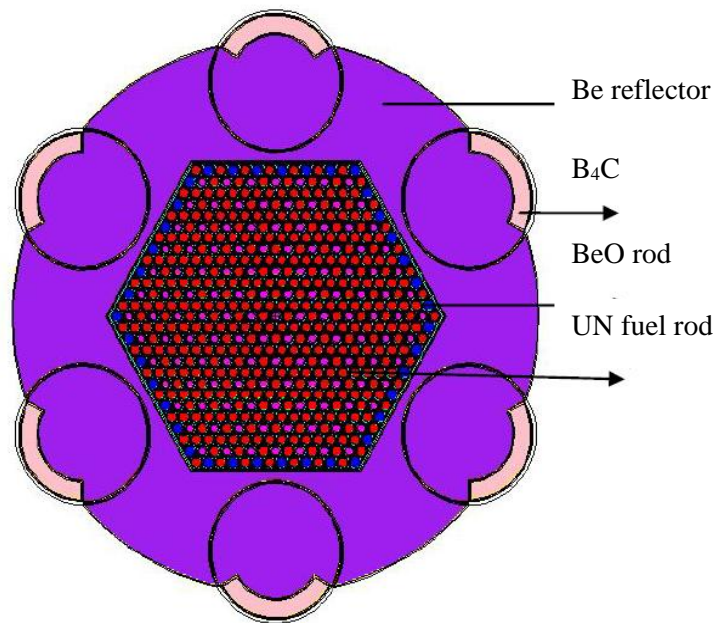


FIGURE 1. Schematic of SAFE400 reactor

The design parameters of SAFE400 had shown that it could serve for 10 years at least with 400kW thermal power operation or 100kW electrical power using Brayton conversion system. Meanwhile, it could be passively safe for the launch or reentry accident by using 0.051cm thickness Re as SSA in the fuel pin and heat-pipe rod as described in the reference 7.

Primary Analysis of SAFE400

MCNP could perfectly calculate the steady state parameters of nuclear reactor, such as the effective multiplication factor k_{eff} , the effective delay neutron fraction, neutron flux distribution, energy spectrum and other criticality parameters [14]. Therefore, MCNP was used to analyze the performance of SAFE400 in this paper. Based on 10000 source particles with 50 inactive cycles and 400 active cycles in every calculation, the determination results of SAFE400 were given in Table 1, and the energy spectrum was shown in Fig.2.

TABLE 1. The performance of SAFE400

Parameter	k_{eff} (cold, control drum out, BOL) ^a	k_{eff} (cold, control drum in, BOL)	the effective delay neutron fraction β	$\Delta\rho(10a)$ ^b
Designed results	1.0342	0.9584	0.00677	-0.00776
Calculation results	1.05015±0.00036	0.94207±0.00034	0.00677	-0.00631

a: BOL was just beginning of life;

b: reactor continued work with full power operation for 10 years.

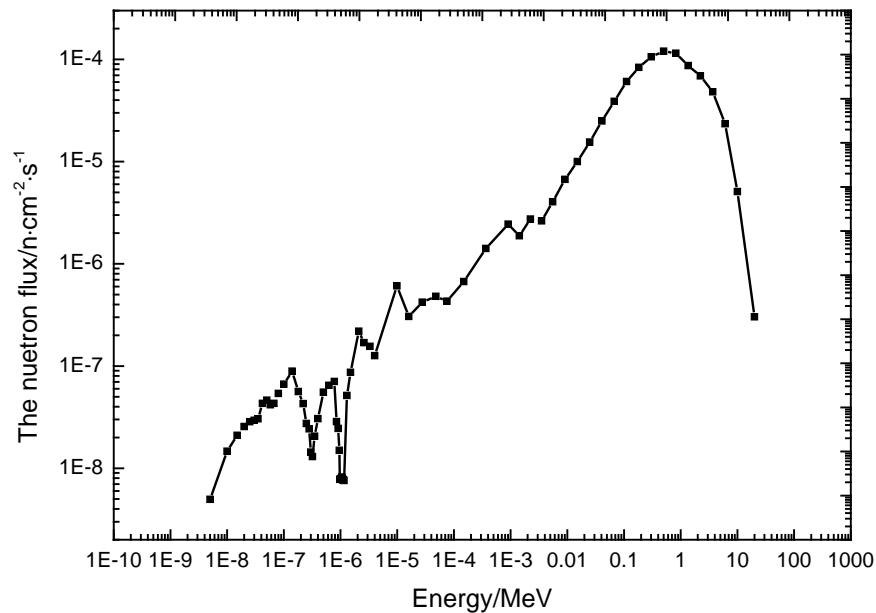


FIGURE 2. The energy spectrum in activity core

The errors of the steady state parameters in calculation results were less than 2% compared with the designed value in paper, and the average neutron energy was high to 1.03MeV which made the energy spectrum very hard. Meanwhile, from the table 1, it could be found that the calculation result about k_{eff} or excess reactivity in BOL was a little bigger than designed value, but the calculation result about k_{eff} (shutdown in BOL) and burn-up were a little smaller than the designed one. The reasons of this difference in results were maybe that: 1) the geometry of component except fuel rod, heat-pipe and reflector rod in calculation model was maybe different from the real designed one; 2) the composite of material was different from the designed value. In general, the calculation model was very similar with the real designed one and it could be benchmark reactor to the following analysis.

ANALYSIS OF CRITICALITY SAFETY IN REENTRY ACCIDENT

Immersion Accident Following Reentry Accident

When reentry accident happened, the reactor core would be usually impacted by desert or sea (decided by onboard location). On this occasion, the multiplication factor of reactor had to be increased if the reactor kept generally integrity, because the leakage neutron would be reflected into activity core and moderated by sand or water (immersion material). Thus, the criticality safety of reactor was highly determined by the designed parameters and the effect of reactivity control systems, such as control drum, SSA or other burnable poison.

In order to analyze the criticality safety performance of SAFE400, it was necessary to determine the effect of control drum, Re, heat-pipe which were helpful to deal with reentry accident, based on the following situation as shown in Table 2.

TABLE 2. The accident scenario following reentry accident*

Control system	Control drum	SSA	Heat-pipe	Gap in core
action of the control system	1) in; 2) out; 3) N/A	1) normal; 2) N/A	1) normal; 2) broken	1) normal; 2) filled with immersion material.
accident type	1) out; 2) N/A	N/A	broken	filled with immersion material.

* Assuming that the reactor kept unchanged after immersion accident happened.

As shown in Table 2, the control drums were all normally in active when SSA was not available, or heat-pipe was all broken, or the gap in activity core was filled with the immersion material.

In other way, the common immersion accidents of SAFE400 were that SAFE400 was flooded by ocean, river, and desert, thus SAFE400 was assumed to be immersed by different typical materials, such as seawater, water, dry-sand and wet-sand, respectively. The seawater was composed of 96.9 wt% water (H₂O) and 3.1 wt% salt (NaCl); and the wet-sand mainly was composed of 85.8 wt% silica (SiO₂) and 14.2wt% seawater.

Primary Results and Discussion

The immersion reactivity of SAFE400 for the different accident scenario was calculated by MCNP and the results were shown in table 3. And it could be seen from this table that the dry-sand immersion accident was the most serious accident if the immersion material did not fill into activity core or heat-pipe. But the water immersion accident became the most serious accident once immersion material filled in the gap of activity core. The reason was that the immersion material moderated the fast neutron and made the fuel absorption reaction increment, therefore, the energy spectrum became harder when the immersion material filled into the gap of activity core, as shown in Fig.3.

It also could be found from Table 3 that the immersion reactivity of SAFE400 was the biggest, and changed with the different immersion type when all the control drums were inactive, but the criticality of SAFE400 almost kept unchanged and was in deep sub-criticality when the control drum system was in active. Meanwhile, the criticality of SAFE400 was little over 1.01 for all the immersion cases when the SSA was unavailable. Therefore, the control drum system was the key tool to ensure the nuclear criticality safety of heat-pipe reactor in immersion accident following launch abortion accident.

The heat-pipe rod of SAFE400 could not keep undamaged when reentry accident happened, so the amount of broken heat-pipe would influence the criticality safety of SAFE400 in the immersion situation. The calculation results of SAFE400 in Table 3 verified this consideration that the seawater or water immersion reactivity of SAFE400 was clearly near critical state when all the heat-pipes were broken and all the control drums were normally in work.

Of course, because the volume of gap between the reactor core and reflector layer and other parts was relatively smaller than the volume of entire reactor, the immersion reactivity of SAFE400 got just few increment than the value of the case of “control drum in” as shown in Table 3.

TABLE 3. The multiplication factor of reactor for the different accident scenario

Control system	Control drum			SSA	Heat-pipe	Gap in core
	in	out	N/A	N/A	broken	Filled with immersion material
k_{eff} of reactor in the seawater immersion accident	0.95111 ±0.00036	1.07210 ±0.00042	0.95513 ±0.00042	1.00425 ±0.00041	0.99768 ±0.00038	0.95513 ±0.00042
k_{eff} of reactor in the water immersion accident	0.95190 ±0.00034	1.07386 ±0.00041	0.97470 ±0.00041	1.00806 ±0.00042	0.99789 ±0.00037	0.95580 ±0.00037
k_{eff} of reactor in the dry-sand immersion accident	0.95957 ±0.00036	1.08396 ±0.00040	1.03507 ±0.00039	1.01033 ±0.00038	0.96849 ±0.00037	0.96610 ±0.00032
k_{eff} of reactor in the wet-sand immersion accident	0.95571 ±0.00036	1.07839 ±0.00039	1.01316 ±0.00039	1.00916 ±0.00040	0.98089 ±0.00037	0.96248 ±0.00035

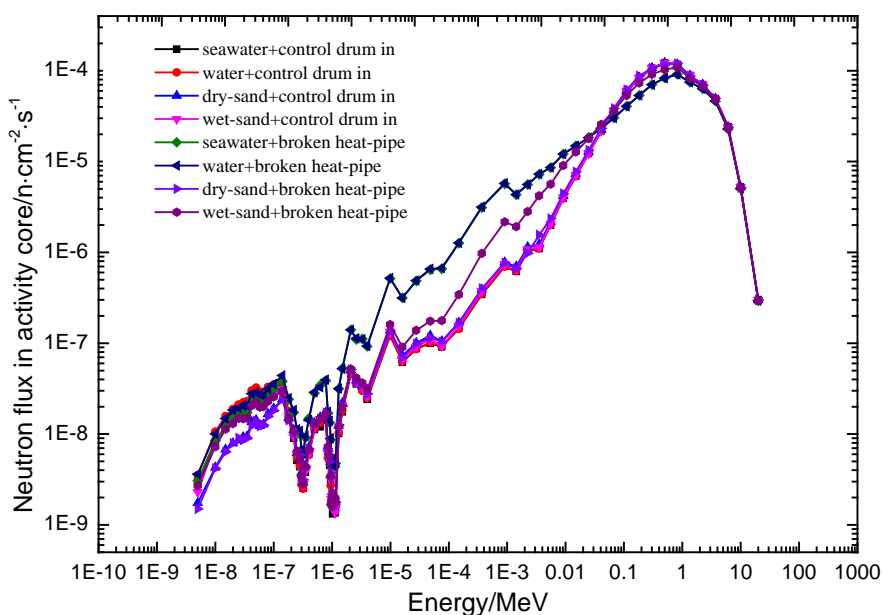


FIGURE 3. The energy spectrum of both accident type of “control drum in” and “broken heat-pipe” in the different immersion accident

Through the analysis of different immersion accidents and comparisons between these four control-systems in Table 3, it could be found that the function of the control drums was the most important for the criticality safety, especially in the immersion accident. And the reactivity of SAFE400 almost kept constant when the control drums were brought into function, which had given another hint that the decrement of the inherent reactivity of bare core was also helpful to ensure the criticality safety of heat-pipe reactor in the immersion accident.

DECREMENT OF REACTIVITY OF THE ACTIVITY CORE

In order to verify the importance of bare core of heat-pipe reactor in dealing with immersion accident, the enrichment of ^{235}U was decreased to 90% and the other structure and material parameters kept unchanged, when the performance of the revised model of SAFE400 was calculated by MCNP as shown in Fig.4. And its initial k_{eff} (BOL) was 1.02019 ± 0.00036 , which was 1.35% less than the designed value of SAFE400 as shown in Table 1.

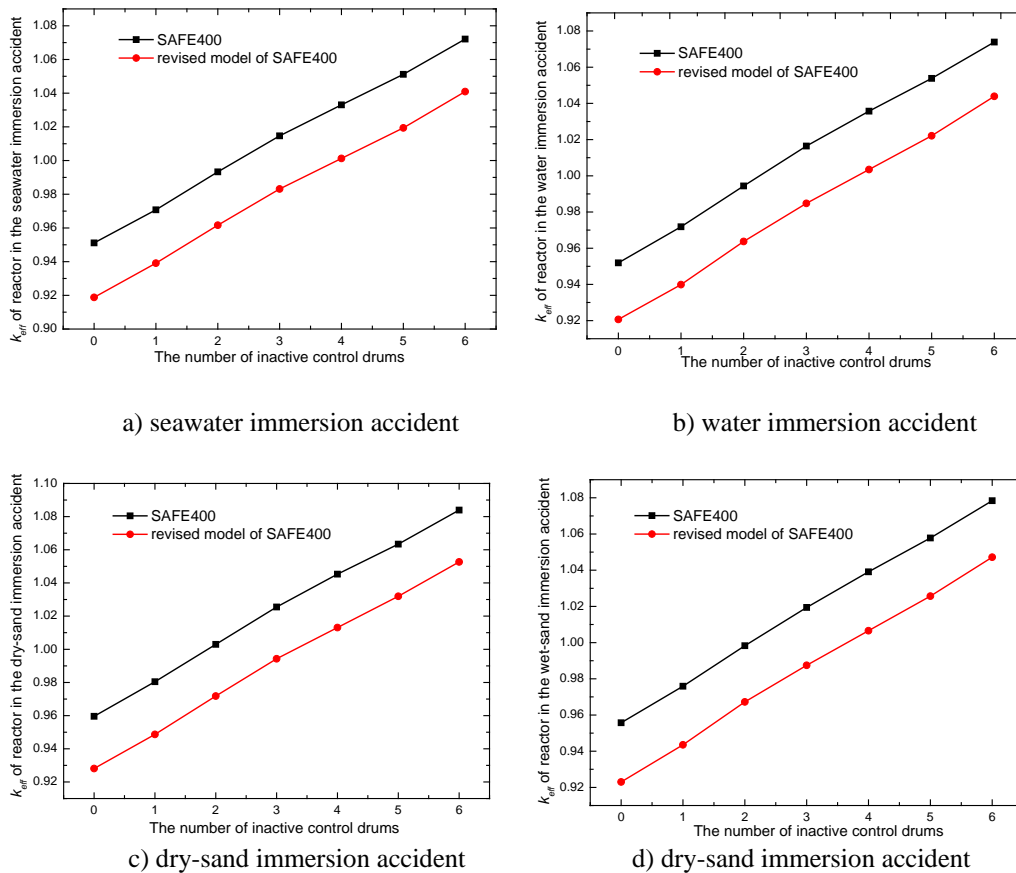


FIGURE 4. The performance of revised model of SAFE400 in immersion accident compared with the design one.

It could be found from Fig.4 that the immersion reactivity of revised model of SAFE400 decreased by 10% at least through the decrement of the enrichment of ^{235}U , and its immersion criticality would be super-critical only when over two control drums lost function. Therefore, the criticality safety for the revised model of SAFE400 had got much improvement.

Obviously, the decrement of the reactivity of bare core was helpful to ensure the criticality safety of heat-pipe reactor in the immersion accident. But, unfortunately, the reactivity of bare core could not decrease much so that it maybe could not work for 10 years with full power operation. In other words, the decrement of the reactivity of bare core also could not guarantee heat-pipe reactor with absolute criticality safety. Especially, the heat-pipe may be broken in the immersion accident which would make reactor in worse situation. So the criticality safety of heat-pipe

reactor depended on the improvement of the reliability of control drum system, or making the heat-pipe nuclear reactor completely broken, which was better to prevent super-criticality accident and ensure the criticality safety than the method of keeping reactor integrity and sub-critical after the launch abortion accident happened.

CONCLUSION

This paper firstly analyzed the performance of heat-pipe reactor based on the model of SAFE400, and then determined its reactivity in different immersion accident following the launch abortion accident. The calculation results had shown that the design of SAFE400's control system, such as control drum, SSA and reflector outside of activity core, played important role in dealing with immersion accident. Meanwhile, this paper tried to decrease ^{235}U enrichment in the fuel to help the performance of SAFE400 in immersion accident. These results calculated by MCNP had forwardly shown that 1) the decrement of the inherent reactivity of bare core was also helpful to ensure the criticality safety of heat-pipe reactor in the immersion accident; 2) in other way, the criticality safety of SAFE400 highly depended on the improvement of the reliability of control drum system. But any type of control system could not completely ensure the criticality safety of reactor.

Heat-pipe reactor was possible to face more accident scenario, such as the accident of broken heat-pipe which maybe influenced the performance of reactor in the immersion accident. And the best choice of heat-pipe reactor was completely disintegrated to ensure its criticality safety when the reliability of control system could not get guaranteed. This paper was helpful for the designs of heat-pipe reactor in the future.

NOMENCLATURE

k = Neutron multiplication factor

ρ = Reactivity

ACKNOWLEDGMENTS

Great gratitude to the support of Institute of Nuclear Physics and Chemistry in this research and the helps from our colleagues.

REFERENCES

- [1] O'Brien R C., "Safe radioisotope thermoelectric generators and heat sources for space applications," *J Nucl Mater*, **377** (3): 506-521, (2008).
- [2] Summerer L, Stephenson K., "Nuclear power sources: a key enabling technology for planetary exploration," *Proceedings of the Institution of Mechanical Engineers, Part G: Journal of Aerospace Engineering*, **225** (2): 129-143, (2011).
- [3] Mason L, Poston D, Qualls L., "System Concepts for Affordable Fission Surface Power," *Space Technology and Applications International Forum (STAIF 2008)*. Albuquerque, USA, (2008).
- [4] Dieckamp, H.M., "Nuclear Space Power Systems," **Atomic International**, Canoga Park CA. USA. 1967.
- [5] Nikitin V, Ogloblin B, Sokolov E, et al. "Yennisei space nuclear power system," *Atomic Energy*, **88** (2): 98-110, (2000).
- [6] Deane N, Murata R, Kruger G., "SP-100 reactor design and performance," IEEE, *Proceedings of the 24th Intersociety Energy Conversion Engineering Conference*. Washington, DC., USA. (1989).
- [7] Poston D I, Kapernick R J, Guffee RM., "Design and analysis of the SAFE-400 space fission reactor," *Space Technology and Applications International Forum (STAIF 2002)*. Albuquerque, USA, (2002).
- [8] Bushman A., Carpenter D. M., Ellis T. S., et al. "The Martian Surface Reactor: An Advanced Nuclear Power Station for Manned Extraterrestrial Exploration," MIT, USA. **MIT-NSA-TR-003**, (2004).
- [9] EL-Genk M., Hatton S., Fox C., and Tournier J. "SCoRe – Concepts of Liquid Metal Cooled Space Reactors for Avoidance of Single Point Failure," *Proc. Space Technology and Applications International Forum (STAIF-*

- 2005), Melville, USA. (2005).
- [10] Amiri B. W., Sims B. T., Poston D. I., and Kapernick R. J. "A Stainless-Steel, Uranium Dioxide, Potassium-Heatpipe-Cooled Surface Reactor," *Proc. Space Technology and Applications International Forum (STAIF-2006)*, Melville, USA. (2006.)
- [11] Maise G., Powell J., and Pariagua J. "SUSEE: A Compact, Lightweight Space Nuclear Power System Using Present Water Reactor Technology," *Proc. Space Technology and Applications International Forum (STAIF-2006)*, Melville, USA. (2006).
- [12] King J. C. and El-Genk M. S. "Solid-Core Gas-Cooled Reactor for Space and Surface Power," *Proc. Space Technology and Applications International Forum (STAIF-2006)*, Melville, USA. (2006).
- [13] Poston D. I., Kapernick R., Dixon D., et al. "Reference Reactor Module Design for NASA's Lunar Fission Surface Power System," *Proceeding of nuclear and emerging technologies for space 2009(NETS2009)*. Atlanta, USA. (2009).
- [14] Briemeister J., "MCNP: A General Monte Carlo N-Particle Transport Code (Version-4C) ," **Los Alamos National Laboratory**, USA. (2000).

Control System Requirements for a Nuclear Thermal Propulsion System

A. Hasse¹, M. Smith¹, B. Pershke¹, S. Gilliam¹, D. Adams¹, L. Qualls²

¹*Dept. of Nuclear Engineering, University of Tennessee, Knoxville*

²*Reactor and Nuclear Systems Division, Oak Ridge National Laboratory*

Abstract. A dynamic simulation model was developed to investigate coolant/propellant pump, control drum, flow performance, and core responses necessary for a successful startup of a moderated Nuclear Thermal Propulsion (NTP) system. The system parameters are based on the Small Nuclear Reactor Engine (SNRE) design developed at Los Alamos National Laboratory. Simulink was used as the modeling software to solve a system of coupled differential equations that describe the hydrogen flow (coolant and propellant), control drum actuation, and the core power temperature and response. Multiple Matlab scripts were constructed to interface and control the simulation model, which allowed accelerated iterative testing over a wide range. The results of these simulations were put into time dependent profiles for temperature, temperature differentials, core reactivity and system pressure. Reduced data sets from the collections of these time dependent profiles allowed for the creation of response functions for each tested parameter. Through the analysis and characterization of these response functions (such as the behavior of maximum temperatures, temperature changes, power surges, reactivity insertions, etc.), specific system parameter limits were outlined to ensure the predictability, safety and reliability of the system. Results of these simulations and the resulting control system requirements this specific model-based SNRE design are presented. This model and the resulting system requirements serve as a first order framework in preparation for the next, more detailed, phase of NTP system simulation.

Keywords: Nuclear Thermal Propulsion, NTP, Control System

INTRODUCTION

NASA has an interest in a manned mission to Mars and Nuclear Thermal Propulsion (NTP) systems may provide a more effective solution for this initiative than present chemical rocket technology can offer. Most modern chemical rockets use a fuel-oxidization system to create combustion where the reaction creates exhaust that is expelled through a nozzle in order to create thrust. Chemical propulsion systems are useful for getting a payload off the Earth's surface and into orbit, but are inefficient in regards to fuel consumption when compared to NTP systems. The amount of a rocket's useable propellant divided by the rocket's gross mass is a common metric for fuel efficiency. This metric is referred to as the propellant mass fraction, or PMF. For example, the Ares V Earth Departure Stage has a PMF of approximately 88%, leaving only 12% of the total rocket mass for mission payload [2]. the expected PMF of NTP systems is approximately 30% which allows for higher payloads (70%) per mission and could potentially reduce the number of launches required for multi-launch missions. These potential savings could potentially reach billions of dollars per mission, thus allowing NTP systems to serve as a more economical and improved propulsion alternative for future manned missions to Mars [3].

The purpose of this project was to develop a simplified simulation model that used baseline values from the Small Nuclear Rocket Engine (SNRE) design developed at Los Alamos National Laboratory (LANL) to simulate startup behavior of this style of NTP system but also be capable of adaptation to new NTP configurations as well. With simulations developed in Matlab and Simulink, a variety of operational scenarios were tested to outline a set of control systems parameters necessary for the successful startup of the simulated NTP system. The results came in the form of

time-dependent profiles and response functions from a variety of parameters of interest including material temperature, core reactivity, coolant/propellant temperature, and coolant/propellant flow rate. The results were compared to reference SNRE baseline results to determine comparable functioning of this new simulation model. Finally, parametric testing was performed to determine specific parameter thresholds essential to predictable, safe and reliable startup of the system.

Simulation Design Selection

Because of the abundance of past research material on the subject, the SNRE design was chosen as the basis of this research project. The SNRE system is a combination of thermal fluid dynamics and nuclear physics. Starting with the core, the basic construction consists of a sub-critical reactor consisting of hexagonally shaped fuel elements made from a ceramic compound of Uranium-Graphite with Zirconium cladding (U,Zr)C [1]. The core consists of 564, 89 cm long hexagonal fuel elements with 19 Zirconium clad cooling channels (Figure 1). The 241 dual purpose tie-tubes serve as both structural support for the core and hydrogen conduit for pre-heating in the system. Both the fuel elements and the tie-tubes are geometrically arranged throughout the core in a pattern similar to Figure 1.

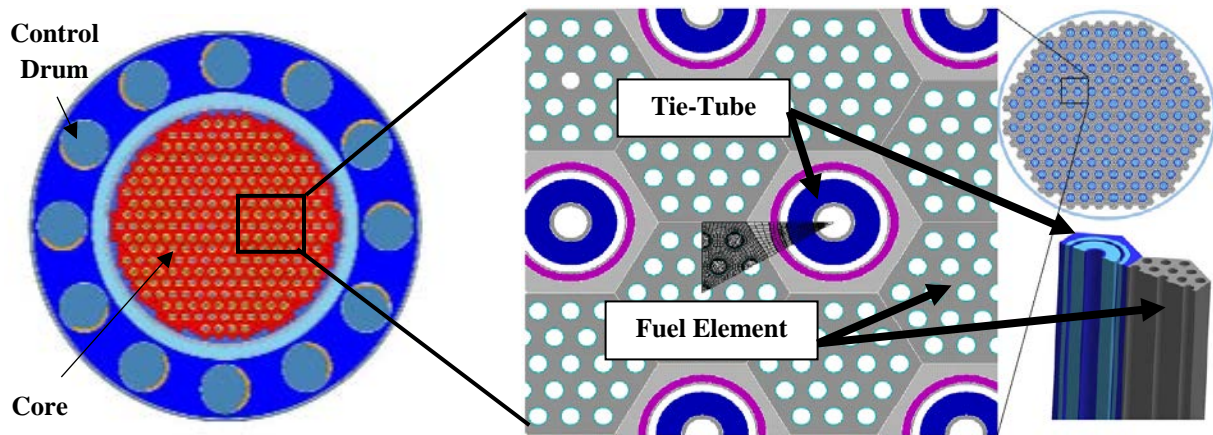


FIGURE 1. Control drum configuration around reactor core and cross-sectional view of tie-tube and fuel element [1].

The fuel enrichment, composition and geometry are designed such that the core is naturally at a sub-critical state. 12 control drums are distributed evenly around the core and may be actuated by either pneumatic or mechanical means (Figure 1). Approximately 120 degrees of the face of each drum is plated with a neutron absorbent material while the remaining 240 degrees are a neutron reflective material (beryllium) [1]. To initiate a critical core, the drums are rotated such that the reflective portion of each drum is facing the center of the core. This configuration increases the reactivity of the core by lessening the neutron leakage factor and begins to bring the core critical. The drums are designed to be positioned at 90 degrees at full reactor power and temperature.

Hydrogen serves as both the system coolant and engine propellant for the SNRE system. It is stored at approximately 20 K in liquid form in a pressurized, cryogenic ullage reservoir. A pump is used to pull liquid hydrogen from the reservoir and distribute it through the system's cooling passages for the nozzle, the reflector drums, a two-fold pass in the tie-tubes and finally through the fuel. The purpose of this two-fold pass through the tie-tubes is to preheat the hydrogen for insertion directly into the fuel elements and to heat hydrogen to a point that can drive turbomachinery located at the top of the core. After use in the turbomachinery, the hydrogen is passed to the fuel element's cooling/propellant channels where it is super-heated to approximately 2900 K, accelerated and fed to the rocket nozzle where it is ultimately used as propulsion [4]. Specific parameter values regarding materials, dimensions and various specifications used in the fuel, ullage, coolant/propellant and core system design are shown below in Table 1.

TABLE 1. Design Specifications for SNRE.

Engine System Component	Value	Reactor System Component	Value
Thrust (klb _f)	16.4	Active Fuel Length (cm)	89.0
Chamber Inlet Temp (K)	2695	Effective Core Radius (cm)	29.5
Chamber Pressure (psia)	450	Engine Radius (cm)	49.3
Nozzle Expansion Ratio	100:1	Number of Fuel Elements	564
Specific Impulse (s)	875	Number of Tie Tube Elements	241
Engine Thrust-to-Weight	2.92	Max Enrichment (wt% U-235)	93
		Max Fuel Temp (K)	2860
		Margin to Fuel Melt (K)	40

*All data courtesy of Schnitzler, Borowski, and Fittje [5].

METHODOLOGY

To assess the performance of the NTP design, a computer simulation was chosen as the most practical approach to outlining preliminary control system requirements needed for successful startup. Although the SNRE system was well documented for design and performance parameters, various assumptions were made when translating the original SNRE theory to the analytical models of this project. This was done as a means to create a representative, yet introductory, simulation model and involved sacrificing certain elements of system fidelity to allot for projected time constraints of the project. For example, the values calculated for the maximum allowable rate of temperature change, or thermal shock, for the fuel and tie tubes was estimated quantitatively, while if this were a funded R&D project slated for actual mission planning, this particular value would be determined by modeling in CAD and subjecting the model to intensive thermal analysis along with prototyping and field testing to determine more accurate failure parameters [6]. With an understanding of the depth of realistic representation involved in this model, the system layout will be discussed, and relative assumptions will be stated. Some of these assumptions are listed following:

1. Hydrogen flow is uncoupled from system control and maintained at a constant rate
2. No radiative heat-loss to space considered
3. No conductive heat-loss of hydrogen to other components in flow loop
4. All radial conductive heat-transfer between the fuel and the tie tubes is ignored

System Design

The physics of the system model can be compartmentalized into three main subsystems: reactor point kinetics, heat transfer, and fluid dynamics. Inside each of these subsystems, various physics “blocks” modeling individual physical processes were developed. These processes were individually researched and equations describing each process was determined. The equations were used to make initial hand calculations to confirm the general accuracy of the relationship between the proposed mathematical model and the physics process at hand. If an equation was deemed appropriate for the process it was written into the Simulink model and incorporated into the greater system. These equations will be discussed in detail in the following sections.

Point Kinetics

The values for the variables in the point kinetics equations were based off literature referencing a similar sized reactor core with similar fuel structure [7]. The constant values for the mean neutron lifetime (Λ), delayed neutron fraction (β_i) and individual decay constants (λ_i) are outlined below in Table 2.

TABLE 2. SNRE point kinetics values.

Variable	Symbol	Value	Units
Delayed Neutron Fraction	β_i	0.065	N/a
Decay Constant	λ_i	0.077	sec ⁻¹
Mean Neutron Lifetime	Λ	0.001	sec

*All data courtesy of M.M. El-Wakil [7].

This model is derived from the governing point kinetics equation, shown in Equations 3-4. For these equations, $\frac{\partial n(t)}{\partial t}$ is the rate of change of neutron density in n/cm³/sec, ρ is the reactivity of the system in dollars, β is the total delayed neutron fraction, Λ is the prompt neutron lifetime in seconds, $n(t)$ is the neutron density in neutrons/cm³, λ_i is the i-th generation radioactive decay constant in seconds⁻¹, and $C_i(t)$ is the average concentration of the i-th generation delayed neutron precursor in n/cm³. By solving the neutron density in the core at any time step, the energy released is estimated by assuming each neutron causes a single fission event equal to 200 MeV. The thermal power output is computed by simply converting MeV to Joules at each time step thus providing energy per unit time, or power output. This output is then fractionalized by the SNRE baseline design peak power value (362 MW) and passed to the heat transfer equations in the core and tie-tubes. This simulation assumes 85% of the total power is deposited in the fuel element coolant channels while the remaining 15% is deposited in the hydrogen in the tie-tubes.

$$\frac{\partial n(t)}{\partial t} = \frac{(\rho - \beta)}{\Lambda} n(t) + \sum_{i=1}^6 \lambda_i C_i(t) \quad (3)$$

$$\frac{\partial}{\partial t} C_i = \lambda_i C_i + \frac{\beta_i}{\Lambda} \quad (4)$$

Heat Transfer

An iterative approach with six steps for each conductive heat transfer length was used specifically within the core and tie tubes. For example, the volumetric power deposition to hydrogen in a single coolant channel in a fuel element is found by assuming 85% of the total power that is deposited into all fuel elements (Joules) then divided by the number of fuel elements in the core (546) and the number of coolant channels per fuel element (19). This solution could be performed over the entire length of each heat transfer section but greater fidelity and accuracy of final bulk temperatures was obtained by the iterative solution process throughout the total length of the heat transfer conduit. Therefore, by dividing the single coolant channel power deposition by the number of iterative step lengths (6) for a single coolant channel in the fuel, the volumetric power deposition was ascertained for the convective heat transfer model. This same logic is applied to the tie-tubes except with 15% of total core power being deposited into all tie-tubes divided by the number of tie tubes (241) and the number of iterative step lengths. Equation 5 shows how the volumetric power deposition (Q_{in}) is incorporated into subsequent convection heat transfer processes.

$$T_{out} = \frac{\pi DLh\Delta T + Q_{in}}{\dot{m}C_p} \quad (5)$$

Using Equation 5, the specific dimensions of the fuel coolant channels were incorporated into the Simulink model. The circumferential surface area of each channel was described by multiplying the inner-diameter (D) by pi and one sixth of the total length (L). This was multiplied by the heat transfer coefficient of hydrogen (h) and the temperature differential (ΔT) between the coolant channel wall and the mean hydrogen temperature. These values multiplied together equal the total power deposition due to convection in the conduit which is added to the volumetric power deposition (Q_{in}). To convert the total power deposition in a single leg of a heat transfer to an exit temperature (T_{out}), the power is divided by the mass flow rate (m) and specific heat (Cp) of the hydrogen. This identical solution was

performed six subsequent times to find the final exit temperature of a single pass through any given heat transfer conduit. Although a fuel coolant channel was used as the example, the same method was implemented for the tie-tubes only accounting for the different tubing dimensions and material constants.

Fluid Dynamics

In an actual hydrogen-cooled NTP system, the hydrogen is in liquid, gaseous and combined two-phase states at various times and places during the operational process. Modeling of these phase transitions and combined two-phase fluid dynamics is complex, and many assumptions were made for the state of hydrogen throughout the system. For these simulations, hydrogen was modeled only as an ideal gas while phase changes, sonic velocities and compressible flow considerations were not included. While not exact, this assumption gives a reasonable estimate of how the hydrogen gas will behave in most sections of the NTP system based on temperature, pressure, and volume changes from external perturbations. With that said, ignoring compressible flow in rocket propulsion systems may seem like a gross oversight but this work was focused on the function of hydrogen as a coolant and moderator in a nuclear reactor capacity and no effort was made to model the performance of the final leg of the hydrogen process as gasses approach sonic velocities and are passed through a rocket nozzle.

Model Tests

After completing the Simulink model, the next step was to develop a way to efficiently run multiple simulations that could automatically test a wide range of specific system variables. In addition, each series of simulations was designed to automatically generate 25 post processing data sets outlining various parameters of interest within the system (temperatures, flow rates, reactivity, etc.). These rapid testing and data processing methods allowed for efficient analysis of system performance while troubleshooting the model. Three main parameters were determined as high priority for identifying optimal system performance:

1. Determine the proper sequence for a successful startup
2. Understand the importance of hydrogen flow and articulate a range of allowable flow rates under certain conditions
3. Describe a range of acceptable drum control rotation speeds and final drum positions

The following parameters were determined as high priority factors to be monitored during simulations and to serve as metrics for startup diagnostics and system thresholds.

1. Temperature of fuel and tie tubes
2. Rate of change of fuel and tie tube temperature
3. Thermal power output of core

The reason that these are high priority factors is because of material stresses and potential material failures. Melting temperatures are of great concern but the rate of temperature changes, or thermal shock, were found to be a highly limiting factor on system performance as well. Along with the material concerns, general system power performance (or lack thereof) was of great interest too. Minimum thermal output from the core is approximately 362 MW_{th} and specific values for material melting temperatures and thermal shock limits can be seen in Table 3.

TABLE 3. Material Properties for SNRE System.

Component	Material	⁺ Melting Temperature (K)	⁺ Marginal Operating Temperature (K)	*Thermal Shock Maximum (K/sec)
Fuel Element	(UZr)C	2900	2860	1000
Tie-Tube	Inconel-718	1609	1569	2000

All data courtesy of ⁺Schnitzler and ^{}K.D. Kingrey [5, 6].

Before generating operational recommendations, it was essential to test the model for accuracy against accepted values of previously researched SNRE computational models. Table 4 shows some values this simulation achieved along with their accompanying values from the previous SNRE models.

TABLE 4. Comparison of Results to SNRE Published Data.

Parameter	Published SNRE Data	Simulation Results
Core Steady State Temp (K)	2728	2740 ± 20
Tie Tube Steady State Temp (K)	429	540 ± 10
Steady State Power (MW _{th})	362	370 ± 5

*All data courtesy of Schnitzler, Borowski, and Fittje [5].

RESULTS

After showing that the simulation was comparable to previous SNRE investigations, multiple series of simulations were developed to illustrate how the range of a parameter of interest affects the performance of the system. For example, a parameter, such as hydrogen flow, would run an initial simulation that would illustrate the effects of an extremely low flow. The model would predict that materials will exceed their melting temperatures. The next simulation would incrementally increase the hydrogen flow and then run the full simulation again. In this example, the parameter's range of effect on the system could be observed from low-end failure (melt down) to high-end failure (inefficient use of hydrogen) to outline the optimum performance range between. This logic and process was applied to the following sequences and parameters of interest:

1. Startup sequence (relationship of hydrogen flow start-time and drum rotation start-time)
2. Hydrogen flow magnitude
3. Drum rotational velocity.

The results of interest for each simulation series are presented in two forms: time dependent profiles and the reduced data sets for each time dependent profile. In the time-dependent profiles, the value of the parameter of interest (temperature, power, etc.) are displayed on the ordinate axis while the time of the profile will be displayed on the abscissa axis. All time dependent profiles testing a single parameter will display multiple simulations in a single graph for each iteration of the parameter of interest. Each full simulation for each iterative step of the parameter will be represented by a separately colored line so the change of the system's performance can be observed as the parameter is changed over a series of values.

The reduced data sets will display a particular point of interest from a time dependent profile, like the maximum or minimum value of the entire simulation. The graphs for the reduced data sets will display this single value of interest from the previous time dependent profile on the ordinate axis while the iterated parameter's value for each simulation will be displayed on the abscissa axis. This allows rapid observation of critical values from the time dependent profiles and makes trends of the system performance more identifiable.

Startup Sequence

To test the startup sequence, two possible scenarios were tested. First, the control drums were initiated without any hydrogen flow in the system. This was achieved by having the drum start-time iterate from 0-1,000 seconds in 100 second increments while the hydrogen flow start-time was always at 500 seconds. This means that of the 11 simulations ran, the first five showed the effects of drum rotation without hydrogen in the system and the second five showed the effects of starting the drums with hydrogen in the system. Figure 2 shows the time-dependent temperature profiles in the core (left) and tie tubes (right) for each simulation. The solid line represents the melting temperature of each material and the dashed line indicates the 40K operational margin from melting temperatures. All relevant parameters and their values for this set of simulations can be found in Table 5.

TABLE 5. Parameter Values to Test Startup Sequence.

Parameter	Variable or Constant	Value or Range
Hydrogen Start Time (sec)	Variable	0-1000
Drum Start Time (sec)	Constant	500
Hydrogen Flow (kg/s)	Constant	8
Drum Rotational Velocity (degrees/sec)	Constant	1

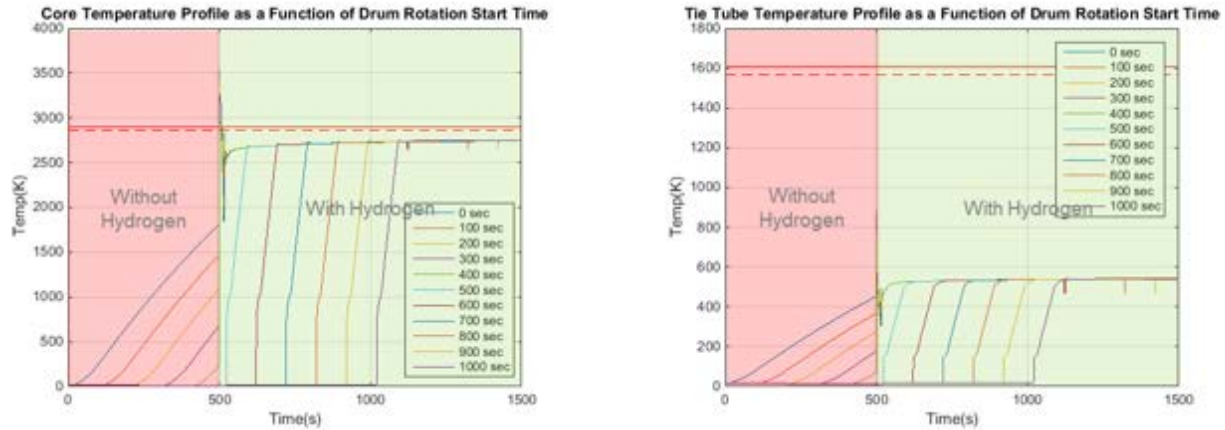


FIGURE 2. Core and tie tube temperature profiles due to varying drum rotation start times.

The pink-shaded region shows the area when the drums begin rotating before the hydrogen flow. At $t=500$ seconds, the hydrogen begins flowing. From there, the green-shaded region shows the area where the hydrogen flow starts before the drums begin to rotate. The graph on the left shows that when the drums begin rotating before the hydrogen flow begins, the core temperature exceeds the fuel melting temperature (simulations with start times from 0-400 seconds). However, on the right, the tie tube temperature does not exceed its melting point for any of the simulations. This is further illustrated below in Figure 3, which shows only the maximum temperature achieved for the core and tie tube for each of the 11 time-dependent profiles shown in Figure 2.

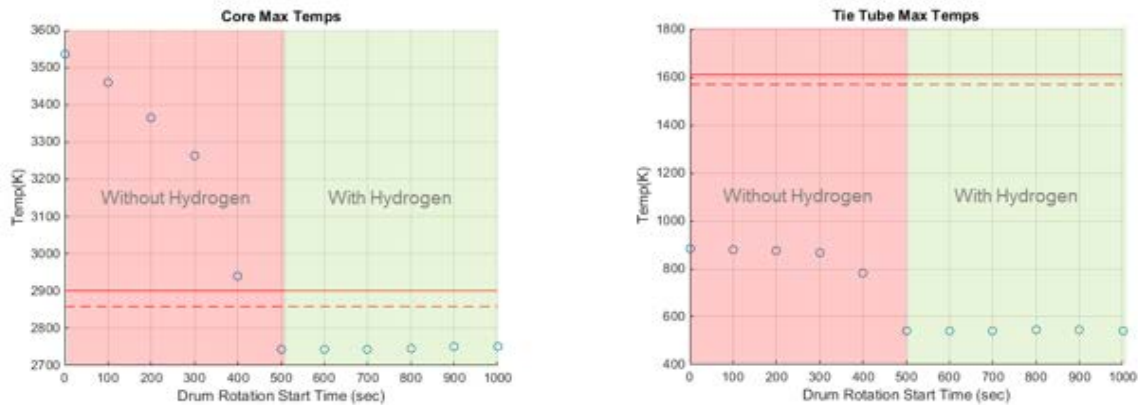


FIGURE 3. Reduced data of control drum rotation start time intervals showing maximum core and tie tube temperatures.

Hydrogen Flow

The next variable of interest that was tested was the hydrogen flow rate. Hydrogen acts as a coolant, moderator, and propellant for a thermal NTP system, Therefore, a high degree of understanding of the system response caused by hydrogen flow is crucial for ascertaining optimum performance of the system. To identify the effects of hydrogen flow on system performance the magnitude of flow was incrementally simulated from 1 - 20 kg/second in increments of 1 kg/second (twenty individual simulations). The reduced data set of maximum temperatures achieved in the core (left) and tie-tubes (right) is shown in Figure 4. It should be noted that all hydrogen flows are assumed to transition to full flow instantaneously in these simulations. All relevant variables and variable ranges for the hydrogen flow simulations may be found in Table 6.

TABLE 6. Parameter Values to Test Hydrogen Flow Rate.

Parameter	Variable or Constant	Value or Range
Hydrogen Start Time (sec)	Constant	0
Drum Start Time (sec)	Constant	0
Hydrogen Flow (kg/s)	Constant	1-20
Drum Rotational Velocity (degrees/sec)	Constant	1

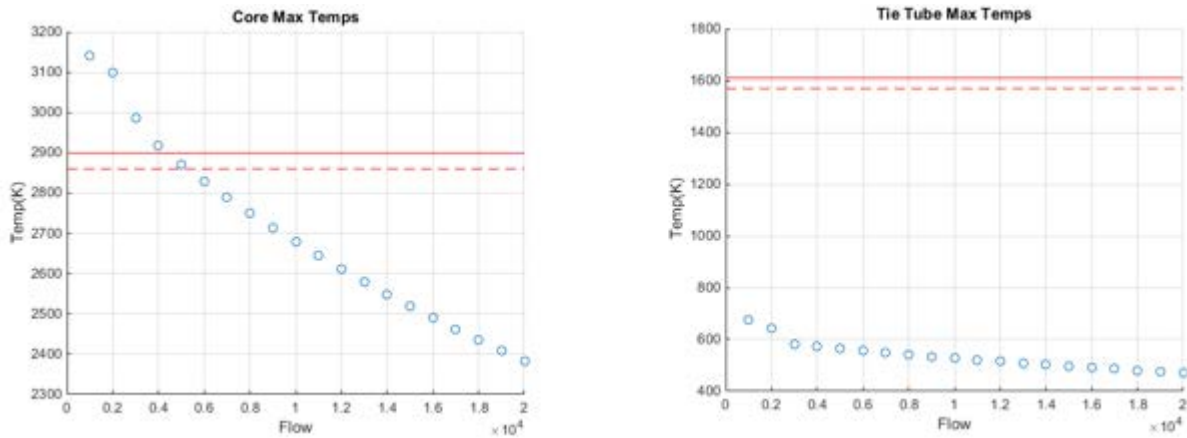


FIGURE 4. Reduced data sets of maximum core and tie tube temperatures as a function of flow rate.

Figure 4 shows that the flow must be above a value of ~6 kilograms per second to ensure that the core does not exceed its melting temperature. From these sets of graphs, it can be seen that the hydrogen flow rate must be equivalent to or exceed 6 kilograms/second in order to prevent the core from melting down.

Control Drum Rotation Speed

The final series of simulations that were performed involved varying the control drum rotation speed. Since neither the sequencing nor the hydrogen flow rate could control the temperature differentials, it was hoped that the control drum rotation speed would. It was found that for simulations of drum rotational speed between 0.1 – 2.1 degrees/second that no simulations exceeded the melting temperatures for the fuel or tie-tubes so these results are not presented here. However, the control drum rotational velocity does greatly affect the startup transient duration. The SNRE is designed to accelerate for only 20 minutes, therefore it is exceedingly important that the startup transient be no more than 10% of the total time, or 2 minutes. Slower ramp-up speeds, while conservative with temperature differentials, are extremely wasteful of the limited propellant volume so an optimum nominal rotational speed fast enough to be efficient yet slow enough not to cause thermal shock is desired.

Figure 5 illustrates that the control drum speed does have a significant influence on the temperature differentials, as evidenced by the linear trend that surpasses the thermal shock limits of the fuel around drum rotational velocities of ~0.7 degrees/second. These findings show it is necessary that the control drum rotational velocity be limited to less

than or equal to 0.7 degrees/second to avoid any thermal shock issues that can arise from extreme temperature differentials. Parameter values for all control drum rotation speed simulations are presented in Table 7.

TABLE 7. Parameter Values to Rest Control Drum Rotation Speed.

Parameter	Variable or Constant	Value or Range
Hydrogen Start Time (sec)	Constant	0
Drum Start Time (sec)	Constant	0
Hydrogen Flow (kg/s)	Constant	8
Drum Rotational Velocity (degrees/sec)	Constant	0.1-2.1

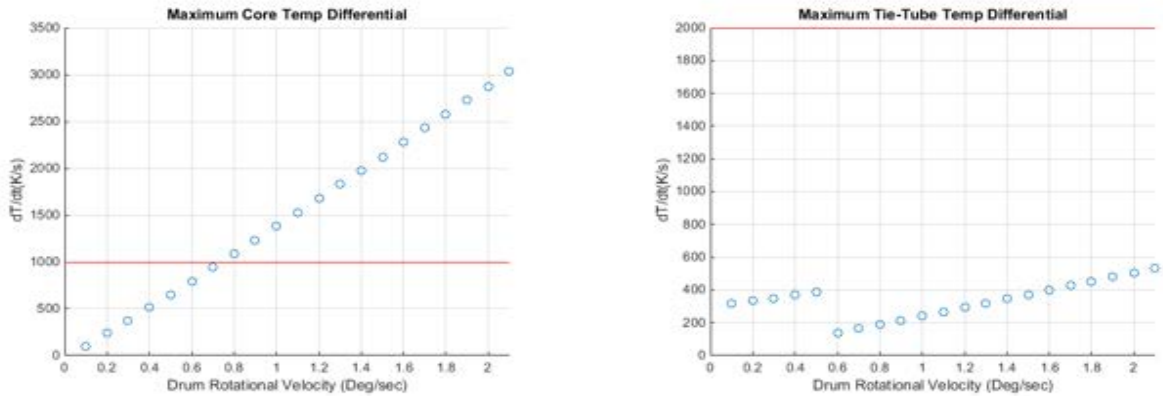


FIGURE 5. Maximum temperature differentials in the core and tie tubes as a function of drum rotational velocity.

CONCLUSION

The Simulink model developed is a preliminary first order approximation of an extremely complex process. The findings and methods presented in this paper serve only as recommendations for this specific model but may serve as a framework for future models attempting higher resolution simulations.

Future work may include an in-depth Monte Carlo analysis of the core to investigate variations in reactivity fluctuations caused by hydrogen insertion along with more precise heat deposition maps of the core and control drums. Other work would include more exhaustive fluid dynamics analysis using sophisticated computational fluid dynamics techniques. Furthermore, a computational and physical analysis of structural material must be developed to assess the effects of extreme temperatures, high hydrogen concentrations, thermal shock, vibrations, and material degradation due to extreme radiation exposure.

It was found that Simulink is a viable software package to model the point kinetics equations and simplified thermal hydraulic behavior of a dynamic SNRE system. The Simulink model and corresponding Matlab code offers an efficient way to rapidly conduct parametric studies on this NTP system to determine specific control requirements. From this model, a variety of simulations were run to determine the starting sequence, the hydrogen flow rate, and the control drum rotational velocity necessary to produce a safe and effective start-up of a moderated NTP system. Using data from these simulations along with known system requirements from past literature, a set of specific observations were developed for the SNRE system. These observations include:

1. The rotational velocity of the control drums should be limited to 0.7 degrees/second. This ensures that the temperature differentials are within an acceptable range and that the start-up transient takes up no more than 10% of the total assumed burn time of 20 minutes.

2. The nominal steady state flow rate of hydrogen through the system should be between 8 and 9 kilograms/second. This is in agreement with that reported for the SNRE and illustrates that the Simulink model is in reasonable agreement.
3. The hydrogen flow and the control drum rotation should be started at approximately the same time during the startup transient. This ensures that the core remains below the accepted limit of its marginal melting temperature.

The results and observations in this report are from preliminary and simplified analyses and do not reflect the needs of an actual NTP engine. This work points toward future work in which more detailed flow representation and higher fidelity models will be used. Specifically, the dynamic nature of the hydrogen in the system and its interaction in with core dynamics require a much more sophisticated modeling approach. This later work will inform the requirements for an eventual NTP instrumentation and control system.

REFERENCES

- [1] B. Schnitzler, "Neutronics Models and Analysis of the Small Nuclear Rocket Engine (SNRE)," presented at the 43rd AIAA/ASME/SAE/ASEE Joint Propulsion Conference & Exhibit, Cincinnati, OH, 2007.
- [2] J. B. Holt and T. S. Monk, "Propellant Mass Fraction Calculation Methodology for Launch Vehicles and Application to Ares Vehicles," NASA, Marshall Space Flight Center, Huntsville AL2009.
- [3] H. S. Nam and e. al., "Innovative concept for an ultra-small nuclear thermal rocket utilizing a new moderated reactor," Department of Nuclear and Quantum Engineering Korea Advanced Institute of Science and Technology, Republic of Korea, 2015.
- [4] M. E. M. Stewart and B. Schnitzler, "Multidisciplinary Simulation of Graphite-Composite and Cermet Fuel Elements for NTP Point of Departure Designs," presented at the AIAA Space 2015 Conference and Exposition, 2015.
- [5] B. Schnitzler, S. Borowski, and J. Fittje, "25,000-lbf Thrust Engine Options Based on the Small Nuclear Rocket Engine Design," presented at the 45th AIAA/ASME/SAE/ASEE Joint Propulsion Conference and Exhibit, Denver, 2009.
- [6] W. D. Kingery, H. K. Bowden, and D. R. Uhlmann, Introduction to Ceramics, 2nd ed. New York, NY: Wiley, 1976.
- [7] M. M. El-Wakil, "Nuclear heat transport," ed. Scranton Pa.: Scranton Pa. International Textbook Co.,1971.

Updated Mars Mission Architectures Featuring Nuclear Thermal Propulsion

Mitchell A. Rodriguez¹, Thomas K. Percy²

¹Jacobs Engineering Group, Jacobs ESSSA Group, Huntsville AL 35806

²NASA Marshall Space Flight Center, Huntsville AL 35812

Abstract. Nuclear thermal propulsion (NTP) can potentially enable routine human exploration of Mars and the solar system. By using nuclear fission instead of a chemical combustion process, and using hydrogen as the propellant, NTP systems promise rocket efficiencies roughly twice that of the best chemical rocket engines currently available. The most recent major Mars architecture study featuring NTP was the Design Reference Architecture 5.0 (DRA 5.0), performed in 2009. Currently, the predominant transportation options being considered are solar electric propulsion (SEP) and chemical propulsion; however, given NTP's capabilities, an updated architectural analysis is needed. This paper provides a top-level overview of several different architectures featuring updated NTP performance data. New architectures presented include a proposed update to the DRA 5.0, as well as an investigation of architectures based on the current Evolvable Mars Campaign (EMC), which is the focus of NASA's current analyses for the Journey to Mars. Architectures investigated leverage the latest information relating to NTP performance and design considerations, and address new support elements not available at the time of DRA 5.0, most notably the Orion crew module and the Space Launch System (SLS). The paper provides a top level quantitative comparison of key performance metrics, as well as a qualitative discussion of improvements and key challenges still to be addressed. Preliminary results indicate that the updated NTP architectures can significantly reduce the campaign mass, and subsequently, the costs for assembly and number of launches.

Keywords: Nuclear Thermal Propulsion, NTP, Architecture, Transportation, Mars.

INTRODUCTION

NTP has long been considered a leading contender for human exploration missions to Mars. Traditional chemical propulsion systems derive their thrust from the combustion of propellants and are, therefore, limited by the heat capacity, combustion temperatures, and physical properties of their combustion products. Electric propulsion, while offering significantly higher fuel efficiency in the form of high specific impulse, is limited in thrust requiring either megawatt-class power production or extremely long flight times to Mars. These limitations lead to either very large spacecraft assemblies or unacceptably long exposure to the deep space environment for human flights to Mars. Historically, NTP has been viewed as providing a desirable balance of thrust and specific impulse to support both acceptable flight times and manageable spacecraft sizes.

The physical challenges of a human journey to Mars are often coupled with programmatic challenges. For all proposed human Mars exploration plans, significant technology development is required, not only in transportation, but in many areas. These technology shortfalls result in significant projected development costs and extended timelines. They also introduce a significant amount of risk for the Mars program. This often leads those who propose human Mars exploration plans to attempt to strike a balance between performance and technology development. For a technology such as NTP, if this balance tips more towards affordability and reduced technology development, the proposers will often try to find ways to marginally improve lower performing transportation technology options rather than try to absorb what are traditionally perceived to be the more challenging technology programs associated with NTP.

NTP was most recently considered as a transportation alternative for human Mars exploration in NASA's DRA 5.0, published in 2009¹. This architecture considered both chemical propulsion and nuclear propulsion for use as human

Mars transportation systems, and presented the pros and cons of each option. In general, the findings supported previous claims that NTP would reduce spacecraft size and required number of heavy lift launches, but would require more technology development, at a higher price, when compared to an oxygen-hydrogen chemical propulsion architecture. These findings were consistent with many previous human Mars exploration studies, further supporting the notion that the question of NTP versus chemical propulsion is one of balancing technology development challenges with performance.

There are two recent developments of note on this front. The first is an example of the traditional approach to finding creative ways to improve the performance of transportation technologies that are perceived to be less technologically challenging than NTP. The most recent body of work completed by NASA on the topic of human Mars exploration is captured in the work of the EMC study team run out of NASA Headquarters². The transportation alternatives investigated in the EMC focused on the use of SEP to the greatest extent possible in order to increase the aggregate specific impulse of the Mars transportation systems, while supplementing this low thrust technology with high-thrust chemical propulsion where necessary to address the flight time issues associated with SEP^{3,4}. This represents the latest attempt to find creative ways to overcome the performance shortfalls of nearer-term transportation technologies as a way to side-step the technology developments associated with NTP.

The second development is a potential challenge to the traditional perceptions of NTP. At the same time that the EMC is attempting to redefine the human Mars architecture, a group of propulsion technologists from across the agency have been investigating the use of low enriched uranium (LEU) as the nuclear fuel for NTP reactors⁵. The use of LEU has the potential to shift the paradigm of NTP development and testing by reducing the regulation and oversight burden and making nuclear rockets easier to test. The overall programmatic impact is the reduction of the cost associated with NTP development which challenges the community's perception of the development cost and technical challenges. If these reductions are truly realized, NTP may be viewed more favorably for human Mars exploration.

Given these two recent developments, this paper provides an overview of a quick-look analysis of crew delivery to Mars in 2033 using NTP. This analysis combines some of the mission operations investigated in the EMC studies with the higher performance of the LEU NTP system. The results are compared to the DRA 5.0 NTP results to show differences derived from changes in the operational concept. The results are also compared to the latest EMC chemical propulsion crew delivery architectures to show impacts from the higher performance of the NTP system.

GROUND RULES & ASSUMPTIONS

This quick investigation was limited to a comparison of a crew transportation stack for Mars. A complete mission architecture for Mars exploration will also include delivery of cargo elements including a series of Mars landers however, this was beyond the scope of this preliminary investigation. The intent is to expand on the analysis outlined in this paper to include a complete look at both crew and cargo delivery for future publication. Therefore, this section will focus on the ground rules and assumptions for the crew stack. The proposed NTP crewed architecture will use a mission sequence similar to what was proposed in DRA 5.0, with a few changes leveraging lessons learned from the most recent EMC investigations. Like DRA 5.0, the NTP architecture will involve a single crew stack with three tanks; a core tank, an inline tank, and a drop tank.

The DRA 5.0 architecture performed aggregation in a 407 km circular low Earth orbit (LEO), whereas the EMC proposed aggregation orbits in cis-lunar space – specifically, lunar distant retrograde orbit (LDRO). In the former, the NTP system quickly becomes volume-limited due to the low density of liquid hydrogen. In the latter, individual elements are mass-limited based on the throw capacity of the SLS used to deploy to LDRO and the substantial mass of the NTP engine core. In the new architecture, the aggregation orbit is a high elliptical orbit (HEO). The range of the examined orbit sizes vary from 407 x 25,000 km to 407 x 350,000 km. In this situation, the NTP stack can avoid

the volume-limiting issues of a LEO aggregation, while also staying within the mass limitations of a conservative SLS launch payload profile.

For the purposes of this study, the 2033 Mars opportunity was selected as a test case for the NTP architecture. In the EMC, this 2033 mission is an orbital mission to Mars and is the first mission in the campaign to deliver humans to the Martian system. The mission sequence for the crew stack involves launching the engine and tanks to HEO, followed by the transit habitat and mission logistics payloads. The crew would then join the stack and begin a 30-day period of habitat commissioning and preparation operations in HEO. At the end of this 30-day period, the crew stack would initiate the trans-Mars injection (TMI) burn, setting it on a 231-day transfer to Mars. After the transfer, a Mars orbit insertion (MOI) burn is performed, to bring the stack into a 1-sol Martian orbit. This mission will be a long-stay mission, so the NTP crew stack would loiter in orbit around Mars for 538 days. At the end of the Mars stay, the trans-Earth injection (TEI) burn is performed, and a 198-day transfer follows. Finally, an Earth orbit insertion (EOI) burn is performed to capture into a HEO, after which a crew capsule from Earth rendezvous with the stack to take the crew and science samples home. Fig. 1 provides an overview this mission.

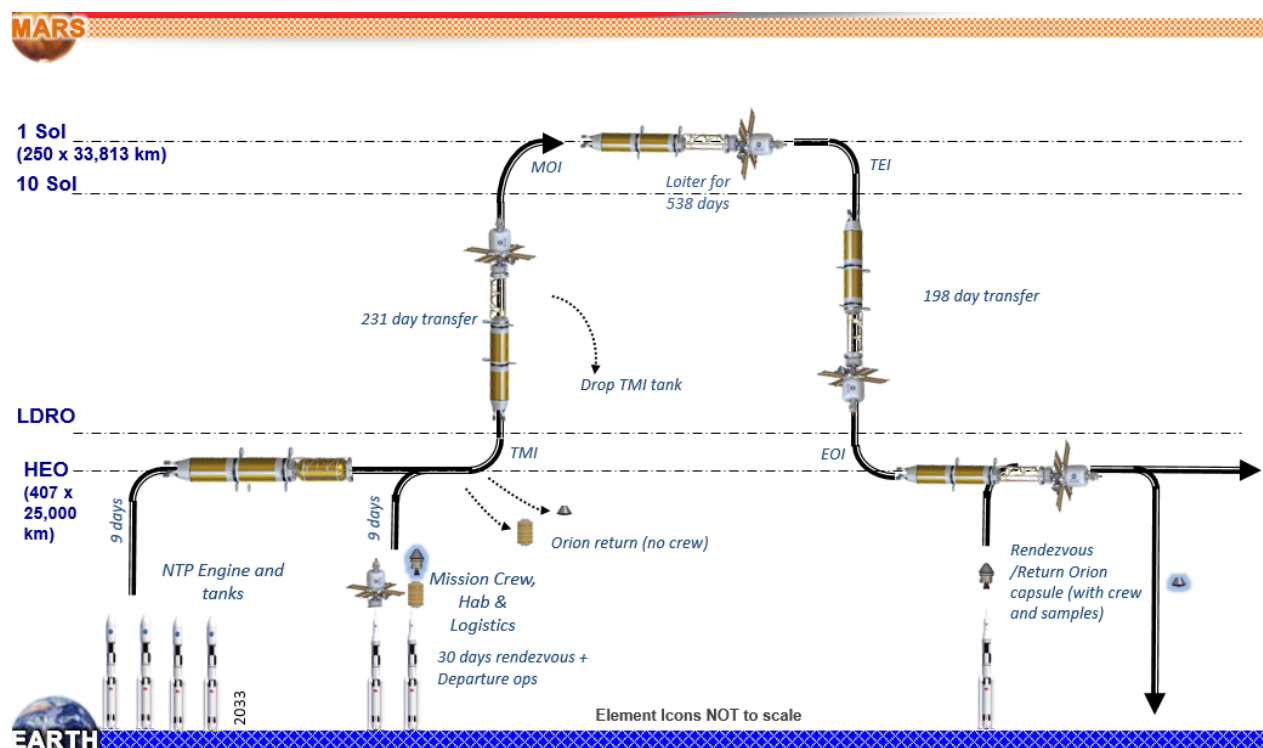


FIGURE 1. Bat chart for 2033 NTP Mars mission.

To provide context for the results comparison later in this paper, it is instructive to summarize the differences between the NTP architecture investigated in this analysis and the DRA 5.0 and EMC architectures. In comparing to the EMC, the most significant difference is the use of NTP which provides 540 seconds of additional specific impulse when compared to the oxygen-methane propulsion used in the EMC. Additionally, as discussed above, the aggregation point is in HEO rather than flying all elements all the way out to LDRO. For this analysis, the NTP architecture uses the same logistics and habitation modules that were developed under the EMC architecture so the payload delivery requirements are the same between both architectures. One notable operational change that has been introduced in the EMC is the concept of pre-deploying the Earth return propulsion for the crew flight. In the EMC architecture, the Earth return propulsion stages are delivered to Mars ahead of the crew using SEP cargo delivery vehicles. This reduces the size of the crew stack leaving Earth but introduces a new risk to the crew flight in that the crew must perform a rendezvous and dock sequence in Mars orbit to return home. The NTP architecture investigated in this paper does not

use this approach to reduce stack mass, choosing instead to take advantage of the higher performance of the NTP system to reduce crew risk.

In addition to the aggregation orbit difference between the NTP architecture and the DRA 5.0 reference, several other differences should be noted. First, the payload mass is approximately 15 mt less in the current architecture than in DRA 5.0. This is mostly due to the decision to not carry a crew capsule to Mars and back and, instead, perform a propulsive capture upon Earth return. This propulsive capture at Earth is another significant difference between the two architectures and is a carryover from the EMC. The Earth-Mars flight time and the Mars stay time for the current architecture are slightly longer than in DRA 5.0 which serves to reduce the MOI ΔV . The overall performance and design of the NTP systems are the same in both architectures. Differences in the performance metrics outlined below are a result of the combination of these differences and more work is planned in the future to isolate the contributions of each difference; however, this was not within the scope of the current effort.

RESULTS & CONCLUSION

The quick-look evaluation of an NTP crew delivery mission to Mars in 2033 provided two notable results. The first relates to the use of HEO aggregation orbits. Deep space exploration architectures that require multiple launches can take advantage of the capability of SLS to aggregate the mission elements in orbits with higher apogees than LEO. This balances the work load for climbing out of Earth’s gravity well between launch vehicle and in-space propulsion elements. The NTP architecture in DRA 5.0 was limited to aggregation in LEO which led to larger Earth departure ΔV requirements thus increasing the size of the propulsion elements on the crew stack. Figure 2 shows the benefits of increased apogee. As the apogee is increased, the TMI ΔV is reduced, thereby reducing the overall size of the crew stack. However, the SLS lift capability is also reduced with higher apogees. One observation to note is that at around 100,000 km apogee altitude, the number of SLS launches required for the stack aggregation increases from five to six. Therefore, it would be desirable to maintain an aggregation orbit with an apogee below this point. The stack mass reduction from an apogee of 25,000 km to 100,000 km is just under 60 mt, or roughly 25%, making this parameter a powerful tool for reducing overall launch mass.

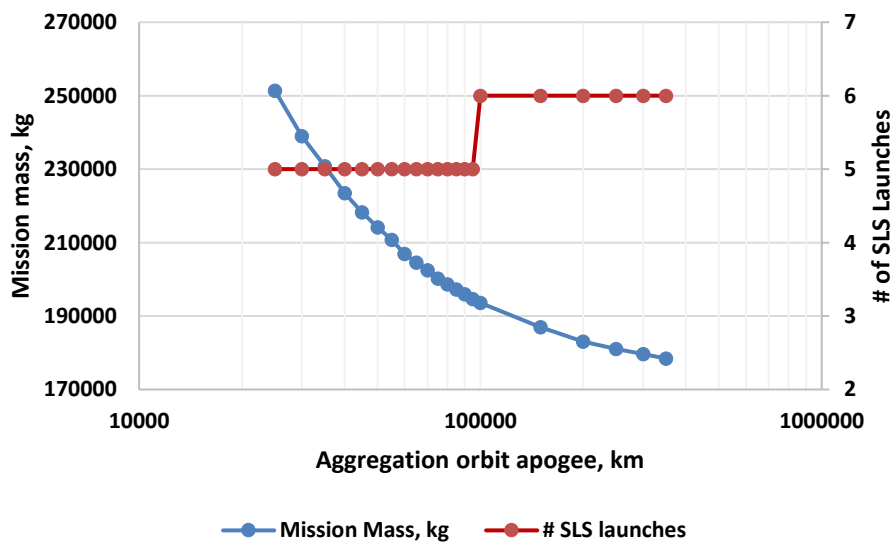
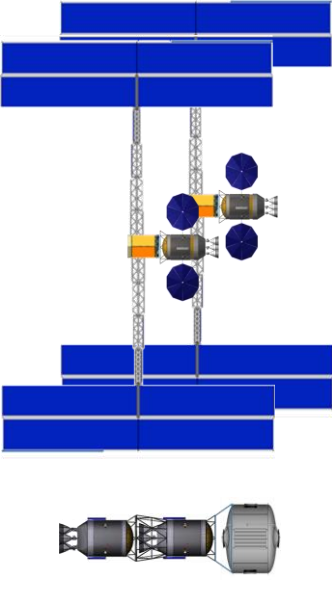


FIGURE 2. Crew stack mass and SLS launch count as a function of aggregation orbit.

The higher apogees provide both benefits and risks. A large range of potential HEO orbits for the architecture provides flexibility for other architecture elements in the crew stack, as well as flexibility in the launch cadence. However, there are several risks associated with HEO orbits. Elements parked in these HEO orbits must pass through the van Allen belts, exposing elements to elevated radiation dosages. If the perigee altitude of the orbit is below 2000 km, elements must also pass through the LEO debris fields which can pose a collision threat to aggregating crew stack components and may require additional deployment time to ensure that mission-critical events are being handled properly. Additional concerns include the handling of Mars injection windows, as the windows change significantly when the orbit becomes more elliptical (injection windows are decidedly more generous in a 407 km circular orbit or in LDRO, which DRA 5.0 and EMC support, respectively). Finally, one must also account for orbit station keeping in the propulsion budget for aggregated elements in the HEO orbits.

The second notable result from this quick-look investigation is how the newly proposed NTP architecture compares to previous proposed architectures, most notable the DRA 5.0 and EMC architectures. Table 1 shows a side-by-side comparison of the three crewed vehicle options.

TABLE 1. Comparison of DRA, EMC and proposed NTP options.

 <p style="text-align: center;">DRA 5.0 NTP</p>	 <p style="text-align: center;">EMC SEP/Chemical</p>	 <p style="text-align: center;">Proposed NTP</p>
Single stack	Pre-deployed return stack	Single stack
LEO aggregation	LDRO aggregation	HEO aggregation (varies)
5 Ares V launches	6 SLS launches	5-6 SLS launches (varies)
356.4 mt	270.1 mt	251.4 mt

In comparison to DRA 5.0, the results for the crew mass as a function of aggregation orbit show that even at the smallest-examined aggregation orbit, the updated HEO NTP crew stack is significantly less massive than the DRA 5.0. The maximum examined crew mass of 251.4 mt (see Figure 2) for a 407 x 25,000 km orbit is smaller than the DRA 5.0 mass of 356.4 mt by about 30%. A number of factors contribute to this mass reduction:

- 1) Lower payload mass – the DRA 5.0 payload is heavier by about 15 mt which affects the stack mass. This directly relates to the decision not to perform a direct entry upon Earth return, instead choosing to propulsively capture at Earth, which eliminates the need to carry a crew capsule to Mars and back.

- 2) Slower trajectory – DRA 5.0 uses a shorter trip time than the proposed alternative, so although the trip time is longer, the required ΔV is lower, which contributes to the reduced stack mass.
- 3) Higher aggregation orbit – DRA 5.0 uses a LEO aggregation orbit, which substantially increases the starting stack mass as more ΔV is required from the mission stack to leave Earth’s gravity well.

The resulting campaign crew mass for the 25,000 km apogee stack is lower than the 2033 mass for a split SEP-Chem crew stack of 270.1 mt, by about 8%. The mass decrease is affected (and tempered) by the following factors:

- 1) Higher Specific Impulse – NTP systems provide more than twice the specific impulse of the oxygen-methane stages in EMC, resulting in a lower stack mass.
- 2) A single-stack architecture versus split architecture –the EMC option requires a pre-deployment of return assets to Mars, which means that the outbound crew stack will be lighter.
- 3) Higher fixed mass – NTP engine cores are substantially heavier than chemical stages, so the fixed mass in the crew stack remains higher than the fixed mass in the EMC option (especially when one considers that the chemical stages are successively dropped after each burn, whereas the NTP core stage remains for the duration).

It is notable that even with the changes in mass, the number of heavy lift vehicle (HLV) launches are similar across all three architectures considered. Although an exact comparison cannot be made to DRA 5.0 with its use of the Ares V launcher, the similarities in launch count can be attributed to the tradeoff between supportable payload and aggregation orbit; the proposed NTP option has a lower mass, but the HEO aggregation orbit means that more ΔV is offloaded to SLS.

While this quick-look investigation is an instructive first step, more work will need to be completed to fully understand the benefits and potential challenges associated with the proposed NTP architecture. Future work would involve addressing several of the issues discussed above. In particular, a comparison of injection windows as a function of HEO apogees should be examined. Optimizing the orbit apogee to minimize the issues associated with Van Allen belt exposure, as well as debris field risks, should also be pursued.

Additional work is also planned which will focus on the entire campaign instead of a single mission. This will involve a more in-depth sensitivity analysis of the various assumptions in DRA 5.0 and EMC to isolate their individual impacts on key parameters. These assumptions range from the trajectory profiles and mission timelines, to the payload masses and assembly details (aggregation orbit, assembly timeline, etc.). This will help to identify the sensitive areas in the mission architectures for DRA 5.0 and EMC, and thus provide the insights needed to help improve the performance and reduce the costs of the proposed NTP HEO option. While more work is required to gain a full understanding of the impact that NTP can have on a Mars exploration campaign such as the EMC, this quick-look comparison does show some promising results that would favor continued investment in NTP technologies with an eye toward human exploration of the solar system.

REFERENCES

- [1] Drake, Bret, (ed.), “Human Exploration of Mars Design Reference Architecture 5.0.” NASA SP-2009-566, July, 2009.
- [2] Craig, D., Troutman, P., and Hermann, N. “Pioneering Space Through the Evolvable Mars Campaign.” AIAA Space 2015, AIAA-2015-4409, Pasadena, CA, 2015.
- [3] Percy, T. P., McGuire, M., and Polsgrove, T. “In-Space Transportation for NASA’s Evolvable Mars Campaign.” AIAA Space 2015, AIAA-2015-4519, Pasadena, CA, 2015.

- [4] Merrill, R.G., Chai, P., Jones, C.A., Komar, D.R., and Qu, M. "An Integrated Hybrid Transportation Architecture for Human Mars Expeditions." AIAA Space 2105, AIAA-2015-4442, Pasadena, CA, 2015.
- [5] Houts, M.G., Mitchell, D.P., et al. (2015) "NASA's Nuclear Thermal Propulsion Project." AIAA/SAE/ASEE Joint Propulsion Conference, July 2015, Orlando, FL.

Zirconium – Rates of Reaction for a Common Getter Material

Christofer E. Whiting¹, Chadwick D. Barklay¹, and David F. Woerner²

¹Research Institute, University of Dayton, 300 College Park, Dayton, OH 45469

²Jet Propulsion Laboratory/California Institute of Technology, 4800 Oak Grove Drive, Pasadena, CA 91107
937-229-2570; chris.whiting@udri.udayton.edu

Abstract. Zirconium can be added to a spacecraft system to getter (i.e., consume) potentially reactive gas species before they can interact with other sensitive materials. Typical processing techniques can minimize most reactive gas species, but some, like water, can be so pervasive and persistent that they are nearly impossible to completely eliminate. The role of a getter, therefore, is to act as a sacrificial material and consume any residual reactive species before they have an opportunity to interact with other sensitive components. This means that a getter needs to provide a mechanism for removing a reactive gas species that is both fast and thermodynamically favorable. While the thermodynamic reactivity of zirconium is well-documented, the reaction rates of zirconium under a variety of conditions are not as well-understood.

Zirconium getters in palladium coffins were placed within a reaction chamber and allowed to react with a controlled atmosphere at 630 °C. Composition of the gas phase was quantitatively monitored as a function of time, and reaction rates were calculated. Reaction rates for these palladium encapsulated zirconium getters were measured for water, hydrogen, and methane. The reaction rate for hydrogen was observed to be first-order with respect to the quantity of hydrogen and the surface area of the zirconium. The presence of gas phase water and surface oxide appear to interfere with the reaction between zirconium and hydrogen, causing the reaction rate to slow down. The reaction rate for water was observed to be first-order with respect to the quantity of water and the surface area of zirconium. No interferences with the reaction between water and zirconium were noted. The reaction rate for methane was observed to be first-order with respect to the quantity of methane. In general, the reaction rates for these species are, in descending order: hydrogen, water, and methane. The difference in these rate constants are large enough that in some cases it may be possible to make the assumption that hydrogen will be completely removed by the getter before significant quantities of water can react; and both hydrogen and water will be completely removed before significant quantities of methane can react.

Keywords: Zirconium, palladium, getter, reaction rate

INTRODUCTION

Zirconium and zirconium-based alloys are commonly used as getters for oxygen, water, hydrogen, methane, nitrogen, carbon monoxide, and carbon dioxide [1-4]. The thermodynamics and kinetics of a zirconium getter tend to improve at higher temperature for all of these species except for hydrogen. Zirconium is a better getter for hydrogen at lower temperatures. At high temperatures, gas phase hydrogen and zirconium reach a chemical equilibrium [3,4]. In addition, if the hydrogen in the gas phase is removed or consumed by another material, the zirconium, in order to maintain the chemical equilibrium, will release hydrogen it had previously gettered back into the gas phase [1-3]. This is why systems that are required to getter hydrogen as well as other species are frequently designed with 2 zirconium getters: a hot getter for all the species except hydrogen, and a “cold” getter for the hydrogen. As an example, Cárdenas, *et al.* suggest that to effectively remove both hydrogen and methane from a helium gas stream requires one zirconium alloy getter at 200 °C for hydrogen and another at ≥ 400 °C for methane [1].

Because zirconium metal is so reactive, contact with other materials may be enough to induce a reaction. Even materials that are considered to be highly stable, such as alumina, are capable of reacting with zirconium metal at high temperatures. In order to eliminate these contact based reactions, it is common to encapsulate zirconium in a noble metal, such as palladium. As a result, this report will test the fundamental reaction rates for palladium encapsulated zirconium as a potential getter for spacecraft components.

EXPERIMENTAL

Testing Apparatus

Figure 1 presents a schematic of the apparatus that was used to perform the reaction rate studies. Briefly, the reaction and water tubes were constructed out of 5.08 cm o.d. high purity alumina that were inserted into cylindrical furnaces. The furnaces were separately controlled via temperature controllers. Control thermocouples were placed in contact with the tube at the center of the furnace. High temperature silicone o-ring based compression flanges were attached to the ends of the tube to provide a leak tight ceramic-to-metal transition. Stainless steel tubing with compression fittings were used to connect the flanges to the other system features, including: a vacuum pump, UHP argon, and the various reagent gases used for calibration and reaction. A series of needle valves were used to isolate and control gas flow in all portions of the apparatus. Digital pressure gauges were inserted into the stainless steel lines to monitor the pressure inside the alumina tubes. A 0.16 cm o.d. sampling line was tapped into the metal face of the compression flange to allow the residual gas analyzer (RGA) to continuously sample the contents of the reaction tube. When experimental test conditions required water concentrations that exceeded the vapor pressure of water at room temperature, heating tape was added to the system to keep all four compression flanges, RGA sampling lines, and the stainless steel transfer tubing at ≥ 120 °C.

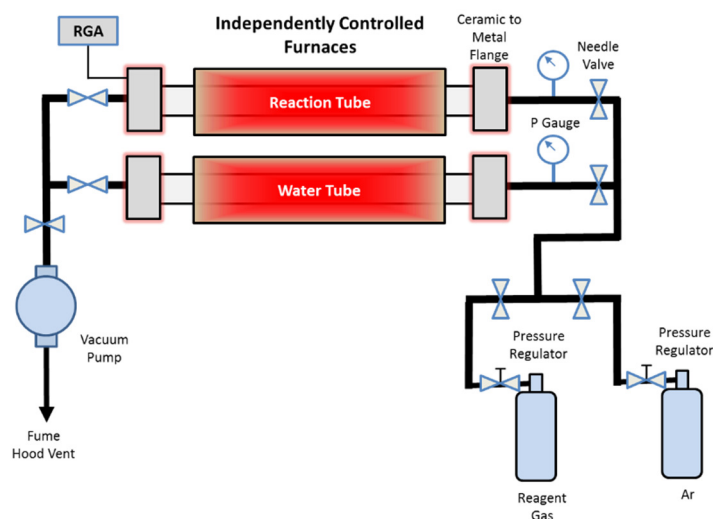


FIGURE 1. Schematic of the Apparatus Used to Perform the Zirconium Getter Experiments

Materials

High purity zirconium metal (99.9+%) was placed into palladium coffins constructed out of high purity 0.1 mm foil (99.9+%). Zirconium surface areas were obtained from a geometric calculation of the metal used in the experiment. Reagent gases of water (460 ppm_v), hydrogen (4.98%), and methane (1.96%) were obtained as certified standards in argon. The hydrogen and methane standards were used as both a calibration gas for the RGA and as a reagent for the gettering reactions. The water standard was used for calibration purposes only.

Powdered Microtherm Super-G insulation was used as the water source in most of these experiments. According to the manufacturer, this insulation typically has 1-2% adsorbed moisture, by mass. In an attempt to keep the amount of moisture uniform between experiments, the powdered insulation was pretreated in a humidity chamber for 4 h at 65

°C and 95% humidity. After pre-treatment, the powdered insulation was stored in a humidity chamber at room temperature (~21 °C) with 100% humidity.

Methods

Atmospheres with specific water contents were typically generated by placing a measured quantity of powdered Microtherm Super-G into the water tube. The amount of Microtherm used varied depending on the desired starting concentration of water. If standard experimental procedures were followed, 1.00 g of pretreated Microtherm in the water tube produced an atmosphere with ~15 000 ppm_v (1.5%) water in the reaction tube.

Standard procedures were as follows. A zirconium getter was encapsulated in a palladium coffin and placed in the center of the reaction tube. Powdered Microtherm was placed in a high purity alumina boat in the center of the water tube. The specific quantity of Microtherm was dependent on the desired experimental conditions. After sealing both tubes, they were evacuated and filled with UHP argon 4 times at room temperature. The tubes were then filled with UHP argon to nominally 108 kPa. The water tube was then heated to 650 °C while the reaction tube was heated to 630 °C. After these temperatures were obtained, a 15 min hold was applied to assure that the moisture was fully desorbed from the Microtherm. Then, UHP argon was added to the water tube to increase the pressure to 225 kPa, and the reaction tube was evacuated. The water tube and reaction tube were then opened to each other and the pressures were allowed to equilibrate, which resulted in a reaction tube pressure of ~110 kPa. UHP argon was then added to the reaction tube to obtain a final tube pressure of 138 ± 1 kPa.

For experiments that contained a mixture of water with hydrogen or methane, the water atmosphere was generated by the standard procedure, and the final pressurization of the reaction tube with UHP argon was replaced by a final pressurization with the reagent gas (i.e., either the methane or hydrogen standard). For experiments that contained only methane or hydrogen, the water tube was not utilized. Instead, the reaction tube was pressurized directly with the reagent gas and UHP argon to obtain the desired concentrations.

Some experiments were performed that contained nominally 20% (v/v) water. In these experiments, ~0.25 mL of liquid deionized water was placed into the alumina boat in the center of the water tube. The water tube was evacuated and filled twice. All four compression flanges, RGA sampling lines, and transfer tubing were also wrapped in heating tape and heated to ≥ 120 °C. Standard procedures were followed in every other regard for these 20% experiments.

RESULTS AND DISCUSSION

Gettering Rate for Water

Figure 2 presents an example of typical data obtained from a getter experiment that contains just gas phase water. Figure 2 (left) presents the concentration vs. time data while (right) is a first-order rate law plot of the data. The rate law plot clearly shows that the reaction rate is first-order with respect to the partial pressure of water.

It is interesting to note that Figure 2 (right) shows that at about 2 500 ppm_v (i.e., $\ln[\text{H}_2\text{O}] \sim 7.8$), the rate law plot starts to curve slightly, indicating a change in mechanism. This phenomenon can be observed at approximately the same concentration in every water containing experiment, regardless of the conditions of the experiment. The change in mechanism was observed when the getter was used, new, larger/smaller, broken into 2 pieces and in the same coffin, broken into 2 pieces and in separate coffins, and multiple full getter assemblies. The curvature is also observed in the four experiments where the initial water concentration was near or below 2 500 ppm_v (2 680, 2 610, 1 090, and 460 ppm_v). Figure 3 presents a first-order rate law plot obtained from the 2 610 ppm_v experiment, and it shows that the rate is slower and exhibits gradual curvature over the whole experiment. In addition, the typical rate of change observed in Figure 3 is similar to the rates of change observed later in Figure 2 (right). The consistency of this effect across all experiments helps to indicate that the change in the rate limiting step is not due to water, the properties of the zirconium getter, or the properties of the palladium. As a result, it is concluded that the origin of this change in rate at low water concentrations is due to the specific characteristics of the instrument. The fact that the second reaction rate appears to be limited by the instrument means this is not a fundamental change in the chemical reaction, and that the fundamental rate between water and a palladium encapsulated zirconium getter should be considered constant across all concentrations.

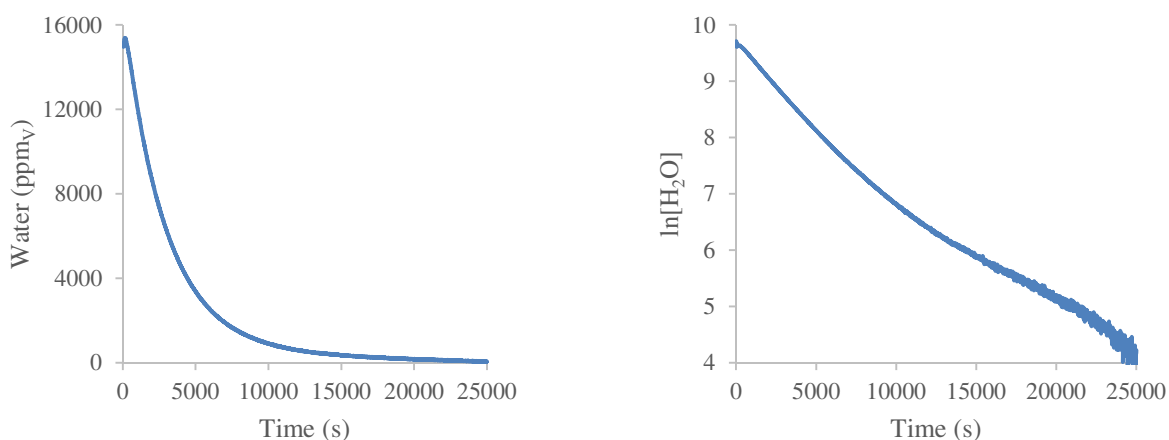


FIGURE 2. Typical gettering rate data for water. (Left) Concentration vs. time. (Right) First-order rate law plot.

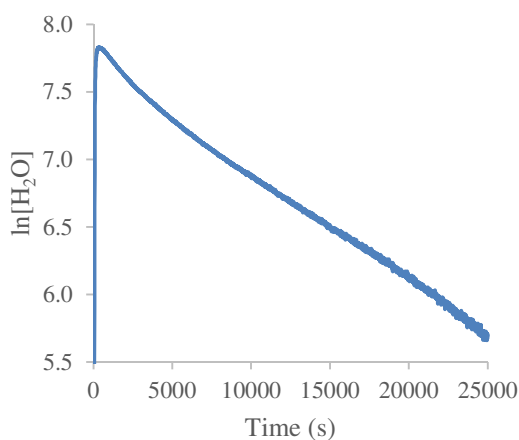


FIGURE 3. First-order rate law plot obtained from an experiment containing 2 610 ppm_v water showing that the experiment was under the effect of the slower, instrument-driven mechanism that dominates below ~2 500 ppm_v.

Table 1 presents the rate data from the experiments that contained gas phase water, except for the four experiments with initial concentrations near or below 2500 ppm_v. Those experiments are not included in Table 1 because the rate data was confounded by the change in rate mechanism discussed previously. The first column of rate constant data (k') considered the rate to have a first-order dependence on the concentration of water. The second column of rate constant data (k) considered the rate to have a first-order dependence on both the concentration of water and the zirconium surface area. Data in Table 1 is presented using the same order of magnitude factor for ease of comparison.

Table 1 shows that when an experiment is performed using 2 full getter assemblies, the rate constant that was not dependent on surface area (i.e., k') approximately doubled. This suggests that the reaction rate also has a first-order dependence on the zirconium surface area. When the rate constant is considered to be first-order with respect to the concentration of water and zirconium surface area, the data shows that the reaction rate is constant with an average $k = 4.33 \pm 0.13 \times 10^{-5} \text{ cm}^2 \text{ s}^{-1}$. This results in the following rate law: $\text{Rate} = (4.33 \times 10^{-5} \text{ cm}^2 \text{ s}^{-1}) * [\text{H}_2\text{O}] * \text{SA}$, where the water term can be in any concentration (or pressure) units and the SA term is in cm^2 .

Table 1 also presents the data for an experiment with 153 000 ppm_v water (0.211 bar). While the results from the early portion of the experiment appear to indicate that the reaction rate is faster, there were some challenges in obtaining an accurate measurement of this experiment. A notable pressure drop was observed in the tube during the early portion of the experiment. At 153 000 ppm_v, the gas phase water represents a significant portion of the pressure in the tube, which means the pressure in the tube will drop considerably as the getter consumes the water.

Unfortunately, the tube pressure has a significant effect on the RGA signal, which means that the signal was decreasing as a function of total tube pressure. If the reaction rate is analyzed late in the reaction (i.e., between 8 000 and 15 000 s), after most of the water has already reacted (i.e., much slower pressure drop), the resulting rate constant is similar to the rate constants obtained in other water experiments. This information suggests that the rate constant for the gettering of water is unchanged at higher concentrations, such as 153 000 ppm_v (0.211 bar).

TABLE 1. Gettering rate data for water.

Getter Configuration	Getter ID ^A	Initial [H ₂ O] (ppm _v)	Other Gases (ppm _v)	k' (x10 ⁻⁵ s ⁻¹) ^B	k (x10 ⁻⁵ cm ⁻² s ⁻¹) ^C
Standard	4	10 600	--	29.1	4.39
Standard	4	10 100	--	28.5	4.30
Standard	5	6 900	--	31.1	4.49
Standard	5	4 790	--	29.1	4.20
Standard	6	15 900	--	31.0	4.35
Standard	7	12 300	--	30.0	4.47
Activated	2	24 800	--	30.3	4.20
2 Full Getter Assemblies	6&8	25 100	--	61.3	4.47
Broken in 2 Pieces 1 Coffin	6	48 500	--	35.7	4.35
Broken in 2 Pieces 2 Coffins	6 (w Box 8)	3 360	--	33.5	4.09
Standard	0	153 000 (early)	--	39.2	5.72
Standard	0	153 000 (late) ^D	--	30.0	4.38
Standard	8	26 100	10 000 (CH ₄)	37.0	5.59

^A When the same getter is used in multiple experiments, the order is presented sequentially in the table.

^B Rate constant that does not consider the effect of surface area

^C Rate constant that does consider the first-order effect of surface area

^D Rate data taken between 8 000 and 15 000 s

Data from Table 1 makes it possible to conclude that, in regards to the gettering rate of water, the palladium surface area has no direct effect on the rate. This is supported by the fact that the rate constants produced by a getter broken into two pieces in a single coffin compared to the same two pieces in two different coffins were both statistically similar to the average rate constant. While it may still be possible that the palladium is playing an important role in the overall gettering mechanism (e.g., providing a catalytic pathway for the dissociation of water into hydrogen and oxygen), the palladium does not play a role in the actual rate limiting step. This means that the palladium can be treated as invisible for the purposes of understanding the gettering rate for water.

Experiments that were performed with both water and methane produced rate constants that were slightly higher than the rate constant for just water. This is due to the fact that water will also react with methane to form carbon monoxide and hydrogen. Evidence of this reaction is observed in Figure 4, which presents the observed quantities of carbon monoxide and methane during a control experiment (i.e., no getter). Figure 4 presents the methane and carbon monoxide quantities as a function of time. The slopes of these two data sets are similar in magnitude but opposite in sign, suggesting that the carbon monoxide produced in this control experiment is due to the reaction of methane with water. Signals for O₂ and CO₂ produced a concentration of zero for those species over the course of the experiment. The small difference in the magnitude of the slopes in Figure 4 is most likely due to the RGA sampling line pulling enough gas out of the reaction tube over the experiment – ~10% over 25 000 s – to cause a notable pressure drop. A slow pressure decrease over time like that causes negative slopes to appear slightly more negative and positive slopes to be slightly less positive, which is observed in Figure 4.

The loss of methane is also very slow, with a change in concentration of only 1 450 ppm_v over 25 000 s (6.9 h), which is comparable to the increase in the rate of reaction for water. This information seems to suggest that the increased reaction rate observed during the water and methane experiment is due to the water-methane chemical reaction. If the reaction rate for water is only being increased by the water-methane gas phase reaction, it suggests that methane does not change the fundamental water reaction rate.

In addition to the major conclusions presented above, the Getter ID column in Table 1 can be used to show that the same getter can be used for multiple experiments without effecting the rate. This implies that the getter reaction with water is quite robust, and that any changes in the getter due to the consumption of oxygen or hydrogen atoms from the water do not impact the reaction rate. Similarly, one getter was “activated” by heating the zirconium up to 1000

°C in vacuum for 1 h, and this getter produced the same rate constant as the other non-activated getters. The process of activation is nominally performed to help dissolve oxygen at the surface of the zirconium getter and improve the activity of the getter. The fact that repeated use of the same getter and the process of “activation” do not change the reaction rate with water implies that the experimental temperature (630 °C) is high enough to readily solubilize oxygen and hydrogen in the zirconium matrix and that the incorporation of hydrogen and/or oxygen into the zirconium will not reduce the reaction rate with water.

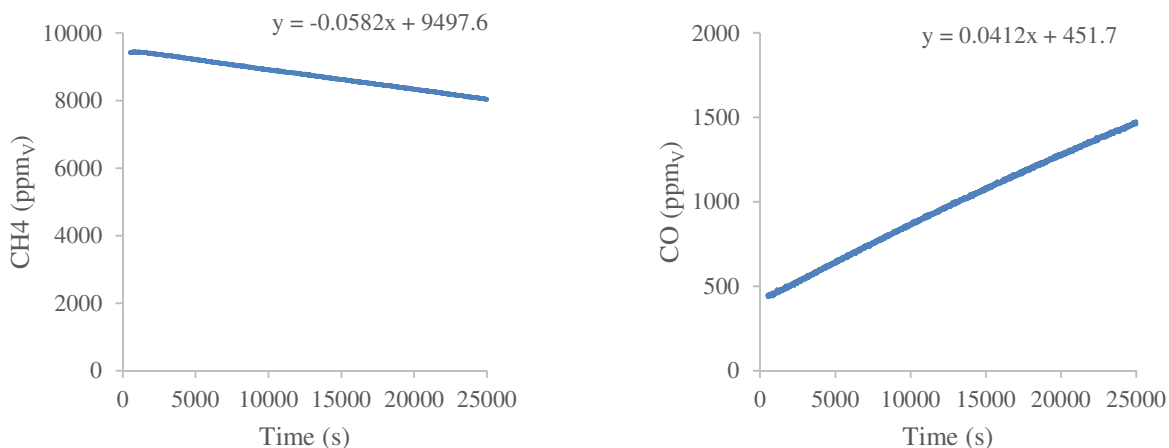


FIGURE 4. Control experiment between nominally 20 000 ppmv water and 10 000 ppmv methane showing a complimentary consumption of methane and in-growth of carbon monoxide over time.

Gettering Rate for Hydrogen

Figure 5 presents the results from a typical hydrogen gettering experiment. The rates are clearly very fast and first-order with respect to the quantity of hydrogen.

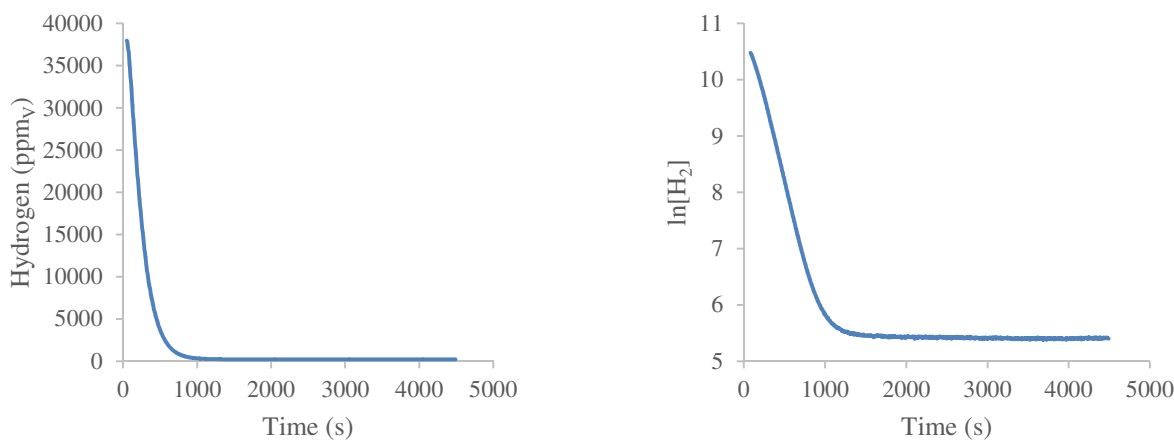


FIGURE 5. Typical gettering rate data for hydrogen in the presence of palladium encapsulated zirconium. (Left) Concentration vs. time. (Right) First-order rate law plot.

Table 2 presents the data obtained during the hydrogen gettering experiments. All of the experiments were performed on the same getter assembly/sample, and the experiments were performed in order from the top to bottom of Table 2. The first column of hydrogen rate constant data is presented as k' (i.e., first-order with respect to concentration). The second column of hydrogen rate constant data is presented as k (i.e., first-order with respect to concentration and zirconium surface area). The rate constant data for water is presented as k . All rate data in Table 2 uses the same order of magnitude factor for ease of comparison.

Data from Table 2 shows that, compared to water, the reaction of hydrogen with the getter is more complex. The first two experiments show that repeat experiments with an atmosphere of 49 800 ppm_v hydrogen produce essentially the same first-order rate constant. This suggests that the gettering of hydrogen does not significantly impact the ability of the getter to consume more hydrogen. However, when the same getter was then exposed to atmospheres containing water, the reaction rates for hydrogen appear to change. In the third experiment with this getter assembly, the experimental atmosphere contained 9040 ppm_v water. During subsequent experiments (i.e., the fifth experiment), the gettering rate of hydrogen appears to decrease significantly. This seems to imply that oxidation of the zirconium surface inhibits the reaction with hydrogen.

TABLE 2. Gettering rate data for hydrogen.

Getter Configuration	Initial [H ₂] (ppm _v)	Initial [H ₂ O] (ppm _v)	Hydrogen		Water k (x10 ⁻⁵ cm ² s ⁻¹)	H ₂ Baseline (ppm _v)
			k' (x10 ⁻⁵ s ⁻¹)	k (x10 ⁻⁵ cm ² s ⁻¹)		
Standard	49800	--	589	76.5		223
Standard	49800	--	585	75.9		257
Standard	--	9040	--	--	4.54	--
Standard	11500	12600	251	32.6	4.74	296
Standard	49800	--	483	62.7		318
Broken in 2 Pieces 1 Coffin	49800	--	572	74.3		335

Water also appears to directly interfere with the hydrogen reaction rate. This can be observed during the fourth experiment in Table 2, which contained 12 600 ppm_v water and 11 500 ppm_v hydrogen. In this fourth experiment, the rate of hydrogen consumption dropped by more than 50%. This decrease is large enough that the consumption of oxygen from water, and the subsequent production of hydrogen, cannot explain this change. This strongly suggests that the water is somehow interfering with hydrogen-getter reaction.

These results suggest that both the presence of water and the oxide can interfere with the hydrogen gettering reaction. It is interesting to note that the more significant inhibitor appears to be gas phase water. Determining the exact mechanism that causes the gettering of hydrogen to change in the presence of water and/or a surface oxide would be challenging and is beyond the current scope of this work.

It is also interesting to note that the gettering rate of water does not appear to be inhibited by hydrogen. In the third experiment, the getter was exposed to 9040 ppm_v of water with no hydrogen, and the rate was approximately the same as for samples that were not exposed to significant quantities of hydrogen (c.f., Table 1). In the fourth experiment, the getter was exposed to both water and hydrogen, and the water consumption rate was still approximately the same. This strongly suggests that the reaction rate of water is not affected by hydrogen in the atmosphere or in the getter.

The gettering rate for hydrogen also appears to be very fast. Even when it is inhibited by the presence of water, the reaction rate of hydrogen is almost an order of magnitude faster than the reaction rate of water. This is beneficial because it may allow users to make the simplifying assumption that the rate for hydrogen is fast enough that it will essentially react with the getter instantaneously compared to the rate for water.

Another interesting observation for the hydrogen experiments is that the quantity of hydrogen in the gas phase appears to reach a stable baseline at a value that is around 200-300 ppm_v. Table 2 also suggests that as the getter consumes more hydrogen, the amount of equilibrium gas phase hydrogen increases. These results are corroborated by literature reports that indicate that a hot zirconium-based getter will reach an equilibrium with gas phase hydrogen [3,4]. Previous reports on the gettering activity of zirconium and hydrogen suggest that the zirconium will act as a hydrogen “battery.” This means that the zirconium will attempt to keep a constant level of hydrogen in the gas phase. If that hydrogen is consumed by, or reacts with, another material, then the zirconium will release more hydrogen into the gas phase. As a result, it is possible that all of the hydrogen consumed by the zirconium could be available to react with other materials.

Gettering Rate for Methane

Of the three chemicals studied here, the gettering rates for methane appear to be the most complex. Figure 6 presents typical rate data for the consumption of methane, and it becomes immediately apparent that the rate of reaction is extremely slow. Over 60% of the methane is still present after 7 hours of reaction time.

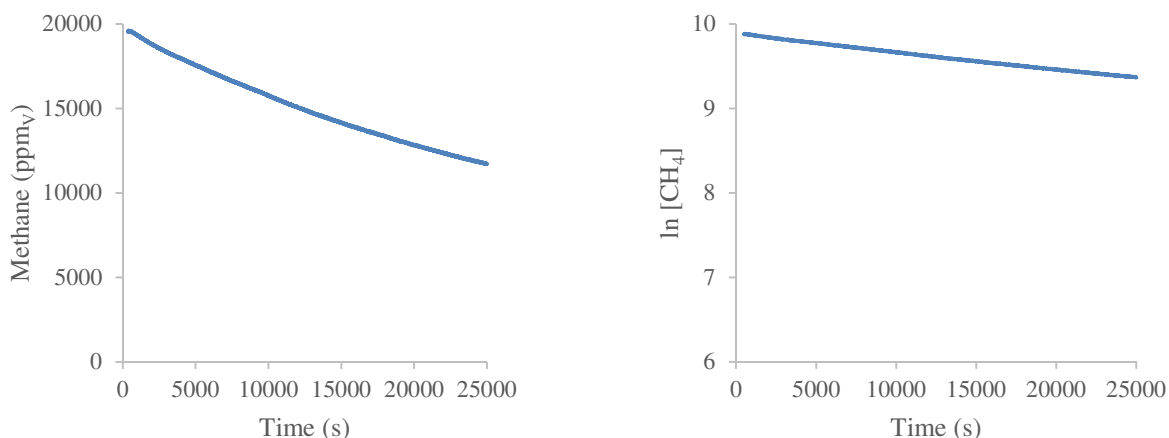


FIGURE 6. Typical gettering rate data for methane in the presence of a palladium encapsulated zirconium getter. (Left) Concentration vs. time. (Right) First-order rate law plot.

Table 3 presents the first-order rate law data from the methane experiments with no regard to the effect of the getter surface area. In other words, the rate data in Table 3 is presented as k' . While it is likely that the methane rate will also be dependent on the surface area of the getter, the only experiment that was performed with a different surface area had some significant complications. Since, there is no direct experimental evidence showing a dependence on the surface area, the rate constant data was not adjusted to account for the getter surface area. Therefore, when comparing the methane data to other data, it is important to compare k' values.

TABLE 3. Gettering rate data for methane.

Getter Configuration	Getter ID	Initial [CH ₄] (ppm _v)	Initial [H ₂ O] (ppm _v)	Early Rate k' ($\times 10^{-5} s^{-1}$)	Late Rate k' ($\times 10^{-5} s^{-1}$)	Previous Getter Exposure
Standard	3	19600	--	2.09	Same	Nothing
Broken in 2 Pieces 1 Coffin	3	19600	--	1.12	Same	Methane
Standard	8	8850	26100	10.2	2.41	Water
Standard	7	10800	27200	5.57	1.99	Water

The first experiment listed in Table 3 presents a methane reaction that was performed on a fresh getter. The second experiment listed in Table 3 was performed using the same getter, except in this experiment the getter was broken into 2 pieces in order to increase the surface area. Interestingly, the second experiment was slower than the first experiment. This suggests that the getter underwent a significant change during the first reaction with methane, and altered the ability for the getter to react with more methane. Literature reports indicate that the gettering of methane can leave behind carbon at the surface of the getter [1]. This can create an issue if the reaction temperature is not high enough to cause the carbon to rapidly diffuse into the zirconium. In this case, the carbon/carbide at the surface of the zirconium can cause the rate of reaction for the getter to be slowed down. While this observation seems to be supported by the literature, some of the data presented here seems to conflict with that conclusion. This conflict is primarily supported by the fact that the methane reaction rate appears first-order over the entire experiment (Figure 6). A first-order reaction cannot adequately explain a reaction that is both consuming methane and causing a change in the getter that further changes the reaction rate. Given this stability observed over the course of the first experiment, why does the second experiment suddenly produce a rate constant that is ~50% smaller? This conflict of the data makes it difficult to draw strong conclusions.

Table 3 also shows that when water and methane are mixed, the reaction rate for methane increases. This is most likely due to the fact that, as discussed previously, methane and water react. The increase in k' for water (c.f., Table 1) is approximately the same as the increase in k' for methane (c.f., Table 3), which suggests that that the increase in

reaction rates for water and methane are due to the gas phase water-methane reaction. Since the increase in methane consumption can be explained by the reaction with water, it is possible to conclude that the presence of water does not influence the fundamental methane gettering rate.

Due to the complexities caused by trying to analyze rate data that is the result of 2 different reaction (i.e., methane-water and methane-getter), the data for the methane and water experiments was analyzed both early (i.e., < 10 000 s) and late (i.e., > 17 000 s) in the experiment. Analyzing the early data produced results that are difficult to draw strong conclusions from, but analyzing the late data produced results that were similar to the methane-getter reaction without the presence of water. During the late portion of the experiment, the amount of water present was small (i.e., < 750 ppm_v), which will cause the methane-water reaction to become very slow and have minimal impact on the overall rate. Therefore, rate constants obtained from the late portion of the experiment should produce results that are due solely on the fundamental methane reaction rate.

Results from the late experiments are reasonably similar to results obtained from fresh getters, which suggests that the build-up of surface oxide due to the reaction with water does not have a strong impact on the methane reaction rate. This conclusion is corroborated by the fact that both getters used in the methane-water reactions had been exposed to water previously, and they still produce methane reaction rate data that is similar to an unused getter.

Data in Table 3 shows that, when compared to the water-getter reaction, the rate constant for just the methane-getter reaction is over an order of magnitude smaller. This is beneficial because it may allow users to make the simplifying assumption that the rates of consumption for water and hydrogen are both fast enough that they will essentially react with the getter instantaneously compared to the rate for methane.

CONCLUSIONS

Reaction rates were measured between a palladium encapsulated zirconium getter and water, hydrogen, and methane. Results indicate that the reaction with hydrogen is much faster than the reaction with water; and the reaction with water is much faster than the reaction with methane. These observations may allow for the following approximations to be made: the reaction with hydrogen will be complete before a significant quantity of water is allowed to react, and the reaction with water will be complete before a significant quantity of methane is allowed to react.

Reaction rates for the gettering of water were observed to have a first-order dependence on the surface area of the zirconium and the partial pressure of water. These features were observed to be constant across all water partial pressures, which included a maximum partial pressure value of 0.211 bar. Replicate experiments with water also did not affect the reaction rate, suggesting that the experimental temperature of 630 °C is high enough to make sure the surface of the zirconium remains “activated.” A gas phase reaction between methane and water was observed that caused both chemicals to be consumed and produce carbon monoxide. It was also observed that neither hydrogen nor methane had any impact on the fundamental reaction rate of water. When the concentration of water dropped to ~2500 ppm_v, the observed change in water concentration became dominated by a new mechanism that appears to be an artifact of the properties of the instrument. The low concentration mechanism is not expected to impact the fundamental reaction rate.

Reaction rates for the gettering of hydrogen were observed to have a first-order dependence on the surface area of zirconium and the partial pressure of hydrogen. Both gas phase water and the presence of a zirconium oxide surface layer appear to cause the hydrogen reaction to slow down, but repeat experiments with hydrogen do not appear to impact the reaction rate. Upon completion of the hydrogen reactions, about 200-300 ppm_v hydrogen remained in the gas phase.

Reaction rates for the gettering of methane were observed to have a first-order dependence on the partial pressure of methane. Data analyzing the effect of zirconium surface area on the reaction rate were inconclusive. Data analyzing the effect of repeat experiments with methane were also inconclusive. A gas phase reaction between methane and water was observed. However, the presence of water does not appear to affect the fundamental methane getter reaction rate.

ACKNOWLEDGMENTS

The authors would like to thank the Jet Propulsion Laboratory and the National Aeronautics and Space Administration Radioisotope Power Systems Office for funding this work. The authors would also like to acknowledge the U.S. Department of Energy and Aerojet Rocketdyne for supplying the zirconium metal. The University of Dayton was funded through subcontract #: 1517709.

REFERENCES

- [1] Cárdenas, R.E., Stewart, K.D., and Cowgill, D.F., "Gettering of hydrogen and methane from a helium gas mixture," *J. Vac. Sci. Technol. A*, **32**, 060602-5 (2014).
- [2] Nigrey, P.J., "An Issue Paper on the Use of Hydrogen Getters in Transportation Packaging," *Sandia National Laboratories*, SAND2000-0483, Albuquerque, NM (2000).
- [3] Albrecht, H., Kuhnes, U., and Asel, W., "Application of SAES and HWT gas purifiers for the removal of impurities from helium-hydrogen gas mixtures," *J. Less-Common Met.*, **172-174**, 1157-1167 (1991).
- [4] Kherani, N.P., Shmayda, W.T., and Jalbert, R.A., "Tritium Removal from Inert Gases using ST 198 Alloy," *CFFTP*, CFFTP-G-88039, Mississauga, Ontario, Canada (1998).

Robust Exploration and Commercial Missions to the Moon Using NTR / LANTR Propulsion and Lunar-Derived Propellants

Stanley K. Borowski¹, Stephen W. Ryan¹, Laura M. Burke^{1,2},
David R. McCurdy², James E. Fittje², and Claude R. Joyner³

¹NASA Glenn Research Center, Cleveland, OH 44135

²Vantage Partners, LLC at Glenn Research Center, Brook Park, OH 44142

³Aerojet Rocketdyne, West Palm Beach, FL 33410

telephone: (216) 977-7091, email: Stanley.K.Borowski@nasa.gov

Abstract. The nuclear thermal rocket (NTR) has frequently been identified as a key space asset required for the human exploration of Mars. This proven technology can also provide the affordable “access through cislunar space” necessary for commercial development and sustained human presence on the Moon. In his “post-Apollo” Integrated Space Program Plan (1970–1990), Wernher von Braun, proposed a reusable nuclear thermal propulsion stage (NTPS) to deliver cargo and crew to the Moon to establish a lunar base before undertaking human missions to Mars. The NTR option was selected by von Braun because it was a demonstrated technology capable of generating both high thrust and high specific impulse ($I_{sp} \sim 900$ s) – twice that of today’s best chemical rockets. In NASA’s Mars Design Reference Architecture (DRA) 5.0 study, the crewed Mars transfer vehicle used three 25 klb_f “Pewee” engines – the smallest and highest performing engine tested in the Rover program – along with graphite composite fuel. Smaller lunar transfer vehicles – consisting of a NTPS using three ~16.5 klb_f “Small Nuclear Rocket Engines (SNREs)”, an in-line propellant tank, plus the payload – can enable a variety of reusable lunar missions. These include cargo delivery and crewed lunar landing missions. Even weeklong “tourism” missions carrying passengers into lunar orbit for a day of sightseeing and picture taking are possible. The NTR can play an important role in the next phase of lunar exploration and development by providing an affordable in-space lunar transportation system (LTS) that can allow initial outposts to evolve into settlements supported by a variety of commercial activities such as in-situ propellant production used to supply strategically located propellant depots and transportation nodes. The utilization of iron-oxide (FeO)-rich volcanic glass or lunar polar ice (LPI) deposits (each estimated at billions of metric tons) for propellant production can reduce the launch mass requirements from Earth and can enable reusable, surface-based lunar landing vehicles (LLVs) using liquid oxygen/hydrogen (LO₂/LH₂) chemical rocket engines. Afterwards, LO₂/LH₂ propellant depots can be established in lunar equatorial and polar orbits to supply the LTS. At this point a modified version of the conventional NTR – called the LO₂-augmented NTR, or LANTR – would be introduced into the LTS allowing bipropellant operation and leveraging the mission benefits of refueling with lunar-derived propellants for Earth return. The bipropellant LANTR engine utilizes the large divergent section of its nozzle as an “afterburner” into which oxygen is injected and supersonically combusted with nuclear preheated hydrogen emerging from the engine’s choked sonic throat—essentially “scramjet propulsion in reverse.” By varying the oxygen-to-hydrogen mixture ratio, LANTR engines can operate over a range of thrust and I_{sp} values while the reactor core power level remains relatively constant. Eventually, a LANTR-based LTS can enable a rapid “commuter” shuttle with “one-way” trip times to and from the Moon on the order of 36 hours or less. Even if only 1% of the extracted propellant from identified volcanic glass and polar ice deposits were available for use in lunar orbit, such a supply could support daily commuter flights to the Moon for many thousands of years! An evolutionary mission architecture is outlined and a variety of lunar missions and transfer vehicle designs are examined, along with the increasing demands on propellant production as mission complexity increases. A comparison of vehicle features and engine operating characteristics, for both NTR and LANTR engines, is also provided along with a brief discussion on the propellant production issues associated with using volcanic glass and LPI as source material.

Keywords: NTR, LANTR, Lunar-Derived Propellant

INTRODUCTION AND BACKGROUND

Today there is considerable discussion within NASA, the Congress and industry regarding the future direction and focus of the United States' human space program. According to NASA, the direction and focus is a "Journey to Mars" [1] sometime around the mid-to-late 2030's. While NASA's sights are set on Mars, there is another destination of greater interest to the worldwide space community – the Moon. Located just 3 days from Earth, the Moon is an entire world awaiting exploration, future settlement and potential commercialization. It has abundant resources and is an ideal location to test and demonstrate key technologies and systems (e.g., surface habitation, long-range pressurized rovers, surface power and resource extraction systems) that will allow people to explore, work, and live self-sufficiently on another planetary surface. Lunar missions also provide a unique proving ground to demonstrate another important in-space technology – Nuclear Thermal Propulsion (NTP). Essential for human missions to Mars, high performance NTP can play an important role in "*returning humans to the Moon to stay*" by providing an affordable in-space LTS that can allow initial lunar outposts to evolve into permanent settlements engaged in and supported by a variety of commercial activities [2,3].

Despite NASA's "been there, done that" attitude towards the Moon, a human lunar return mission has a strong appeal to many others who would like to see humans again walk on its surface and to whom the Apollo program has become a distant memory. Plans for human surface missions and settlements on the Moon in the 2025 – 2030 timeframe are being openly discussed by Europe, China, and Russia [4,5,6]. A number of private companies in the United States – Bigelow Aerospace [7], Shackleton Energy Company (SEC) [8], and most recently, the United Launch Alliance (ULA) in their "Cislunar-1000" plan [9] – are also discussing possible commercial ventures to the Moon during this same time period.

Lunar-derived propellant (LDP) production – specifically lunar-derived liquid oxygen (LLO₂) and liquid hydrogen (LLH₂) – offers significant mission leverage and are central themes of both SEC's and ULA's plans for commercial lunar development. Samples returned from different sites on the Moon during the Apollo missions have shown that the lunar regolith has a significant oxygen content. Discovered on the final Apollo (17) mission, FeO-rich volcanic glass beads have turned out to be a particularly attractive source material for oxygen extraction [10]. Subsequent lunar probe missions have provided data indicating the possible existence of large quantities of water ice trapped in deep, permanently shadowed craters located at the Moon's poles [11]. If this resource is accessible and can be extracted economically, then it would provide a valuable source of both LLO₂ and LLH₂.

Besides LDPs, an efficient, proven propulsion technology with reuse potential is also important to ensure affordable "access through cislunar space." The NTR is that technology. It generates both high thrust and high specific impulse ($I_{sp} \sim 900$ s) – twice that of today's highest performing LO₂/LH₂ chemical rockets – but it is essentially a mono-propellant engine using only LH₂ to maintain the reactor fuel elements at their required operating temperature. The heated hydrogen gas exiting the reactor is then exhausted out the engine's nozzle to generate thrust. A key question then is *How can the high performance of the NTR and the leverage potential of LDP best be exploited?* The answer is the "*LO₂-Augmented*" NTR (or LANTR) – a LH₂-cooled NTR outfitted with an O₂ "*afterburner nozzle*" and feed system [12,13,14]. LANTR combines NTR and supersonic combustion ramjet engine technologies. The result is a versatile high performance engine that allows "bipropellant" operation and a robust nuclear LTS with unique capabilities that can take full advantage of the mission leverage provided by using LDPs.

In light of the current interest in LDPs [8,9,15], and as part of its ongoing efforts to quantify the benefits of using NTP for future lunar missions, GRC has been examining the unique mission capabilities that may be possible by infusing LANTR propulsion into a nuclear-powered LTS that utilizes LDPs. This paper provides a brief summary of our initial analysis results to date and touches on the following topics. First, the benefits and options for using LDPs are discussed along with the production issues associated with using volcanic glass and LPI as source material. Next, a system description of the NTR and the LANTR concept are presented along with performance projections for the engine as a function of the oxygen-to-hydrogen (O/H) mixture ratio (MR) used in the afterburner nozzle. An evolutionary mission architecture with assumptions is then outlined and the benefits of using LDP in terms of reduced vehicle size, launch mass and engine burn time are quantified. A sampling of different missions, lunar transfer vehicle (LTV) types, and transit times is then presented, along with the associated LDP refueling needs as the mission complexity and ΔV requirements increase.

BENEFITS AND OPTIONS FOR USING LUNAR-DERIVED PROPELLANTS

Previous studies conducted by NASA and its contractors [16,17] have indicated a substantial benefit from using lunar-derived propellants – specifically LLO₂ in the lunar space transportation system. In a LTS using LO₂/LH₂ chemical rockets, ~6 kilograms (kg) of mass in low Earth orbit (LEO) is required to place 1 kg of payload on the lunar surface (LS). Of this 6 kg, ~70% (4.2 kg) is propellant and ~85.7% of this mass (3.6 kg) is oxygen assuming the engines operate with an O/H MR of 6:1. Since the cost of placing a kilogram of mass on the LS is ~6 times the cost of delivering it to LEO [18], the ability to produce and utilize LLO₂ from processed lunar regolith, or LLO₂ and LLH₂ from the electrolysis of LPI deposits, can provide a significant mission benefit. Providing LLO₂ and LLH₂ for use in fuel cells, life support systems and the chemical rocket engines used on LLVs, allows “higher value” cargo (people, manufacturing and scientific equipment, etc.) to be transported to LEO and on to the Moon instead of bulk propellant mass.

Samples brought back on the Apollo missions have shown that oxygen is abundant in the lunar regolith (~43% by mass) and can be extracted from the mineral “ilmenite (FeOTiO₂)” or from “FeO-rich” orange and black volcanic glass beads, discovered on the Apollo 17 mission to Taurus-Littrow [19], using the hydrogen reduction process. The process produces water that is then electrolyzed to obtain oxygen and hydrogen – a portion of which is recycled back as the catalyst. Reduction experiments conducted at the Johnson Space Center [20,10] have shown the glassy (orange) and crystalline (black) beads to be an attractive feedstock producing oxygen yields up to 4.7wt%. They are fine grained (see Figure 1) and can be fed directly into a LLO₂ production plant with little or no processing prior to reduction. More importantly, vast deposits of these volcanic glass beads have been identified at a number of candidate sites on the lunar nearside including Mare Serenitatis (close to the Taurus-Littrow landing site), Mare Vaporum, Rima Bode, and Sinus Aestuum [21]. At the southeastern edge of Mare Serenitatis alone, it is estimated the existing pyroclastic deposits could produce well in excess of 2 billion metric tons (t; 1 t = 1000 kg) of LLO₂. The estimated total power (in kW_e) to produce LLO₂ from volcanic glass is ~21 x LLO₂ production rate (in kg/hr) [12].

Recently, the Clementine, Lunar Prospector [11], and Chandrayaan-1 [22] lunar probe missions have provided data indicating the possible existence of large quantities of water ice (estimated at 100’s of millions to billions of metric tons) trapped in deep, permanently shadowed craters located at the Moon’s poles (shown in Figure 1). Lunar polar ice deposits are important because the recovered water can supply both oxygen and hydrogen (at a ratio of 8:1), assuming the deposits can be economically accessed, mined, processed and stored for their desired use.

Higher ΔV budgets are required to access lunar polar orbit (LPO) sites and the candidate craters are deep and extremely cold (~50 K / -370 F) posing major challenges for mining and processing these cold ice-bearing materials [23]. Concepts have been proposed to excavate and extract LPI-derived water [24] a portion of which would be electrolyzed on the Moon to supply ascent/descent propellant to “water tanker” LLVs that would deliver the remaining water resource to an orbiting propellant depot for electrolysis and storage there. The required electrolysis cell input power (in kW_e) is ~4.9 x H₂O electrolysis rate (in kg/hr). The quantities of LDPs needed and the total power requirements (for mining, H₂O separation and electrolysis) will depend on the mission type and frequency.

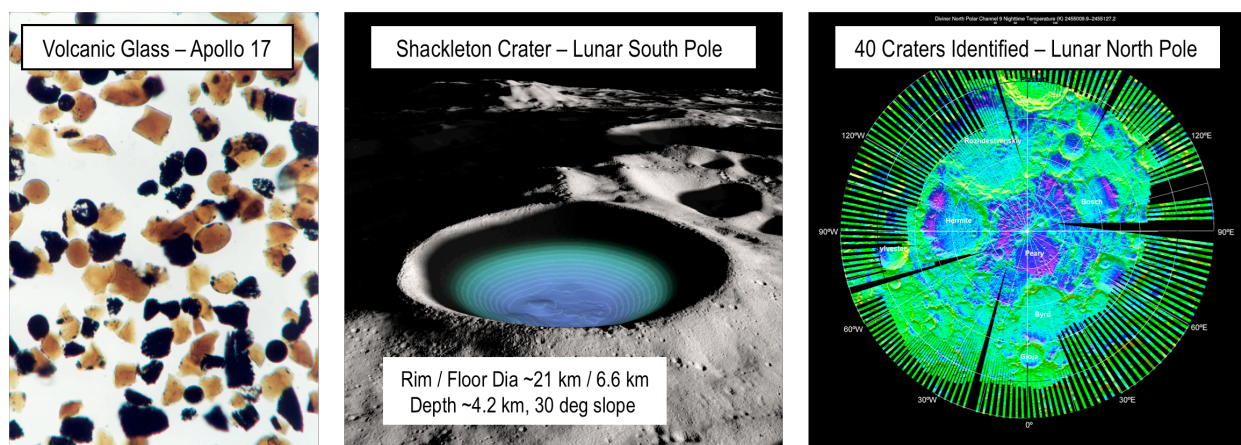


FIGURE 1. Volcanic Glass Feedstock and Candidate Craters for LPI Deposits at the Lunar South and North Poles

NTR / LANTR SYSTEM DESCRIPTION AND PERFORMANCE CHARACTERISTICS

The NTR uses a compact fission reactor core containing “enriched” uranium (U)-235 fuel to generate 100’s of megawatts of thermal power (MW_t) required to heat the LH_2 propellant to high exhaust temperatures for rocket thrust [25]. In an “expander cycle” engine (Figure 2), high pressure LH_2 flowing from a turbopump assembly (TPA) is split into two paths with the first cooling the engine’s nozzle, pressure vessel, neutron reflector, and control drums, and the second path cooling the engine’s core support tie-tube assemblies. The flows are then merged and the heated H_2 gas is used to drive the TPAs. The hydrogen turbine exhaust is then routed back into the reactor pressure vessel and through the internal radiation shield and upper core support plate before entering the coolant channels in the reactor’s fuel elements. Here it absorbs energy produced from the fission of U-235 atoms, is superheated to high exhaust temperatures ($T_{ex} \sim 2700$ K or more depending on the uranium fuel loading), then expanded out a high area ratio nozzle ($\sim 300:1$) for thrust generation. Multiple control drums, located in the reflector region surrounding the reactor core, regulate the neutron population and reactor power level over the NTR’s operational lifetime.

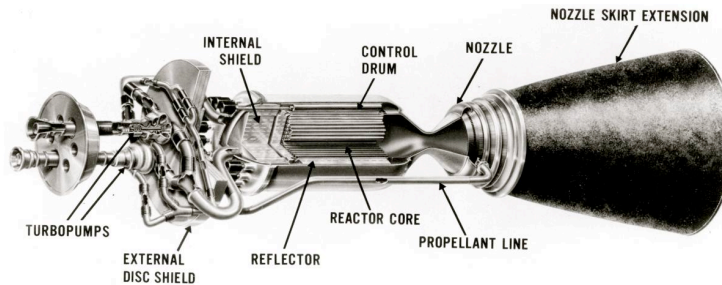


FIGURE 2. Schematic of “Expander Cycle” NTR Engine with Dual LH_2 Turbopumps

Recent studies showing the benefits of NTP for a variety of exploration and commercial lunar missions [2,3] have used a “common” NTPS employing a 3-engine cluster of SNREs. Each SNRE has a power output of ~ 365 MW_t and produces ~ 16.5 klb_f of thrust. Its graphite composite fuel operates at a peak temperature of ~ 2860 K and the corresponding hydrogen exhaust temperature is ~ 2734 K. With a chamber pressure of 1000 psia, a hydrogen flow rate of ~ 8.30 kg/s and a nozzle area ratio (NAR) of $\sim 300:1$, the engine’s I_{sp} is ~ 900 s. The total engine length and nozzle exit diameter are ~ 5.8 m and ~ 1.53 m, respectively, and the engine’s thrust-to-weight ratio is ~ 3.02 . Additional reactor and engine parameters for the updated SNRE are found in Reference [3].

In order to take full advantage of available LDPs, each SNRE is outfitted with an O_2 “afterburner” nozzle containing the O_2 injectors and an O_2 feed system. The oxygen is stored as a cryogenic liquid at low pressure and must be pressurized and gasified prior to its injection into the nozzle. This is accomplished by diverting a small fraction of the engine’s hydrogen flow ($\sim 3\%$) to an oxidizer-rich gas generator that drives a LO_2 TPA used to deliver the gasified LO_2 to injectors positioned inside the afterburner nozzle downstream of the throat [13,14]. Here it mixes with the hot H_2 and undergoes supersonic combustion adding both mass and chemical energy to the rocket exhaust. Transitioning to “LANTR mode” operation has many advantages. It provides a variable thrust and I_{sp} capability (shown in Table 1), shortens engine burn times, extends engine life and allows bipropellant operation.

TABLE 1. SNRE / LANTR Performance Characteristics as a Function of O/H Mixture Ratio

O/H Mixture Ratio	0	1	2	3	4	5
Delivered I_{sp} (s)	900**	725	637	588	552	516
Thrust Augmentation Factor	1.0	1.611	2.123	2.616	3.066	3.441
Thrust (lb_f)	16,500	26,587	35,026	43,165	50,587	56,779
Engine Mass (lb_m)	5,462	5,677	5,834	5,987	6,139	6,295
Engine T/W	3.02	4.68	6.00	7.21	8.24	9.02

** Fuel Exit / Hydrogen Exhaust Temperature = 2734 K, Chamber Pressure = 1000 psia and NAR = 300 to 1

EVOLUTIONARY NUCLEAR LTS ARCHITECTURE AND RESULTS

The enhanced mission capability resulting from the combined use of LANTR propulsion and LLO₂ was quantified and reported on [12] by GRC more than 20 years ago. At that time the primary LDP and source material considered was LLO₂ and volcanic glass, and only Earth-supplied LH₂ was used. An evolutionary LTS was analyzed focused on using high performance NTP to maximize delivered surface payload (PL) on each mission. The increased PL was dedicated to installing modular LLO₂ production units with the intent of supplying LLO₂ to surfaced-based LLVs initially, then to the in-space LTVs at the earliest possible opportunity. This assessment re-examines this evolutionary nuclear LTS architecture and expands it to also include the use of LPI as the source material.

Figure 3 shows the variation in LTV size, initial mass in low Earth orbit (IMLEO), increased mission capability and engine burn time resulting from the development and utilization of LLO₂. Figure 3a shows a fully reusable nuclear LTV (NLTV) for a crewed lunar landing mission that departs from LEO (407 km) and captures into a 300 km altitude equatorial low lunar orbit (LLO). The NLTV consists of three elements: (1) a common NTPS with three SNRE-class engines; (2) an in-line LH₂ tank; and (3) the PL element. The NTPS and in-line element use a common propellant tank (~15.7 m in length) that carries ~39.7 t of LH₂. The PL element includes the *Orion* multi-purpose crew vehicle (MPCV) carrying 4 crewmembers, a single stage LLV carrying two 2.5 t PL pallets, plus a saddle truss that connects the forward PL element to the rest of the NLTV. At the end of the mission, the NLTV returns to Earth carrying the spent LLV and captures into a 24-hr elliptical Earth orbit (EEO) that has a lower ΔV requirement. In order to return to LEO, the NLTV's IMLEO would nearly double to ~347.8 t!

The first significant step in LDP production occurs when lunar outpost assets and LLO₂ production levels become sufficient to support a lunar surface-based LLV. By not having to transport a “wet” LLV to LLO on each flight, the NLTV now has a lower starting mass in LEO plus sufficient onboard propellant to return to a lower, higher energy EEO as shown in Figure 3b. As LDP production increases further and LLO₂ becomes available in LLO, from either a tanker LLV or from an evolving propellant depot, the NLTV's SNREs are outfitted with LO₂ feed systems and afterburner nozzles and the large in-line LH₂ tank is replaced by a smaller LO₂ tank (shown in Figure 3c). Using only Earth-supplied LH₂ but refueling with ~47 t of LLO₂, the NLTV is now able to return to LEO. Also because of optimized LANTR operation utilized during the round trip mission, the total engine burn time is cut in half as well.

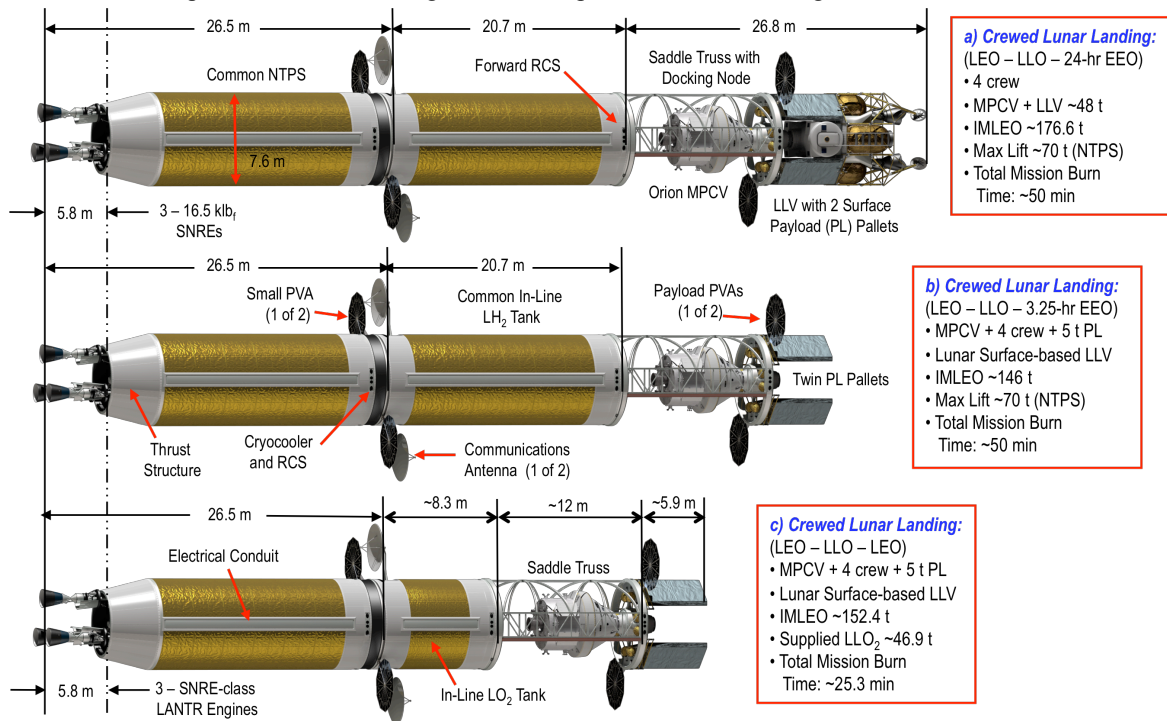


FIGURE 3. Variation in NLTV Size, IMLEO, Mission Capability and Engine Burn Time Resulting from the Development and Utilization of LLO₂ and the Transition to LANTR Operation

GROWTH MISSION OPTIONS AND ASSOCIATED REFUELING NEEDS

Over time we envision the development of a totally space-based LTS with different types of NLTVs operating between transportation nodes located in LEO, LLO and LPO. One-way transit times to and from the Moon on the order of ~72 hours would be the norm initially. Eventually, however, as lunar outposts grow into permanent settlements staffed by visiting scientists, engineers and administrative personnel representing both government and private ventures, more frequent flights of shorter duration could become commonplace. To cut transit times between LEO and LLO in half to ~36 hours will require an ~25% increase in the mission's ΔV budget (from ~8 to 10 km/s) so versatile LANTR engines with adequate supplies of LDP for refueling will be key to ensuring LTVs of reasonable size. Examples of space-based LANTR LTV concepts discussed in this section are shown in Figure 4.

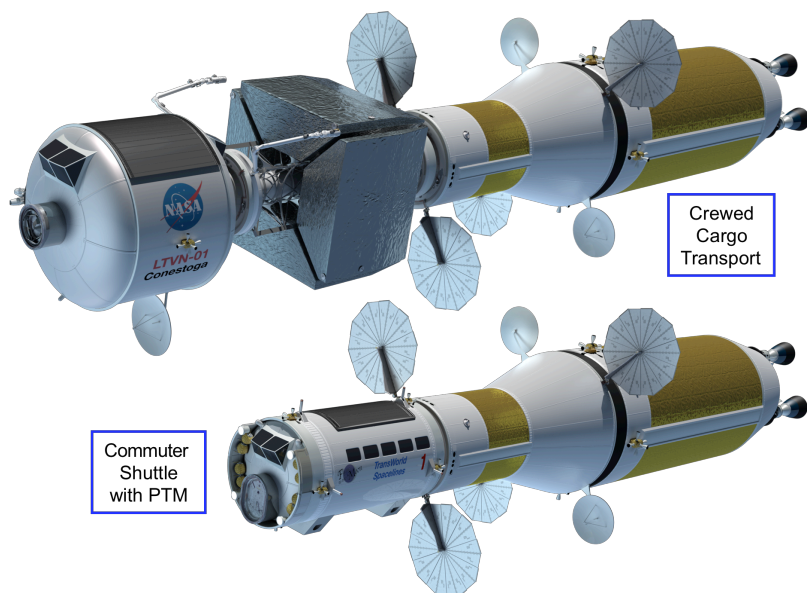


FIGURE 4. Space-based LANTR LTVs using a Common NTPS and Customized In-Line LO₂ Tank

Two different options for obtaining LDP are considered here. The first produces LLO₂ from abundant volcanic glass deposits located just north of the lunar “equatorial corridor” and the second both LLO₂ and LLH₂ from LPI deposits necessitating capture and departure from LPO. In Option 1, the LANTR LTVs use only Earth-supplied LH₂ (ELH₂) but refuel with LLO₂ for Earth return. Initially, the LANTR LTVs will transport ELH₂ to LLO for use by the LLVs and the hydrogen reduction processing plants producing the LLO₂. Later, once a propellant depot is established in LLO, it will be routinely supplied with LLO₂ transported from the surface using tanker LLVs. Similarly, dedicated NTR LH₂ tanker vehicles will supply the depot with ~25 t of ELH₂ on individual flights. In Option 2, it is assumed that tanker LLVs will transport H₂O to a propellant depot in LPO where it will be electrolyzed and stored there for subsequent use. The LANTR LTVs operating out of LPO will refuel with LLO₂ primarily but will also be able to “top off” their NTP stages using the excess LLH₂ from the H₂O electrolysis process for Earth return.

Table 2 provides a sampling of different missions, vehicle types, and trip times that have been examined along with the associated LLO₂ refueling requirements assuming volcanic glass and LPI as the source materials. All the cases shown use the same common NTPS described in the previous section and shown in Figures 3 and 4. Case 1, a crewed LTV mission, carrying the Orion MPCV and 5 t of cargo (shown in Figure 3c), uses an oversized in-line LO₂ tank consisting of two 7.6 m diameter ellipsoidal domes and requires ~47 t of LLO₂ for Earth return. Case 2 is a space-based crewed cargo transport (similar to that in Figure 4). It has its own dedicated habitat module weighing ~10 t, plus a 4-sided, concave star truss that has attached to it four 1.25 t PL pallets. The LO₂ tank is smaller and customized for this particular application resulting in a lower IMLEO and LLO₂ refueling requirement (~35 t).

Cases 3 and 4 show the impact on the crewed cargo transport mission of reducing the Earth-Moon transit times from 72 hours down to 48 and 36 hours, respectively. Because the LH₂ propellant loading in the NTPS is fixed at ~39.7 t for these missions, the LANTR engines run “O₂-rich” on the return leg (MR = 5, I_{sp} ~516 s) so the LLO₂ refueling requirement for Case 4, with a 36-hour transit time, increases to ~71.6 t – more than double that needed for Case 2.

TABLE 2. LANTR Missions, Vehicle Types, and Refueling Needs Using Volcanic Glass and LPI

Case Description *	Objective	Trajectory/Orbits **	In-line LO ₂ Tank	Results
1. Crewed LANTR LTV with MPCV and 12 m saddle truss carrying 5 t cargo to LLO	Determine LLO ₂ refueling needed to deliver 5 t cargo to LLO	72 hour 1-way transit times; LEO – LLO – LEO $\Delta V \sim 7.984$ km/s	7.6 m OD x ~5.23 m L (~163.5 t LO ₂)	IMLEO ~ 152.4 t; ~48.8 t LO ₂ supplied in LEO; ~46.9 t LLO ₂ refueling in LLO
2. Crewed space-based LANTR LTV with 9.9 t hab module and 11 m star truss carrying 5 t cargo to LLO	Determine LLO ₂ refueling needed to deliver 5 t cargo to LLO using alternative LTV configuration	72 hour 1-way transit times; LEO – LLO – LEO $\Delta V \sim 7.996$ km/s	4.6 m OD x ~3.4 m L (~35.9 t LO ₂)	IMLEO ~ 131.1 t; ~35.9 t LO ₂ supplied in LEO; ~35.1 t LLO ₂ refueling in LLO
3. Crewed space-based LANTR LTV with 9.9 t hab module and 11 m star truss carrying 5 t cargo to LLO	Determine LLO ₂ refueling needed to deliver 5 t cargo to LLO while also cutting transit times to 48 hrs	48 hour 1-way transit times; LEO – LLO – LEO $\Delta V \sim 8.695$ km/s	4.6 m OD x ~4.1 m L (~48.0 t LO ₂)	IMLEO ~ 143.4 t; ~48.0 t LO ₂ supplied in LEO; ~47.0 t LLO ₂ refueling in LLO
4. Crewed space-based LANTR LTV with 9.9 t hab module and 11 m star truss carrying 5 t cargo to LLO	Determine LLO ₂ refueling needed to deliver 5 t cargo to LLO while also cutting transit times to 36 hrs	36 hour 1-way transit times; LEO – LLO – LEO $\Delta V \sim 9.838$ km/s	4.6 m OD x ~6.1 m L (~81.2 t LO ₂)	IMLEO ~ 177.4 t; ~81.2 t LO ₂ supplied in LEO; ~71.6 t LLO ₂ refueling in LLO
5. LANTR commuter shuttle carrying 15 t Passenger Transport Module (PTM) to LLO then back to LEO	Determine LLO ₂ refueling needed to deliver the PTM to and from LLO with transit times of 36 hrs	36 hour 1-way transit times; LEO – LLO – LEO $\Delta V \sim 9.835$ km/s	4.6 m OD x ~5.4 m L (~69.3 t LO ₂)	IMLEO ~ 160.6 t; ~69.3 t LO ₂ supplied in LEO; ~67.9 t LLO ₂ refueling in LLO
6. LANTR commuter shuttle carrying 15 t PTM to LPO then back to LEO	Determine LLO ₂ refueling needed to deliver the PTM to and from LPO with transit times of 36 hrs	36 hour 1-way transit times; LEO – LPO – LEO $\Delta V \sim 10.006$ km/s	4.6 m OD x ~6.0 m L (~80.0 t LO ₂)	IMLEO ~ 172.5 t; ~80.0 t LO ₂ supplied in LEO; ~72.1 t LLO ₂ refueling in LLO
7. LANTR commuter shuttle carrying 15 t PTM to LPO then back to LEO	Determine LLO ₂ refueling needed to deliver the PTM to and from LPO; NTPS tops off with excess LLH ₂	36 hour 1-way transit times; LEO – LPO – LEO $\Delta V \sim 10.047$ km/s	4.6 m OD x ~4.6 m L (~56.4 t LO ₂)	IMLEO ~148.2 t; LTV refuels with ~55.3 t LLO ₂ and NTPS tops off with ~6.9 t excess LLH ₂
8. Rapid commuter shuttle carrying 15 t PTM to LPO then back to LEO	Determine feasibility of 24 hour transits using twin LANTR engines; NTPS tops off with excess LLH ₂	24 hour 1-way transit times; LEO – LPO – LEO $\Delta V \sim 13.225$ km/s	4.6 m OD x ~8.3 m L (~116.6 t LO ₂)	IMLEO ~204.3 t; LTV refuels with ~105.6 t LLO ₂ and NTPS tops off with ~13.2 t excess LLH ₂

* Cases 1 – 8 use a “Common LH₂ NTPS” (7.6 m D x ~15.7 m L); Propellant depots assumed in LEO, LLO and LPO; LANTR engines use optimized MRs

**LEO – 407 km, LLO – 300 km equatorial, LPO – 300 km polar orbit; Total round trip mission ΔV values shown include g-losses

The use of LANTR engines and LDPs could also enable the development of a commercial “commuter shuttle” service with 1-way trip times to and from the Moon ranging from 36 to 24 hours. The LANTR commuter shuttle (shown in Figure 4) carries a forward Passenger Transport Module (PTM) that contains its own life support, power, instrumentation and control, and reaction control system. It provides the “brains” for the LANTR-powered shuttle which is home to the 18 passengers and 2 crew members while on route to the Moon [12]. Arriving in LLO, the PTM detaches and docks with a waiting “Sikorsky-style” LLV that delivers it to the lunar surface. From here the PTM is lowered to a “flat-bed” surface vehicle for transport over to the lunar base and passenger unloading.

Case 5 is a commuter shuttle LTV that carries a 15 t PTM to LLO and back, has 36-hour 1-way trip times, and uses only ELH₂. It has an IMLEO of ~161 t and refuels with ~68 t of LLO₂. Case 6 is similar to Case 5 but operates between LEO and LPO. Because of the higher ΔV budget needed to access LPO, the shuttle’s IMLEO and LLO₂ refueling requirements are larger at ~173 t and ~72 t, respectively. The total burn time on the LANTR engines for the round trip mission is ~25.3 minutes. Also, with the engines running O₂-rich and producing ~170.3 klb_f of total thrust, the g-loading on the passengers during the final EOC burn varies from ~0.75 to ~1.5g.

Case 7 shows the benefit of utilizing the excess LLH₂ produced from the depot’s H₂O electrolysis process to top off the NTPS’ LH₂ tank. By supplying the commuter shuttle with just under 7 t of LLH₂, LLO₂ refueling decreases by ~17 t and the shuttle’s IMLEO decreases by more than 24 t. By switching to a “twin engine” NTPS, and again topping off with ~13 t of excess LLH₂, 24-hour 1-way transit times are also possible as shown in Case 8. This rapid shuttle capability comes at the expense of increased mission ΔV (~13.2 km/s), IMLEO (~204 t) and LLO₂ refueling (just under 106 t), but the passenger g-loading during the EOC burn is more manageable varying from ~0.5 to ~1g.

SUMMARY AND CONCLUSIONS

The NTR offers significant benefits for lunar missions and can take advantage of the leverage provided from using LDPs – when they become available – by transitioning to LANTR propulsion. This enhanced version of NTP

provides a variable thrust and I_{sp} capability, shortens burn times, extends engine life, and allows combined LH_2 and LO_2 operation. Its use together with adequate supplies of LDP for refueling can lead to a robust nuclear LTS with unique mission capabilities that include short transit time crewed cargo transports and commuter shuttles.

ACKNOWLEDGMENTS

The author (SKB) acknowledges the NTP Project, the Nuclear Power and Propulsion Technical Discipline Team (NTDT), and Mark Klem (GRC) for their support of this work. The author also expresses his thanks to Bob Sauls (bob.sauls@xp4d.com) for the digital images depicting the GRC vehicle designs shown in Figures 3 and 4.

REFERENCES

- [1] NASA's Journey to Mars – Pioneering Next Steps in Space Exploration, National Aeronautics and Space Administration, NP-2015-08-2018-HQ, Washington, DC, (October 2015).
- [2] Borowski, S. K., McCurdy, D. R., and Burke, L. M., "The Nuclear Thermal Propulsion Stage (NTPS): A Key Space Asset for Human Exploration and Commercial Missions to the Moon," AIAA-2013-5465, (September 2013); also NASA/TM-2014-218105, (October 2014).
- [3] Borowski, S. K., et al., "Affordable Development and Demonstration of a Small Nuclear Thermal Rocket (NTR) Engine and Stage: How Small is Big Enough?," AIAA-2015-4524, (August 31–September 2, 2015); also NASA/TM-2016-219402, (December 2016).
- [4] David, L., "Lunar Leap: Europe is Reaching for a Moon Base by the 2030s," Space.com (December 30, 2015).
- [5] Aliberti, M., *When China Goes to the Moon*, ESPI, Springer Wien, New York, (2015).
- [6] Grush, L., "Russia Announces Plans to Send Humans to the Moon in 2029," TheVerge.com (October 28, 2015)
- [7] Boyle, A., Science Editor, "To the Moon? Bigelow Aerospace and NASA Look at Private Exploration," NBC News and nbcnews.com (April 19, 2013).
- [8] Wall, M., "Mining the Moon's Water: Q&A with SEC's Bill Stone," Space.com (January 13, 2015).
- [9] David, L., "Inside ULA's Plan to Have 1,000 People Working in Space by 2045," Space.com (June 29, 2016).
- [10] Allen, C. C., Morris, R. V., and McKay, D. S., "Experimental Reduction of Lunar Mare Soil and Volcanic Glass," *Journal of Geophysical Research*, **99**, pp. 23,173-23,185, (November 1994).
- [11] http://nssdc.gsfc.nasa.gov/planetary/ice/ice_moon.html, "Ice on the Moon - A Summary of Clementine and Lunar Prospector Results," (December 10, 2012).
- [12] Borowski, S. K., and Dudzinski, L. A., "2001: A Space Odyssey Revisited – The Feasibility of 24 Hour Commuter Flights to the Moon Using NTR Propulsion with LUNOX Afterburners," AIAA-97-2956, (July 1997); also NASA/TM-1998-208830/REV2, (June 2003).
- [13] Joyner, C. R., et al., "TRITON: A Trimodal capable, Thrust Optimized Nuclear Propulsion and Power System for Advanced Space Missions," AIAA-2004-3863, (July 2004).
- [14] Bulman, M. J., et al., "LANTR Engine System Integration," AIAA-2004-3864, (July 2004).
- [15] Spudis, P. D., and Lavoie, A. R., "Using the resources of the Moon to create a permanent, cislunar space faring system," AIAA-2011-7185, (September 2011).
- [16] Davis, H. P., "Lunar Oxygen Impact upon STS Effectiveness," Eagle Engineering Report No. 8363, Eagle Engineering, Inc., Houston, Texas (May 1983).
- [17] Frisbee, R. H., and Jones, R. M., "An Analysis of Propulsion Options for Transport of Lunar Materials to Earth Orbit," AIAA-83-13444, (June 1983).
- [18] Sullivan, T. S., and McKay, D. S., Using Space Resources, NASA Johnson Space Center, pp.4, (1991).
- [19] Gregory, W. H., "Orange Soil Could Revive Lunar Projects" *Aviation Week & Space Technology*, pp. 41-44, (January 1, 1973).
- [20] Allen, C. C., Morris, R. V., and McKay, D. S., "Oxygen Extraction from Lunar Soils and Pyroclastic Glass," *Journal of Geophysical Research*, **101**, pp. 26,085-26,095, (November 1996).
- [21] Hawke, B. R., Coombs, C. R., and Clark, B., "Ilmenite-rich Pyroclastic Deposits: An Ideal Lunar Resource," in proceedings of *20th Lunar and Planetary Science Conference*, Houston, pp. 249-258, (1990).
- [22] Rincon, P., Science reporter, "Ice deposits found at the Moon's north pole," BBC News, The Woodlands, Texas, (March 2, 2010).
- [23] <http://permanent.com/lunar-mining-the-moon.html>, "Lunar Polar Water Ice & Volatiles in Shadowed Craters,"
- [24] Duke, M. B., Gustafson, R. J., and Rice, E. E., "Mining of Lunar Polar Ice," AIAA-98-1069, (January 1998).
- [25] Koeing, D. R., "Experience Gained from the Space Nuclear Rocket Programs (Rover/NERVA)," Los Alamos National Laboratory, Report LA-10062-H, Los Alamos, NM, (May 1986).

Optimization of Radiation Shielding for Space Nuclear Propulsion

Jarvis A. Caffrey^{1a,1b}

^{1a}*School of Nuclear Science and Engineering, Oregon State University, Corvallis, OR 97333*

^{1b}*NASA Marshall Space Flight Center, Huntsville, AL 35811
256-544-8464, jarvis.a.caffrey@nasa.gov*

Abstract. A genetic algorithm has been developed for optimization of a radiation shield with applications for nuclear propulsion and for other nuclear technologies. The multi-objective evolutionary algorithm (MOEA) searches for ideal combinations of dimensions and material composition among multiple layers of shielding. The methods are currently tailored for development of a shadow-shield for use in a nuclear thermal propulsion (NTP) stage, but the same methods can be extended to nearly any geometry with minimal effort. The algorithm couples with MCNP6 to perform transport calculations upon a population of candidate shield designs, then evaluates the results to compare the mass and transmitted dose or energy. Pareto-search mechanisms are employed to evaluate each candidate's fitness and determine its likelihood of passing traits to the next generation of candidate shield designs. In unconstrained optimization, this method gradually converges upon a set of Pareto-optimal solutions. Benefits of this method over other optimization techniques include the ability to explore the effect of discrete parameter changes to a design (e.g. material composition) in addition to continuous parameters (e.g. layer thickness), greater avoidance of false convergence upon local maxima, and flexibility in evaluating a diverse set of problems. Challenges of maintaining design diversity, expediting calculation time, and selecting appropriate algorithm parameters are also addressed.

Keywords: Radiation, shielding, optimization, genetic algorithm.

INTRODUCTION

Nuclear thermal propulsion (NTP) is a viable technology for a near-term interplanetary mission, as its high available specific impulse combined with high thrust make for an attractive alternative compared to its closest feasible competitors (chemical and solar electric propulsion). The high performance of NTP enables greater mission flexibility in launch opportunities, and more importantly, fast transfer times that reduce risk from long-term life support, microgravity, and cosmic radiation exposure. Nuclear reactors used in NTP emit radiation in the form of neutrons and gammas that must be shielded, but this is an engineering challenge that can be solved with little remaining uncertainty. The risks posed by engine-emitted radiation are known, quantifiable, and can be minimized unlike many of the risks presented by extended spaceflight. This work explores a method of optimizing shield forms to minimize mass with consideration of either thermal or dose effects.

Evolutionary Algorithms

Evolutionary algorithms, also known as genetic algorithms, are a class of optimization techniques that has more recently become a favored method for optimization of complex problems. The basic premise of this technique is to encode the various parameters that describe the problem into a vector that could be considered analogous to a chromosome. The problem is then approached in a similar manner as the process of biological evolution, in which the user enforces some constraints or pressures on a population of candidate designs and 'breeds' them to produce increasingly high-performing solutions over successive generations.

Overview

The process begins by producing an initial population of candidate designs, typically randomly selected within some predefined limits, said to bound the ‘parameter space’. Each candidate parameter set represents an individual, and the parameters are fed as inputs into an objective function. The results of this objective function are then compared with each other within ‘objective space’, where each candidate is assigned a score based upon a ‘fitness function’. The score may also be driven by other factors such as relative uniqueness of a solution, in order to preserve a diverse set of candidate individuals. Individuals from the population are then preferentially selected based upon their fitness score, typically with some degree of randomness, and paired with other individuals in the population. The traits of those individuals are then combined in a process known as cross-over. The newly created individuals then replace the previous generation, although some methods preserve a high-performing fraction of the prior generation. The new generation is then scored for fitness as before, and the process repeats for a set number of generations or until some convergence criteria are met, as shown in Figure 1.

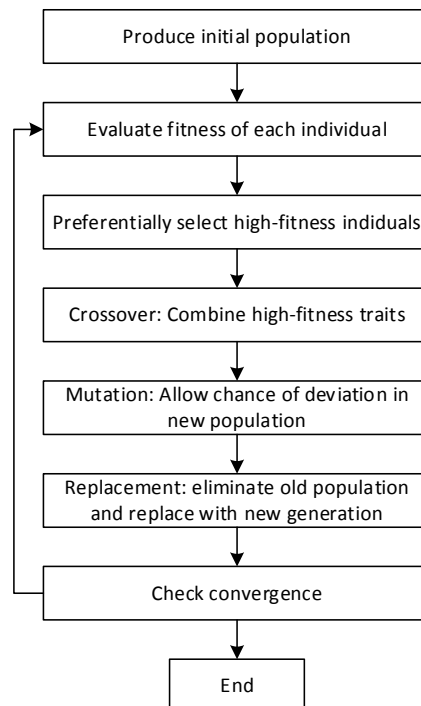


FIGURE 1. Generalized workflow of a genetic algorithm, or evolutionary algorithm.

Multiobjective Evolutionary Algorithms

Multiobjective evolutionary algorithms (MOEA) can be considered a sub-class of genetic algorithm in which multiple objectives must be considered at once. For instance, in a shield design, if the user is only concerned with minimizing dose, then that could be considered a single-objective problem. If, however, the user intends to minimize dose and also reduce the total mass (a far more realistic engineering problem) then the problem is considered multiobjective. MOEAs require some special considerations in order to apply the principles of general evolutionary algorithms, namely with regard to evaluating the fitness of each candidate individual. With a properly built fitness function, or some other method of evaluating relative fitness, the methods of evolutionary algorithms work very well to produce Pareto sets of optimal solutions. Most recent advances in MOEA methods are discussed briefly in the survey by Zhou et al. [2], as well as in some leading texts: [3] and [4].

Pareto sets

If the entire set of possible shield configurations were to be plotted in terms of total mass versus some the relevant quantity of interest, such as dose at a point beyond the shield, then the entire design space would be characterized by a field of possible solutions. At the edge of this field exists a hypothetical curve that bounds the design space and

which represents the unconstrained optimal shield designs for all possible system masses. This curve is known as the Pareto Front. For a discrete set of design solutions, those the solutions that exist closest to this front are known as the Pareto Set. [1]

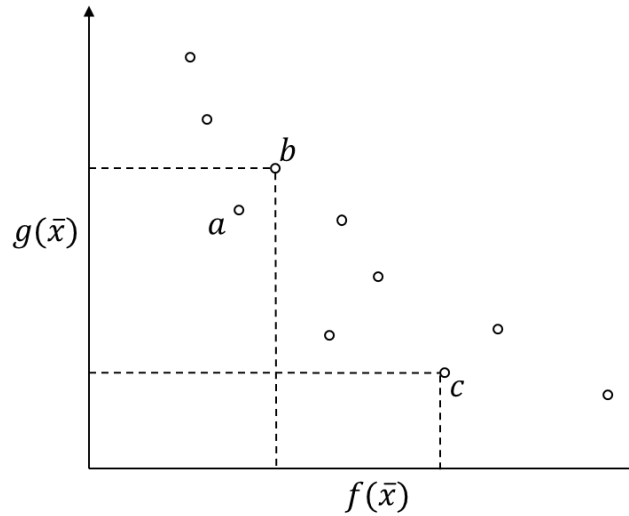


FIGURE 2. Example of non-dominated solutions (a and c) versus dominated solutions (b) in the objective space of a multi-objective problem. $f(\bar{x})$ and $g(\bar{x})$ represent competing objective functions. Each point represents a unique combinatorial selection or vector of parameters within \bar{x} in parameter space.

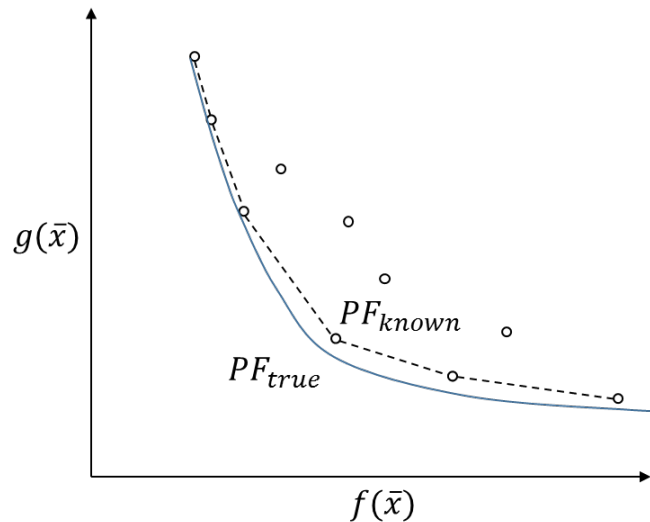


FIGURE 3. When selected from a discrete set of solutions, the non-dominated set forms the *known* Pareto front. This frontier is only a discontinuous approximation of the *true* Pareto front, which can never be fully represented unless an analytical solution is available. Individual points of PF_{known} may not even be good approximations of PF_{true} . It is the goal of multiobjective optimization to build a solution set of PF_{known} that closely approximates PF_{true} .

METHODS

A specialized genetic algorithm was developed to help explore the design space and establish an optimized shield geometry. As mentioned previously, genetic algorithms have the advantage of broadly sampling the entire design space, but they require the definition of a fitness function in order to score the relative merit of any given design. Such a fitness function is difficult to define for complex shield systems in multiobjective optimization.

Fitness

In a single-objective problem where only one output value is of concern, the fitness function may be a simple translation of the objective function (i.e. the smallest value represents the greatest fitness). In multiobjective problems, the fitness function must account for the relative merits of each objective. In some cases this can be accomplished by applying a weighted sum of single-objective fitness values. There is an abundance of choice in this matter, though, and while many fitness functions for specific problems have been crafted and accepted in literature, it is generally agreed that the definition of a useful fitness function is a matter of some creativity [4].

Fitness metrics were determined in this work using Euclidean distance between points and line segment approximations of PF_{known} in the objective space. With each generation, a new non-dominated set was determined and a Pareto front was produced as line segments connecting this Pareto set.

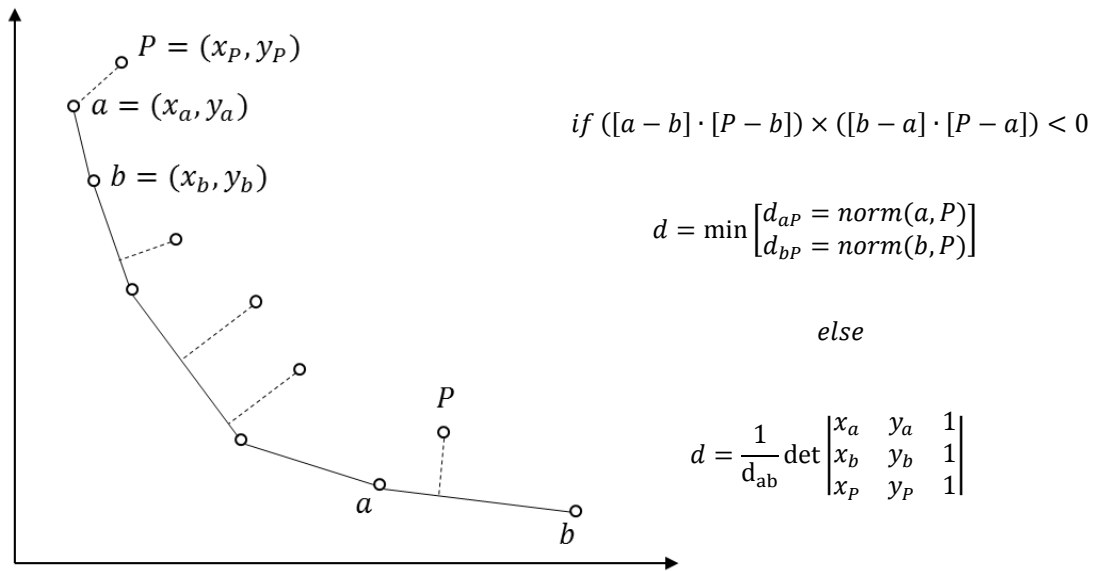


FIGURE 4. Description of the distance-to-Pareto fitness metric used in this work. For dominated points (P) lying outside the orthogonal bounds of any line segment of PF_{known} , the distance to the nearest point (a) on the frontier represents that point's performance metric. For points within the orthogonal bounds of PF_{known} , the shortest distance to the nearest line segment represents the performance metric. All points on PF_{known} have a distance of zero.

Crowding and Diversity

Problems arise in genetic algorithms when the diversity of the population is not maintained, and crowding of individuals occurs at certain portions along the Pareto front. This is first classified in early work by De Jong [5], and many methods of addressing the problem have been devised. Possible solutions include measuring the distance of any individual to its parent point and preferentially selecting the most well-spaced offspring [6], or introducing a metric for diversity of the population by determining the distance to nearest neighbors. For higher dimensional problems (problems with more than three objectives) the nearest neighbor density metric can be defined by calculating the volume of the hyper-rectangle with corners bounded by the adjacent points [4]. A simple nearest neighbor metric was employed in this work, defined as the Euclidean distance to the nearest point in objective space, with both axes normalized relative to the maximum value in each objective.

Selection

Translating the fitness of a candidate point into a probability of selection may be performed in several ways. The two general methods used in common practice are roulette and rank-order selection. In roulette selection, the relative fitness is directly translated into a probability function, often by simply dividing the fitness by the sum of all fitness values in a set, as in (1).

$$P_i = \frac{F_i}{\sum_{j=1}^N F_j} \quad (1)$$

The alternative rank-order selection can be useful in cases where extremely large differences in fitness may make it nearly impossible for lower-fitness individuals to ever be selected. Rank-order methods are therefore useful in maintaining population diversity, though often at the expense of poor convergence rates. In this method, each individual is given a sorted rank based upon its relative fitness compared to all others. A set probability of selection, P_c , is defined, and the selection process works by parsing through each individual in order of rank (highest fitness first), and selecting that individual with a probability of P_c using random number selection. If that individual is not selected, then the test is performed on the next individual in line with the same probability of selection, P_c .

Archiving/Elitism

A method of archiving is performed to avoid the attrition of high-performing candidates from prior generations. In the absence of an archive set, the information gained in the previous generation is lost after selection and recombination. This would not be a problem if could be assured that every new individual produced better performance than its parents, but that is often not the case. Maintaining an archive of 'best-yet' solutions allows the highest performing individuals to continually contribute to the selection pool. Selection of archive size plays an important role in developing a well-defined Pareto front. It was generally observed that an archive size of at least 40 individuals produced a well-defined curve along the Pareto front. Archiving also serves to counteract some of the deleterious effects of high mutation rates, preventing the frontier from losing ground due to random occurrence of poor-performers but accommodating the preservation of randomly produced high-performers.

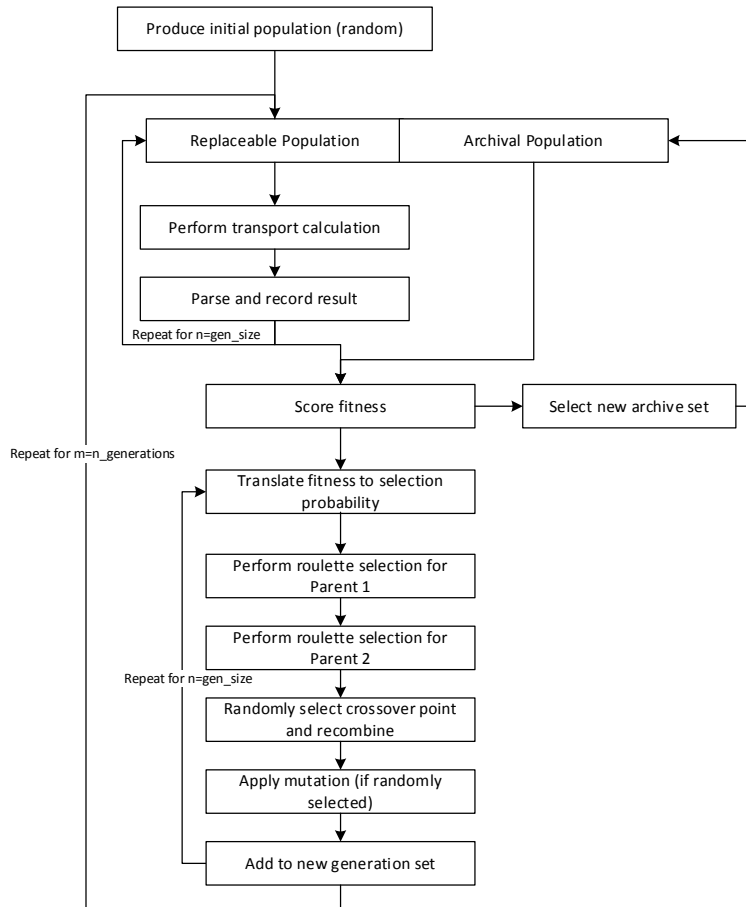


FIGURE 5. General schematic of the MOEA method applied in this work.

Pruning function

A pruning function is utilized to eliminate excessive numbers of points and preferentially select points that are on the Pareto front and more sparsely located. This function operates by calculating distance between its nearest neighboring points on the normalized objective space. For each point, the distance to the nearest neighbor is calculated and stored in an array, along with a logical indicator of whether the point is on the Pareto front, reference index for itself and for its neighbor, and distance to each point's second-nearest neighbor. The array is then sorted in order of nearest-neighbor distance and the function marches through each point-pair to find the best candidate for elimination based the following criteria, in order of priority:

- 1) Dominated solution, unless all points are non-dominated then continue with criteria 2 & 3
- 2) Smallest nearest neighbor distance of all point-pairs
- 3) Smallest second-nearest neighbor distance of the two paired points

Once that point is found, the index is recorded and the point is eliminated from the next iteration. The function iterates until the desired size is achieved.

RESULTS

Metrics for MOEAs

Performance of various algorithms and optimization parameters should be compared so that the methods with fastest convergence rate are utilized. Given that the true Pareto front cannot be solved analytically in this problem and is not known a priori, there are a limited set of metrics that may be used for this purpose. The only such metric that can evaluate the progress of an optimization toward convergence without assuming a true Pareto front is termed the Overall non-dominated vector generation (ONVG) metric [4]. This is simply the number of non-dominated solutions within

each generation, or the number of points that make up the current Pareto front. The ONVG is not a particularly robust metric, however, as it says little about the quality of the frontier in terms of its proximity to the true Pareto front. It can also be unresponsive to dramatic changes to the frontier, as points can often be removed and replaced on the frontier at approximately the same rate. This would be shown as a static ONVG metric (implying convergence) even as the frontier may continue to progress closer to the true Pareto front.

As the true Pareto front is unknown in these cases, and given that the most informative metrics for generational performance (i.e. how well the algorithm is producing high-performing designs between generations) require some knowledge of the true Pareto front, then it may be necessary to approximate the true Pareto front statistically using a large sample size. The approximation is unlikely to be perfect and does not help to actively determine the performance of a previously unexplored dataset while that optimization is underway, but it can be a useful way to examine the relative performance of various algorithms and their parameters after a sufficiently large dataset is produced. With multiple runs of the same optimization parameters, a large dataset is generated and a Pareto front calculated from the aggregation of all points is used as an effective PF_{true} . The Generational Distance (GD) can then be calculated as the sum or mean of the Euclidean distances between every point on PF_{known} and its nearest approach to PF_{true} , evaluated across the entire dataset.

Test case comparisons

A series of test cases were evaluated to compare performance of the algorithm with various parameter adjustments. The test case utilized a banked surface source of a reactor core, that included flux exiting both the top plane and the cylindrical wall. Four layers of shielding were evaluated with arbitrary thickness restrictions between one and six centimeters, and radius restricted between 30 and 60 centimeters. The scoring region was assumed to be a circular surface of 420cm radius, approximating the exposed face of a propellant storage tank. The surface was defined as one facet of a voided macrobody located 400cm above the core centerline. Total energy flux was scored, and normalized to represent Watts of heat produced during the operation of a reactor at 500 MW power.

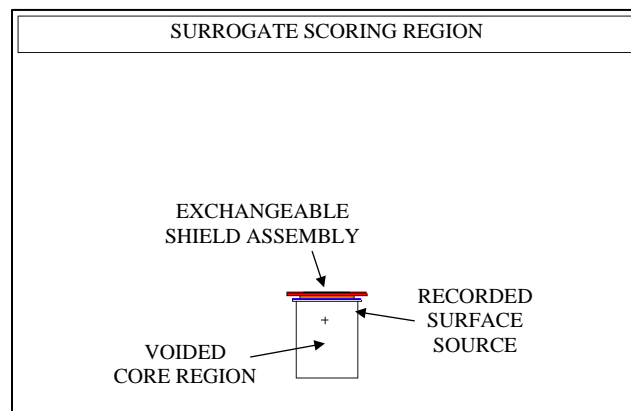


FIGURE 6. Test case scenario schematic. Surface current across one surface of the upper void volume is used as a surrogate for total energy deposition (primarily thermally) into a stage tank. This speeds calculation time significantly, allowing a general Pareto Set of optimal designs to be generated. This set may then be applied to a higher-fidelity calculation for dose or thermal deposition in a stage tank, with the results generally scaling linearly with that of the surrogate calculation. The core region is voided, with particles emitted from a recording surface taken from a criticality calculation of the reactor core.

This set of test cases used a relatively small archival set, with only 40 individuals and 20 new individuals per generation. The effect of this small archive is an unstable convergence, where the GD convergence metric is heavily influenced by the random production of points away from the Pareto front. The effect of increasing archive size is generally beneficial, as it reduces the attrition of prior non-dominated points. Large archives do not add any significant computational expense in terms of the costly objective function (MCNP runs), but they do add to the required memory storage and time required to evaluate relative fitness. In this case, that is a very small fraction of the total process time, however, so large archive sizes would be considered significantly beneficial.

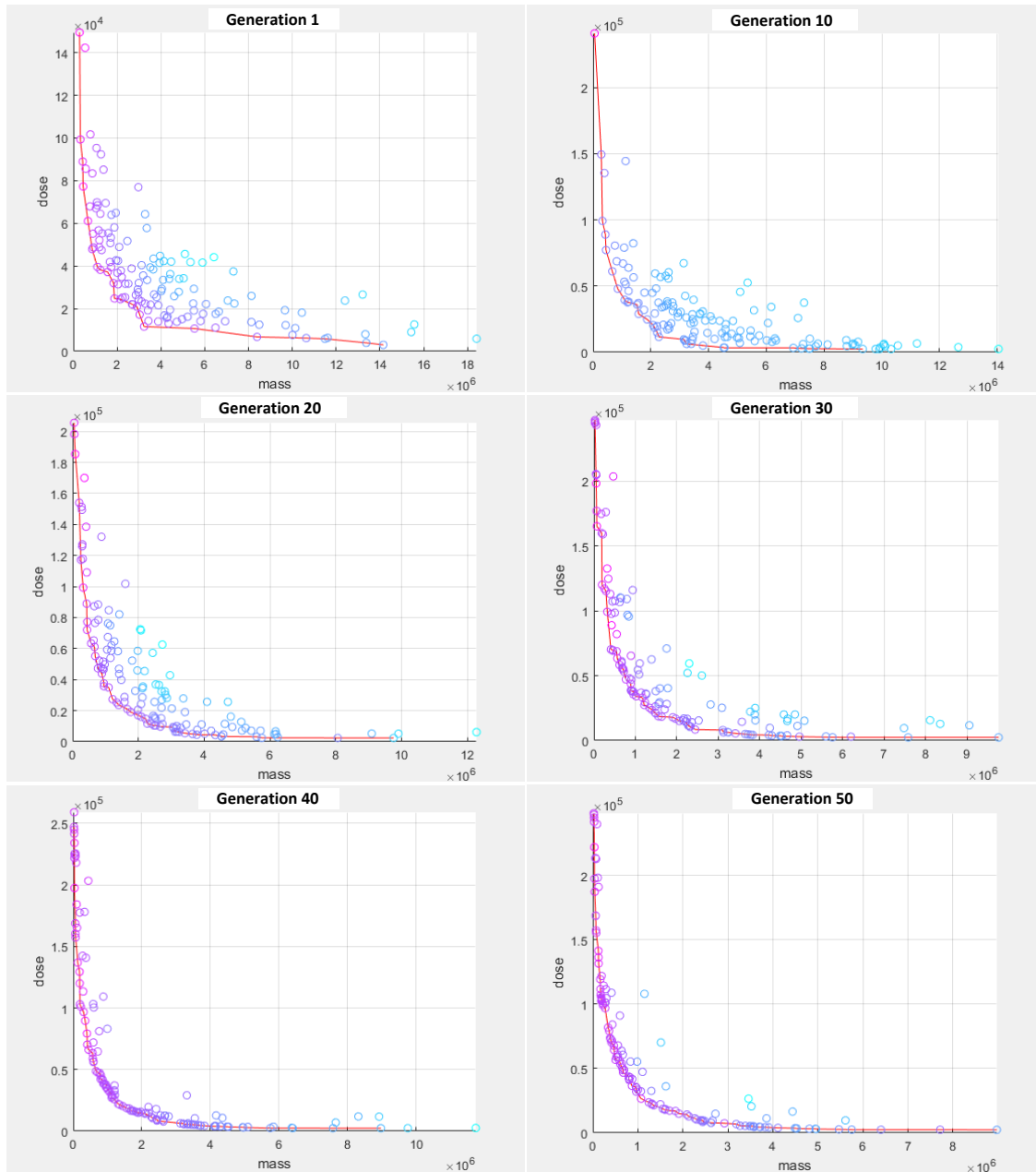


FIGURE 7. Example of the typical progression of all points in an optimization run. The first generation is randomly produced, and is broadly distributed through much of the design space. Coloration represents relative fitness, calculated in this case as a weighted sum of scores generated as a function of distance to the nearest point on the Pareto front (red line) and as a function of distance to the nearest neighboring point. The number of non-dominated points visibly increases with progressive generations, except between generations 40 and 50, indicating some degree of convergence.

Upon completion of each optimization run, the output of interest consists of an array of Pareto-optimal shield properties correlated to their objective output values. Selection of point designs and further analysis can proceed with consideration of other system constraints, either in terms of a thermal/dose limit or in terms of mass.

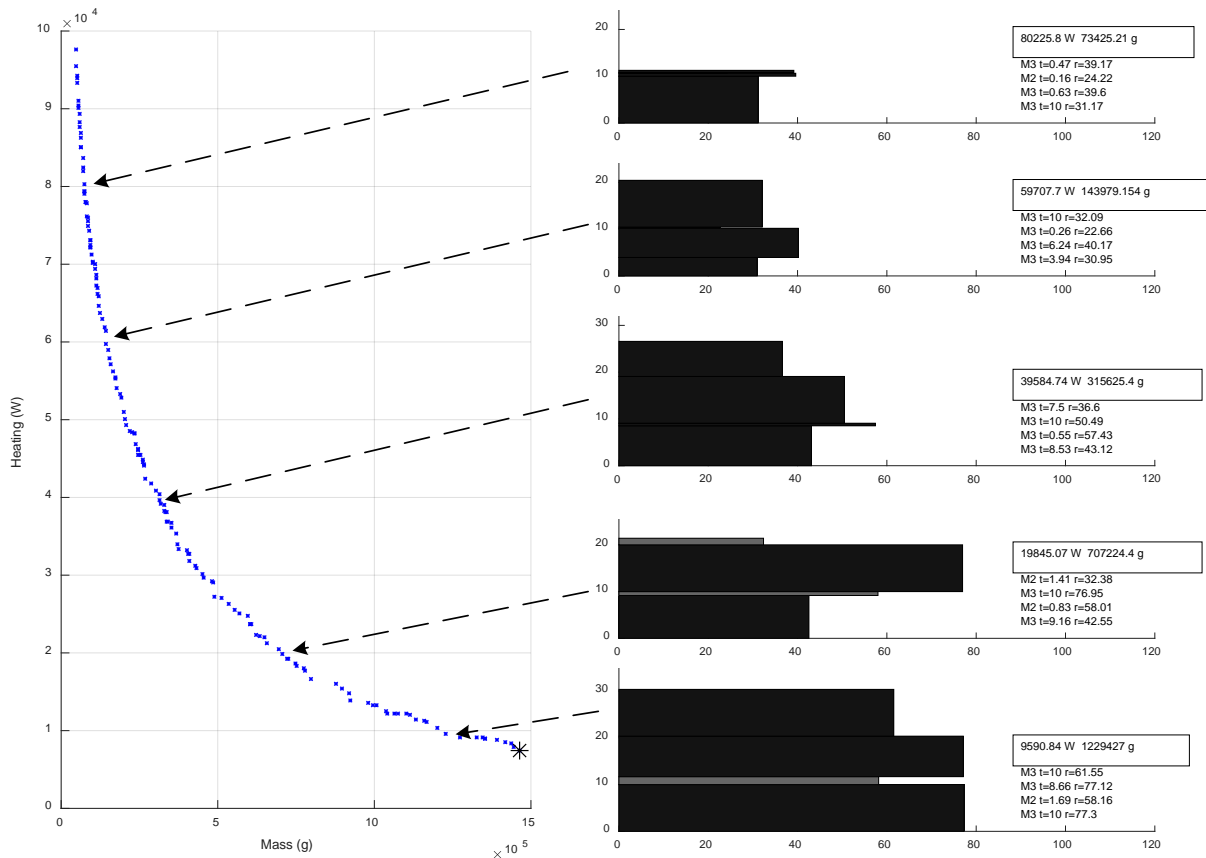


FIGURE 8. Survey of the Pareto optimal set for a test case. Total system mass and heating displayed to the right of each design (shown as a radial profile cutaway), along with layer parameters of material, thickness (cm), and radius (cm). M2 (dark grey) represents tungsten, M3 (black) represents boron carbide.

CONCLUSION

The MOEA explored in this work allows for extensive exploration of the design space of shielding for a nuclear thermal propulsion stage. Competing benefits and mass penalties of layer material selection, thickness, and diameter are evaluated simultaneously. The method also generates unconstrained Pareto sets of solutions is also a great benefit in early design processes, where trades of mass for dose or heating require such curves rather than optimized point designs. This process will prove to be useful in the design of a Mars exploration stage, in which mass may be traded into the crew habitat for combined engine/cosmic-ray shielding options.

REFERENCES

- [1] M. Caramia and P. Dell’Olmo, *Multi-objective management in freight logistics: Increasing capacity, service level and safety with optimization algorithms*. Springer Science & Business Media, 2008.
- [2] A. Zhou, B.-Y. Qu, H. Li, S.-Z. Zhao, P. N. Suganthan, and Q. Zhang, “Multiobjective evolutionary algorithms: A survey of the state of the art,” *Swarm Evol. Comput.*, vol. 1, no. 1, pp. 32–49, 2011.
- [3] K. Deb and D. Kalyanmoy, *Multi-Objective Optimization Using Evolutionary Algorithms*. John Wiley & Sons, Inc., 2001.

- [4] C. C. Coello, G. B. Lamont, and D. A. van Veldhuizen, *Evolutionary Algorithms for Solving Multi-Objective Problems*. Springer Science & Business Media, 2007.
- [5] K. A. De Jong, “An Analysis of the Behavior of a Class of Genetic Adaptive Systems.,” University of Michigan, Ann Arbor, MI, USA, 1975.
- [6] S. F. Galan and O. J. Mengshoel, “Generalized Crowding for Genetic Algorithms,” in *Proceedings of the 12th Annual Conference on Genetic and Evolutionary Computation*, New York, NY, USA, 2010, pp. 775–782.

Survey of Fuel System Options for Low Enriched Uranium (LEU) Nuclear Thermal Rockets

Kelsa Benensky¹, Paolo Venneri², Michael Eades², and Samantha Rawlins³

¹*Department of Nuclear Engineering, University of Tennessee, Knoxville, TN 37909*

²*Ultrasafe Nuclear Corporation, 188 Piedra Loop, Los Alamos, NM 87544*

³*Department of Physics, University of Michigan, Ann Arbor, MI 48109*
kbenensk@vols.utk.edu

Abstract. Nuclear thermal propulsion (NTP) is a non-chemical propulsion technology capable of high specific impulse (850 - 900 s) and high inherent thrust (100 – 2,200 kN), extensively tested in the United States and former Soviet Union. The most recent development efforts have focused on recapturing fuel production capabilities and optimizing small thrust engine designs based on historic NTP programs. However, recent fuel production efforts have shown that fuel cannot be identically recaptured and that future development could benefit from modern manufacturing technologies, as demonstrated by the production of high density cermet fuel compacts by spark plasma sintering. Further, neutronic analyses have shown that low enriched uranium (LEU) fueled nuclear thermal rockets can be designed using legacy fuel systems based on limits learned from past U.S. NTP development programs. LEU engine designs are expected to significantly reduce the high maintenance cost and perceived political hurdles of developing nuclear thermal rocket systems traditionally associated with high enriched uranium (HEU) fuel systems. All in all, these findings warrant a review of relevant materials to support future NTP design efforts. The purpose of this presentation is to review high temperature structural materials applicable to NTP fuel systems. Materials will be characterized based upon their limiting thermal-mechanical properties, chemical compatibility, neutronic performance, and manufacturability. The focus of this presentation will be largely on legacy fuel system designs; however, high temperature structural fuel matrix materials explored through other terrestrial nuclear fuel development programs will be assessed.

Keywords: Nuclear Thermal Propulsion, Fuel Elements, NERVA/Rover, Composite, CERMET, Carbide

INTRODUCTION

A non-chemical propulsion technology, nuclear thermal propulsion uses the energy released from fission to directly heat a propellant, which is expanded through a nozzle to provide 100 – 2,200 kN thrust. Use of high operating temperature nuclear fuel and hydrogen propellant allows for specific impulses (I_{sp}) of 850 – 900 s to be achieved. These attributes of high thrust levels and I_{sp} allow for reduced trip times and increased cargo payloads for interplanetary missions. Historic engine designs have been optimized to meet past performance needs by minimizing engine sizes for a given thrust level using high enriched uranium (HEU) fuel. However, recent studies have shown that low enriched uranium (LEU) engine designs containing less than 20 wt% ^{235}U content, are capable of achieving comparable performance to HEU engine designs [1-4]. Use of LEU fuel has the potential to reduce the high maintenance cost and perceived political hurdles of developing nuclear thermal rocket systems traditionally associated with high enriched uranium (HEU) fuel systems. Further, LEU NTR engine designs can enable the potential for private industry development and licensing. Additionally, the use of modern manufacturing technologies, such as spark plasma sintering or melt infiltration, has the potential to facilitate the manufacture of more desirable microstructures or enable manufacture of new classes of fuel systems, which may be specifically advantageous for use in a LEU NTR engine. The purpose of this paper is to survey material candidates for LEU NTP fuel systems in order to guide down selection of the most viable structural matrix candidates based on selective

material properties and known material performance under known engine operating conditions. Material candidates which best satisfy the needs of operation within a nuclear thermal rocket environment are assessed using infinite lattice calculations.

Proposed NTP fuels must enable the performance benefits of an NTR. Therefore, nuclear fuel systems must allow for operating temperatures in excess of 2500 K and resist interaction with the corrosive hydrogen propellant. Due to the dependence of core power and mechanical loading profiles on fuel system geometry and mass, developed fuel elements need to ensure low fuel mass loss and retain strength and structural stability for the range of operating conditions of the rocket lifetime. High fuel element operating temperatures may result in vaporization at the surface of the fuel system or cause thermal stresses between the fuel matrix and relevant interfaces such as protective claddings, coatings, or dispersed fuel particles. Fuel elements must be able to survive thermal shock incurred during start up for a single burn and recover from previous use to upkeep performance during multiple restarts of the engine. Key attributes of fuel systems for an LEU NTR must enable:

- High operating temperature: low vaporization, thermodynamic stability
- Low thermal neutron absorption
- Mechanical/structural stability over a wide range of operating temperatures: predictable mechanical properties to accommodate thermal stresses or changes in physical properties with temperature, irradiation
- Chemical compatibility with coolant, fuel particles, and relevant claddings

The following section presents a literature review of high temperature materials to support nuclear space applications and known fuel performance under limiting nuclear thermal propulsion applications.

STATE OF THE ART

Very few materials can withstand the operating conditions necessary for operation of a nuclear thermal rocket. At the minimum, LEU fuels must have high melting temperature and low neutron absorption cross sections to enable maximum temperature during operation and allow for critical geometries to be attained. Material candidates that are incompatible with the hydrogen propellant will require protective coatings to protect against chemical attack. Only few elements exist with a melting temperature above 2700 K: Ir (2719 K), Nb (2740 K), Mo (2890 K), Ta (3290 K) Os (3310 K), Re (3438 K), W (3695 K), and C (4300 K) [5]. These elements are mostly transition metals, with the exception of carbon, which as graphite sublimates at 4000 K in a vacuum [5]. High temperature compounds with melting temperatures above 2700 K include transition metal and refractory carbides, oxides, borides, silicides, sulfides, phosphides, and intermetallides. Of these applicable high temperature materials, graphite [6, 7], transition metals [8, 9], and transition metal carbide based fuel systems [10] have been developed and tested in past NTP development programs of the United States. These candidates are assessed on their applicability to support LEU NTP engines, fuels must at the minimum allow for criticality to be achieved in the LEU NTR and similar performance to historic engine designs by allowing for engine operating temperatures of 2500 K and above.

High Melting Temperature Elements: Graphite and Transition Metals

Fundamental Considerations for Graphite Fuel Systems to Support NTP

Compared to other materials, graphite offers the ability for exceptionally high operating temperatures, good high temperature strength, relative ease in fuel form manufacture, low thermal neutron absorption, and a large established irradiation database/operational experience. Graphite based fuels were the first fuels developed for nuclear thermal propulsion in the United States through the Nuclear Engine for Rocket Vehicle Application (NERVA)/Rover program. Throughout the program, fuel forms evolved from dispersed UO_2 or UC_2 particle impregnated graphite plates to extruded hexagonal fuel elements containing a dispersed uranium-zirconium carbide, (U,Zr)C, fuel web with coolant channels for hydrogen flow [6]. The NERVA/Rover program was the only program to test fuels in NTP prototype engines. Over 20 test reactors containing graphite based fuels were ground tested throughout the duration of the program (1955 – 1972) [7]. This was the only fuel type that has been tested in a fully assembled reactor core with the prototype conditions of a nuclear thermal rocket.

The key advantage of graphite based fuels for LEU NTP application is the low thermal neutron absorption cross section and high scattering cross section of carbon. This allows the structural graphite matrix to also function to

moderate the neutron flux within the core. Graphite based fuels have acceptable thermal conductivity and high temperature strength, which allows for the reduction of local hot spots and reliable mechanical response during operation. Due to the extensive database of operating experience, the failure modes of graphite based fuels are well known and is reviewed elsewhere [6, 11-13]. The largest risks associated with developing graphite based fuel systems is associated with the incompatibility of graphite with the hot hydrogen propellant, which alters the reactor power profile during operation and degrades the structural integrity of the matrix. Exposed graphite must be coated using protective coatings/claddings to prevent exposure to the hot hydrogen environment and subsequent corrosion. Minimizing incurred thermal stress and dimensional instability of graphite fuels is key maintain coating integrity.

Fundamental Considerations for Transition Metals to Support NTP

Six transition metals have been identified and tested as high temperature materials for nuclear space applications: Ir, Nb, Ta, Re, Mo, and W [14-17]. Selection from this group is significantly narrowed when considering neutron cross section, material thermal stability, and chemical compatibility. Transition metals which can withstand such high temperature operation and are extremely heat and wear resistant are often referred to as refractory metals. The advantages of refractory metals are their capability for high temperature operation, high temperature strength, high thermal conductivity, and high ductility at the operating temperatures desired for nuclear thermal propulsion. When selecting refractory metals for LEU nuclear fuel systems neutron cross section, high temperature stability, and chemical compatibility are the most important parameters to consider. Secondary material properties that should be considered includes the evaluation of the ductile to brittle transition temperature (DBTT) for body centered cubic (BCC) alloys. High DBTT increases difficulty in fuel manufacture and reduces a materials ability to resist crack propagation. Irradiation and hydrogen embrittlement is known to increase the DBTT and could degrade the mechanical response the fuel during re-start conditions. Iridium is a high melting temperature element from the Platinum group. Iridium is extremely inert and typically used for encapsulating the power sources for radio thermoelectric generators (RTGs) [18]. However, its high natural neutron absorption cross section of 425 b makes it unsuitable as a structural material in the active core of a NTR [19].

The advantage of Nb and Ta compared to other refractory metals are their low ductile to brittle transition temperature, below 0°C (273 K) which is desirable for fuel fabrication and to ensure ductile fuel response over the range of operating temperatures along the fuel length [17]. These metals can maintain their strength for very high temperature operating conditions and have been investigated as structural components for space power systems. However, at temperatures below 800°C (1073 K), Nb and Ta easily uptake hydrogen and have high hydrogen solubility [20]. Fuel operating in low temperature regions near the inlet is susceptible hydrogen embrittlement during operation and the total length of the fuel is susceptible to hydrogen uptake during core cooldown. Hydrogen ingress is not desired. Hydrogen uptake reduces metal ductility, may also result in the formation of low melting temperature metal hydrides, and affects the neutronic power profile during operation or restart. At very high operating temperatures, Ta and Nb are incompatible with UO₂ and UC fuel. Ta and Nb tend to reduce UC fuel and form refractory metal carbides. While UO₂ is stable within Ta and Nb, the metals will interact with free oxygen produced during high temperature UO₂ operation to form lower melting temperature oxides [17, 21, 22]. It has been suggested through previous studies that high temperature coatings such as W may be acceptable to mitigate the interaction, however, use of W coatings introduce a neutronic penalty [17].

Of the transition metals, only Mo, W, and Re are thought to be suitable matrix materials for NTP fuel systems. Mo and W are BCC type alloys with a high DBTT, making these materials more brittle and difficult to manufacture compared to Nb and Ta. Rhenium has a hexagonal close packed (HCP) crystal structure and is typically alloyed with Mo or W to produce a more ductile material response. Mo and W have undergone extensive development and separate effects testing [8, 23] (high temperature irradiations, hot hydrogen testing, thermal cycling, and thermal shock), while Re based fuels have only been demonstrated to be compatible with UO₂ to temperatures of ~2500 K [24]. Re has a high thermal absorption cross section for all stable isotopes and is not a good candidate for LEU NTP despite its desirable ductility. Additions of Re should be limited when used. From 1962 – 1968, General Electric's 710 Gas Reactor program developed and tested Mo and W metal matrix fuels with distributed uranium dioxide (UO₂) or uranium nitride (UN) fuel particles [8]. Ultimately, it was observed that the vapor pressure of Mo became significant at 2470 K, limiting its expected performance as an alloying element [25]. Due to the higher melting temperature and better thermal stability of tungsten in the hydrogen environment, later fuel development focused on W-based fuels.

The development of W-matrix ceramic-metallic (cermet) fuels addresses the specific design challenges encountered in the Rover/NERVA program. Tungsten is compatible with the hydrogen propellant and exhibits superior high temperature strength and endurance [26]. The main drawbacks of W-cermet fuel are high thermal neutron cross section and high DBTT, which results in difficulty in the manufacture and machining of full length fuel elements. Although W has a high thermal absorption cross section, cermet fuels allow for higher volume loadings of fuel within the matrix. Most reference engine designs use fuel loadings of 60 vol% within the matrix to compensate for the high natural thermal absorption cross section of W. This fuel loading is almost a factor of two higher than graphite matrix fuels, which in order to maintain structural integrity, must be limited to loadings of 35 vol% or less [6]. LEU NTR designs using a W-cermet fueled core have been demonstrated, but require the use of external moderating elements and enrichment of natural W in the W-184 isotope. W-cermet fuels have been the subject of high temperature irradiation and hot hydrogen testing through past program developments, which has led to a good understanding of fuel behavior and potential failure pathways [9, 11, 25]. The largest risks associated with the operation of W-cermet fuel systems is attributed to the vaporization and migration of UO_2 fuel during high temperature operation, which leads to loss of reactivity and structural integrity of the fuel system [9]. Modern manufacturing methods such as via spark plasma sintering (SPS) can allow for the production of tungsten elements close to theoretical density in order to retain fuel during operation [27, 28].

High Melting Temperature Compounds: Refractory Carbides

Figure 1 demonstrates all elements and high temperature compounds with melting temperatures above 2500°C, which include transition metal and refractory carbides, oxides, borides, silicides, sulfides, phosphides, and intermetallides. Silicides, phosphides, and sulfides have too low a melting temperature (< 3000 K) and are not capable of achieving high operating temperatures necessary for comparable performance to reference LEU NTR designs. Boron and rhenium containing compounds will function as neutron absorbers within the reactor core and will not allow for the critical design of a LEU NTR. High melting temperature oxides, nitrides, and carbides are capable of high temperature operation with low thermal neutron absorption cross sections. Oxides are not recommended in the reducing hot hydrogen environment due to high expected vaporization rates and high temperature thermodynamic instability [29]. While both carbide and nitride compounds offer hot hydrogen compatibility, refractory carbide compounds offer the highest known melting points and superior high temperature stability with lower thermal neutron absorption cross sections. Therefore, of all known high temperature compounds, carbides have highest potential for use in a LEU NTR due to their low absorption cross sections, high temperature stability, and hot hydrogen compatibility.

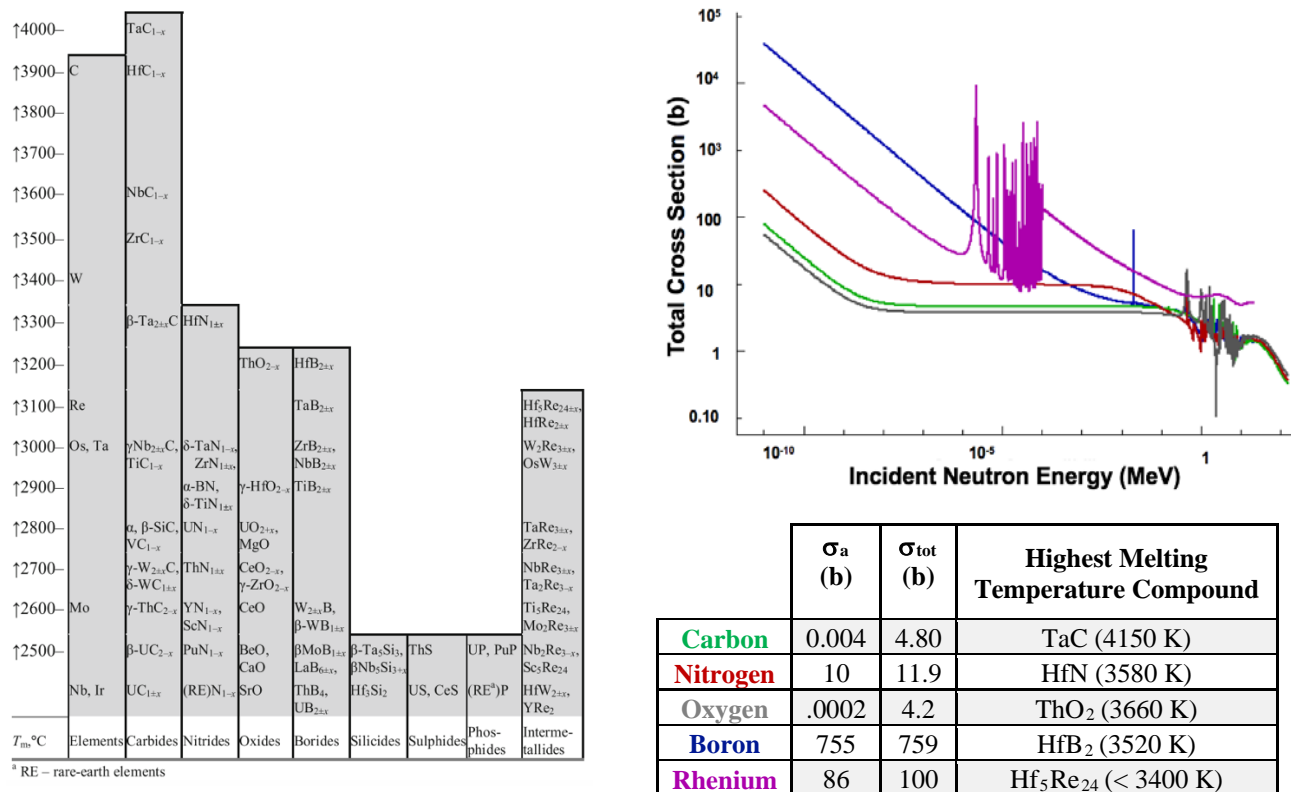


FIGURE 1. Comparison of the neutronic properties of different ultra-high temperature compounds [5, 30]
Fundamental Considerations for Transition Metal Carbides to Support NTP

Transition metal carbides have the highest known melting temperatures for all known compounds and are chemically compatible with hydrogen. Because of this, refractory carbides are recognized to have the potential for highest NTP fuel operation temperatures (3000 – 3400K) and fuel endurance at temperature [31-33]. Refractory carbide materials, zirconium carbide (ZrC) and niobium carbide (NbC), were initially developed for the U.S. NTP program as coatings to protect graphite based fuel systems of the Rover/NERVA program. Due to the recognized brittle nature of refractory carbides, there has not been a proposed engine design with a structural refractory carbide matrix, despite the potential for extremely high temperature operation. Instead, transition metal carbide fuel systems are typically proposed to form a solid solution with uranium carbide fuels to form extremely high melting temperature fuels that demonstrate thermal and chemical stability in the reducing hydrogen atmosphere [6, 10, 23, 34]. All-carbide solid-solution fuels were studied and tested extensively by the former soviet union [23, 34, 35] and tested during the Nuclear Furnace test late in the NERVA/Rover program [10]. In these designs, fuels did not function as structural matrices and latter fuel development aimed to manufacture geometries which could better withstand the power densities and corresponding thermal loadings of the NTR core [34, 36]. The major limitations of all-carbide fuels are their extreme brittleness and limited solubility with uranium carbide at elevated temperatures, which reduces total U-loading within the fuel [37, 38].

Recent advances in the production of fully ceramic microencapsulated (FCM) matrix fuels, have supported the viability of refractory carbide matrix candidates for light water reactor (LWR) fuel systems. Manufacture of discrete fuel particles embedded within a refractory carbide matrix, such as silicon carbide, of greater than 40 vol% has been demonstrated [39]. Further, recent development of carbide fiber reinforced ceramics, using melt infiltration techniques, has demonstrated the development of high density SiC, ZrC, HfC, and TaC, which reduce typical processing time and exhibit superior high temperature operating performance than traditional manufacture of fiber reinforced composites [40]. Due to the poor thermal shock resistance of past all-carbide fuel forms, matrix fiber reinforcement may be necessary. In many performance applications, the use of fiber reinforced matrix composites has increased the use of high performance ceramics by enhancing the brittle material's resistance to thermal shock and increasing material durability. For example, originally studied for use in space shuttle turbopumps, Herbell et. al. demonstrated fiber reinforced SiC composites could withstand the thermal shock from temperature gradients of

up to 2173 K (1900 °C) without significant degradation [41]. Modern manufacturing developments in melt infiltration techniques have demonstrated outstanding performance of carbon fiber reinforced carbide ceramic composites by allowing for higher achievable densities compared to higher purity chemical vapor infiltration (CVI) techniques [40]. Testing of ZrC-C_f composites has been completed in oxidizing chamber environments up to ~2673 K and shown outstanding high temperature performance and corrosion resistance compared to traditional techniques [42]. Still a knowledge gap remains for high temperature irradiation performance of carbide composites. Low and intermediate temperature irradiation testing has been completed on FCM type LWR fuels and carbide composite structures [43, 44]. In general, carbides such as SiC and ZrC show excellent resistance to irradiation effects and good fiber stability at temperatures of interest to LWR applications. Fiber reinforced SiC composites developed for cladding applications in LWRs, fibers tested between temperatures between 1073 – 1573 K (800 - 1300°C) did not exhibit significant decreases in fiber strength decrease for doses up to ~6 dpa [44]. However, at higher operating temperature regimes (1073 - 1473 K), the onset of non-saturable void swelling is expected [45]. While refractory carbides appear to promise excellent performance and the ability to combine the best aspects of both cermet and graphite composite fuels: hot hydrogen compatibility, low natural thermal neutron absorption cross sections, and extremely high temperature operation, development status is the lowest out of all other potential material candidates. Known feasibility issues will need additional new development to address and due to low development status, performance limitations may remain unknown.

Discussion

The current development status, known performance limits have been discussed. Table 1 summarizes this knowledge and presents thermal scattering and absorption cross sections of relevant isotopes to support LEU NTP structural matrix concepts. Tungsten, graphite, and refractory carbide based fuels are most applicable for LEU NTR applications. Graphite offers the highest moderating power, (figure 2) extremely high operating temperature potential, and the largest database of operational experience. However, the major drawbacks of graphite based fuel systems are their incompatibility with the hydrogen propellant and poorer tensile properties, which requires significant design and development to avoid loss of structural support and hot hydrogen corrosion. Originally developed in parallel to the NERVA/Rover graphite fuel systems, W-cermet fuel systems addressed the limiting properties of the graphite matrix by allowing for superior high temperature strength and endurance, as well as offer compatibility with the hydrogen propellant. Unfortunately, the large absorption cross section of natural W requires isotopic enrichment to W-184 and high volume loadings of UO₂ or UN fuel. UO₂ and UN are thermodynamically unstable at temperatures necessary for operation and require significant development and design to retain fuel within the W-matrix in order to maintain reactor neutronics and fuel dimensional stability. Due to the efforts of historic NTP fuel development programs, design solutions have been postulated and determined for the major failure modes of each system. However, no fuel system has yet reached the development status to be flight ready. Refractory carbides were the last fuel system investigated in the United States and were the attention of significant development in the Russian NTP program [34, 35]. Refractory carbides offer the highest melting temperatures, high temperature thermal stability, and have low corresponding absorption cross sections. The low vaporization rates of refractory carbides at high temperature (figure 2) can enable longer fuel lifetimes and increased fuel endurance compared to reference fuel systems. Refractory carbides may be better suited as a structural matrix rather than restricted to UC containing compounds. High moderating power and capability for increased uranium loadings of refractory carbide matrix fuels, compared to traditionally developed fuels, can allow for small engine size geometries desired for the LEU NTR without isotopic enrichment of the matrix. The neutronic reactivity potential of each of the presented matrix concepts are presented in the following section.

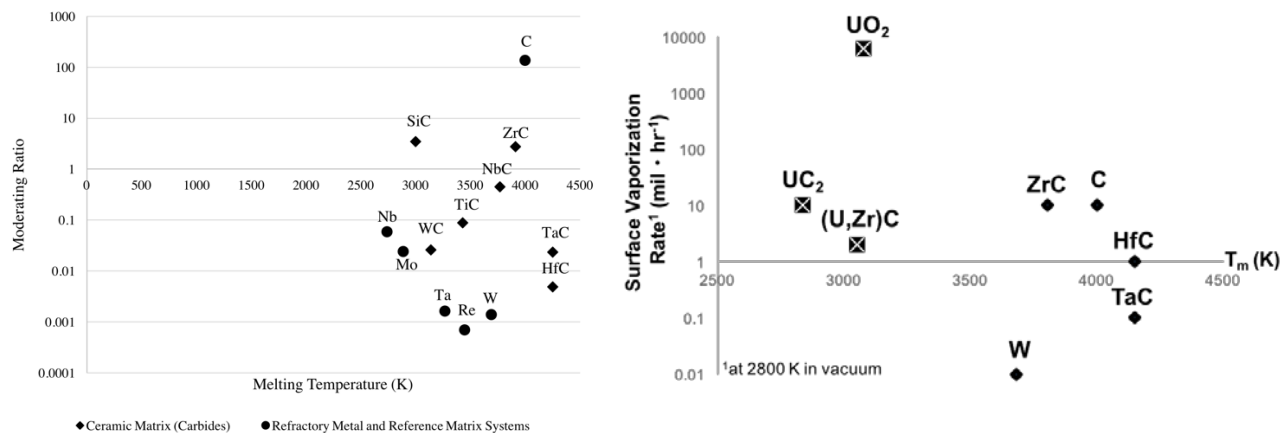


FIGURE 2. Left. Calculated moderating ratios of graphite, transition metal, and refractory carbide candidates [5, 19]. **Right.** Surface vaporization limits total fuel operational lifetime. Surface vaporization rates are displayed for nuclear thermal propulsion material candidates after [11].

TABLE 1. Properties of Elements of interest for Structural Nuclear Thermal Propulsion Fuel Systems [5, 19].

Element	σ_s (b)	σ_a (b)	Natural Abundance (at%)	Melting Temperature (K)	Key Attributes	Limiting Feasibility Issues
Iridium ¹⁹³ Ir	14 -	425 111	- 62.7	2719	• Extremely Inert	• Low melting temperature • Highest thermal absorption cross section
Niobium	6.26	1.15	-	2740	• Low DBTT	• Readily hydrides below 1073 K • Interacts with common U-containing compounds at high temperature
Molybdenum	5.71 ⁹² Mo: 6.00 ⁹⁴ Mo: 5.81 ⁹⁸ Mo: 5.44 ¹⁰⁰ Mo: 5.69	2.48 0.019 0.015 0.127 0.4	- 14.6 9.1 24.3 9.7	2890	• Hot hydrogen compatibility • Low thermal absorption cross section	• Vapor pressure limits to operating temperatures below 2470 K

TABLE 1 (cont.). Properties of Elements of interest for Structural Nuclear Thermal Propulsion Fuel Systems [5, 19].

Element	σ_s (b)	σ_a (b)	Natural Abundance (at%)	Melting Temperature (K)	Key Attributes	Limiting Feasibility Issues
Tantalum	6.01	18.3	-	3270	<ul style="list-style-type: none"> • Low DBTT • High operating temperature potential 	<ul style="list-style-type: none"> • Readily hydrides below 1073 K • Interacts with common UC, UN at high temperature • High thermal absorption cross section
Rhenium	11.5	89.7	-	3438	<ul style="list-style-type: none"> • No DBTT • High operating temperature potential • Hot hydrogen compatibility 	<ul style="list-style-type: none"> • High Absorption Cross Section
Tungsten	4.60	18.3	-	3695	<ul style="list-style-type: none"> • Hot hydrogen compatibility • High operating temperature potential • High uranium fuel loading 	<ul style="list-style-type: none"> • High DBTT • High thermal absorption cross section
¹⁸² W	6.10	20.7	26.50			
¹⁸³ W	5.7	10.1	14.31			
¹⁸⁴ W	7.03	1.7	30.64			
Graphite	5.55	0.0035	-	4000 ¹	<ul style="list-style-type: none"> • High operating temperature potential • Manufacturability • Lowest absorption cross section 	<ul style="list-style-type: none"> • Chemically incompatible with hot hydrogen • Poor mechanical properties in tension
Carbides			-			
SiC	7.25	0.16		3000 ¹	<ul style="list-style-type: none"> • Highest operating temperature potential 	<ul style="list-style-type: none"> • Highest DBTT
WC	10.15	18.30		3140	<ul style="list-style-type: none"> • Low absorption cross section 	<ul style="list-style-type: none"> • Poor thermal shock resistance
TiC	9.90	6.09		3430	<ul style="list-style-type: none"> • Hot hydrogen compatibility 	<ul style="list-style-type: none"> • Lowest development status
ZrC	12.01	0.19		3910		
NbC	11.81	1.15		3770		
HfC	15.79	104.1		4250		
TaC	11.56	20.60		4250		

¹Sublimation temperature in vacuum

COMPARISON OF MATRIX CONCEPTS: INFINITE LATTICE CALCULATIONS

Methodology

Infinite lattice calculations were completed to assess the viability of refractory carbide matrix fuel candidates for use in a low enriched uranium nuclear thermal rocket. To evaluate the performance potential of refractory carbide matrix fuels, the calculated reactivity via the infinite lattice multiplication constant (k_{inf}) is compared to reference composite graphite matrix and tungsten matrix cermet fuel systems developed for current small thrust LEU engine designs. For the initial survey, refractory carbides with the highest moderating ratios were surveyed: SiC, ZrC, and TiC. The proposed refractory carbide matrix fuels are modeled as a homogenized material with 35 vol% UO₂ loading at 19.75 w/o U-235 enrichment. The reference graphite composite matrix was modeled based upon a derivative of the NERVA/Rover Small Nuclear Reactor Engine (SNRE) design requirements with 19.75 w/o U-235 enrichment of the fuel. The graphite composite is composed of a 35 vol% (U,Zr)C fuel web dispersed within a graphite structural matrix with a 15vol% void fraction to accommodate fission product damage. Total uranium loading of the graphite composite matrix fuel is limited to 0.64 g/ccm. Reference tungsten matrix fuels are based upon the enriched LEU-cermet fuels for the Space Capable Cryogenic Thermal Engine (SCCTE) reference core. The cermet fuel is modeled using 60% volume loading of UO₂ with 6 molar % ThO₂ and a W structural matrix composed of 95 w/o enriched W-184.

In each case, fuel elements were modelled using an extruded hexagonal geometry with 19 axial coolant channels based upon a typical NERVA geometry. Simulated fuel elements are 58 cm (1.906 ft) length with a flat-to-flat distance of 1.905 cm (0.75 in.) and constant coolant channel radii of 0.1125 cm (0.045 in.). Reflecting boundary conditions were applied to all six sides to simulate an infinite lattice. Each fuel type was studied with and without external moderating elements. To determine the effect of moderation on fuel reactivity, fuels were arranged in 1:1, 1:2, 1:3, and 2:1 moderator ratios with reference $ZrH_{1.8}$ containing moderator tie-tube elements optimized in previous studies [1, 46]. Figure 3 shows the infinite lattice configurations for the 1:0, 1:1, 1:2, 1:3, and 2:1 fuel to moderator (F:M) ratios. The infinite lattice calculations were completed using MCNP6 v1.1 with the ENDF/B-VII.1 neutron library. Each calculation used 360,000 particles per cycle with 7,232 active and 42 inactive cycles. The standard deviation associated with the calculated k_{inf} values are all below 0.00025, providing sufficient confidence in the statistical validity of the results. The calculations were completed using room temperature cross-sections for the tie-tube moderator elements and 1600 K cross sections for the fuel and the UO_2 s(a,b) card.

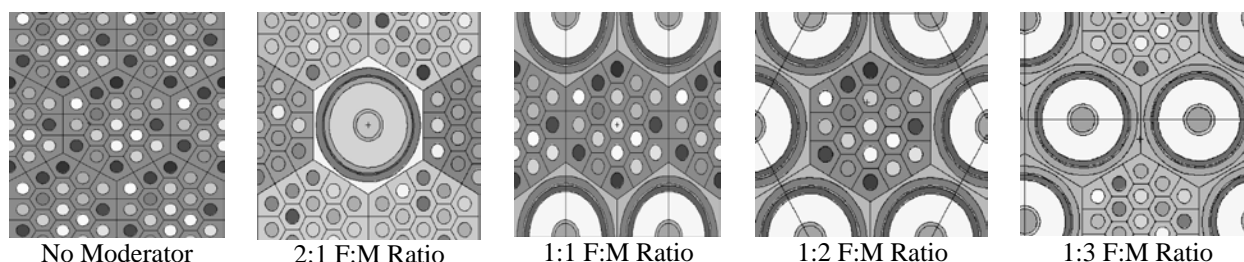


FIGURE 3. Schematic of the infinite lattices configurations with moderator elements for LEU fuel analyses.

Presentation and Discussion of Infinite Lattice Calculation Results

Refractory carbide matrix fuels exhibited superior k_{inf} values to the reference designs of SULEU cermet fuels and SNRE composite fuels (figure 4). Enriched tungsten cermet fuels performed the poorest with regard to calculated k_{inf} values. Refractory carbide and graphite matrix candidates have lower cross sections and atomic masses and are thus capable of greater slowing down power than even the best W-isotopes. Although graphite has the highest moderating power of all of the presented high temperature materials (figure 2), reduced fuel loadings necessary to maintain fuel mechanical integrity and produce the high melting temperature (U,Zr)C fuel web does not allow for initial criticality using LEU without external moderating elements. Because of the ability of refractory carbides to be discretely loaded with particles of uranium containing compounds (such as UN, UC, UO_2 , etc.), higher overall U loading and moderating powers may be achieved, allowing for criticality without use of an external moderating element. Best k_{inf} performance is achieved with the use of a SiC matrix, however, SiC does not have the potential for as high operating temperatures as other refractory carbide matrix candidates. Moderated ZrC matrix fuel systems behave similarly to moderated graphite composite fuels and have potential for much higher operating temperatures in the hot hydrogen environment, ZrC and TiC fuels also have the potential unmoderated LEU engine designs.

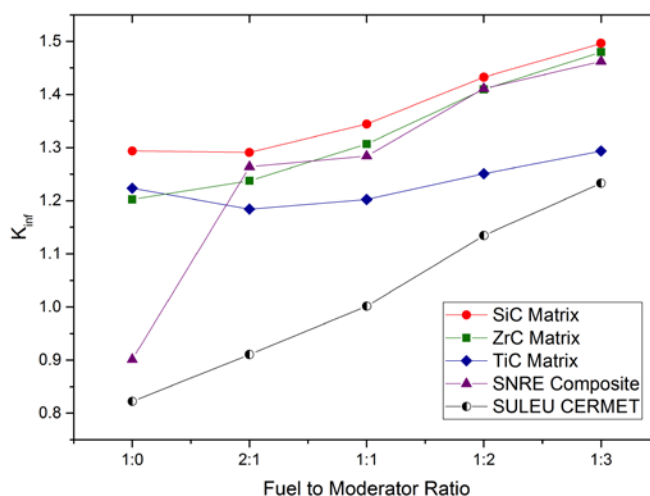


FIGURE 4. Calculated k_{inf} of nuclear thermal propulsion fuel system candidates.

CONCLUSION

Ultra-high temperature materials to enable nuclear thermal propulsion and LEU engine designs do exist, at varying levels of development status. It has been previously demonstrated that reference graphite and tungsten fuel systems developed during previous fuel programs can be used in a LEU engine with the assistance of isotopic enrichment or external moderating elements. Previous programs have shown that all-carbide fuel systems have the potential for the highest operating temperatures and good fuel endurance due to their extremely high melting temperatures and hot hydrogen compatibility. Refractory carbide fuel systems can allow for critical LEU engine designs without enrichment or external moderating elements, but exhibit the lowest level of development status. Ultimately, it should be kept in mind that the refinement of fuel design and specifications of the NERVA/Rover and GE-710 reactor programs was due to accumulated operational experience and reaction to experimental test data. For example, original NERVA/Rover graphite matrix fuels utilized discrete fuel particles dispersed within the graphite matrix, but later shifted design to the lower U density (U,Zr)C fuel web in order to reduce the buildup of thermal stresses between fuel particles and the graphite matrix which lead to intra-matrix cracking and fuel failure. This performance data is extremely valuable to accelerate initial future development/optimization efforts of derived LEU type engines and fuels. The presented study compares un-optimized refractory carbide matrix fuels to reference LEU reactor fuel systems only in order to qualify refractory carbide matrix performance. In order to verify the applicability of refractory carbide matrix fuels, initial experimental studies should aim to quantify acceptable fuel loadings, necessary fuel coatings, impact of thermal stresses, chemical stability at the matrix-particle or matrix-fiber interfaces, thermodynamic stability of the matrix under high temperature irradiation in a hot hydrogen environment, as well as capture limiting operating regimes. More detailed fuel studies to optimize fuel geometry and engine sizing are suggested to better qualify the performance of a loaded refractory carbide NTR and quantify the impact of fuel moderation on meeting engine performance and operating requirements.

ACKNOWLEDGMENTS

Kelsa Benensky is sponsored by a NASA Space Technology Research Fellowship.

REFERENCES

- [1] Venneri, P.F. and Y. Kim, *A feasibility study on low enriched uranium fuel for nuclear thermal rockets – II: Rocket and reactor performance*. Progress in Nuclear Energy, 2016. **87**: p. 156-167.
- [2] Joyner, C.R., et al., *Engine Design Attributes Relative to HEU and LEU Core Approaches for a Small Thrust NTP*, in *52nd AIAA/SAE/ASEE Joint Propulsion Conference*. 2016, American Institute of Aeronautics and Astronautics.
- [3] Patel, V., et al., *Comparing Low Enriched Fuel to Highly Enriched Fuel for use in Nuclear Thermal Propulsion Systems*, in *52nd AIAA/SAE/ASEE Joint Propulsion Conference*. 2016, American Institute of Aeronautics and Astronautics.
- [4] M. Eades, W.D., C. R. Joyner II, *Comparison of LEU and HEU Cermet Nuclear Thermal Propulsion Systems at 16,000 lbf Thrust*, in *Nuclear and Emerging Technologies for Space 2016*. 2016, USRA: Huntsville, AL.
- [5] Shabalín, I.L., *Ultra-High Temperature Materials I: Carbon (Graphene/Graphite) and Refractory Metals*. 2014: Springer Netherlands.
- [6] Taub, J.M., *A Review of Fuel Element Development for Nuclear Rocket Engines*. 1975: Los Alamos, New Mexico 8754.
- [7] Finseth, J., *Overview of Rover Engine Tests Final Report*. 1991: Huntsville, Alabama 35806.
- [8] *710 High-Temperature Gas Reactor Program Summary Report*. 1967: Cincinnati, Ohio 45215.
- [9] Haertling, C. and R. Hanrahan, *Literature review of thermal and radiation performance parameters for high-temperature, uranium dioxide fueled cermet materials*. Journal of nuclear materials, 2007. **366**(3): p. 317-335.
- [10] Lyon, L.L., *Performance of (U,Zr)C-graphite (composite) and of (U,Zr)C (carbide) fuel elements in the Nuclear Furnace 1 test reactor*. 1973, ; Los Alamos Scientific Lab., N.Mex. (USA). p. Medium: ED; Size: Pages: 63.
- [11] Stewart, M. and B.G. Schnitzler, *A Comparison of Materials Issues for Cermet and Graphite-Based NTP Fuels*, in *49th AIAA/ASME/SAE/ASEE Joint Propulsion Conference*. 2013, American Institute of Aeronautics and Astronautics.

- [12] Pelaccio, D.G., M.S. El-Genk, and D.P. Butt, *Hydrogen corrosion considerations of carbide fuels for nuclear thermal propulsion applications*. Journal of Propulsion and Power, 1995. **11**(6): p. 1338-1348.
- [13] Pelaccio, D.G., M.S. El-Genk, and D.P. Butt. *A review of carbide fuel corrosion for nuclear thermal propulsion applications*. 1993. United States.
- [14] Cooper Jr, R. *Potential Refractory Alloy Requirements for Space Nuclear Power Applications*.
- [15] El-Genk, M.S. and J.-M. Tournier, *A review of refractory metal alloys and mechanically alloyed-oxide dispersion strengthened steels for space nuclear power systems*. Journal of Nuclear materials, 2005. **340**(1): p. 93-112.
- [16] Zinkle, S.J., et al., *Overview of materials technologies for space nuclear power and propulsion*. AIP Conference Proceedings, 2002. **608**(1): p. 1063-1073.
- [17] National Research, C., S. Committee on Advanced Nuclear, and S. Symposium on Advanced Compact Reactor, *Advanced compact reactor systems proceedings of a symposium ; National Academy of Sciences, Washington, D.C., November 15-17, 1982*. 1983, Washington, D.C.: National Academy Press.
- [18] Rinehart, G.H., *Design characteristics and fabrication of radioisotope heat sources for space missions*. Progress in Nuclear Energy, 2001. **39**(3): p. 305-319.
- [19] Sears, V.F., *Neutron scattering lengths and cross sections*. Neutron News, 1992. **3**(3): p. 26-37.
- [20] Charlot, L.A., *Reaction of Hydrogen with Niobium and Tantalum in the ATR Gas Loop*. 1965, Battelle Northwest Laboratory: United States.
- [21] Savitskii, E.M., *Physical Metallurgy of Refractory Metals and Alloys*. 2012: Springer US.
- [22] Gangler, J.J., W.A. Sanders, and I.L. Drell, *URANIUM DIOXIDE COMPATIBILITY WITH REFRACTORY METALS, CARBIDES, BORIDES, NITRIDES, AND OXIDES BETWEEN 3500 AND 5000 F*. 1960, ; National Aeronautics and Space Administration. Lewis Research Center, Cleveland. p. Medium: X; Size: Pages: 28.
- [23] Bhattacharyya, S.K., *An Assessment of Fuels for Nuclear Thermal Propulsion*, T.D. Division, Editor. 2001, Argonne National Laboratory: Argonne, Illinois 60439.
- [24] Knight, T., D. Kaoumi, and S. Anghaie, *Rhenium compatibility with uranium dioxide at elevated temperatures*. AIP Conference Proceedings, 2001. **552**(1): p. 865-868.
- [25] F, H., N. J, and C. C, *Particle fuels technology for nuclear thermal propulsion*, in *Conference on Advanced SEI Technologies*. 1991, American Institute of Aeronautics and Astronautics.
- [26] Chandler, W.T. and R.J. Walter, *Hydrogen Effects in Refractory Metals*, in *Refractory Metal Alloys Metallurgy and Technology: Proceedings of a Symposium on Metallurgy and Technology of Refractory Metals held in Washington, D.C., April 25-26, 1968. Sponsored by the Refractory Metals Committee, Institute of Metals Division, The Metallurgical Society of AIME and the National Aeronautics and Space Administration, Washington, D.C., I. Machlin, R.T. Begley, and E.D. Weisert, Editors*. 1968, Springer US: Boston, MA. p. 197-249.
- [27] Webb, J.A., et al., *SPS Fabrication of Tungsten-Rhenium Alloys in Support of NTR Fuels Development*. 2011, Idaho National Laboratory (United States). Funding organisation: DOE-NE (United States).
- [28] Webb, J.A. and I. Charit, *Fabrication of Cermets via Spark-Plasma Sintering for Nuclear Applications*. JOM, 2014. **66**(6): p. 943-952.
- [29] Herbell, T.P., et al., *Effect of hydrogen on the strength and microstructure of selected ceramics*. 1990.
- [30] Chadwick, M.B., et al., *ENDF/B-VII.1 Nuclear Data for Science and Technology: Cross Sections, Covariances, Fission Product Yields and Decay Data*. Nuclear Data Sheets, 2011. **112**(12): p. 2887-2996.
- [31] Panda, B., R.R. Hickman, and S. Shah, *Solid Solution Carbides are the Key Fuels for Future Nuclear Thermal Propulsion*, in *Joint Army-Navy-NASA-Air Force Propulsion Meeting*. 2005: Monterey, CA.
- [32] M. G. Houts, S.K.B., J. A. George, T. Kim, W. J. Emrich, R. R. Hickman, J. W. Broadway, H. P. Gerrish, R. B. Adams, *Nuclear Cryogenic Propulsion Stage*, in *Nuclear and Emerging Technologies for Space*. 2012, University Space Research Association: The Woodlands, Texas.
- [33] Koenig, D.R., *Experience Gained from the Space Nuclear Rocket Program (Rover)*. 1986, Los Alamos National Laboratory: Los Alamos, New Mexico 87545.
- [34] Anatolii, G.L. and I.F. Ivan, *Selecting and using materials for a nuclear rocket engine reactor*. Physics-Uspekhi, 2011. **54**(3): p. 305.
- [35] Lanin, A., *Nuclear Rocket Engine Reactor*. 2012: Springer Berlin Heidelberg.
- [36] Youchison, D., et al., *A Tricarbide Foam Fuel Matrix for Nuclear Thermal Propulsion*, in *42nd AIAA/ASME/SAE/ASEE Joint Propulsion Conference & Exhibit*. 2006, American Institute of Aeronautics and Astronautics.
- [37] Holleck, H., et al., *U Uranium: Uranium Carbides*. 2013: Springer Berlin Heidelberg.

- [38] Butt, D.P. and T.C. Wallace, *The U—Zr—C Ternary Phase Diagram above 2473 K*. Journal of the American Ceramic Society, 1993. **76**(6): p. 1409-1419.
- [39] Powers, J.J., *Fully Ceramic Microencapsulated (FCM) Replacement Fuel For LWRs*. 2013.
- [40] Stiglich, J., et al. *Processing and Testing of Ultrahigh Temperature Fiber-reinforced Ceramic and Metal Matrix Composites*. in *AeroMat 2016*. 2016. Bellevue, WA: ASM International.
- [41] Herbell, T.P. and A.J. Eckel. *Ceramic matrix composites for rocket engine turbine applications*. in *ASME 1992 International Gas Turbine and Aeroengine Congress and Exposition*. 1992. American Society of Mechanical Engineers.
- [42] Wright, M.J., G. Ramachandran, and B.E. Williams, *Lightweight, Ultra-High-Temperature, CMC-Lined Carbon/Carbon Structures*. 2011: NASA Glenn Research Center; Cleveland, OH, United States.
- [43] Snead, L.L., et al., *Stability of SiC-matrix microencapsulated fuel constituents at relevant LWR conditions*. Journal of Nuclear Materials, 2014. **448**(1–3): p. 389-398.
- [44] Katoh, Y., et al., *Continuous SiC fiber, CVI SiC matrix composites for nuclear applications: Properties and irradiation effects*. Journal of Nuclear Materials, 2014. **448**(1–3): p. 448-476.
- [45] Snead, L.L., et al., *Handbook of SiC properties for fuel performance modeling*. Journal of Nuclear Materials, 2007. **371**(1–3): p. 329-377.
- [46] Venneri, P.F. and Y. Kim, *A feasibility study on low-enriched uranium fuel for nuclear thermal rockets – I: Reactivity potential*. Progress in Nuclear Energy, 2015. **83**: p. 406-418.

Autonomy for Space Reactor Power Systems

David M. Sikorski, Richard T. Wood

*Department of Nuclear Engineering, University of Tennessee, Knoxville, TN 37996
563-210-9889; dsikorsk@vols.utk.edu*

Abstract. The application of nuclear reactors for space power and propulsion presents unique operational and control challenges. Terrestrial nuclear power plants have relied upon varying degrees of direct human control and decision-making for operations as well as periodic human interaction for maintenance. However, physical inaccessibility of the reactor system and conditions for planetary or deep-space missions, such as communication time delays or blackouts, constrain the degree of human interaction possible for space reactor power systems (SRPS). To provide the necessary mission assurance, the SRPS must be able to respond to rapid events and adapt to evolving or degraded conditions without immediate human intervention for operations or any opportunity for repair or refurbishment. Thus, space reactor power systems must provide capabilities for operational autonomy. The desirable characteristics of autonomous control include intelligence, robustness, optimization, flexibility, and adaptability. This paper will discuss the basis for space reactor autonomy and describe the requirements for autonomous control of an SRPS.

Keywords: Autonomy, Reactor Control, Space Reactor

INTRODUCTION

A space reactor power system (SRPS) can provide reliable, mass efficient, long term power for both space and planetary surface applications. The application of nuclear reactors for space power and propulsion presents unique operational and control challenges. Terrestrial power plants rely upon direct human control and decision-making for operations as well as interaction for maintenance. In contrast, the physical inaccessibility of a space reactor system combined with conditions for planetary or deep space missions, such as communication time delays or blackouts, significantly restricts the opportunity for human interaction. It is possible that planetary surface power systems may face less extreme isolation conditions than deep space power systems due to potential human proximity and limited maintenance capabilities. However, human safety, resource limitation, usage priority, and economics are among the considerations favoring the minimization of direct and continuous human interaction for the management of the SRPS. To provide the necessary mission assurance, the SRPS must be able to respond to rapid events and adapt to evolving or degraded conditions without immediate human intervention for operations or any opportunity for repair or refurbishment. Thus, space reactor power systems must provide capabilities for operational autonomy.

Terrestrial reactors may also benefit from operational autonomy. Although traditionally terrestrial reactors consist of large scale plants for power generation, developing countries aiming to reduce reliance upon carbon emitting power sources may lead to an increase in consideration of small modular reactors to generate power for less established infrastructures. The Generation IV reactor concept goals of optimized investment recovery and economic efficiency promote reductions in plant operations and staffing. Higher levels of automation, fault tolerance, and advanced diagnostics are needed to provide autonomous operations for both Gen IV systems, as well as the SRPS. In essence, both terrestrial nuclear systems and deep space and planetary SRPS-enabled missions would benefit from this kind of operational autonomy.

AUTONOMY

Autonomy can be understood by examining the distinction between automated and autonomous control. Consideration of the Greek root words illustrates the difference. *Automatos* means self-acting while *autonomos* means self-law. Similarly, automated control involves self-action while autonomous control involves self-governance, or independent action. The self-action of automation does not suggest autonomous behavior or independent action; however, it is an inherent characteristic of autonomy. An automated system may function without supervision and includes at least a limited authority within the control system, however it may not govern its own actions. In other words, automated control executes straightforward, predefined actions, while an autonomous system may make decisions and determine its own action. Thus, autonomous control implies an embedded intelligence.

Automated control is typically implemented through rigidly defined control loops for individual processes. These control actions are provided by predetermined, fixed algorithms with application only to the localized system. Although real-time interaction is unnecessary for normal operations, the significant decisions are left to human operators. In contrast, autonomy integrates plant control, diagnosis, and decision-making. Diagnosis and decision-making provide adaptability to changing conditions, and may even include self-maintenance. This functionality is made possible via flexible control architecture design. Although automated control exists in many applications, autonomous control experience is much more limited.

As previously mentioned, automated control is an inherent characteristic of autonomy. Thus, autonomy extends the scope of primary control functions but may include automated control in all modes of operation. Autonomy may also include continuous monitoring and diagnosis of performance, safety, and component health. This diagnostic information provides data for flexible control to address anticipated and unanticipated events, protection of life-limited components such as batteries and actuators, and adaptation to changing conditions. The autonomous control system may also use this data for validation and maintenance of control system performance.

Key characteristics of autonomy include intelligence, robustness, optimization, flexibility, and adaptability[1]. System intelligence reduces the need for human interaction and decision making. This implies inherent authority over planning and decision-making, which allows for a whole-system, integrated approach. Planning, decision-making, and anticipatory actions are performed based on system knowledge and event prediction. State identification and condition monitoring is facilitated by real-time diagnostic and prognostic abilities. Intelligence may also make use of real-time data as a tool for self-validation.

Robustness is achieved by an environmentally rugged implementation, accounting for design uncertainties and unmodeled dynamics, fault management, and self-maintenance or self-healing. Fault management consists of fault avoidance, fault removal, fault tolerance, and fault forecasting. Fault avoidance can be accomplished through formal software design methods, object oriented software architecture, and software module reuse. Fault removal can be achieved through formal software inspection, data flow testing, and fault injection testing. Fault tolerance can involve redundancy, design diversity, high reliability implementation, and error detection and recovery. Fault forecasting includes reliability modeling, data collection and data driven modeling, operational profiling, and rare event prediction. Finally, self-maintenance and self-healing may be enabled by making use of captured design knowledge and prognostics for predicting failures, fault detection and isolation, and other self-correcting features.

Optimization is characterized by rapid response to demands, minimal deviation from target conditions, and efficient actuator actions. These capabilities are made possible by enabling flexibility and adaptability of the control system. Otherwise known as functional reconfigurability, flexibility and adaptability features make use of diverse measurements, communications, and alternate control solutions to adapt to a changing or degrading environment. This functionality is ultimately enabled by the inherent ability of the autonomous control system to make decisions and reconfigure itself.

The characteristics discussed above represent the possibilities of autonomy but they do not constitute a necessary set. Therefore, autonomous control can be viewed as providing a spectrum of capabilities with automated control representing the lowest extreme or baseline of the continuum. The incorporation of increasing intelligence and fault

tolerance moves the control capabilities further along the spectrum of capabilities. Higher degrees of autonomy are characterized by greater fault management, more embedded planning, and goal-setting, and even self-healing. The realization of full autonomy involves learning, evolving, and strategizing independent of human interaction or supervision.

APPLICATIONS OF AUTONOMY IN SPACE

NASA has implemented autonomy in space for surface exploration and spacecraft applications. Autonomy provides reduced mission cost, increased communication efficiency, and allows for independent operation during communication blackouts. Autonomy for surface exploration rovers includes functionality for navigation, target identification, and science package manipulation. Spacecraft autonomy has focused on guidance, navigation, and control.

Rover autonomy has been demonstrated by examples from Mars surface exploration efforts. The Mars Pathfinder rover Sojourner first began exploration of the Martian surface in July 1997[2] with limited autonomous capability. Although requiring repetitive ground monitoring, Sojourner's autonomous functionality consisted of navigation, resource management, and contingency response. Rover autonomy capability was later expanded with the twin Mars exploration rovers, Spirit, and Opportunity. These rovers had capabilities for autonomous planning, navigation, obstacle detection, and resource management.

Spacecraft autonomy has been demonstrated by the Deep Space 1 mission. The spacecraft was launched in October 1998 as a platform for testing high-risk advanced technologies in space[3]. The Deep Space 1 craft employed autonomous navigation as well as an experimental artificial intelligence system called Remote Agent (RA). The Remote Agent system was designed to execute spacecraft activities and perform on-board planning. This system was activated during the mission and was allowed to take control of the spacecraft for a limited period of time.

These examples demonstrate the applications of space based autonomous control and its ability to perform tasks under the necessary degree of autonomy desired. However, as discussed in the following section, there are many challenges to address in order to enable autonomous control of an SRPS.

CHALLENGES AND REQUIREMENTS

The control and protection paradigm of the space reactor differs from that of terrestrial reactors in that terrestrial reactors have traditionally relied upon immediate and readily available human interaction. This includes both direct control and decision making for operation and periodic intervention for maintenance and refurbishment. The SRPS, however, must allow for remote, continuous, and often unattended operations for missions that may last in excess of a decade. Due to communication delays and blackout, reliance upon human interaction for continuous supervision and management is not feasible. Thus, a high level of autonomy is needed.

The characteristics of an SRPS autonomous control system are determined by the challenges and constraints of launching and operating a nuclear reactor in space with minimal human interaction. Launch requirements limit the mass and volume of the system, and therefore redundancy and diverse systems are limited. This limitation affects system robustness by reducing fault tolerance. In order to improve system robustness, functional and environmental robustness must be emphasized. For deep space or planetary surface power, inaccessibility and communication constraints mean that maintenance is unlikely or impossible, resulting in the need for long-life dependability. Automated control capability which has been developed and demonstrated would allow ground control to assume a supervisory role without the need to take direct, active control[4]. However deep space operations require the ability to detect, diagnose, and adapt to evolving or degrading conditions as well as rapidly respond to anticipated events without requiring a reactor scram. Space reactor power must also be available on demand due to the critical and time sensitive nature of some spacecraft maneuvers. Along with the likelihood that restart capability would be unavailable for an SRPS, this requires that a reactor scram in response to events must be minimized or entirely

avoided. Thus, in contrast to terrestrial nuclear power plants, mission assurance must be emphasized over reactor protection.

Essentially the autonomous control system must provide capability to meet necessary control objectives while overcoming substantial uncertainty, disturbance, and degradation without the necessity of human intervention. As such, the system is to act as an extension of the human controller, assuring reliable and continuous operation of the SRPS for extended lifetimes and harsh conditions, with the need for only occasional human supervision.

FUNCTIONALITY

Basic Functionality

Necessary autonomous control functions of the SRPS are chosen based on the anticipated operational modes, including startup, normal operation, reactor protection, contingent operation, and end-of-mission shutdown. At minimum, the SRPS controller should be capable of automatic switching between normal operational modes. Furthermore, the system must allow for the protection of the reactor in the circumstance that desired operational conditions cannot be achieved[5].

Normal power operation phases include power ascension, steady state power and load following, and power reduction. Under normal conditions, operation can be simple as inherent feedback effects preserve stability and provide for load following in response to minor fluctuations. Transients in thermal loading such as turbine failure are treated as off-normal events. Examples of other off-normal events include design uncertainties, load and power interruptions, control element jamming, interference or interruption of actuator signals, degradation and damage of heat rejection system, control processor faulting, software errors due to rare events, sensor failure, interference or interruption of sensor signals, sensor drift, signal conditioning, electronics drift, sensor noise, and communication failures or retransmissions. Rapid power runback would serve as the most likely protective action. When SRPS operation is restricted due to environmental or power system limitations, contingent operation may occur.

Off-Normal Event Response

Autonomy becomes especially relevant in response to off-normal events. Responses include both a reflexive and deliberative element. The reflexive element addresses reactor protection. In contrast to terrestrial reactors where a reactor scram is the primary defense against adverse and off-normal conditions, it is likely that the SRPS must be required to operate until the end of mission, as restart may not be possible. Therefore, reactor protection is provided by diversity and redundancy to anticipate challenges to regular power operation. One means of protection is a limitation system. This system defines acceptable operating regimes and overrides actions that would drive the system out of the prescribed limitation boundaries. Thus, it acts as a bounding system, providing checks against operation outside of desirable conditions. The system's primary response is to run back reactor power to safe low-power conditions, if necessary. However, as it is imperative that power remains available during spacecraft operations, the SRPS controller must be able to disable this protective element or expand its operational boundaries on demand from either the spacecraft or mission control.

The deliberative element of off-normal event response addresses mission assurance. It is the deliberative (i.e. determination and decision) nature that most distinguishes autonomous control from conventional automation. In the context of operational control, this functionality involves the detection of and response to degradation or failure. One crucial portion of the deliberative element is fault management which provides for detection, diagnosis, and adaptation under changing SRPS conditions. The necessary functionality of a fault management system includes detection and identification of device faults, detection and identification of anticipated events and transients, tracking of system parameter changes, and configuration control. The first of these is achieved through a model-based and/or data-driven algorithms. Empirical models or first principles estimation can be used in parameter tracking. Each of these capabilities can be used to create a system dynamics model that can be adjusted and employed for fault prediction or control system performance evaluation. Lastly, configuration control functions are also needed for managing transitions among predefined control strategies and algorithms, as is necessary for fault

recovery. The deliberative element also includes monitoring, diagnostics, and validation of the performances of both the SRPS and the control system itself. Thus, the control system can identify incipient events (transients or failures) and perform anticipatory, rather than reactionary action. Furthermore, the system can determine measures to protect vulnerable and life-limited components and ensure constant and reliable reactor operation.

Additional Functionality

As previously stated, SRPS autonomous control centers around automated control under normal operating conditions. Thus, the control system's main function is the generation of commands to achieve a prescribed operational state. Additional functionality supporting confirmation of control system performance includes command verification, interconnected system control coordination, and strategy enforcement, among other features. Implementation of such features often involves many diverse algorithms for comparison with controller command, management of events according to some predetermined sequence, inclusion of feedforward action, or representation of unmodeled dynamics, and control strategy adaptation.

To manage performance, the SRPS autonomous control functionality must continuously assess the condition of the control system and the SRPS to determine when predetermined adjustments to the controller should be made. These assessments include monitoring of the control system effectiveness, identification of the dynamic state of the SRPS, and determination of the condition of key system components. State estimation algorithms, component condition monitoring, process system diagnostics, and control parameter adaptation can all be employed for such assessments.

Data management and communications are related capabilities and have both traditional and autonomous functionality intended to support system integration and autonomy. Data acquisition and signal processing provide the necessary data for control and monitoring, and signal validation provides information on data quality. The functional elements of communications include data and control signals at the device level, information and commands at the system level, and status and demands at the spacecraft level. To effectively integrate data and information at each level, a well-defined functional architecture is required. This architecture must further be coupled to a capable physical infrastructure supporting the reliable and timely flow of information. Such a conceptual architecture presented by Wood et al[5] is provided in figure 1.

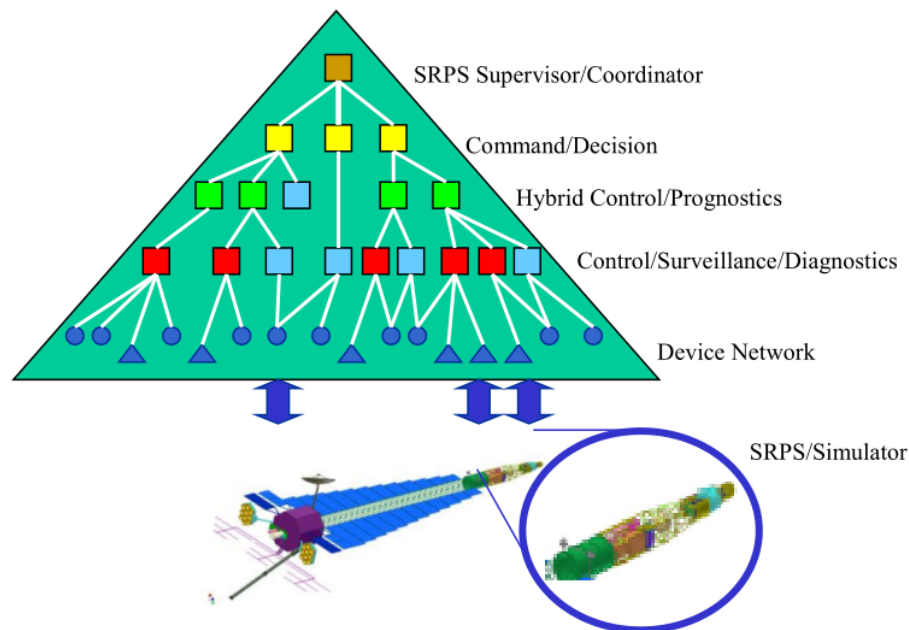


FIGURE 1. A hierarchical framework concept for autonomous control and system integration of an SRPS.

This diagram illustrates the hierarchy of information and functionality as previously described, with an additional supervisory level, and multiple control levels with diagnostic and prognostic functionality.

ENABLING AUTONOMOUS CONTROL

Assessment of autonomous control requirements is necessary early in the SRPS design process to determine the level of autonomy needed. This required degree of autonomy is affected by mission requirements, technological readiness, design trade-offs, and resource constraints. The level of responsibility entrusted to the autonomous control system and the degree of mission risk mitigated by the system will determine the extent to which the characteristics of autonomy are realized.

There are many factors which can influence the degree of autonomy selected for an SRPS control system. These include the potential for human interaction, performance goals, system demand complexity, technological constraints, mission risk, and balancing simplicity (reliability), and complexity (adaptability). The level of autonomy used for SRPS control is greatly affected by the trade-offs between reliability and mission assurance. While it is important to maintain a reliable SRPS control system, this is meaningless if the system cannot handle SRPS degradation. Such a case will lead to a reliable control system that is rendered useless due to the changes in the SRPS.

Finally, as previously mentioned, there is not a strong experience base for autonomous control. Specifically, autonomous control has yet to be implemented in the operation of a functioning terrestrial power plant. An investigation of the state of reactor control and autonomous control technologies reveals a technology gap indicative of a need for research, development, and demonstration (RD&D) activities toward the realization of autonomous control for an SRPS. Key elements of this necessary RD&D include establishment of a suitable functional architecture, development of foundational modules for the support of autonomy, and demonstration of the capabilities and applications of autonomous control.

CONCLUSION

For applicability to space missions, the SRPS control system must allow for continuous, remote, unsupervised operation in extreme environments in excess of a decade. Uncertainties, degradation, rare events, and communication delays present instrumentation and control challenges that cannot be satisfactorily addressed by automated control systems. Autonomous control is required by such a system requiring response to rapidly changing and degrading conditions without prompt human intervention.

Wood et al[5] suggests autonomous control can provide:

- intelligence to confirm system performance and detect degraded or failed conditions,
- optimization to minimize stress on SRPS components and efficiently react to operational events without compromising system integrity,
- robustness to accommodate uncertainties and changing conditions, and
- flexibility and adaptability to accommodate failures through reconfiguration among available control system elements or adjustment of control system strategies, algorithms, or parameters.

Nonetheless, autonomous control has yet to be realized for an operating nuclear power system. Thus, RD&D is required to lay the groundwork for the implementation of an autonomous control system for an SRPS. Environmentally robust sensors, fault management and reliability assessment methods, software reliability quantification, system diagnostics, component prognostics, intelligent control, and decision algorithms are among the many areas of research that should be explored in order to further the development of autonomous control.

REFERENCES

- [1] Wood, Richard T., "Enabling Autonomous Control for Space Reactor Power Systems," Proceedings of the 5th International Topical Meeting on Nuclear Plant Instrumentation, Controls, and Human Machine Interface Technology. (2006).
- [2] Mishkin, Andrew H., et al., "Experiences with Operations and Autonomy of the Mars Pathfinder Microrover," Aerospace Conference, **1998 IEEE. Vol2**, (1998).
- [3] Rayman, M. D., et al., Results from the Deep Space 1 Technology Validation mission," Proceedings of the 50th International Astronautical Congress, American Institute of Aeronautics and Astronautics, **Acta Astronautica 47**, 475-488 (1999)
- [4] Winks, R.W., Wilson, T.L., and Amic, M., "B&W PWR Advanced Control System Algorithm Development," Proceedings of the Advanced Digital Computers, Controls, and Automation Technologies for Power Plants, **EPRI TR-100804**, (1992).
- [5] Wood, Richard T., et al., "Autonomous Control capabilities for Space Reactor Power Systems," AIP Conference Proceedings. (2004).

TERRA Project: a Brazilian View for Nuclear Energy Application to Space Exploration

Lamartine Guimarães^{1,2}, Guilherme Borges Ribeiro¹, Jamil Alves do Nascimento³,
Élvis Falcão de Araújo¹, Francisco Antônio Braz Filho¹, Artur Flávio Dias¹ and
Valeria S.F.O. Leite¹

¹*Institute for Advanced Studies, São José dos Campos, SP, Brazil 12228-001*

²*UNIP, São José dos Campos, SP, Brazil*

³*National Independent Contractor retired, São José dos Campos, SP, Brazil
55-12-3947-5474; and guimarae@ieav.cta.br, lamartine.guimaraes@pq.cnpq.br*

Abstract. The TERRA project is a Brazilian effort to develop the enabling technologies to generate electric power in space. Those technologies are an micro reactor core concept, a Stirling convertor for small to medium and a Brayton convertor for medium to large electric power output. Besides those technologies, it is also considering heat pipes design and passive multi fluid turbines. The first reactor core concept was completed this year (2016), a complete paper is being prepared and it is in the review process. A Stirling machine was built and it works quite reasonably. A copy of this Stirling machine was built and is now undergoing testing. The Brayton cycle initial design project was intended to use a gas furnace to simulate the nuclear heat. A design retrofit was necessary and decision was made to change the furnace from gas to electric. A detail electric design project was requested to the market. This detail design was delivered this last august. It is hoped that the 300 kW electric furnace will be requested next year. A program to design heat pipe is being developed to evaluate a combination of the structural and working fluid materials. A new benchmark is under development to test the passive multi fluid turbine. A passive multi fluid turbine is an evolution of the Tesla turbine. All these events will be presented at the conference with a little more of detail.

Keywords: reactor core concept, Brayton cycle, Stirling machines, heat pipe, passive multi fluid turbine.

INTRODUCTION

The TERRA project [1,2,3,4] is a Brazilian effort to develop the enabling technologies to generate electric power in space. It is important to emphasize that the expression “enabling technology” is used specifically for the Brazilian case. Also, in the Brazilian case, it is considered the possibility to apply this technology to generate heat and electric energy at the ocean floor as technology to help to explore the pre-salt oil or at isolated places far away from the National electric grid and at a National accident scenario where there would be a total loss of the National electric grid. The TERRA name is a Portuguese acronym that means, “*advanced fast reactor technology*.” For the TERRA project, the interested power ranger is in-between 0.1 to 1000 kWe. The technologies of interest at this moment are being pursued as independent and they fall in the level 2 at the TRL NASA scale [5]. Also, due to the desired power range the conceptual devices are call “micro”, as in micro core or micro reactor. The word micro refers to the core and the power plant only. The specific technologies of interest to the TERRA project are: a micro reactor core concept [6,7], a Stirling convertor and a Brayton convertor [8,9,10]. The Stirling convertor is desired for a small to a medium electric power output and that means the range between 0.1 to 200 kW. The Brayton cycle is envisioning for a medium to a large electric power output, which means the upper part of the previous scale, 200 to 1000 kW. Besides those technologies, it is also looking into heat pipes design and passive multi fluid turbines [11,12]. The heat pipes are envisioning for two types of roles. The first to extract heat from the core and to deliver it to the convertor. And the second one to dissipate the excess heat naturally generated by thermal cycles. The passive multi fluid turbine is a bet

from the TERRA project in which, it is believed that this kind of turbines may improve thermal cycle efficiency or substitute completely conventional gas turbines. The passive multi fluid turbine is an evolution of the Tesla turbine. In addition, an acronym was created to it based on Portuguese language – TPFM, which means exactly passive multi fluid turbine.

This contribution is divided in five sections in which it is discussed some challenges found in each development. In addition, it gives a status of the development and hints where it leads.

FIRST MICRO REACTOR CORE CONCEPT

The first micro reactor core concept was obtained by a series of argumentation, supposition and very hard computational calculation [6,7] using the Monte Carlo N-Particle program MCNP. Figure 1 presents a scheme of the first micro core reactor concept. Some of its form has inspiration on [13,14,15]. That form may be found in other places and efforts [16]. Figure 1a is a radial cut each hexagon is a fuel element. The yellow dots are graphical representation of heat pipes. The red color, or the in-between the dots, represents the mixture of fuel plus lead. The fuel is constituted of micro spheres of UN highly enriched for this calculation. The hexagonal can is made of Mo13Re. Criticality is only achieved with the set of seven elements. The hexagonal can, called canister has a 125 mm from wall to wall. Which means a core of 375 mm in (pseudo) diameter. Figure 1b presents a longitudinal cut, perpendicular to the first one. It is important to emphasize that both figures are not to scale. From edge to edge, there are 556 mm. As may be noted, the core is fully covered by reflector and shielding. All calculations indicate that the proposed arrangement would work at full power for 8 years. Which is a minimum time requirement. Some of the initial suppositions may be too conservative. A few variations of this design would be verifying the effect in size, arrangement and power level, by reducing enrichment, experimenting with UO₂, and considering a more detailed thermo-hydraulics. In addition, this is, certainly a first result. It requires rechecking. Nevertheless, this is a good refining starting point.

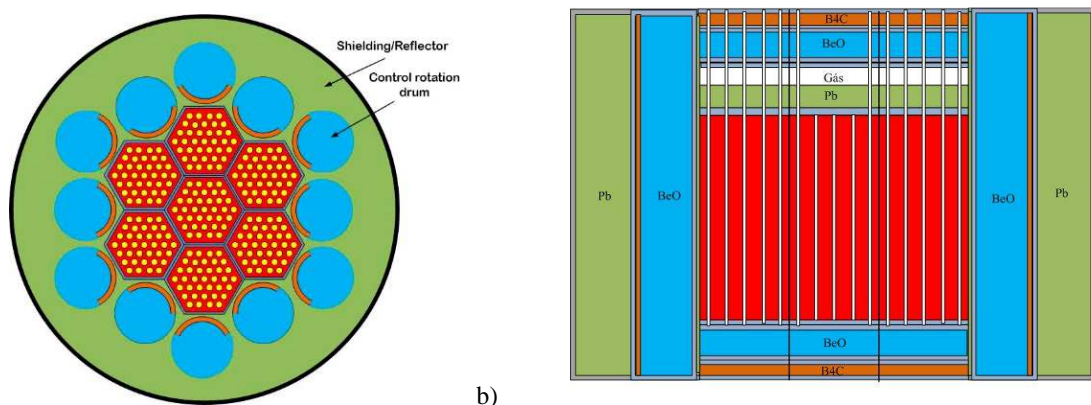


FIGURE 1. a) Represents a radial cut of the micro nuclear reactor. Each hexagon has 125 mm from wall to wall. b) Represents a transversal cut of the micro nuclear reactor. From edge to edge, it holds 556 mm. It is important to emphasize that both figures are not to scale.

STIRLING HEAT CONVERTOR MACHINE

The first work with Stirling machines, at the Institute for Advanced Studies (IEAv), dated from 2011/2012. At that time, it was received a Stirling machine as a donation from *Empresa Brasileira de Pecuária e Agricultura* (EMBRAPA), to our interest studies [4], shown at Figure 2a. These studies did not result in a successful device at first [1]. In addition, the materials used to build the EMBRAPA donation were very poor. That was supposed to be that way once the purpose of EMBRAPA was to build a low-cost device. At IEAV an attempt was made to improve the machine but the one built at that time had serious flaws [1], Figure 2b. In 2015, it was decided to scrap what has been done so far and a new attempt was made with the EMPRAPA model. The basic problems with that machine were

identified and, thus, the machine presented in Figure 3 left side was built. During the year of 2016, the improved copy shown in Figure 3 right side was built.

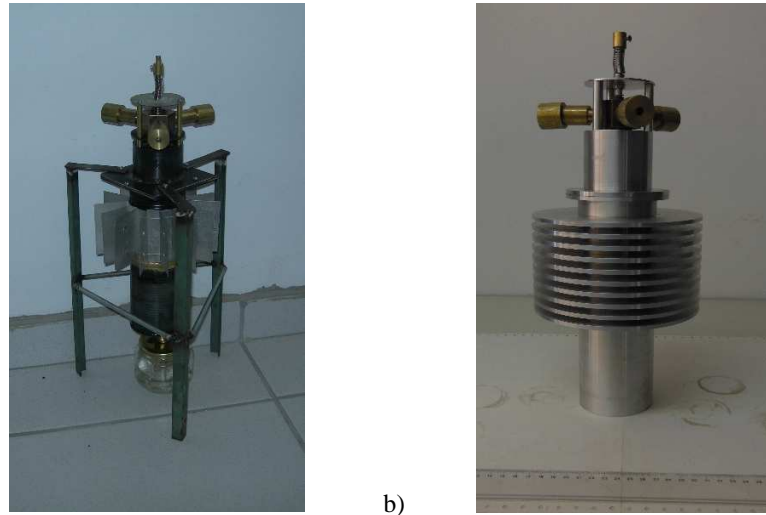


FIGURE 2. Stirling Heat Converter Machines. a) First Stirling machine donated by EMBRAPA. b) First Stirling Machine built at IEAv. The flaw of this one is that the heat sink works as a heat accumulator, no dissipation effect was achieved.



FIGURE 3. Stirling Heat Converter Machines. The left one was the first built and it is dated from 2015. The right one is the second to be built and it is dated from 2016.

The new Stirling machines will be copied and modelled optimization studies are planned. So far mechanical power is extracted from it. A proper inductor is being designed using samarium-cobalt (SmCo) magnets in order transform mechanical into electric energy. In addition, scaling in size is being considered. During the conference a film of the Stirling machine working will be presented.

BRAYTON CYCLE

So far, the Brayton cycle is the more complex and large piece of equipment being built for the TERRA project. Certainly, the Brayton cycle is the preferred energy convertor for the power range between 200 and 1000 kWe [13,16]. That is also the case for the project TERRA. Unfortunately, due to funding continuity problem the building of this Brayton cycle is proven treacherous. The parts completed are both heat exchangers from the heat source and the cold sink and the water box. Figure 4 shows a full schematic of the desired Brayton cycle being built. The water box is arranged over a metal structure it has in side some 4500 liters of water. The water box acts as the heat sink. Under the water box one may see a small wood structure that supports the modified NOELLE 60290. That is an APU for the Mirage M-III airplane. At the IEAv's Thermal Cycle Laboratory, there are two NOELLEs 60290 from Mirage M-III and two from the Mirage 2000, recently (towards October 2016) received. Initially, it was planned to use for the Brayton cycle the Mirage M-III APU. But now with the new ones of the 2000, it is preferred to use the new ones. The change occurred due to an inspection in one of the metal spheres of the turbine bearings was found cracked. Spare parts for the M-III are very difficult to find. Therefore, we solicited the 2000 APU. Now we must disassemble them and remove the combustion chamber. After that a redirection of the working fluid flow path must be realized. This mechanical work will be performed at the IEAv own mechanical shop. The connecting pipes and the flanges are being acquired separately. In 2016, temperature, pressure and flow sensors were acquired. A data processing unity was also acquired. One of the largest piece of equipment is the furnace, which is shown as the grey open box at the side of the dummy. The furnace is an electrical one and capable of generating up to 300 kW, with the operating temperature at the top of 750 °C (1023 K). The detailed executive project for this furnace was obtained this year (2016). It is expected that the furnace according with the specifications will be procured in this 2017. The assemblage of the cycle should start by the end of 2017 and be terminated with first experiment running at the second semester of 2018, hopefully.

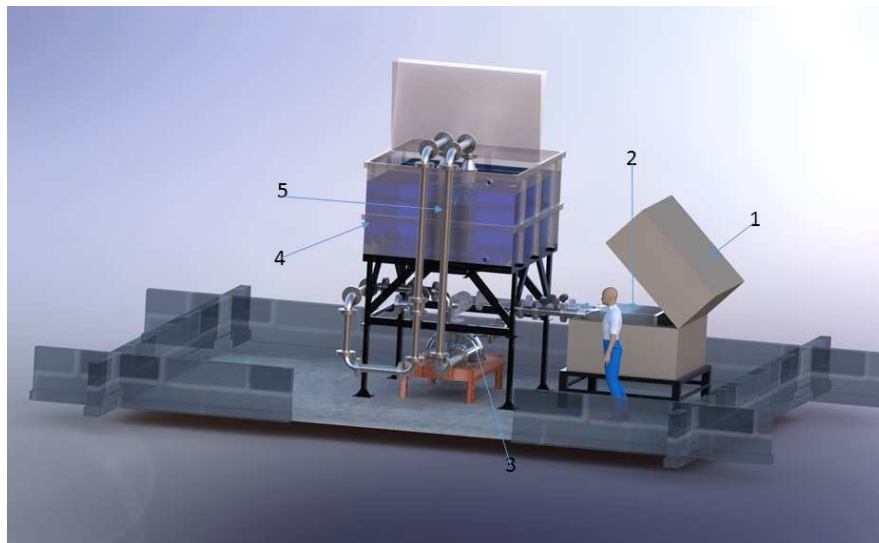


FIGURE 4. The Brayton cycle scheme to be built at IEAv. This drawing is to scale. 1 – 300 kW furnace. 2 – Heat exchanger from heat source. 3 – Noelle 60290 APU turbine. 4 – Water box heat sink. 5 – Heat exchanger inside the water box heat sink.

HEAT PIPE

This year of 2016, there was a breakthrough in heat pipe experiment, at IEAv, as the first thermo-siphon was built and experimented during the month of November. Figure 5 shows the experiment set up fully instrumented. The white PVC tube at the top contain the cold sink and is in contact with the thermo-siphon condenser volume. The wrapped middle part contains the adiabatic section of the thermo-siphon. The thermo-siphon evaporator region is inside a stainless-steel vessel. The stainless-steel vessel is the heat source, and contains a water bath, which warms up by an external gas burner. The water bath boiled at atmospheric pressure (98 ± 1 °C). The thermo-siphon operates best in vertical position once it is the gravity force that brings the condensate back to the evaporator. The thermo-siphon does not have a wick or a groove or a set of both. Nevertheless, a thermo-siphon is an intermediate step to produce heat pipes. This thermo-siphon is made of cooper and uses water as a working fluid. The cooper tube is 1100 mm long and 22 mm of internal diameter. The evaporator and condenser have the same length 300 mm, and the adiabatic part is 500 mm. Higher temperatures will be pursued as the laboratory has an electric furnace that may reach up to 1300 K. The reason for using the set up shown in Figure 5 was safety. Cooper tubes have the tendency to break catastrophically if exposed to moderately high temperatures. Provisions are being made to build a stainless steel thermo-siphon as the next step. All this experience and data will also help the development of a computation model that will allow heat pipe modeling.



FIGURE 5. Shows the first experiment set of a cooper-water thermo-siphon performed in the end of 2016. The thermo-siphon must run in the vertical optimally because it does not have a wick inside the tube.

PASSIVE MULTI FLUID TURBINE

The passive multi fluid turbine (TPMF) is an evolution of the Tesla Turbine [11,12]. The name “passive multi fluid turbine” was created at IEAv. The TPMF is passive in the sense it does not require any external effect to work. All it is required is availability of some fluid with energy content. The “multi fluid” comes from the fact that the same device may operate with any fluid, in any thermodynamic state (liquid, gas or the mixture of both). The basic principle of a Tesla turbine is maintained at the TPMF. Both require a fluid flow tangent to a disk. Shear stress pushes the disk, which is connected to an axis. The push given by the fluid generates rotation kinetic energy on the axis. Some of the initial experiments at IEAv could reach 66,000 RPM on the axis. So far, at IEAv, three (3) of these turbines were built for different purposes and with different materials. The last one is shown in Figure 6a. This TPMF was used in a concept demonstrator showed in Figure 6b. Compressed air feeds to the turbine in a controlled fashion. The objective

is to generate electric energy and turn on the four (light emission diodes) LED lamps at the top of the set up. The turbine axis kinetic energy is converted into electricity and one by one of the LED lamps are turned on. Power was generated in pre-defined way. The load for each lamp was maintained, despite the increase in electric energy to power on each new lamp. The control parameter is the airflow. Obviously, in that case compressed air was provided by an external source, in an open cycle. Figure 7 shows a follow up experiment where a small Rankine cycle was built as a test workbench to produce steam to allow the turbine to operate in a closed loop. That experiment produce results indicating that the TPMF will work nicely in a closed loop. However, the workbench set up had flaws that need fix up. At this moment, the workbench components are being re-drawn and build. One of the problems that happened with the first closed loop workbench affected the production of steam. It was not enough to maintain the turbine pressure inlet at steady state. One had to settle for a very slow decaying ramp through a reasonably long time interval. The new steam generator will have a larger steam production and a larger heat source. One expects that the new workbench will start producing results by the end of 2017. In addition, a new TPMF is being considered and designed. It is important to emphasize that the Rankine workbench is an intermediate step, while the Brayton cycle is under construction. The whole idea is to evaluate the performance of the TPMF at the Brayton cycle. There are two possibilities for using the TPMF in a Brayton thermal cycle. First in tandem with an ordinary gas turbine, taking advantage of the residual heat content of cycle and helping to increase cycle efficiency. Second, as a full substitute of the Brayton cycle gas turbine. The first option is more direct and requires a Brayton cycle working, only. The second option is a bit more complex. Nevertheless, the experiments with the Rankine workbench lead to an interesting preliminary result [12]. That is to utilize the TPMF as passive safety feature added to water reactors, as for instance the Fukushima type. The fact was that during the entire Fukushima accident the availability of high pressure and high temperature steam was great. But there was no means to convert that thermal energy into electric energy and maintain the emergency cooling system properly working. The use of a TPMF as part of the emergency cooling system is a possibility for that. This concept is discussed in some detail at [12].

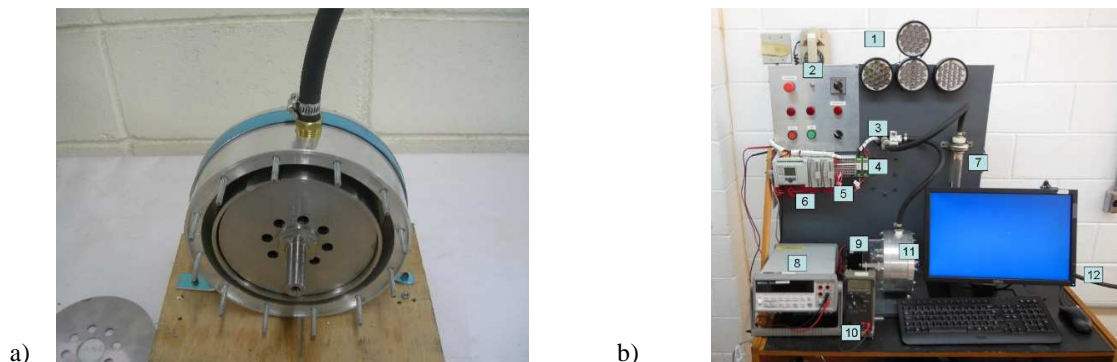


FIGURE 6. a) Vision of the internals of a gas passive multi fluid turbine. b) This experiment set up generates electricity to power the four led lamps on the top portion of the panel. Air flows through the turbine and is controlled through the proper rotation. The meaning of the numbers is: 1 – Set of LED lamps to be fed by the TPMF power. 2 – Panel guiding lamps to display the devices operational status. 3 – Airflow regulating valve. 4 – Coupling relay set. 5 – Borne set. 6 – PLC (Programmable Logic Controller). 7 – Flow meter. 8 – Current meter. 9 – Alternator. 10 – Voltmeter. 11 – TPMF-3 turbine. 12 – Compressed air inlet system.



FIGURE 7. Experimental Rankine workbench to gather TPMF parameters [11].

CONCLUSION

As may be seen from the above discussion all the technologies presented here, as part of the TERRA project, are enabling technologies, from the Brazilian point of view, to the purpose of space application. However, it may be applied to other day-to-day application. Certainly, the TERRA technologies are still in the research and development phase. One estimates that the development phase of most of those is TRL 2, and a few at beginning of TRL 3. The only technology that is not being handled experimentally is the reactor core work. A first concept is ready, and we are to publish a full paper about it.

The Stirling machine will be reproduced. In addition, a proper inductor will be attached. The possibility of flying one of these copies in a sounding rocket is doable given the availability of such rocket at the center. There is also the possibility to pass the Stirling machine to private developer. The Brayton cycle is continuing its development. Budget cuts are the main reason for delays. Each piece of the cycle is expensive. The heat pipe development has had a slow beginning. However, it is picking up speed. The TPMF is also a development that one considers to present to a private developer. Even though the private sector may envision its application in sectors other than space, clearly there will spin offs back to the space application. In all, spite of the economic crises that is holding Brazilian economy, there are opportunities worth pursue.

ACKNOWLEDGMENTS

The Authors would like to thank the “*Conselho Nacional de Desenvolvimento Científico e Tecnológico (CNPq)*,” under the project number 454113/2016-1 that allowed the first author to participate and present this contribution at NETS 2017.

REFERENCES

- [1] Guimaraes, L.N.F., Ribeiro, G.B., Braz Filho, F.A., Nascimento, J.A., Placco, G.M., de Faria, S.M., “Technology Development for Nuclear Power Generation for Space Application,” in proceedings of *International Nuclear Atlantic Conference (INAC 2015)*, edited by ABEN, Rio de Janeiro, RJ, Brazil, 11 pp., (2015).
- [2] Guimaraes, L.N.F., Camillo, G.P., Placco, G.M., Barrios Jr., A.G., Nascimento, J.A., Borges, E.M., Lobo, P.D.C., “Basic Research and Development Effort to Design a Micro Nuclear Power Plant for Brazilian Space Application,” *Journal of British Interplanetary Society*, **54**, 1-6, (2012).

- [3] Nascimento, J.A., Guimaraes, L.N.F., Ono, S., Lobo, P.D.C., “Advanced Micro Reactor for Space and Deep Sea Exploration: a Scientific Brazilian Vision,” in proceedings of *International Nuclear Atlantic Conference (INAC 2011)*, edited by ABEN, Rio de Janeiro, RJ, Brazil, 12 pp., (2011).
- [4] Guimaraes, L.N.F., Nascimento, J.A., Borges, E.M., Lobo, P.D.C., Placco, G.M., Barrios Jr., A.G., “The TERRA Project, a Space Nuclear Micro Reactor Case Study,” in proceedings of *International Nuclear Atlantic Conference (INAC 2011)*, edited by ABEN, Rio de Janeiro, RJ, Brazil, 11 pp., (2011).
- [5] Mankins, J.C., “Technology Readiness Levels”, a NASA white paper, NASA, 1995.
- [6] Nascimento, J.A., Ono, S., Guimaraes, L.N.F., Braz Filho, F.A., Jordao, R., “Conceptual Design and Neutronic Evaluation of a Fast Micro-Reactor for Utilization in Space and Oceans,” to be published.
- [7] Nascimento, J.A., Guimaraes, L.N.F., Ono, S., “Fuel, Structural Material and Coolant for an Advanced Fast Micro Reactor,” *Journal of British Interplanetary Society*, **57**, 381-389, (2014).
- [8] Guimaraes, L.N.F., Camillo, G.P., Placco, G.M., “Closed Brayton Cycle Design for a Space Reactor,” *Transactions of the American Nuclear Society*, **1**, 147-150, (2009).
- [9] Ribeiro, G.B., Braz Filho, F.A., Guimaraes, L.N.F., “Heat Exchanger Optimization of a Closed Brayton Cycle for Nuclear Space Propulsion,” in proceedings of *International Nuclear Atlantic Conference (INAC 2015)*, edited by ABEN, Rio de Janeiro, RJ, Brazil, 14 pp., (2015).
- [10] Guimaraes, L.N.F., Placco, G.M., Marcelino, N.B., Barrios Jr., A.G., Borges, E.M., Nascimento, J.A., “Advances in Power Conversion on the Brayton Cycle Loop of the TERRA Project,” in proceedings of *Nuclear and Emerging Technologies for Space (NETS2013)*, pp. 6747_1-6447_8, (2013).
- [11] Placco, G.M., *Caracterização de uma Turbina de Tesla Operando em um Ciclo Térmico Rankine*, M.Sc. Thesis from Instituto Tecnológico de Aeronáutica, São José dos Campos, SP, Brasil, (2014).
- [12] Placco, G.M., Guimaraes, L.N.F., Santos, R.S., “Passive Residual Energy Utilization System in Thermal Cycles on Water-Cooled Power Reactors,” in proceedings of *International Nuclear Atlantic Conference (INAC 2013)*, edited by ABEN, Rio de Janeiro, RJ, Brazil, 10 pp., (2013).
- [13] Taylor, R. *Prometheus Project Final Report*, National Aeronautics and Space Administration, Jet Propulsion Laboratory, California Institute of Technology, Pasadena, CA, USA, 982-R120461, (2005).
- [14] Mason, L.S., Oleson, S.R., Mercer, C.R., and Palac, D.T., “Nuclear Power System Concepts for Electric Propulsion Missions to Near Earth Objects and Mars,” in proceedings of *Nuclear and Emerging Technologies for Space 2012 (NETS2012)*, 2pp., Paper 3066 (2012).
- [15] Mason, L.S., Gibson, M., and Poston, D., “Kilowatt-class Fission Power Systems for Science and Human Precursor Missions,” in proceedings of *Nuclear and Emerging Technologies for Space 2013 (NETS2013)*, 7pp., Paper 6814, (2013).
- [16] Jansen, F., Bauer, W., Masson, F., Ruault, J.M., Worms, J.C., Detsis, E., Lassoudiere, F., Granjon, R., Gaia, E., Tosi, M.C., Koroteev, A.S., Semenkina, A.V., Tinsley, T., Hodgson, Z., Koppel, C., Guimarães, L.N.F., “DEMOCRITOS Demonstrators for Realization of Nuclear Electric Propulsion of the European Roadmaps MEGAHIT & DiPoP IEPC-2015-91079,” in proceedings of *Joint Conference of 30th International Symposium on Space Technology and Science, 34th International Electric Propulsion Conference and 6th Nano-satellite Symposium*, 10 pp., (2015)
- [17] Gibson, M., Briggs, M., Sanzi, J., Brace, M., Poston, D., Dixon, D., “Heat Pipe Powered Stirling Conversion for the Demonstration Using Flatop Fissions (DUFF) Test,” in proceedings of *Nuclear and Emerging Technologies for Space 2013 (NETS2013)*, 9pp., Paper 6812, (2013).
- [18] Poston, D.I., Dixon, D.D., McClure, P.R., Gibson, M.A., “A Simple, Low-Power Fission Reactor for Space Exploration Power Systems,” in proceedings of *Nuclear and Emerging Technologies for Space 2013 (NETS2013)*, 11pp., Paper 6965, (2013).
- [19] Poston, D.I., McClure, P.R., Dixon, D.D., Gibson, M.A., “The DUFF Experiment - What Was Learned?,” in proceedings of *Nuclear and Emerging Technologies for Space 2013 (NETS2013)*, 12pp., Paper 6967, (2013).
- [20] Dixon, D., McClure, P.R., Beller, T.E., Poston, D.I., Gibson, M.A., Bagg, S.D., “The DUFF Experiment - Why and How,” in proceedings of *Nuclear and Emerging Technologies for Space 2013 (NETS2013)*, 5pp., Paper 6968, (2013).

ELMOE: Europa Lander, Melter, and Oceanic Explorer

Lucas Beveridge¹, Weylin MacCalla², Hannah Moore³, Rittu Sam Raju⁴,
Jonathan Scherr³

¹*Department of Nuclear Engineering and Health Physics, Idaho State University, Pocatello, ID 83209*

²*Department of Electrical, Computer, Software and Systems Engineering, Embry Riddle Aeronautical University,
Daytona Beach, FL 32114*

³*Department of Nuclear Engineering, Texas A&M, College Station, TX 77843*

⁴*Department of Nuclear Engineering and Radiological Sciences, University of Michigan, Ann Arbor, MI 48109*

Abstract. ELMOE has four main sections. The first is the lander, which stays on the surface of Europa to serve as a relay station for sending information back to Earth. Second is the melt probe which is powered by a reactor. Third is the communications system, which relays data back to the lander for transmission to Earth. Finally, a small battery powered submarine is deployed when the probe reaches the ocean, which would operate for about a week. For the melt probe an outside diameter of 25 cm with a power of 250kWt was found to be optimal. A nuclear reactor was designed to provide the necessary heat. Two reactor cores were designed; one which uses HEU and the other which uses LEU. The HEU reactor is smaller and doesn't need active cooling, and so is comparatively simple. The LEU reactor does require active cooling due to the larger core volume, but is politically and economically more attractive. The final LEU design uses NaK coolant. The core thermal hydraulics for both cases were simulated in the multiphysics code COMSOL. Calculations were made to determine shielding requirements. These showed that shielding materials combined would need to be greater than 1 meter thick, which would be impractical. Further study of the shielding is therefore required. For communications, a series of transceiver modules will be left behind the probe as it melts through the ice. This system of several transceiver modules will eliminate the single point of failure possible with a communication tether attached to the melt probe, while also providing a communication link that will last the months long mission. Finally, the submarine would explore Europa's ocean. This submarine would carry instrumentation for data collection and analysis, and power supply for the submarine as well as for the instruments on board.

Keywords: Europa, Jupiter, melt probe, communications, reactor, submarine

INTRODUCTION

The moon Europa is a fully differentiated body orbiting Jupiter. It possesses a metallic core, rocky mantle, liquid water ocean, and icy outer surface. Europa is believed to possess significant geothermal activity due to tidal heating of its mantle from its orbital interaction with Jupiter and the other satellites. As hydrothermal vents on Earth are a source of life that does not require sunlight, it is believed that Europa could possess life on the floor of its liquid ocean.

Several other studies have examined the possibility of sending thermal probes into Europa's ice crust to deploy submarines or gather ocean water samples to search for potential life. However, there are still difficult problems to overcome to make such a mission feasible. In this study, we focused on what we judged to be the more difficult of the engineering problems. Namely, communications, a high-power and compact reactor design (and associated shielding), and a compact submarine to carry a maximum of scientific instrumentation.

MISSION PARAMETERS AND LANDER

To analyze the entire mission, the constraints on the landed mass and lander design had to be worked out. Initially, an overall mass limitation was calculated using the Ideal Rocket Equation to ensure that the mission was a reasonable one. Assumptions included the use of the Space Launch System (SLS) Block II for launch from Earth and the use of nitrogen tetroxide/monomethylhydrazine (NTO/MMH) fuel as propellant for landing on Europa. The allowable mass for the lander, probe, and AUV was found to be approximately 2000 kg.

The lander for this mission would require multiple vital design characteristics including shielding to withstand radiation damage throughout the duration of the mission, some method of containment for the reactor melt probe prior to the melting process, and a method to change the probe's orientation. These methods should allow for the melt probe to land horizontally and rotate upon landing until the tip of the probe contacts the ice. The lander should then include some form of startup hardware for the melt probe to increase reactivity such as a reflector or the inclusion of a drill so the probe can sink into the ice to allow the ice itself to act as a reflector. Using past lander designs, the mass for the lander was estimated to be approximately 100 kg [1].

MELT PROBE REQUIREMENTS

The speed that the probe melts through the ice is determined by the maximum duration that the lander (which relays data to Earth) is expected to operate. The radiation environment around Jupiter is quite severe, so using the Juno spacecraft as a reference [2], we could probably expect the lander to operate for about a year. However, the melt duration shouldn't be more than a few months to allow for slow melting through obstacles, and deeper than expected ice. The ice depth was assumed to be 19 to 25 km deep, but could be greater than 50 km deep [3]. This severely constrains the entire melt probe and everything within it, including the submarine.

The melt rate (descent speed) is ultimately a function of the probe's cross sectional area and power of the melter probe [4]:

$$\frac{dz}{dt} = \frac{0.8 p}{\{\Delta h_f + c_p(273.15K - T_{ice})\} R^2 \pi \rho} \quad (1)$$

The numerator is the heating power with a correction factor for heat conduction losses to the ice. The denominator is the amount of energy required to melt a cylindrical unit mass of ice with radius R at some initial ambient temperature. Obviously, this radius is effectively the outside radius of the probe. The model is somewhat more complicated than this because the ice temperature increases with depth [4]. The temperature as a function of depth can be modeled as:

$$T_{ice}(z) = T_s e^{z(T_b - T_s)/h} \quad (2)$$

The surface temperature was assumed to be the worst-case, which is 50 K (near the poles) [4]. Solving this differential equation, we can find an optimal combination of probe radius and thermal power through parametric calculations. To maximize the melt speed, the power should be as high as possible, and the radius as small as possible. It was decided that the minimum diameter to accommodate a reactor, communications system, and usefully large submarine was about 25 cm. Figure 1 shows a plot of melt depth vs total duration for several reactor powers. To illustrate how long it would take to reach the ocean, the likely maximum and minimum ice depths indicated with horizontal lines. It should be noted that this basic melt-rate model was tested and verified experimentally, and agreed very well with actual melt rates.

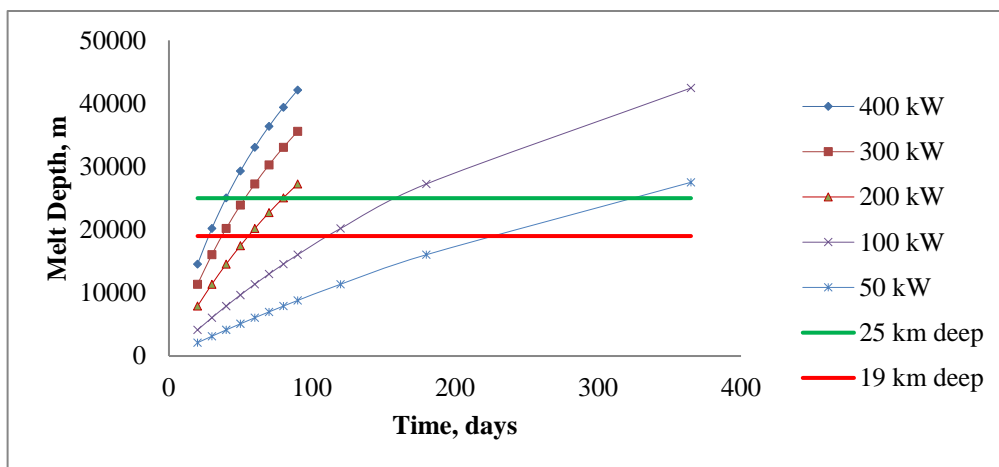


FIGURE 1. Melt Depth vs. Power and Time, 25 cm Outside Diameter

After designing the reactor, and doing thermal hydraulic analysis (which will be discussed in a later section), the maximum reactor thermal power was found to be about 250 kW. From Fig. 1, it's clear that so much power is required for melting that using a radioisotope heater is utterly impractical unless the ice is only a few km deep.

REACTOR DESIGN AND DEVELOPMENT

Reactor Overview

The development of the reactor involved close collaboration between neutronics and thermal hydraulics. Both aspects will be discussed separately but first general considerations will be presented. Table 1 lists considered reactor materials and some general comments. The first three materials are fuels and the next four are moderators. The HEU fueled core uses UN and BeO which gives it a much higher allowable core temperatures than the ZrH moderated LEU core.

TABLE 1. Summary of considered materials. If used as a structural material ZrC would fail at a lower temperature

Material	Failure Temperature	Mode of failure	General comments
U metal	1405 K	Melting	Highest ρ and k
UO ₂	~ 3100 K	Melting	Lowest ρ and k
UN	~ 2500 K	Dissociation	Higher ρ and k
BeO	2780 K	Melting	High ρ and k
Be metal	1287 K	Melting	Lower ρ than BeO, good moderator
ZrH	~ 900 K	Dissociation	Efficient moderator
Graphite	>> 3000 K	Sublimation	Excellent moderator
ZrC	> 3000 K	Melting	Low neutron absorption, ZrH cladding

Neutronics and thermal hydraulics simulations were performed separately but were tightly knit to ensure that a critical core remained cool. The LEU geometry is more complex than the HEU geometry and received far more attention since HEU is less politically attractive. Figures 2 and 3 show horizontal and vertical cross sections of the LEU reactor. It is composed of a square lattice of ZrH_{1.8} with ZrC clad holes. ZrH_{1.8} was chosen even though it is more brittle than its cousin ZrH_{1.6}. A thermo-mechanical analysis is necessary to verify its utility. The cladding prevents the migration of hydrogen out of the lattice. ZrC cladding around the fuel prevents the escape of fission products and NaK leaking into the ZrH. The outside of the lattice is composed of BeO because this material is stronger than ZrH and is a more effective reflector on the periphery of the core. Four channels are open for the control rods. The steel outer vessel is 3 mm thick. The uranium fuel is 19.1 g/cc and is kept to as low a temperature as possible to minimize the effect of thermal expansion. The final burnup for a 300 kW_{th} core for 110 days is ~1.0 MWd/kgU for the LEU core and ~0.6 MWd/kgU for the HEU core. A full thermo-mechanical analysis would determine the acceptability of these values. The layout of the NaK coolant channels concentrates them in the region of highest power. NaK in the inner 12 channels

flows downwards cooling the core while NaK in the outer 8 channels flows upwards and heats the steel vessel thereby melting the ice. The number of channels was chosen as a compromise between the capture of neutrons in the NaK and the ability to cool the core. The placement and number of the channels was not rigorously optimized. Table 2 gives component masses of the LEU core. The LEU active core is 40 cm tall with a 10 cm upper BeO reflector. The reflector is penetrated by control rods and NaK channels. The vessel is 25 cm in diameter. A perfect right cone with an aperture of 60° would be 25 cm wide and 21.732 cm tall and was modeled as such. However, the actual reactor would probably have a blunted tip similar to the nose cones of ballistic missiles. Therefore, the actual cone height would be somewhat less. The BeO in the tip of the cone contributes little to the reactor so losing it should not significantly increase the active height. The fuel diameter is 0.6 cm with a 0.05 cm cladding thickness. Lattice pitch is 1.6 cm. The 12 inner channels are 1.14 cm in diameter while the 8 outer channels are 1.4 cm in diameter.

TABLE 2. Component masses of the LEU core.

Material	Mass (kg)
U metal	33
ZrH _{1.8}	69
BeO	30
Steel	11
ZrC	4.2
NaK	1.3
Total	150

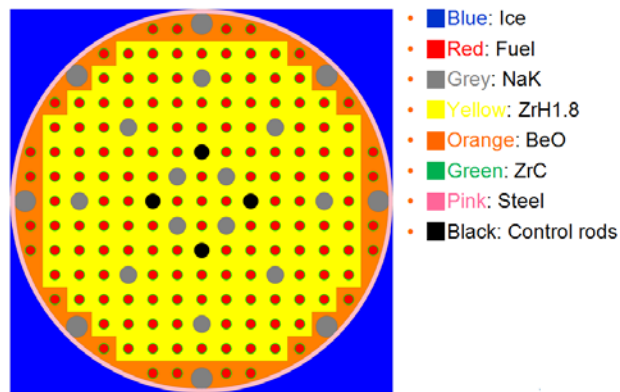


FIGURE 2. Horizontal cross section of the LEU reactor.



FIGURE 3. Vertical cross section of the LEU reactor.

The HEU core does not contain any moderator. It is composed of a solid block of UN that is machined to fit inside the steel vessel. The model does incorporate the curved vessel cone. The high melting point of UN and the high thermal conductivity enables the elimination of active cooling. An HEU core could be designed with less HEU that uses NaK, but this design will not be discussed here. Figure 4 shows the HEU core. 53 kg of HEU is required. 13.5 kg of BeO is

also required as an upper reflector which gives a total mass of 75 kg. This neglects the vessel mass and the control system mass. The HEU core is shorter than the LEU core. In addition to the control rods, the upper BeO reflector moves to keep the reactor far subcritical when traveling to Europa, and prevents criticality in case of a launch accident. The mechanism may be most difficult to design and the reliability of this component may necessitate design changes.

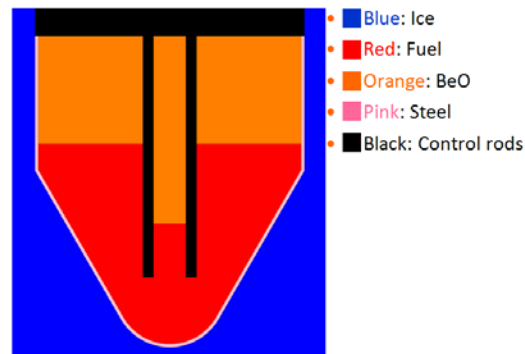


FIGURE 4. Schematic of the HEU core.

Neutronics

Preliminary calculations assumed bare concentric spheres to gain an idea of approximate masses and sizes. A uranium metal sphere surrounded by a 5 centimeters of beryllium or BeO was the ideal geometry. This was then reshaped into the HEU core design. The melting point of uranium was too low, so UN was used instead. The LEU core went through many different iterations. Preliminary calculations showed that U-ZrH had larger critical masses and volumes than a lattice of ZrH and uranium metal. The peak fuel temperature should not approach the melting temperature because of the low linear power of the pins and high thermal conductivity of uranium metal.

The first iterations of LEU lattice used hexagonal lattices. Hexagonal and square lattices were found to perform very similarly. As square lattices are easier to manufacture and design, they were chosen for the final lattice. The original pin size was 1.0 cm in diameter. It was also found that smaller pins have a higher optimal k_{inf} and smaller optimal fuel volume fractions. Larger fuel volume fractions would decrease the non-leakage probability. While no thermo-mechanical analysis was considered, thicker lattices were regarded as less susceptible to failure. This failure could come from shock, vibrations, thermal expansion, or burnup induced expansions. The optimal pitch for larger pins is greater than the optimal pitch for smaller pins, and the difference between pin diameter and pin pitch is greater for larger pins. This translates to a thicker webbing, or ZrH thickness between the pins. It was desired to maximize this value within the core.

Thermal hydraulics analysis suggested that the core needed at least 12 internal NaK coolant channel to adequately cool the core. Removing twelve of the fuel pins and replacing them with coolant channels required increasing the active core height, which contradicted a desire to minimize the weight of the core. These coolant channels were placed between the fuel pins, removing some ZrH. The distance between the fuel pin and NaK channel was now much too small. By switching to smaller pins with a higher k_{inf} , the coolant channels could be relocated into the lattice and the minimum ZrH web thickness was maximized. The desire to fit in the coolant channels and maximize the ZrH thickness dictated the placement of NaK channels in the lattice and the use of smaller pins. Unless the final burnup is to be decreased there is no incentive to increase the fuel volume from optimal. Increasing the diameter of the pins on the periphery does increase k_{eff} . This option was not taken because of the desire to minimize the ZrH thickness.

The best reflector was BeO with fuel pins. Beryllium metal performed similarly but BeO is denser and will weigh the tip of the probe down more than beryllium metal. ZrH had too high of an absorption cross section to be of use on the periphery of the core. The book by Pappalardo et al [3] includes several possible compositions for Europa's ocean and ice. Each composition was simulated and the one that induced the largest positive reactivity was pure bloedite without water. The ultimate salinity of Europa's ocean is approximately that of earth's oceans. Therefore, the composition and salinity of earth's oceans is taken as the environment which induces the lowest possible reactivity. This has the added benefit of being a safety test for the launch vehicle crashing into the ocean and the reactor being submerged.

Table 3 summarizes the behavior of the LEU and HEU cores. The first row in the table represents a possible condition if the reactor fell into earth's oceans after an accident at takeoff. While the composition of Europa's oceans are unknown, the salinity may be close to that of earth's oceans and the first row also represents a possible condition when the reactor breaches the European ocean. All rods are inserted to insure subcriticality. The second row represents a possible condition in the surface of Europa wherein the ice at 100 K is the same salinity of earth's oceans. The next two rows represent the possible reactivity induced by the ice being pure water and there being only bloedite. The fifth row gives the EOL k_{eff} and reactivity lost through burnup. The increase in water temperature inserts positive reactivity. The LEU core loses more ^{235}U than ^{238}U , which lowers the enrichment increasing the likelihood of absorption in ^{238}U . The HEU core just loses ^{235}U . The delayed neutron fraction is lower for an HEU core due to the harder neutron spectrum. Small leaky thermal cores have larger delayed neutron fractions. Faster fission neutrons are more likely to escape the system while the lower energy delayed neutrons are more likely to induce fission. The CR worth of the HEU core is small compared to the upper BeO reflector worth. As ^{10}B is a $1/v$ neutron absorber, it will have a larger effect on a thermal system than a fast system. The upper BeO reflector for the flat HEU core has great neutron importance and a system must be designed which allows for its movement. The BeO in the center of the HEU core does not move. It is a neutron multiplier but its main purpose is to shift the peak power density towards the periphery of the core thereby reducing the peak fuel temperature.

TABLE 3. Summary of reactor behavior

Scenario	LEU	HEU
273K saline water (rods in)	$k_{eff}= 0.921$	$k_{eff}= 0.944$
100K saline ice	$k_{eff}= 1.013$	$k_{eff}= 1.013$
Pure ice vs salty	$\rho=1400$ pcm	$\rho=2900$ pcm
Bloedite vs salty	$\rho=3000$ pcm	$\rho=5700$ pcm
EOL (110 days at 300 kWth)	$k_{eff}= 1.032, \rho=-1000$ pcm	$k_{eff}= 1.04, \rho=-100$ pcm
β_{eff}	$\rho=770$ pcm	$\rho=710$ pcm
CR worth	$\rho=12600$ pcm	$\rho=2600$ pcm
BeO worth	Not applicable	$\rho=8000$ pcm

Thermal Hydraulics

As previously mentioned, both reactor thermal designs were iterated with the neutronics to find workable systems. The thermal analysis was conducted in COMSOL Multiphysics. The LEU core was quite troublesome, since the model had to incorporate turbulent fluid dynamics as well as heat transfer in a complex geometry. Both had constant temperature boundary conditions ($T = 273\text{K}$) on the surfaces contacting the ice, and 250kW volumetric heat generation in the active core regions. The LEU model used the $k-\omega$ turbulence model, and had in inlet velocity to each channel of 10 m/s, and a constant outlet pressure. Again, better modeling and optimization may be desirable. Incorporating thermal expansion could help direct further optimization. Figure 5 shows the temperature distribution in the two reactors. Both are within material limits, and the HEU core could operate at even higher powers.

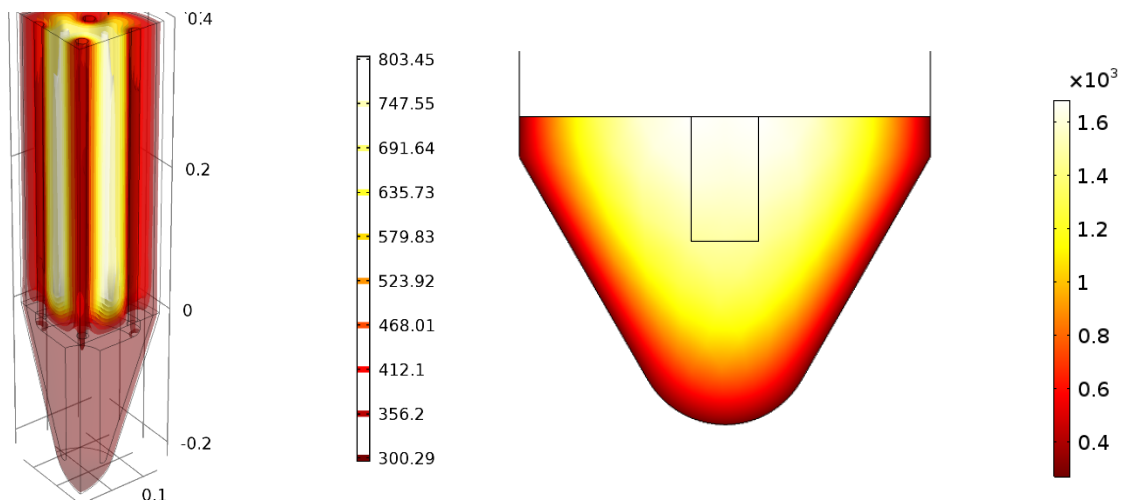


FIGURE 5. Temperatures inside the LEU reactor, and the HEU reactor. All temperatures are in Kelvin.

Shielding

Shielding would be necessary to ensure that instrumentation in the submarine could remain functioning while near the reactor melt probe during the melting process. A total ionizing radiation of 6 krad was chosen as this was the total ionizing radiation that was calculated for the instrumentation on Juno [2]. The dose limit for the instrumentation inside the submarine was estimated to be 2.08 rad/hr for the estimated four-months during melting.

TABLE 4. Summary of shielding materials considered.

Shielding Materials	Density (g/cm ³)	Shielding Type
B ₄ C	2.4	Neutron
Lithium Hydride	0.78	Neutron
Depleted Uranium	19.1	Photon
Lead	11.34	Photon
Tungsten	19.25	Photon

Using the estimates stated above, hand calculations and MCNP models were done to determine shielding requirements. The results are shown in Tables 5 and 6. Photon doses were higher than expected. This might be due to a possible streaming path as photons scatter around the shield through the water. For depleted uranium calculations, 0.7% of fissions in the reactor and shielding system were determined to be occurring within the depleted uranium itself, causing a higher photon dose than previously expected.

TABLE 5. Summary of MCNP results for shielding material effectiveness.

Shielding Dimensions	Neutron dose at top of shield (% of dose w/o shielding)	Photon dose at top of shield (% of dose w/o shielding)
10 cm Void	100%	100%
10 cm B ₄ C	17%	45%
10 cm LiH	14%	63%
10 cm U	56%	10%
10 cm Pb	60%	12%
10 cm W	24%	10%

TABLE 6. Shielding results compared to dose limitation.

Shielding Dimensions	Neutron dose at top of shield (neutrons*rad/hr)	Photon dose at top of shield (photons*rad/hr)	Mass of shield (kg)
100 cm U	0.00	751	881
100 cm Pb	0.00	64	523
100 cm W	0.00	17	888
Dose Limit	Not available	2.08	N/A

Tungsten was chosen as the photon shield while lithium hydride was chosen as the neutron shield. Calculations showed that shielding materials combined would need to be greater than 1 meter thick, which would be impractical for our purposes. However, due to lack of computational power, precise thicknesses could not be determined. Future work would be required to produce more specific results.

COMMUNICATIONS

In order for the mission to be successful, the data collected from within the ocean of Europa needs to be transmitted through the ice of Europa to the surface, where it can be sent to earth. In addition, the communications system needed to fit within the 25cm diameter of the probe, withstand up to 30MPa of pressure, and be tether-less to eliminate a single point of failure. To accomplish this, a trail of RF transceiver modules will be left behind the melt probe as it melts through the ice, as done by previous Europa melt probe designs [5], [6]. Each of these modules will function as a repeater, collecting data transmitted from the module below it, and transmitting data to the module above it. The

design of these system is composed of the structural design of the transceiver modules, the deployment system to embed them into the ice, and the antenna design.

The transceiver modules are cylinders with a diameter equal to the diameter of the melt probe, and will be attached to the back end of the melt probe using a tether that travels through the center of each of the modules, but will be severed as each one is deployed. The modules will contain a battery, transceiver, and a heat source to keep the electronics functioning properly. This will then be filled with epoxy before being encased in Aluminum 5083-O to withstand the pressure and cold. Each module could be deployed using ballistic spears that will simultaneously cut through the tether and pierce into the ice, releasing the module from the probe and fixing it into the ice. Compressed gas can eject the deployment spears.

The antenna was designed to have a resonate frequency at 500MHz, because of its ability to penetrate ice [6]. A rectangular, circularly polarized patch antenna was designed to meet the requirements described above. The antenna used a 0.5 cm FR-4 Substrate, and was approximately 13.25 cm in length and width. It was approximately circularly polarized at 500 MHz, with an S11 parameter of -9.26 dB. Parametric studies were conducted with COMSOL Multiphysics.

The placement of the transceivers will depend on the temperature of the ice as well as the chemical composition of the ice. Figure 8 below shows the possible placement of the transceiver modules using link margin analysis [6]. Because the composition and temperature of Europa's ice are not fully known, the placement of the modules was estimated using an assumption of water ice with NaCl of 13 ppm. This also assumed that the ice temperature varied linearly from the surface of the moon to the ice-water interface.

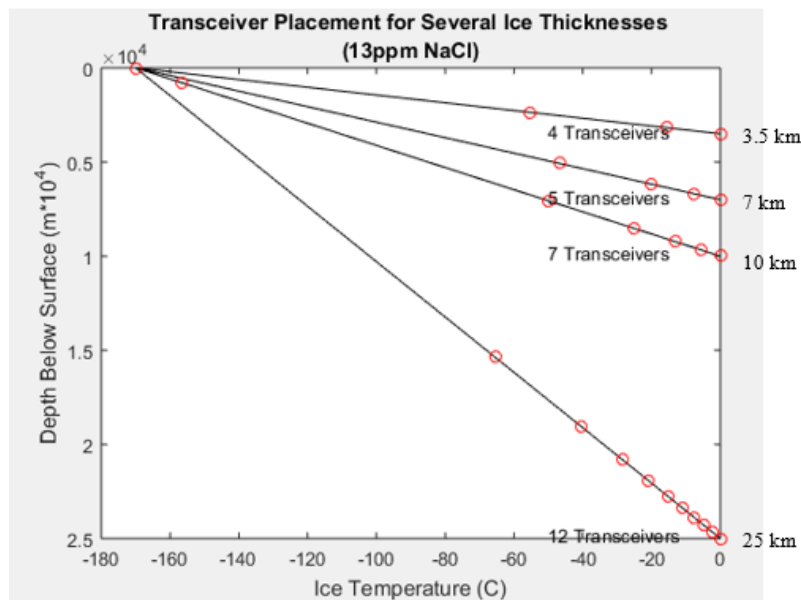


FIGURE 6. Transceiver Placement

The solid lines in Figure 6 represent the temperature of the ice at certain depths, and the red circles represent the placement of the transceiver modules.

Because this may not be a very good approximation of the actual conditions on Europa, it is estimated that 10-20 of these modules will be needed to communicate through the ice. Each transceiver module will be approximately 3 kg based on materials alone, which creates a mass of 30-60 kg added to the mass of the mission. Using this or a similar design, it will be possible to communicate data from the ocean of Europa to the surface to be sent to Earth.

SUBMARINE

The submarine plays the role of exploring Europa's subsurface ocean. This submarine would carry instrumentation for data collection and analysis, and power supply for the submarine as well as for the instruments on board. A maximum scientific instrumentation payload of 20 kg was taken into consideration while designing this submarine.

For the submarine to fit behind the melt probe, the maximum diameter allowed was 24 cm. The oceanic pressure on Europa increases by 1 MPa for every km under the ocean surface. The submarine is designed to withstand a pressure of 30 MPa without crushing or buckling. Two different submarine models which varied in their mobility were designed. One that can move horizontally to explore wider regions, and another that primarily moves vertically to reach greater depths.

The horizontal submarine is more mobile and flexible, but also more complex than the simple design of vertical submarine. The diameter and length for both are 21 cm and 147 cm respectively. A length to diameter ratio of 7 was chosen to reduce the total drag caused due to pressure drag and skin friction. Aluminum 6061-T6 is used as the material for this submarine due to its light weight, high strength, good corrosion resistance, good workability, and good thermal conductivity [7]. Both submarines are designed to withstand a pressure of 30 MPa. A wall thickness of 1 cm was used along with ribs to prevent crushing or buckling. Both theoretical and COMSOL analysis gave a critical load factor over 2 for crushing, and a critical load factor over 5 for buckling. Increasing the thickness or adding more ribs to the submarine would enable these submarines to withstand higher pressure. Figure 7 below shows the theoretically calculated load factors.

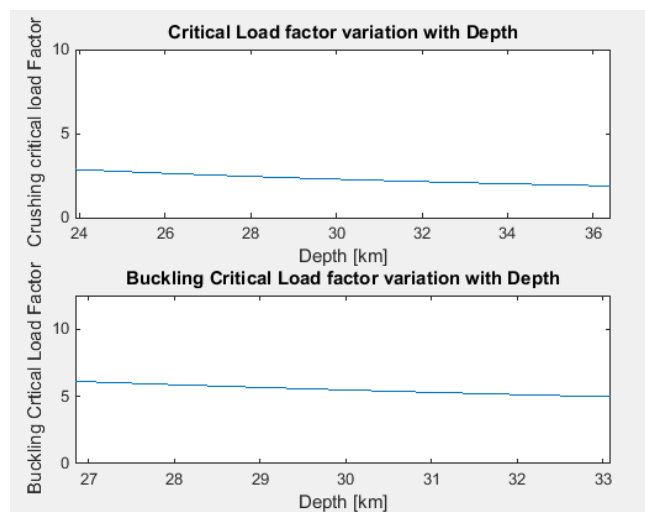


FIGURE 7. Theoretically calculated critical load factors for crushing and buckling at target depth of 30 km

As mentioned before, these submarines vary in their mobility in Europa’s subsurface ocean. The simple vertical submarine only travels vertically and it is neutrally buoyant. After deploying from the melt probe, it travels vertically downward to a target region where it will collect samples and do analysis. Since it has no propulsion system, the only power requirement is for the instruments. The vertical submarine weighs only 50 kg and requires less than 50 W electric when all the instruments are in use. One drawback to this design is that the target region should be vertically below where it was deployed from the melt probe.

The horizontal submarine is designed to move vertically as well as horizontally using its propulsion and navigation system. It weighs 100 kg and requires 60 N vertical force to keep it at a certain depth. A maximum horizontal speed of 2 m/s can be achieved by applying 30 N of thrust. A conventional propeller can be used for this purpose. Propulsion systems and brushless DC motors already exist that would suffice for this purpose [8], [9]. Navigation systems are estimated to consume 100 to 200 W. The stability of the submarine is adjusted using a sail and the fins (much like a terrestrial submarine).

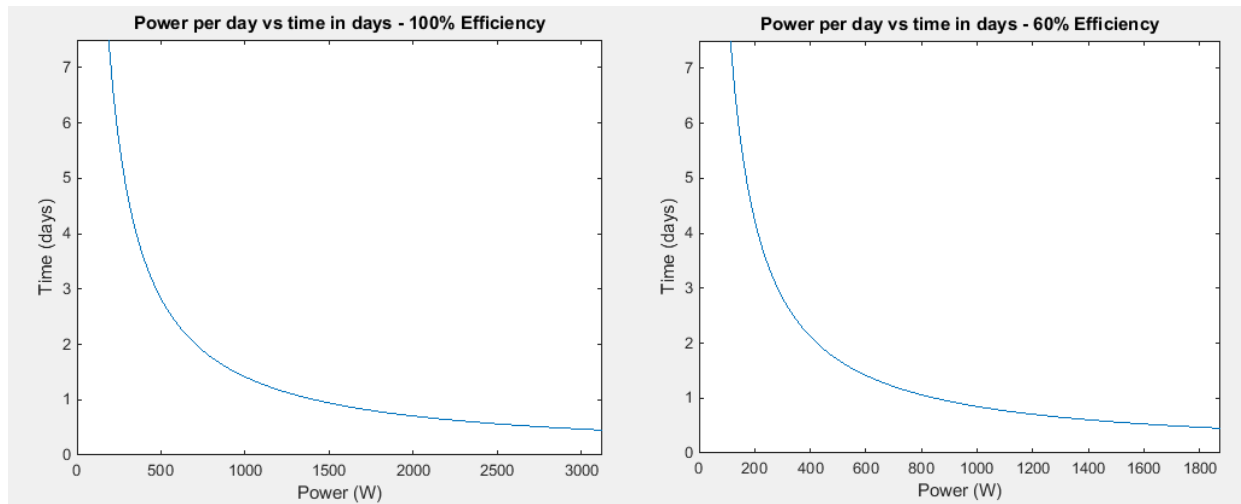


FIGURE 8. Lifetime of the submarine based on the power consumption per day at 100 percent efficient and at 60 percent efficient

Figure 8 shows the lifetime of the submarines based on the power consumed for an assumed battery capacity of 212 Wh/kg [10]. For the horizontal submarine, a lifetime of 7 days is expected at 100 percent efficiency. However, only 4 days is expected at 60 percent battery efficiency. For the vertical submarine, the lifetime is longer due to the lower power requirements.

CONCLUSIONS

Although there have been numerous studies of melt probes and deployable submarines for exploring Europa, there are still some key technologies that present serious difficulties. One of these is the small reactor capable of reaching high power densities, while being controllable with little isolation from the environment. Although the reactors studied here are not fully optimized, they show that it is certainly feasible. The HEU reactor would be far easier to build and could operate at higher powers, but isn't politically attractive.

Another of the difficult technologies is a communications system that can transmit through the ice. Tethered communication is too risky since the ice would only have to shift slightly to sever a cable. However, communicating via radio is possible with a good deal of redundancy, although more work needs to be done to optimize the antennas for circular polarization.

It's also clear that building a small instrumented submarine capable of operating for days or weeks, and that can dive deep into the ocean is also quite feasible.

NOMENCLATURE

z	=	Depth into ice (measured from surface)	ρ	=	Ice mass density
t	=	Time	T_s	=	Surface temperature
p	=	Thermal power of melter	T_b	=	Temperature of ice/ocean interface
Δh_f	=	Water heat of fusion	h	=	Total ice thickness
c_p	=	Ice heat capacity	k_{inf}	=	Neutron multiplication for an infinite reactor
T_{ice}	=	Ambient ice temperature	k_{eff}	=	Effective neutron multiplication for reactor
R	=	Melt probe radius			

ACKNOWLEDGMENTS

The authors would like to thank the staff at the Center for Space Nuclear Research for all their assistance and guidance throughout our project. In particular, we'd like to thank Dr. Stephen Herring, Vishal Patel, Juha Nieman, and Delisa Rogers.

REFERENCES

- [1] J. Powell, J. Powell, G. Maise and J. Paniagua, "NEMO: A mission to search for and return to Earth possible life forms on Europa," *Acta Astronautica*, **vol. 57**, no. 2-8, pp. 579-593, 2005.
- [2] R. Boyle, "Popular Science," 5 August 2011. [Online]. Available: <http://www.popsci.com/technology/article/2011-08/juno-probe-launches-today-study-solar-systems-biggest-planet-plus-how-survive-space>. [Accessed 25 July 2016].
- [3] R. T. Pappalardo, Europa, University of Arizona Press, 2009.
- [4] J. Biele, J. Garry, S. Sheridan, A. Morse, S. Barber, I. Wright, H. Tug and T. Mock, "Melting Probes at Lake Vostok and Europa," in *Proceedings of the Second European Workshop on Exo/Astrobiology*, Graz, Austria, 2002.
- [5] W. B. R. & F. J. Zimmerman, "Cryobot: An Ice Penetrating Robotic Vehicle for Mars and Europa," in *IEEE Aerospace Conference*, Big Sky, Montana, 2001.
- [6] S. Bryant, "Ice-Embedded Transceivers for Europa Cryobot," in *IEEE Aerospace Conference*, Big Sky, Montana, 2002.
- [7] T. Hyakudome, "Design of Autonomous Underwater Vehicle," *International Journal of Advanced Robotic Systems*, **vol. 8**, no. 1, pp. 122-130, 2011.
- [8] MOOG, Inc., "Steering, Diving, and Propulsion Systems for Autonomous Undersea Vehicle (AUV) and Torpedoes," MOOG, 2016. [Online]. Available: <http://www.moog.com/markets/defense/naval-systems/auv-controls.html>. [Accessed July 2016].
- [9] Innerspace Corp, "THRUSTER SPECIFICATIONS," 2016. [Online]. Available: <http://innerspacethrusters.com/thruster-specifications/>. [Accessed July 2016].
- [10] Eagle Picher Technologies, LLC Yardney Division, "Lithium-Ion Section," 2015. [Online]. Available: <http://yardney.com/lithium-ion-2/ncp350-1/>. [Accessed July 2016].